Analysis and Design of the Periodic Structure Based Low-Profile Planar High-Gain Antennas

by

Alireza Foroozesh

A thesis submitted to the Faculty of Graduate Studies
in partial fulfillment of the requirements for the degree of
Doctor of Philosophy

Department of Electrical and Computer Engineering
The University of Manitoba
Winnipeg, MB, Canada

Copyright © 2007 by Alireza Foroozesh

THE UNIVERSITY OF MANITOBA

FACULTY OF GRADUATE STUDIES
*****
COPYRIGHT PERMISSION

Analysis and Design of the Periodic Structure Based Low-Profile Planar High-Grain Antennas

BY

Alireza Foroozesh

A Thesis/Practicum submitted to the Faculty of Graduate Studies of The University of

Manitoba in partial fulfillment of the requirement of the degree

DOCTOR OF PHILOSOPHY

Alireza Foroozesh © 2007

Permission has been granted to the University of Manitoba Libraries to lend a copy of this thesis/practicum, to Library and Archives Canada (LAC) to lend a copy of this thesis/practicum, and to LAC's agent (UMI/ProQuest) to microfilm, sell copies and to publish an abstract of this thesis/practicum.

This reproduction or copy of this thesis has been made available by authority of the copyright owner solely for the purpose of private study and research, and may only be reproduced and copied as permitted by copyright laws or with express written authorization from the copyright owner.

To my parents, and my sister
for their love and support

and

To all teachers and mentors
who show the ways
and
never ask for the rewards

Abstract

Recently, some classes of periodic structures have been revisited in the electromagnetic area. A lot of attention is being paid to periodic structures, whose electromagnetic characteristics are not found in natural materials. They are called *metamaterials*. Among these periodic structures are *artificial magnetic conductors (AMCs)*. Magnetic conductors do not exist in nature. However, using periodic structures they can be synthesized to some extent. In particular, using periodic patches or metallic gratings on a grounded dielectric slab, one can artificially produce synthesized surfaces. Their synthesis and application are investigated in this thesis.

The transverse equivalent network (TEN) model will be extended to analyze cavity resonance antennas with artificial ground planes in this thesis. Employing this CAD-tool, a comprehensive study is done on the far-field properties of cavity resonance antennas with artificial ground planes.

Using artificial surfaces as the ground plane of this class of antennas, it is shown that a compact-size high-directivity antenna can be designed. Basically, one of the main achievements of this thesis is that the antenna directivity is obtained as high as the conventional cavity resonance antenna having an electric conductor ground plane, while the height of the antenna is reduced to almost half. Different artificial ground planes and superstrate configurations are used to design a number of high-gain low-profile as well as high-gain dual-band dual orthogonally-polarized antennas. Effects of the polarization and angular dependency of the reflection characteristics of the artificial ground planes on the antenna performance are demonstrated and investigated through numerous rigorous examples. The main contribution of this thesis is demonstration of the beneficial impact of the angular and polarization dependence of the artificial ground planes. It is shown that the fact that an antenna over an artificial ground plane exhibits higher directivity than the cases over conventional ground planes is mainly due to the angular and polarization dependence of the ground planes.

Acknowledgements

I would like to express my gratitude to my advisor, Prof. Lotfollah Shafai, for his financial support, life lessons, and the freedom he granted me in my research. I am grateful to him for his patience during the course of this project and all the technical discussions we had.

One of the best thing that happened to me during my studies at the University of Manitoba was the friendship with Dr. Malcolm Ng Mou Kehn. I am indebted to him for all discussions we had on different topics of electromagnetics. His help and collaboration in developing the MoM code used in this thesis is gratefully acknowledged and appreciated.

Profs. Lot Shafai, Joe LoVetri, Greg Bridges, Sima Noghanian, Shuan Lui, Benqi Guo taught me very valuable materials in the courses that I had with them. It is my duty to thank them all and mention it here.

As my advisory committee, Profs. Loly and LoVetri cooperated with me the most. I would like particularly to thank Prof. LoVetri for reading my thesis so carefully and the in-depth comments he made. He took my thesis as seriously as I ever wanted, cared about my writings, and corrected it.

I am thankful to Prof. Jean-Jacques Laurin, first for accepting to be my external examiner and coming to Winnipeg on a very cold day, second for his insight and broad vision over my work, and finally for his discussions and suggestions.

I appreciate the help of Mehran Fallah-Rad, Brad Tabachnik, Cory Smit and Al Symmons for fabricating of the antennas and electromagnetic structures, facilitating the measurement set-ups or performing the experimental tests.

Coming to a new country and adapting to it in a short period of time is not an easy task. Receiving helps from other people will make it easier. I was very

lucky that I had very close and extremely kind relatives in north America who supported me a lot. I would like to take this opportunity to thank my uncle Mahmoud, my aunt Villa, my cousin Mahsa and their very esteemed families for all the supports they offered me. I am not sure if I could settle down in Winnipeg within a perfect timing, if they had not helped me.

I found many good friends in Canada. Their friendship is very valuable to me. I am indebted in particular to: Behraad Bahreyni, Pouya Sekhavat, Farshid Najafi, Reza Ghorbani, Mehran Fallah-Rad, Behzad Kordi, Alireza Tadjalli, Alireza Haj-Hosseini, Keyhan Kobravi, and all supportive friends in our office, the unforgettable room #700. I would also like to thank my good friends in Iran and elsewhere and particularly, Ali Alizadeh, Babak Nassrer-Sharif, Mehdi Shirazi, Esrafil Jedari, Abbas Pirhadi, Majid Fozunbal and Alireza Mehrnia for remembering me and contacting me in different occasions. I truly appreciate their sincere friendship. I am also thankful to my former supervisor, Prof. Mohammad Hakkak in ITRC, for contacting me and his advice.

Last but definitely not the least, I want to thank my parents and my sister for all the sacrifice they made and their supports, encouragements and love, they provided me, when I needed them the most. My father and my mother, totally forgot their wishes and instead put the life priorities based on the improvement of their children. I really hope there will be a day that I can serve them as they deserve. I am particularly thankful to my mother for all pieces of advice and encouragements she patiently gave me through the long distance phone calls. If she was not there for me, I would certainly not be at this stage today.

Contents

1 Introduction **1**

1.1 Motivation and objective of the research 1

1.2 Structure of this thesis 3

2 Artificial Magnetic Conductors **8**

2.1 Perfect electric conductors and perfect magnetic conductors . 9

2.2 Circuit analogy of AMC implementation 10

2.3 AMC implementation as a surface 15

2.4 AMC bandwidth 19

2.5 Effects of various parameters on AMC characteristics 21

2.6 AMCs with shorting pins 43

2.7 Other types of AMCs 53

2.8 Conclusions 57

3 Surfaces consisting of infinitely-long periodic metallic strips on the grounded dielectric slab **59**

3.1 Characterization of a grounded dielectric slabs loaded by periodic conducting grating strips 61

3.2 Point matching method (PMM) 66

3.2.1 TE^y (H-polarized case) 66

3.2.2 TM^y (E-polarized case) 71

3.2.3 Verification and Numerical results 73

3.3 Entire-domain basis functions 74

3.3.1 TE^y (H-polarized case) 74

3.3.2 TM^y (E-polarized case) 82

3.4 Method of moment (MoM) solutions 86

3.5 Numerical results and Verifications 87

3.6 Conclusions 97

4 High-gain Planar Antennas with High-permittivity Dielectric Superstrate and Artificial Ground Planes 99

4.1 Formulation of the problem using TEN method 101

4.2 Calculation of the far-field properties 104

4.3 Radiation properties study through some examples 105

4.3.1 Antenna with 1-layer superstrate and PEC ground plane 106

4.3.2 Antenna with 1-layer superstrate and PMC ground plane 107

4.3.3 Antenna with 1-layer superstrate and AMC ground plane 112

4.3.4 Antenna with 2-layer superstrate and either PEC or PMC ground plane 122

4.3.5 Antenna with AEC/AMC ground plane 123

4.4 Analysis of electric Hertzian dipole over different ground plane without superstrate using TEN 135

4.5 Conclusions 144

5 High-gain Planar Antennas with Highly-Reflective Surface Superstrate and Artificial Ground Planes 147

5.1 Formulation of the problem using TEN method 148

5.2 Calculation of the far-field properties 151

5.3 Radiation properties study through some examples 151

5.3.1 FSS design 151

5.3.2 Cavity resonance antennas with PEC or PMC ground planes and FSS superstrate 156

5.3.3 Cavity resonance antennas with AMC ground planes and FSS superstrate 159

5.3.4 Dual-band highly-reflective FSS design 160

5.3.5 Cavity resonance antennas with AEC/AMC ground planes and FSS superstrate 163

5.4 Conclusions 171

6 Summary and Directions for Future Work 173

6.1 Future work regarding chapter 2 178

6.2 Future work regarding chapter 3 178

6.3 Future work regarding chapter 4 179

6.4 Future work regarding chapter 5 179

6.5 Generalization of the theory 179

Appendices 182

A Decomposition of the field expressions to TE and TM modes 182

B Method of Moment Analysis 185

B.1 Expansion of Electric Strip Currents into Entire-Domain Basis Functions 185

B.2 Spectral Electric Field Radiated by Spectral Basis Electric Strip Current 188

B.3 Spatial Electric Field Radiated by Entire Strip Array 189

B.4 Spectral Excitation Current Source and its Radiated Electric Field 189

B.5 Galerkin Weighting of Boundary Condition 190

Bibliography **192**

List of Figures

1.1 Two major classes of metamaterials according to [1, 2]. 2

2.1 Reflection coefficient in transmission line. 10

2.2 (a) A simple conventional resonator. (b) reflection coefficient of a lossless transmission line when it is terminated by a simple resonator. 12

2.3 Reflection coefficient vs. frequency for a typical transmission line as shown in Figure 2.2 with intrinsic impedance of $Z_0 = 376.73\ \Omega$, terminated by a simple resonator with $C = 0.4$ pF and $L = 124$ nH. (a) Reflection coefficients over a wide range of frequency. (b) Zoomed reflection phase in the vicinity of resonant frequency. 13

2.4 Reactance of a short-circuit transmission line with intrinsic impedance $Z_d = 108.77\ \Omega$ vs. frequency. $l = 6$ mm and $\beta_d = \frac{\omega}{c}\sqrt{\epsilon_r}$ where c is the velocity of light and $\epsilon_r = 12$. 14

2.5 (a) A transmission line, with $Z_d = 108.77\ \Omega$ terminated by a resonator consisting of a capacitor and distributed inductance made of piece of short circuit transmission line. $Z_d = 108.77\ \Omega$, $\beta = \frac{\omega}{c}\sqrt{\epsilon_r}$, $\epsilon_r = 12$, $l = 6\ mm$ and $Z_0 = 376.99\ \Omega$. (b) Reflection coefficient phase in a transmission line shown in (a). 15

2.6 Grounded dielectric slab loaded by metallic patches. (a) Artificial magnetic conductor (AMC) structure which is subject to the normal incident plane wave. (b) Unit cell of such a structure and the characteristics of the materials used in the structure. . 17

2.7 Reflection coefficient phase of the structure shown in Figure 2.6 when it is subjected to the normal incident TEM plane wave. . 18

2.8 Surface impedance illustration using Smith chart. 20

2.9 AMC Bandwidth illustration according to the convention introduced in the text. 20

2.10 An AMC unit cell. L and a are the unit cell and patch size, respectively. d is the thickness of the dielectric substrate with relative permittivity constant ϵ_r, relative permeability constant μ_r and loss tangent σ. Dimensions and constitutive parameters are shown in Tables 2.1 to 2.5. 23

2.11 Co-polarized reflection coefficient phase for TE^z incident wave. According to Figure 2.10 and Tables 2.1 to 2.5, corresponding dimensions and materials characteristics are, d_1 and m_1, respectively. 25

2.12 Co-polarized reflection coefficient phase for TM^z incident wave. According to Figure 2.10 and Tables 2.1 to 2.5, corresponding dimensions and materials characteristics are, d_1 and m_1, respectively. 25

2.13 Co-polarized reflection coefficient magnitude for TE^z incident wave. According to Figure 2.10 and Tables 2.1 to 2.5, corresponding dimensions and materials characteristics are, d_1 and m_1, respectively. 26

2.14 Co-polarized reflection coefficient magnitude for TM^z incident wave. According to Figure 2.10 and Tables 2.1 to 2.5, corresponding dimensions and materials characteristics are, d_1 and m_1, respectively. 26

2.15 Co-polarized reflection coefficient phase for TE^z incident wave. According to Figure 2.10 and Tables 2.1 to 2.5, corresponding dimensions and materials characteristics are, d_2 and m_1, respectively. 27

2.16 Co-polarized reflection coefficient phase for TM^z incident wave. According to Figure 2.10 and Tables 2.1 to 2.5, corresponding dimensions and materials characteristics are, d_2 and m_1, respectively. 27

2.17 Co-polarized reflection coefficient magnitude for TE^z incident wave. According to Figure 2.10 and Tables 2.1 to 2.5, corresponding dimensions and materials characteristics are, d_2 and m_1, respectively. 28

2.18 Co-polarized reflection coefficient magnitude for TM^z incident wave. According to Figure 2.10 and Tables 2.1 to 2.5, corresponding dimensions and materials characteristics are, d_2 and m_1, respectively. 28

2.19 Co-polarized reflection coefficient phase for TE^z incident wave. According to Figure 2.10 and Tables 2.1 to 2.5, corresponding dimensions and materials characteristics are, d_3 and m_1, respectively. 29

2.20 Co-polarized reflection coefficient phase for TM^z incident wave. According to Figure 2.10 and Tables 2.1 to 2.5, corresponding dimensions and materials characteristics are, d_3 and m_1, respectively. 29

2.21 Co-polarized reflection coefficient magnitude for TE^z incident wave. According to Figure 2.10 and Tables 2.1 to 2.5, corresponding dimensions and materials characteristics are, d_3 and m_1, respectively. 30

2.22 Co-polarized reflection coefficient magnitude for TM^z incident wave. According to Figure 2.10 and Tables 2.1 to 2.5, corresponding dimensions and materials characteristics are, d_3 and m_1, respectively. 30

2.23 Co-polarized reflection coefficient phase for TE^z incident wave. According to Figure 2.10 and Tables 2.1 to 2.5, corresponding dimensions and materials characteristics are, d_1 and m_2, respectively. 31

2.24 Co-polarized reflection coefficient phase for TM^z incident wave. According to Figure 2.10 and Tables 2.1 to 2.5, corresponding dimensions and materials characteristics are, d_1 and m_2, respectively. 31

2.25 Co-polarized reflection coefficient magnitude for TE^z incident wave. According to Figure 2.10 and Tables 2.1 to 2.5, corresponding dimensions and materials characteristics are, d_1 and m_2, respectively. 32

2.26 Co-polarized reflection coefficient magnitude for TM^z incident wave. According to Figure 2.10 and Tables 2.1 to 2.5, corresponding dimensions and materials characteristics are, d_1 and m_2, respectively. 32

2.27 Co-polarized reflection coefficient phase for TE^z incident wave. According to Figure 2.10 and Tables 2.1 to 2.5, corresponding dimensions and materials characteristics are, d_2 and m_2, respectively. 33

2.28 Co-polarized reflection coefficient phase for TM^z incident wave. According to Figure 2.10 and Tables 2.1 to 2.5, corresponding dimensions and materials characteristics are, d_2 and m_2, respectively. 33

2.29 Co-polarized reflection coefficient magnitude for TE^z incident wave. According to Figure 2.10 and Tables 2.1 to 2.5, corresponding dimensions and materials characteristics are, d_2 and m_2, respectively. 34

2.30 Co-polarized reflection coefficient magnitude for TM^z incident wave. According to Figure 2.10 and Tables 2.1 to 2.5, corresponding dimensions and materials characteristics are, d_2 and m_2, respectively. 34

2.31 Co-polarized reflection coefficient phase for TE^z incident wave. According to Figure 2.10 and Tables 2.1 to 2.5, corresponding dimensions and materials characteristics are, d_3 and m_2, respectively. 35

2.32 Co-polarized reflection coefficient phase for TM^z incident wave. According to Figure 2.10 and Tables 2.1 to 2.5, corresponding dimensions and materials characteristics are, d_3 and m_2, respectively. 35

2.33 Co-polarized reflection coefficient magnitude for TE^z incident wave. According to Figure 2.10 and Tables 2.1 to 2.5, corresponding dimensions and materials characteristics are, d_3 and m_2, respectively. 36

2.34 Co-polarized reflection coefficient magnitude for TM^z incident wave. According to Figure 2.10 and Tables 2.1 to 2.5, corresponding dimensions and materials characteristics are, d_3 and m_2, respectively. 36

2.35 Co-polarized reflection coefficient phase for TE^z incident wave. According to Figure 2.10 and Tables 2.1 to 2.5, corresponding dimensions and materials characteristics are, d_1 and m_3, respectively. 37

2.36 Co-polarized reflection coefficient phase for TM^z incident wave. According to Figure 2.10 and Tables 2.1 to 2.5, corresponding dimensions and materials characteristics are, d_1 and m_3, respectively. 37

2.37 Co-polarized reflection coefficient magnitude for TE^z incident wave. According to Figure 2.10 and Tables 2.1 to 2.5, corresponding dimensions and materials characteristics are, d_1 and m_3, respectively. 38

2.38 Co-polarized reflection coefficient magnitude for TM^z incident wave. According to Figure 2.10 and Tables 2.1 to 2.5, corresponding dimensions and materials characteristics are, d_1 and m_3, respectively. 38

2.39 Co-polarized reflection coefficient phase for TE^z incident wave. According to Figure 2.10 and Tables 2.1 to 2.5, corresponding dimensions and materials characteristics are, d_2 and m_3, respectively. 39

2.40 Co-polarized reflection coefficient phase for TM^z incident wave. According to Figure 2.10 and Tables 2.1 to 2.5, corresponding dimensions and materials characteristics are, d_2 and m_3, respectively. 39

2.41 Co-polarized reflection coefficient magnitude for TE^z incident wave. According to Figure 2.10 and Tables 2.1 to 2.5, corresponding dimensions and materials characteristics are, d_2 and m_3, respectively. 40

2.42 Co-polarized reflection coefficient magnitude for TM^z incident wave. According to Figure 2.10 and Tables 2.1 to 2.5, corresponding dimensions and materials characteristics are, d_2 and m_3, respectively. 40

2.43 Co-polarized reflection coefficient phase for TE^z incident wave. According to Figure 2.10 and Tables 2.1 to 2.5, corresponding dimensions and materials characteristics are, d_3 and m_3, respectively. 41

2.44 Co-polarized reflection coefficient phase for TM^z incident wave. According to Figure 2.10 and Tables 2.1 to 2.5, corresponding dimensions and materials characteristics are, d_3 and m_3, respectively. 41

2.45 Co-polarized reflection coefficient magnitude for TE^z incident wave. According to Figure 2.10 and Tables 2.1 to 2.5, corresponding dimensions and materials characteristics are, d_3 and m_3, respectively. 42

2.46 Co-polarized reflection coefficient magnitude for TM^z incident wave. According to Figure 2.10 and Tables 2.1 to 2.5, corresponding dimensions and materials characteristics are, d_3 and m_3, respectively. 42

2.47 The unit cells of an AMC (a) with and (b) without shorting pins. Relative permittivity of the dielectric is assumed to be 2.5. 43

2.48 Reflection coefficient phase for AMC structure consisting of unit cells shown in Figure 2.47(a). (a) TE-TE polarization. (b) TM-TM polarization. Measured reflection phase was done using waveguide simulator. 45

2.49 Reflection coefficient phase for AMC structure consisting of unit cells shown in Figure 2.47(b). (a) TE-TE polarization. (b) TM-TM polarization. 46

2.50 AMC structure consisting of 20 × 18 unit cells with dimensions shown in Figure 2.47(a). 48

2.51 Truncated periodic structures in TEM waveguides. (a) Unit cells consisting of patch with shorting pins. (b) Unit cells consisting of patch without shorting pins. Dimensions of the unit cells are given in Figure 2.47 49

2.52 Transmission and reflection coefficient magnitudes for the periodic structures. (a) Unit cells with shorting pins in Figure 2.51(a). (b) Unit cells without shorting pins in Figure 2.51(b). 50

2.53 (a) Unit cell of an HIS-EBG structure (with shorting pins) in a rectangular cylinder with proper boundary conditions. Dimensions and other properties of the unit cell are shown in 2.47. (b) Dispersion diagram obtained using the irreducible Brillouin zone. 52

2.54 Three different AMC unit cells with three different metallic etched shapes. (a) Square patch, (b) square ring and (c) Jerusalem Cross. 54

2.55 Co-polarized reflection coefficient phase for TE^z incident wave, corresponding to Figure 2.54 (a). 54

2.56 Co-polarized reflection coefficient phase for TM^z incident wave, corresponding to Figure 2.54 (a) 55

2.57 Co-polarized reflection coefficient phase for TE^z incident wave, corresponding to Figure 2.54 (b) 55

2.58 Co-polarized reflection coefficient phase for TM^z incident wave, corresponding to Figure 2.54 (b) 56

2.59 Co-polarized reflection coefficient phase for TE^z incident wave, corresponding to Figure 2.54 (c) 56

2.60 Co-polarized reflection coefficient phase for TM^z incident wave. corresponding to Figure 2.54 (c) 57

3.1 Grounded dielectric slab loaded by infinitely-long periodic metallic strips. 62

3.2 Reflection coefficient phases at normal incident angle, subject to the plane wave with (a) TE^y and (b) TM^y polarization. The geometry of the problem is shown in Figure 3.1. dimensions are $h = 1.59$ mm, $2w = 5$ mm and $2d = 10$ mm, and the relative permittivity of the dielectric substrate is 2.5. 63
3.3 Schematic of reflection phase retrieving using TEM waveguide. (a) 3D view and (b) top view. Polarization of the incident wave is TE^y. 64
3.4 Schematic of reflection phase retrieving using TEM waveguide. (a) 3D view and (b) top view. Polarization of the incident wave is TM^y. 65
3.5 Grounded dielectric slab loaded by infinitely-long periodic metallic strips. (a) TE^y and (b) TM^y polarization. 67
3.6 Variation of the normalized power of zeroth order reflected wave against the structure period (with respect to the wavelength) for a structure having $w = d/2$, $h = 2d$, and relative permittivity of 3 ($\epsilon_r = 3$) at incident angle of $\theta_i = 60°$. (a) TE^y and (b) TM^y polarization. 75
3.7 Reflection phase at normal incident angle, subject to the plane wave with (a) TE^y and (b) TM^y polarization. The geometry of the problem is shown in Figure 3.1. dimensions are $h = 1.59$ mm, $2w = 5$ mm and $2d = 10$ mm, and the relative permittivity of the dielectric substrate is 2.5. 76
3.8 Grounded dielectric slab loaded by infinitely-long periodic metallic strips. (a) TE^y and (b) TM^y polarization. 77

3.9 Periodic strip grating on a grounded dielectric slab. (a) 3-D view and field decompositions with respect to the z direction. (b) H-polarized and (c) E-polarized side views at $\varphi = 0°$. . . . 88

3.10 Reflection phases at normal incident angle, subject to the plane wave with (a) TE^y and (b) TM^y polarization. The structure is shown in Figure 3.1, and parameters are $h = 1.59$ mm, $2w = 5$ mm and $2d = 10$ mm. 89

3.11 Reflection phases at normal incident angle, subject to the plane wave using modal expansion method with different number of basis functions and Floquet's modes. (a) TE^y and (b) TM^y polarization. The structure is shown in Figure 3.1, and parameters are $h = 1.59$ mm, $2w = 5$ mm and $2d = 10$ mm. 90

3.12 Reflection phases at normal incident angle, subject to the plane wave using MoM with different number of basis functions and Floquet's modes.(a) TE^y and (b) TM^y polarization.The structure is shown in Figure 3.1, and parameters are $h = 1.59$ mm, $2w = 5$ mm and $2d = 10$ mm. 91

3.13 Surface current distributions on the strip versus its width, for different number of basis functions using modal expansion. The incident plane wave is at normal angle. (a) Induced $|J_x|$ due to the TE^y polarization with ($H^i_y = 1A/m$).(b) Induced $|J_y|$ due to the TM^y polarization with ($E^i_y = 1V/m$). The structure is shown in Figure 3.1, and parameters are $h = 1.59$ mm, $2w = 5$ mm and $2d = 10$ mm. 92

3.14 Reflection phases at various incident angles, using entire domain modal expansion with $N = M = 20$.(a) TE^y and (b) TM^y polarization. The structure is shown in Figure 3.1 with periodicity of $d_x = 12$ mm, strip width of $l_x = 7.86$ mm and dielectric slab thickness of $t = 1.6$ mm. 94

3.15 Reflection phases of the conducting periodic strip on grounded dielectric slab versus frequency for various incident angles. The electric field of the incident wave is x-directed.(a) TE^z at $\phi = 90°$ and (b) TM^z at $\phi = 0°$. The structure is shown in Figure 3.1 with periodicity of $d_x = 12$ mm, strip width of $l_x = 7.86$ mm and dielectric slab thickness of $t = 1.6$ mm. 95

3.16 Reflection phases of the conducting periodic strip on grounded dielectric slab versus frequency for various incident angles. The electric field of the incident wave is y-directed.(a) TE^z at $\phi = 0°$ and (b) TM^z at $\phi = 90°$. The structure is shown in Figure 3.1 with periodicity of $d_x = 12$ mm, strip width of $l_x = 7.86$ mm and dielectric slab thickness of $t = 1.6$ mm. 96

4.1 An electric Hertzian dipole embedded in a substrate and covered by a superstrate layer. z_0 is the position of the horizontal electric Hertzian dipole. B and t are the thicknesses of the substrate and superstrate, respectively. 100

4.2 Resonance behavior of the transmission line model of the antenna structure using superstrate dielectric with high permittivity shown in Figure 4.1. 100

4.3 Resonance behavior of the transmission line model of the antenna structure using superstrate dielectric with high permittivity and terminated by an open circuit (PMC). 100

4.4 (a) An electric Hertzian dipole embedded between multilayer dielectric structure and above an impedance surface acting as a ground plane. (b) Transmission line circuit representing transverse equivalent network to calculate the horizontal electric field induced on the electric Hertzian dipole due to the plane wave incidence in the far-field region. 102

4.5 (a) A Hertzian dipole above surface impedance ground plane and beneath a dielectric superstrate layer. (b) TEN model to calculate the horizontal electric field induced on the electric Hertzian dipole due to the plane wave incidence in the far-field region. 106

4.6 Directivity versus air-gap height (d_1/λ_0) and dielectric superstrate thickness (d_2/λ_e) for the cavity resonance antenna shown in Fig. 4.5 with PEC ground plane. Superstrate relative permittivity is $\epsilon_2 = 9.8$. 108

4.7 Radiation patterns of the antenna shown in Fig. 4.5 with PEC ground plane for different superstrate relative permittivities and thicknesses listed in Table 4.1 109

4.8 Directivity versus air-gap height (d_1/λ_0) and dielectric superstrate thickness (d_2/λ_e) for the cavity resonance antenna shown in Fig. 4.5 with PMC ground plane. Superstrate relative permittivity is $\epsilon_2 = 9.8$. 110

4.9 Radiation patterns of the antenna shown in Fig. 4.5 with PMC ground plane for different superstrate relative permittivities and thicknesses listed in Table 4.2. 111

4.10 Three different unit cells as AMC building blocks. (a) AMC1, (b) AMC2 and (c) AMC3 unit cells. 113

4.11 Reflection coefficient phases corresponding to the AMCs with unit cells shown in Figure 4.10. 114

4.12 Surface impedances corresponding to the AMC unit cells shown in Figure 4.10 having reflection coefficient phase shown in Figure 4.11. (a) Surface impedance magnitude (b) surface impedance phase. 115

4.13 Directivity versus air-gap height (d_1/λ_0) and dielectric superstrate thickness (d_2/λ_e) for the cavity resonance antenna shown in Fig. 4.5 with AMC1 ground plane. Superstrate relative permittivity is $\epsilon_2 = 9.8$. 118

4.14 Radiation patterns of the antenna shown in Fig. 4.5 with AMC1 ground plane for different superstrate relative permittivities thicknesses listed in Table 4.4. 119

4.15 Radiation patterns of the antenna shown in Fig. 4.5 with AMC2 ground plane for different superstrate relative permittivities thicknesses listed in Table 4.5. 119

4.16 Radiation patterns of the antenna shown in Fig. 4.5 with AMC3 ground plane for different superstrate relative permittivities and thicknesses listed in Table 4.6. 120

4.17 Hertzian dipole embedded between double-layer dielectric superstrate and a ground plane. 122

4.18 Radiation patterns of the antenna shown in Figure 4.17 having PEC ground plane for superstrate relative permittivity of $\epsilon_r = 9.8$. Dimensions are given in Table 4.7 123

4.19 Radiation patterns of the antenna shown in Figure 4.17 having PMC ground plane for superstrate relative permittivity of $\epsilon_r = 9.8$. Dimensions are given in Table 4.7 124

4.20 Grounded dielectric slab loaded by infinitely-long periodic metallic strips. Periodicity (d_x) is 6 mm, strip width (l_x) is 5.54 mm, and the dielectric thickness (t) is 1.6 mm. The relative permittivity of the dielectric is 2.5. 125

4.21 Corresponding reflection phase versus incident angles of the structure shown in Figure 4.20 in AMC mode with dimensions of d_x= 6 mm, l_x= 5.54 mm, and t= 1.6 mm. The relative permittivity of the dielectric is 2.5 and the operating frequency is 9.5 GHz. 126

4.22 Surface impedance magnitude of the structure shown in Figure 4.20 with dimensions of d_x= 6 mm, l_x= 5.54 mm, and t= 1.6 mm. The relative permittivity of the dielectric is 2.5. Operating frequency for AMC is 9.5 GHz. 127

4.23 Directivity versus air-gap height (d_1/λ_0) and dielectric superstrate thickness (d_2/λ_e) for the cavity resonance antenna shown in Figure 4.5 with the ground plane shown in Figure 4.20 operating in AMC mode. Superstrate relative permittivity is $\epsilon_2 = 9.8$. 128

4.24 Radiation patterns of the antenna shown in Figure 4.5 with the ground plane shown in Figure 4.20, operating in AMC mode, and different superstrate relative permittivities. 128

4.25 Corresponding reflection phase versus incident angles of the structure shown in Figure 4.20 in AEC mode with dimensions of d_x= 6 mm, l_x= 5.54 mm, and t= 1.6 mm. The relative permittivity of the dielectric is 2.5 and the operating frequency is 19.0 GHz. 129

4.26 Surface impedance magnitude of the structure shown in Figure 4.20 with dimensions of d_x= 6 mm, l_x= 5.54 mm, and t= 1.6 mm. The relative permittivity of the dielectric is 2.5. Operating frequency is 19.0 GHz. 130

4.27 Directivity versus air-gap height (d_1/λ_0) and dielectric superstrate thickness (d_2/λ_e) for the cavity resonance antenna shown in Figure 4.5 with the ground plane shown in Figure 4.20, operating in AEC mode. Superstrate relative permittivity is $\epsilon_2 = 9.8$. 132

4.28 Radiation patterns of the antenna shown in Figure 4.5 with the ground plane shown in Figure 4.20, operating in AEC mode, and different superstrate relative permittivities. 132

4.29 Top-view of the dual-polarized antenna configuration with artificial ground plane. Strips are infinitely long in the y-direction. Antenna side view is similar to the one shown in Figure 4.5. . 134

4.30 Product of the antenna directivities in AEC and AMC modes, versus air-gap height and dielectric thickness. Antenna configuration is shown in Figure 4.29. 134

4.31 Radiation patterns of the designed antenna in two different modes. Superstrate relative permittivity is $\epsilon_2 = 9.8$. Antenna configuration is shown in Figure 4.29. 135

4.32 Radiation patterns of an electric Hertzian dipole antenna placed on an infinite PMC ground plane, using TEN model. (a) The E-plane and H-plane radiation patterns over the entire half-space, (b) magnified radiation patterns around the boresight angle. . 138

4.33 Radiation patterns of an electric Hertzian dipole antenna placed at a very close distance above an infinite PEC ground plane ($\lambda/40$), using TEN model. (a) The E-plane and H-plane radiation patterns over the entire half-space, (b) magnified radiation patterns around the boresight angle. 139

4.34 Radiation patterns of an electric Hertzian dipole antenna placed at a quarter-wavelength distance above an infinite PEC ground plane ($\lambda/4$), using TEN model. (a) The E-plane and H-plane radiation patterns over the entire half-space, (b) magnified radiation patterns around the boresight angle. 141

4.35 Radiation patterns of an electric Hertzian dipole antenna placed on an infinite ground plane shown in Figure 4.20 acting in AMC mode, using TEN model. (a) The E-plane and H-plane radiation patterns over the entire half-space, (b) magnified radiation patterns around the boresight angle. 143

5.1 (a) an electric Hertzian dipole embedded between combination of multilayer dielectric and FSS superstrate structure and above and impedance surface acting as a ground plane. (b) Transmission line circuit representing transverse equivalent network to calculate the horizontal electric field induced on the electric Hertzian dipole due to the plane wave incidence in the far-field region. 149

5.2 (a) A Hertzian dipole above surface impedance ground plane and beneath a free-standing FSS superstrate layer. (b) TEN model to calculate the horizontal electric field induced on the electric Hertzian dipole due to the plane wave incidence in the far-field region. 152

5.3 Two different free-standing highly reflective FSS unit cells consisting of metallic patch (right-hand-side) and metallic ring (left-hand-side). 152

5.4 Equivalent admittance of an FSS to be used in TEN model. . 152

5.5 Reflection coefficients of the FSS structures shown in Figure 5.3, (a) magnitude and (b) phase. Operating frequency is 9.5 GHz. 154

5.6 Equivalent admittance of the corresponding FSS structures shown in Figure 5.3, (a) magnitude and (b) phase. Operating frequency is 9.5 GHz. 155

5.7 Directivity versus air-gap height of the antenna configuration shown in 5.2. Four different combinations of ideal ground planes (PEC and PMC) and FSS superstrates (FSS_1 and FSS_2), shown in Figure 5.3, are considered. 157

5.8 E- and H-plane co-polar radiation patterns versus zenith angle of the antenna configuration shown in 5.2. Four different combinations of ideal ground planes (PEC and PMC) and FSS superstrates (FSS_1 and FSS_2), shown in Figure 5.3, are considered. 157

5.9 Directivity versus air-gap length of the cavity resonance antenna configurations shown in 5.2. Three different combinations of AMC ground planes, shown in Figure 4.10, and FSS_1 superstrate, shown in Figure 5.3, are considered. 161

5.10 Radiation patterns of the cavity resonance antenna configurations shown in 5.2. Three different combinations of AMC ground planes, shown in Figure 4.10, and FSS_1 superstrate, shown in Figure 5.3, are considered. 161

5.11 Directivity versus air-gap length of the cavity resonance antenna configurations shown in 5.2. Three different combinations of AMC ground planes, shown in Figure 4.10, and FSS_2 superstrate, shown in Figure 5.3, are considered. 162

5.12 Radiation patterns of the cavity resonance antenna configurations shown in 5.2. Three different combinations of AMC ground planes, shown in Figure 4.10, and FSS_2 superstrate, shown in Figure 5.3, are considered. 162

5.13 Unit cell of a double-band free-standing FSS. Two sets of dimensions are shown for two different design namely FSS_3 and FSS_4. 163

5.14 Reflection coefficient of the FSS_3 and FSS_4 versus frequency subject to the normal incident. Dimensions of the corresponding FSSs are shown in Figure 5.13. (a) magnitude and (b) phase. . 164

5.15 Reflection coefficient magnitude versus incident angle of FSS_3 and FSS_4 shown in Figure 5.13 at (a) 9.5 GHz and (b) 19.0 GHz. 165

5.16 Reflection coefficient phase versus incident angle of FSS_3 and FSS_4 shown in Figure 5.13 at (a) 9.5 GHz and (b) 19.0 GHz. 166

5.17 Directivity versus air-gap length of the cavity resonance antenna configurations shown in 5.2. Four different combinations of ground planes AEC, AMC, PEC and PMC are considered. Artificial ground planes are shown in Figure 4.20 with the dimensions of d_x= 6 mm, l_x= 5.54 mm, and t= 1.6 mm. The relative permittivity of the dielectric is 2.5. Operating frequency for AMC and AEC are 9.5 and 19.0 GHz. The air-gap incremental length in each step is 0.001λ. (a) FSS_3 and (b) FSS_4 superstrates (shown in Figure 5.3) are used for all cases. . . . 168

5.18 E- and H-plane co-polar radiation patterns of the cavity resonance antennas with FSS_3 superstrate layer and different ground planes. Corresponding information is addressed in Table 5.3 and Figure 5.17. Operating frequency is 9.5 GHz for AMC or PMC cases and 19.0 GHz for AEC or PEC cases. 170

6.1 A typical schematic of a region and surface impedance boundary conditions relating electric and magnetic surface currents. . . . 181

B.1 Periodic strip grating on a grounded dielectric slab. 186

List of Tables

2.1 Three different thicknesses of dielectrics 24

2.2 Three different dielectric materials 24

2.3 Unit cell dimensions and AMC bandwidths for the first dielectric (m_1) with three different thicknesses 24

2.4 Unit cell dimensions and AMC bandwidths for the second dielectric (m_2) with three different thicknesses 24

2.5 Unit cell dimensions and AMC bandwidths for the third dielectric (m_3) with three different thicknesses 24

3.1 Normalized power in mode zero (specular mode) for increasing number of modes for a structure having $2d = 0.75\lambda$, $w = d/2$, $h = 2d$, and relative permittivity of 3 and incident angle of $\theta_i = 60°$ 74

4.1 Antenna directivities for PEC ground plane and different dielectric superstrate permittivities. Antennas configuration is shown in Figure 4.5. 107

4.2 Antenna directivities for PMC ground plane and different dielectric superstrate permittivities. Antennas configuration is shown in Figure 4.5. 111

4.3 Corresponding reflection phase of the AMC3 unit cell, for the very close-to-normal incident angles. Both TE and TM polarizations (with respect to z) are considered. The corresponding reflection coefficient phase is shown in Figure 4.11. The corresponding surface impedances are shown in Figure 4.12. 116

4.4 Antenna directivities for AMC1 ground plane and different dielectric superstrate permittivities. Antennas configuration is shown in Figure 4.5. 117

4.5 Antenna directivities for AMC2 ground plane and different dielectric superstrate permittivities. Antennas configuration is shown in Figure 4.5. 117

4.6 Antenna directivities for AMC3 ground plane and different dielectric superstrate permittivities. Antennas configuration is shown in Figure 4.5. 120

4.7 Antenna directivities for ideal PMC and PEC ground plane and different dielectric superstrate permittivities. The antennas configuration is shown in Figure 4.17. Constitutive parameters of the embedding dielectrics are: $\epsilon_{r1} = 1, \epsilon_{r2} = 9.8, \epsilon_{r3} = 1, \epsilon_{r4} = 9.8$ and $\mu_{r1} = \mu_{r2} = \mu_{r3} = \epsilon_{r4} = 1$. 123

4.8 Antenna directivities for different ground planes and dielectric superstrate permittivities. Antenna configuration is shown in Figure 4.5. AMC and AEC ground planes are shown in Figure 4.20 131

4.9 Air-gap heights corresponding to maximum antennas directivities addressed in Table 4.8. The lengths are normalized to the free space wave length (d_1/λ_0). 131

4.10 Dielectric thicknesses corresponding to maximum antennas directivities addressed in Table 4.8. The lengths are normalized to the corresponding wave-length in each dielectric (d_2/λ_ϵ). . . . 131

4.11 Properties of the optimized dual-band orthogonally polarized antenna shown in Figure 4.29. 135

5.1 Resonance air-gap length and their corresponding maximum directivities with different ground plane types and FSS_1 superstrate shown in Figure 5.3. 160

5.2 Resonance air-gap length and their corresponding maximum directivities with different ground plane types and FSS_2 superstrate shown in Figure 5.3. 160

5.3 Resonance air-gap length and their corresponding maximum directivities of the cavity resonance antennas with different ground plane types and FSS_3 superstrate shown in Figure 5.13. Corresponding details are given in Figure 5.17 169

5.4 Resonance air-gap length and their corresponding maximum directivities of the cavity resonance antennas with different ground plane types and FSS_4 superstrate shown in Figure 5.13. Corresponding details are given in Figure 5.17 169

Chapter 1

Introduction

1.1 Motivation and objective of the research

Antennas play a key role in microwave and wireless communication systems. Antenna performance is usually evaluated based on antenna characteristics such as gain, bandwidth and radiation patterns. Since microwave communication systems are usually massive with several integrated sub-systems, compact and small-size components are desirable. This is especially true with mobile systems, where size and weight are primary design requirements.

Antenna researchers have been employing newly revisited electromagnetic periodic structures to design more compact size antennas and improve their performance. These structures are sometimes called *metamaterials*, since they show electromagnetic behavior not found in nature. Two major classes of metamaterials, categorized in the literature [1, 2], are given in Figure 1.1. They are electromagnetic band-gap-type (EBG-type) structures and double-negative-type (DNG-type) materials. Different perspectives of metamaterial categorization can be found in [3, 4, 5].

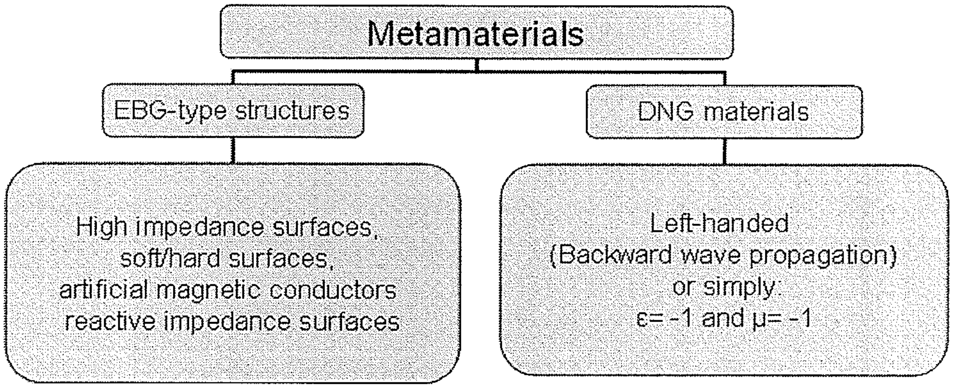
Metamaterials
EBG-type structures
DNG materials
High impedance surfaces, soft/hard surfaces, artificial magnetic conductors reactive impedance surfaces
Left-handed (Backward wave propagation) or simply: ε= -1 and μ= -1

Figure 1.1: Two major classes of metamaterials according to [1, 2].

This thesis only deals with the EBG-type structures (Figure 1.1). In fact, the main focus is on the artificial magnetic conductors (AMCs) and high impedance surfaces (HISs) and their applications to antenna design. These artificial surfaces or *metasurfaces* are synthesized using periodic structures. These periodic structures can control propagation characteristics of electromagnetic fields or boundary conditions of the corresponding electromagnetic structure in desirable ways [1].

The concept of high impedance surfaces (was introduced in contrast to the low impedance surfaces (LISs) or highly conducting surfaces which exist in nature and are recognized as good electric conductors (eg. copper, silver etc.). Unlike the electric conductors or low impedance surfaces, magnetic conductors or high impedance surfaces do not exist in nature. However, using periodic structures, one is able to produce EM surfaces which artificially simulate magnetic conductors. In fact, these surfaces act as magnetic conductors when they are subject to an incident electromagnetic wave at a specific frequency or frequency band. These surfaces are characterized based on their reflection properties when they are subjected to near-to-normal angle of incident electromagnetic wave. These periodic structures are referred to as reactive impedance surfaces (RISs) when they act in a manner between electric conductor and magnetic conductor. All the above cases are investigated based on the reflection properties of a surface subject to incident wave, in a specific frequency range and certain incident angles.

In this work, the main emphasis is on high-gain low-profile planar antenna analysis and design using periodic structures. The resonance cavity antenna will be selected as the high-gain antenna configuration and periodic structures such as AMC and frequency selective surfaces (FSSs) will be selected to make this class of antennas low-profile and high-gain. Although, the same configuration has been proposed in [6, 7] to design low-profile high-gain antenna design, many design considerations and physical insights are not presented in the available literature. For example, the effects of the angular and polarization dependency of the periodic structures on the antenna designs have not been presented in the literature. These issues are addressed in this thesis. As well, a robust model based on transverse equivalent network is presented to calculate the far-field properties of such antennas. This model outweighs the available full-wave analysis because it does not need large amount of computer memory and it is not time-consuming. It is a very appropriate engineering CAD-tool which gives an excellent estimation of far-field properties of the antennas.

1.2 Structure of this thesis

The importance of artificial magnetic conductors and reactive impedance surfaces was introduced earlier in this chapter. These surfaces or structures can be recognized as a subset of a wider category of so-called metamaterial surfaces [8, 9] or meta-substrates [10].

Chapter 2 is devoted to the analysis and design of AMC surfaces. Available commercial software packages offer reliable analysis and design tools for such periodic structures. In order to shed more insight into the physical phenomena occurring in these periodic surfaces, analogy between AMC reflection properties and loaded transmission lines with reactive impedances is presented. Different AMC designs based on different substrate dielectric permittivities will be presented and discussed. Effects of dielectric and conductor losses will be addressed. Various designs with different metallization geometries such as conducting square patch, square ring and Jerusalem cross backed by grounded dielectric slab will be demonstrated and studied as well.

Chapter 3 deals with another class of artificial surfaces consisting of infinitely periodic metallic gratings on a grounded dielectric slab. This surface acts as an AMC when the applied electric field component of the incident wave is perpendicular to the strips and as an artificial electric conductor (AEC) when the applied electric field component is parallel to the strips. One should note that, for the typical double periodic unit cells introduced in Chapter 2 this does not hold, since they show the same reflection properties independent of the principal plane, in which the applied electric field lies. Therefore, such strip-type periodic structures are able to exhibit both AMC and AEC characteristics, depending on the polarization and plane of incidence of the applied electromagnetic field. The property which distinguishes these artificial surfaces from doubly-periodic structures introduced in Chapter 2. Subsequently, strip-type artificial surfaces can operate in two modes: AMC mode, and AEC mode, each pertaining to a certain frequency, polarization, and plane of incidence.

This will be extensively discussed in Chapter 3. Prior to that and in order to be able to analyze such surfaces, different full-wave analysis methods are implemented, tested and developed. In this chapter a computer code based on the method of moment is developed to analyze such structures. The available MoM-CAD software package (Ansoft Designer) is not able to properly analyze such infinitely periodic structures.

Chapter 4 investigates high-gain planar antennas with high-permittivity dielectric superstrates when different types of surfaces are employed as the ground plane. The purpose of using high-permittivity superstrate layer is to enhance the directivity of a planar antenna [11, 12]. On the other hand, artificial surface are used as the ground plane to reduce the profile of these antenna [13]. The effects of application of some of these artificial surfaces on the profile reduction of the planar antennas are investigated and compared to the ideal surface ground planes such as perfect magnetic conductor (PMC) and perfect electric conductor (PEC). It is shown that some of the synthesized AMCs are able to reduce the profile of the antennas almost to half compared to the antennas employing conventional PEC ground planes. As well, it is shown that using strip-type periodic structure ground plane, dual-orthogonally-polarized compact dual-band high-gain antenna can be designed.

In the actual AMC cases, number of the unit cells in the AMC ground plane has to be large in order for the AMC to perform properly. Since full-wave analysis techniques, such as method of moment (MoM), finite difference time domain (FDTD), finite element method (FEM) and transmission line matrix method (TLM) are very time-consuming and need a large amount of computer memory, the transverse equivalent network (TEN) model is extended to calculate the far-field radiation properties of such antennas. This analysis not only circumvents the computational complexity appearing in the full-wave analysis methods, but it also gives insight to the physical problem. The effects of the polarization and angular dependency of the artificial ground planes on the antenna performance are studied. This study has not been addressed in the literature and will be thoroughly explored in this thesis. One should note that the TEN model is a useful CAD-tool in order to shed insight to the phenomenology of this class of antennas. This will be observed through the rigorous study of the angular and polarization effects of the ground planes on the antenna performance in this thesis.

Various antenna designs having different ground plane types, either actual or ideal (PEC or PMC), are introduced in Chapter 4 to demonstrate the applicability of artificial ground planes in high-gain low-profile, as well as high-gain dual-band antennas.

Chapter 5 investigates high-gain planar antennas with highly reflective frequency selective surface (FSS) superstrates in contrast to high-permittivity dielectric superstrate studied in Chapter 4. Conventional and different artificial surfaces are studied as the ground plane in this class of antennas. As mentioned above, the purpose of using an AMC ground plane is to make the high-gain antenna low-profile. This idea has been proposed and investigated using TLM-CAD (Microstripes) in [6] and [7]. This concept has been also verified experimentally in [6]. As discussed for Chapter 4, the transverse equivalent network (TEN) model is extended to calculate the far-field radiation properties of these antennas to circumvent the computational complexity and to shed more light into the physics of the problem. This problem is comprehensively studied in Chapter 5. The importance of the angular and polarization dependence of the ground plane is again emphasized in this chapter through rigorous analysis and examples. Sensitivity of the cavity resonance antennas directivity and its air-gap resonance length to the reflection magnitude of the FSS superstrate is another interesting issue that will be addressed in this chapter.

Various antenna designs having different ground plane types, either actual or ideal, are introduced in Chapter 6 to demonstrate the applicability of artificial ground planes in high-gain low-profile, as well as high-gain dual-band antennas.

Chapter 6 is the concluding chapter. It presents a summary of this work and its contributions along with the recommendations for future work.

Chapter 2

Artificial Magnetic Conductors

This chapter introduces the artificial magnetic conductors (AMCs). AMCs are often synthesized using periodic structures. In the most common form, they are grounded dielectric slabs loaded by periodic metallic patches with or without shorting pins. These periodic structures are highly frequency dependent and can only act as AMCs at their corresponding resonant frequency. In the vicinity of the resonant frequency, they show high impedance surface characteristics.

The organization of this chapter is as follows. Characteristics of perfect electric conductors (PECs) and perfect magnetic conductors (PMCs) are addressed first. Next, AMCs are introduced and their implementation methods are discussed. Then, effects of various parameters such as lossy materials and thickness of the dielectric slab in AMCs are studied. Finally, several new AMC types are introduced and discussed.

2.1 Perfect electric conductors and perfect magnetic conductors

Unlike electric conductors the magnetic conductors do not exist in nature. However, defining and characterizing magnetic conductors as the dual of electric conductors helps electromagnetic practitioners to simplify some of their problems [14].

Boundary conditions on a perfect electric conductor (PEC) and a perfect magnetic conductors are as follows:

$$\text{PEC} : \hat{n} \times \vec{E} = 0, \tag{2.1}$$

$$\text{PMC} : \hat{n} \times \vec{H} = 0. \tag{2.2}$$

On the other hand, the impedance surface of a plane sheet is defined as

$$Z_s = \frac{E_t}{H_t} \tag{2.3}$$

where $E_t = |\hat{n} \times (\hat{n} \times \vec{E})|$ and $H_t = |\hat{n} \times (\hat{n} \times \vec{H})|$ are transverse electric and magnetic fields on the surface, respectively and $\hat{n}$ is the unit vector normal to the surface. More advanced definition of dyadic impedance surfaces can be found in [15]. According to this definition, it can be seen that the surface impedance of a PEC is zero whereas the surface impedance of a PMC is infinite. Therefore, PEC and PMC are equivalent to short-circuit and open-circuit in the transmission line analogy.

To deal more conveniently with PEC and PMC, a new definition is introduced shortly based on the reflection coefficients in transmission line model analogy. Consider a lossless dispersionless transmission line with characteristic impedance Z_o, terminated by the impedance Z_L as depicted in Figure 2.1.

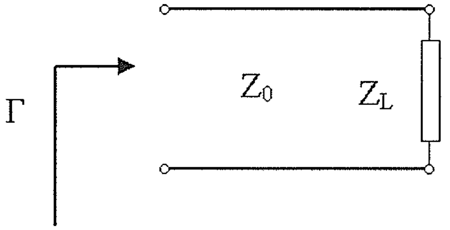

Figure 2.1: Reflection coefficient in transmission line.

The reflection coefficient at the load is calculated as [16]

$$\Gamma = \frac{Z_L - Z_o}{Z_L + Z_o} \tag{2.4}$$

According to equation 2.4, reflection coefficients for a PEC (short-circuit) and PMC (open-circuited) transmission line are -1 and 1, respectively.

Therefore one can say: PEC and PMC surfaces show reflection coefficient magnitudes of unity when they are subjected to a wave incident upon them. The reflection coefficient phase of the former is 180^o whereas of the latter is zero.

2.2 Circuit analogy of AMC implementation

The analogy between an open circuit transmission line and PMC was previously introduced. An open circuit is, in fact, a load impedance whose impedance is infinite. It is known that practical open circuits may introduce an infinite impedance only at low frequencies in an electrostatic regime. However, this cannot be achieved perfectly at microwave frequencies due to the fringing fields and intrinsic impedance of the free space. According to circuit theory, a high impedance (ideally infinite) load can be produced, at the vicinity of the resonant frequency, by a simple resonant circuit consisting of a capacitor in parallel with an inductor.

A simple parallel resonator is shown in Figure 2.2. The equivalent impedance of this circuit Z_L is:

$$Z_L = \frac{-jX_CX_L}{X_C - X_L} \tag{2.5}$$

where X_C and X_L are the magnitudes of capacitive and inductive loads, respectively. From the circuit theory, it is known that resonance occurs when $X_C = X_L$, which will produce a load impedance of infinity (open circuit). In a conventional case, simply X_C is $\frac{-1}{C\omega}$ and X_L is $L\omega$. A transmission line terminated with such a circuit is depicted in Figure 2.2 (b). The load impedance can be easily derived as

$$Z_L = \frac{jL\omega}{1 - LC\omega^2} \tag{2.6}$$

and the reflection coefficient

$$\Gamma = \frac{\frac{jL\omega}{1-LC\omega^2} - Z_0}{\frac{jL\omega}{1-LC\omega^2} + Z_0} \tag{2.7}$$

In phasor notation, one can write the reflection coefficient as

$$\Gamma = |\Gamma|e^{j\Phi_\Gamma} \tag{2.8}$$

where

$|\Gamma| = 1$

$\Phi_\Gamma = \pi - 2\tan^{-1}\left(\frac{L\omega}{(1-LC\omega^2)Z_0}\right).$

Phase of the reflection coefficient of loaded transmission line (Figure 2.2 (b)) with values of $C = 0.4$ pF, $L = 12$ nH and $Z_0 = 377$ Ω is shown in Figure 2.3. As can be seen, the following special cases and asymptotic conditions hold:

1) when $\omega = 0$, $\Phi_\Gamma = \pi$,

2) when $\omega = \frac{1}{\sqrt{LC}}$ (resonant frequency), $\Phi_\Gamma = 0$ and

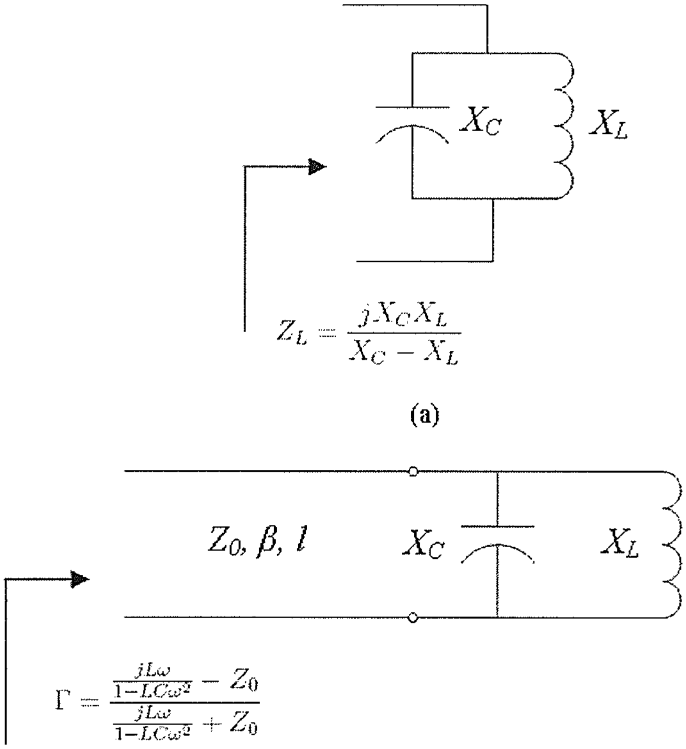
X_C
X_L
$Z_L = \frac{jX_C X_L}{X_C - X_L}$
Z_0, β, l
X_C
X_L
$\Gamma = \frac{\frac{jL\omega}{1-LC\omega^2} - Z_0}{\frac{jL\omega}{1-LC\omega^2} + Z_0}$

(a)

(b)

Figure 2.2: (a) A simple conventional resonator. (b) reflection coefficient of a lossless transmission line when it is terminated by a simple resonator.

3) when $\omega \rightarrow \infty$, $\Phi_\Gamma \rightarrow -\pi$,

which are consistent with equation (2.7). Therefore, using a resonant circuit, one is able to produce a high impedance load which resembles open circuit at a resonant frequency. A method that will be presented shortly, is the implementation of a resonant circuit consisting of a capacitor in parallel with a distributed inductance.

As is known, an open-circuit or a short-circuit piece of transmission line can produce a distributed reactive element. The input impedance of a lossless transmission line with an intrinsic impedance Z_0, and terminated by a load impedance Z_L, can be obtained by [17]

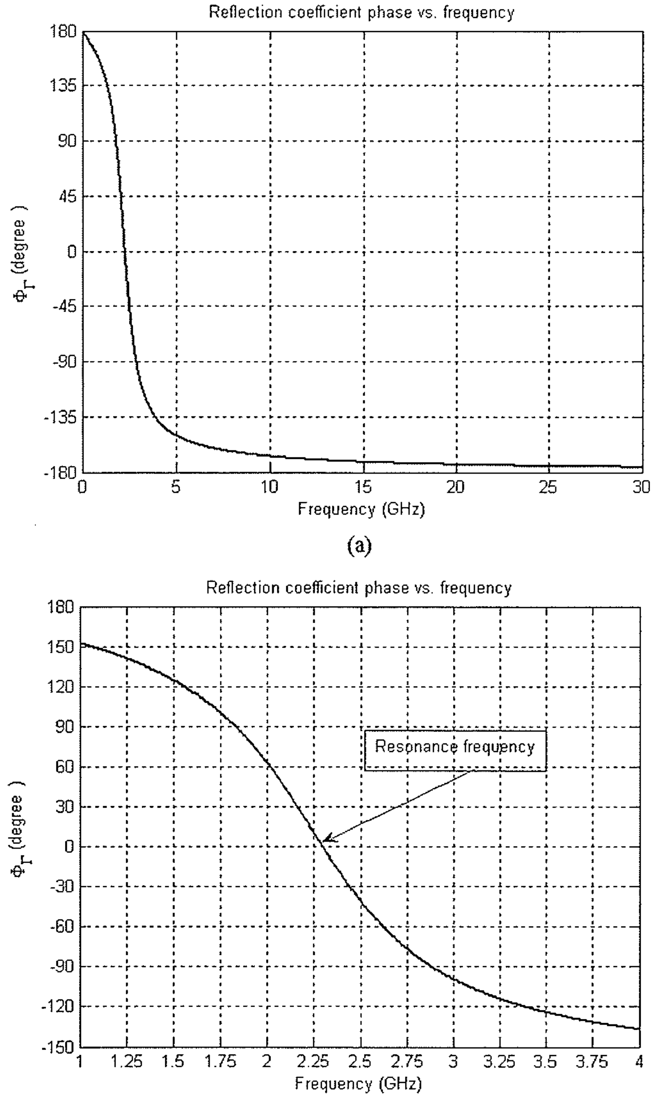

(a)

(b)

Figure 2.3: Reflection coefficient vs. frequency for a typical transmission line as shown in Figure 2.2 with intrinsic impedance of $Z_0 = 376.73\ \Omega$, terminated by a simple resonator with $C = 0.4$ pF and $L = 124$ nH. (a) Reflection coefficients over a wide range of frequency. (b) Zoomed reflection phase in the vicinity of resonant frequency.

$$Z_{in} = Z_0 \frac{Z_L + jZ_0 \tan\beta l}{Z_0 + jZ_L \tan\beta l} \tag{2.9}$$

If the transmission line is terminated by a short circuit, the input impedance

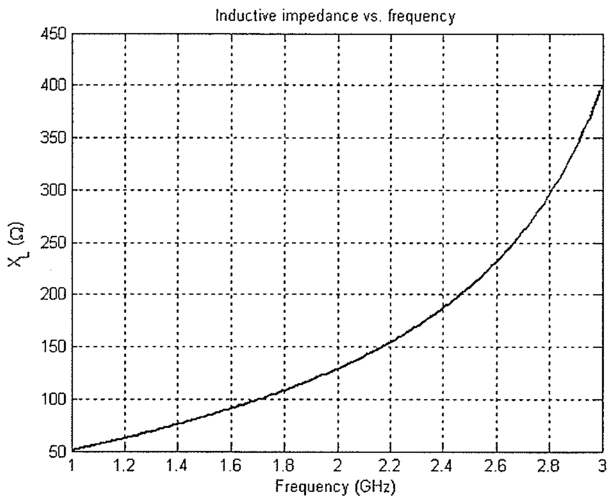

Figure 2.4: Reactance of a short-circuit transmission line with intrinsic impedance $Z_d = 108.77\ \Omega$ vs. frequency. $l = 6$ mm and $\beta_d = \frac{\omega}{c}\sqrt{\epsilon_r}$ where c is the velocity of light and $\epsilon_r = 12$.

is

$$Z_{in} = jZ_0 \tan \beta l \qquad (2.10)$$

Choosing an appropriate length l of the transmission line, one is able to produce an inductive impedance. As a typical example, consider a piece of short-circuit transmission line with length $l = 6$ mm and intrinsic impedance of $Z_d = 108.77\ \Omega$. It produces an inductive impedance in the 1-4 GHz frequency range that can be calculated from $X_L = Z_d \tan \beta_d l$, where $\beta_d = \frac{\omega}{c}\sqrt{\epsilon_r}$, c is the velocity of light and $\epsilon_r = 12$. The reactance of such a structure is shown in Figure 2.4 versus frequency. If this distributed inductive impedance is placed in parallel with a capacitance of 0.4 pF, the equivalent circuit impedance can be obtained from equation (2.5). This combination has been used as a termination load of a transmission line with an intrinsic impedance of 376.99 Ω as shown in Figure 2.5(a). The corresponding reflection coefficient phase is shown in Figure 2.5(b).

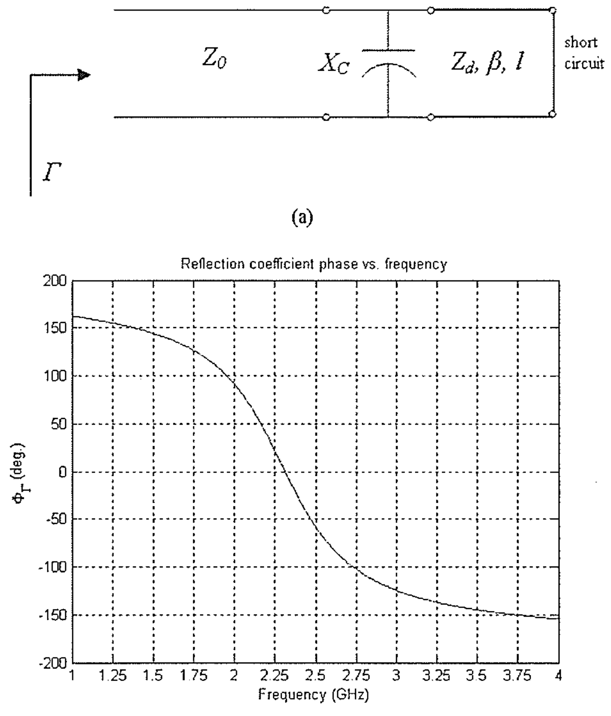

(a)

(b)

Figure 2.5: (a) A transmission line, with $Z_d = 108.77\ \Omega$ terminated by a resonator consisting of a capacitor and distributed inductance made of piece of short circuit transmission line. $Z_d = 108.77\ \Omega$, $\beta = \frac{\omega}{c}\sqrt{\epsilon_r}$, $\epsilon_r = 12$, $l = 6\ mm$ and $Z_0 = 376.99\ \Omega$. (b) Reflection coefficient phase in a transmission line shown in (a).

2.3 AMC implementation as a surface

In the previous section, it was shown that using the resonance phenomenon of a capacitor in parallel with a short-circuit transmission line, one can introduce a very high impedance load at the vicinity of resonant frequency. If this load is placed as a termination of a transmission line, the reflection coefficient phase will be zero at the resonant frequency. Obviously, the reflection magnitude of any reactive impedance (capacitance in parallel with an inductance) is unity. The concept of analogy between transmission line models and electromagnetic surfaces can be useful and inspiring to implement a similar resonance structure to the one shown in Figure 2.5, in 2-D.

In the following, implementation of a *high impedance surface* is explained. At the resonant frequency, where the reflection coefficient phase is zero, this high impedance surface acts as an artificial magnetic conductor when it is subjected to the incident plane wave. The transmission line model analogy is applied as follows.

1- The short-circuit load shown in Figure 2.5 is represented by a PEC surface.

2- The transmission line with characteristics of Z_d, β and l is represented by a dielectric slab with the same properties.

3- The capacitor shown in Figure 2.5 is represented by a capacitive screen. The surface consisting of periodic metallic patches is called *capacitive screen* in a certain frequency band [18], [19], [20].

Eventually a structure such as the one shown in Figure 2.6 is produced. The transmission line analogy to this surface implementation was introduced earlier in Figure 2.5(a).

A unit cell of an AMC structure is shown in Figure 2.6(b). If this unit cell is repeated infinitely, AMC surface will be produced, such as the one shown in Figure 2.6(a). The periodic structures are usually assumed to be repeated infinitely to circumvent the computational complexity. Analysis of such periodic surfaces without backed ground planes are discussed in the applied electromagnetic literature (*frequency selective surfaces (FSSs)* [18, 19, 20, 21]). In fact, periodic boundary conditions (linked boundary conditions) based on Floquet modal analysis in conjunction with a full-wave analysis method (e.g. moment method) are used to analyze infinite periodic arrays of conducting elements in order to extract reflection or transmission properties of that periodic structure [18, 19, 20, 21].

As an example, consider the unit cell of an AMC shown in Figure 2.6(b).

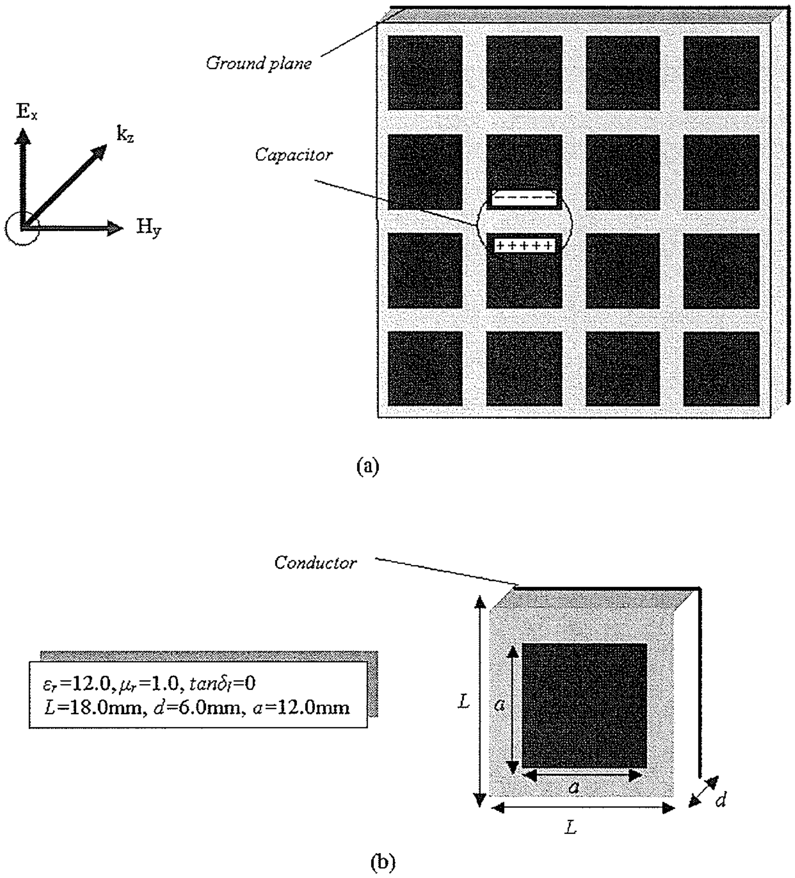
Ground plane
E_x
k_z
H_y
Capacitor
- - - -
+ + + + +
(a)
Conductor
ε_r=12.0, μ_r=1.0, $tan\delta_l$=0
L=18.0mm, d=6.0mm, a=12.0mm
L
a
a
d
L
(b)

Figure 2.6: Grounded dielectric slab loaded by metallic patches. (a) Artificial magnetic conductor (AMC) structure which is subject to the normal incident plane wave. (b) Unit cell of such a structure and the characteristics of the materials used in the structure.

The corresponding reflection coefficient phase of an AMC structure, consisting of an infinite repetition of these unit cells, subject to a normal incident TEM plane-wave is shown in Figure 2.7. The magnitude of the reflection coefficient is obviously unity over the entire frequency band and is not shown for the sake of brevity. The periodic structure shows the AMC performance at the resonant frequency, where reflection coefficient phase is zero. This specific frequency is around 2.3 GHz as shown in 2.7.

These plots are obtained from different software packages. Good agreements (less than 5% frequency shift) can be seen between the obtained results

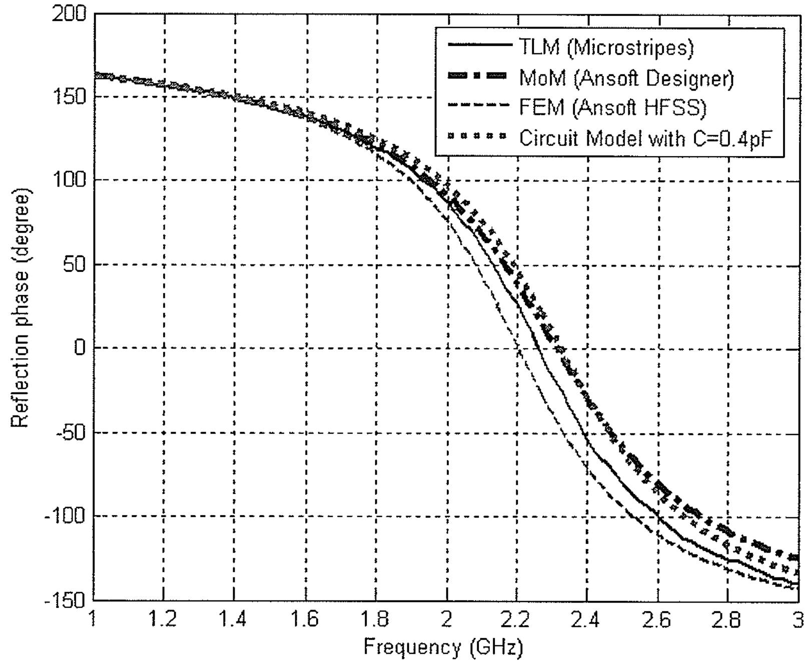

Figure 2.7: Reflection coefficient phase of the structure shown in Figure 2.6 when it is subjected to the normal incident TEM plane wave.

from three different software packages based on three different computational methods. As well, the Ansoft Designer and HFSS software packages have been employed in [22] to analyze the infinitely repeated periodic structure introduced in [23]. Since, it has been shown that the MoM is a very reliable numerical technique in solving periodic structures [23], most analyses and designs throughout this work are based on the Ansoft Designer software package (MoM-CAD tool).

If the MoM-based solution is considered as the reference, the capacitor turns out to have the value about 0.4 pF (curve-fitting).

2.4 AMC bandwidth

As was shown in Figure 2.7, a grounded dielectric slab loaded by periodic patches acts as a magnetic conductor only at the resonant frequency. When the operating frequency is altered from the resonant frequency, the load is reactive (either inductive or capacitive). For example, in Figure 2.7, when the frequency is lower than 2.3 GHz the structure is inductive and when frequency is higher than 2.3 GHz the structure is capacitive. In the literature, AMC bandwidth is usually referred to the frequency band in which the reflection coefficient phase is between $-90°$ and $+90°$. This definition is viewed and illustrated using Smith Chart as follows .

Assume that the Smith chart (Figure 2.8) corresponds to the surface impedance of the structure under study. If the surface has a purely reactive impedance, points on the unit circle correspond to its impedance. This impedance indicates that the surface is both impenetrable and lossless (as has been the case in this study so far). This is because of the fact that all points inside the circle have resistance, as well.

At first, four points are introduced on the unit circle of the Smith chart shown in Figure 2.8, which are needed for the surface bandwidth characterization. The leftmost point corresponds to the PEC surface, since it has a zero impedance. The rightmost point corresponds to the PMC, since it has infinite impedance. The topmost point is the one that introduces $\pi/2$ reflection coefficient phase, since its surface impedance is $j1$. And the bottommost point is the one that introduces $-\pi/2$ reflection coefficient phase, since its normalized surface impedance is $-j1$. These points are shown in Figure 2.8. The right semi-circle corresponds to the impedances that produces reflection coefficient phase between $-90°$ and $+90°$, so the corresponding frequencies are in the AMC bandwidth. When the surface impedance is in this region, the electric field of the reflected wave does not have any component with the opposite phase to the electric field component of the incident wave.

According to this convention, the AMC bandwidth is illustrated in Figure 2.9 for a typical reflection phase diagram (Figure 2.3). As illustrated, the bandwidth is between 1.8 GHz to 2.85 GHz.

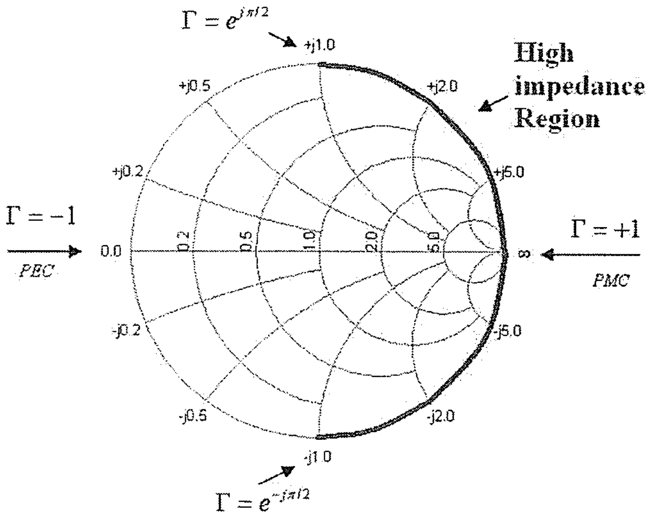
$\Gamma = e^{j\pi/2}$
+j1.0
+j0.5
+j2.0
High impedance Region
+j0.2
+j5.0
$\Gamma = -1$
PEC
0.0
0.2
0.5
1.0
2.0
5.0
∞
$\Gamma = +1$
PMC
-j0.2
-j5.0
-j0.5
-j2.0
-j1.0
$\Gamma = e^{-j\pi/2}$

Figure 2.8: Surface impedance illustration using Smith chart.

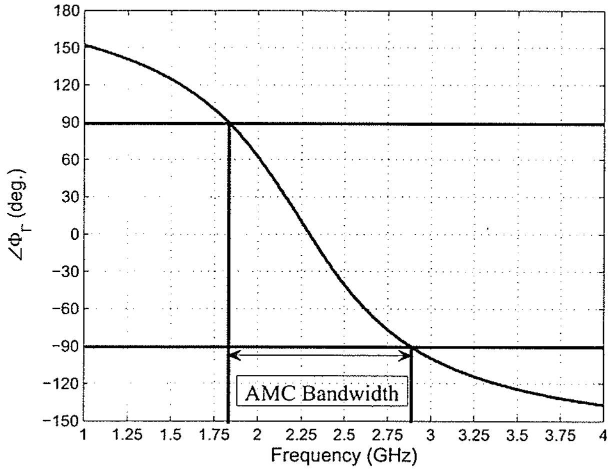

Figure 2.9: AMC Bandwidth illustration according to the convention introduced in the text.

2.5 Effects of various parameters on AMC characteristics

In this section, effects of various parameters such as dielectric permittivity, substrate thickness, losses in both metallic patches and dielectric slab and oblique incident angles are investigated on AMC characteristics. **The operating frequency is 5 GHz and all AMC designs are targeted to show zero reflection coefficient phase for a normal incident plane wave.**

The unit cell of an infinitely periodic structure employed as an artificial magnetic conductor is depicted in Figure 2.10. As shown, a is the dimension of the patch sides, L is the cell size (periodicity of the unit cells) and d is the thickness of the dielectric. Metallic patches and ground planes in all cases are assumed to be copper with a conductivity of 5.8×10^7 Siemens/m.

Effects of different dielectric materials (ϵ_r and different dielectric thicknesses (d) are studied based on the available materials in the antenna laboratory at the University of Manitoba. Three different thicknesses and three different materials are shown in Table 2.1 and 2.2. The combination of these materials provides nine different cases to study. For each different material, three different thicknesses are considered and AMCs are designed accordingly. Corresponding unit cell dimensions and bandwidth are listed in Tables 2.3, 2.4 and 2.5. Corresponding reflection coefficient phases and magnitudes for these nine different cases are shown in Figures 2.11 to 2.46. These plots show co-polarized reflection coefficients for TE^z and TM^z incident plane waves (z direction is normal to the AMC surface). The following observations are made from the plots. Of course, these observation are based on the characterization of these designed AMCs (grounded dielectric slab loaded by square metallic patches) and may not be valid for the AMCs with other types of metallizations (e.g. Jerusalem Cross, rings etc.).

1) When the substrate dielectric is thinner, larger cell and patch sizes are needed to produce resonance at a certain frequency. This is due to the fact that a thin dielectric material backed by conductor introduces low inductance. In order to compensate for that the capacitance value has to be larger to maintain the same resonant frequency. Therefore, larger unit cell and patch sizes are employed to introduce larger capacitance.

2) When the substrate dielectric has lower permittivity, larger cell and patch sizes are needed to produce resonance at a certain frequency. This is because of the fact that the capacitance between adjacent patches are less when the dielectric substrate has lower relative permittivity. To compensate for that the patch and unit cell size are needed to be larger to increase the capacitance. Of course, when the dielectric permittivity decreases the constitutive inductance of the AMC structure (grounded dielectric) increases by the factor of square root of relative permittivity. But the capacitance decreases proportionally.

3) Broader AMC bandwidths can be acquired with thicker dielectrics for the same permittivity. Also, generally, for the fixed thickness, lower permittivity provides wider a bandwidth.

4) The magnitude of the reflection coefficient is not unity when lossy materials are used in the AMC structure. As well, losses are more severe when the dielectric substrate is thinner.

5) At the vicinity of resonant frequency loss is more pronounced. This is consistent with the fact that at resonance, the electric fields inside the dielectric and the surface currents on the metallic patches reach their maximum values. Since, the dielectric loss represented by $\omega\epsilon''|\vec{E}|^2$ and conductor loss represented by $\vec{J}\cdot\vec{E}$, the more intense the field and the current become, the more ohmic

losses are produced.

6) Reflection coefficients are both angular and polarization dependent. Close-to-grazing incident angles, the AMC bandwidth is narrower for the TE polarizations whereas wider for the TM polarizations. Another interesting observation is the fact that the resonant frequency increases as the incident angle increases for both TE and TM polarizations.

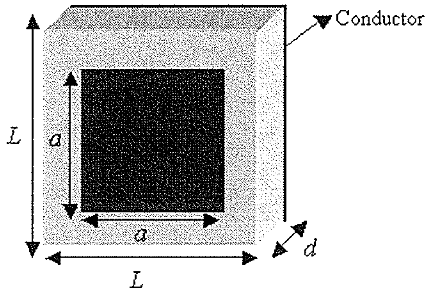

Figure 2.10: An AMC unit cell. L and a are the unit cell and patch size, respectively. d is the thickness of the dielectric substrate with relative permittivity constant ϵ_r, relative permeability constant μ_r and loss tangent σ. Dimensions and constitutive parameters are shown in Tables 2.1 to 2.5.

Table 2.1: Three different thicknesses of dielectrics

Dielectric no.	dielectric thickness (mm)
d_1	0.38
d_2	1.59
d_3	3.175

Table 2.2: Three different dielectric materials

Dielectric no.	dielectric relative permittivity	dielectric loss tangent
m_1	2.5	0.0022
m_2	3.2	0.0033
m_3	9.8	0.002

Table 2.3: Unit cell dimensions and AMC bandwidths for the first dielectric (m_1) with three different thicknesses

	L (mm)	a (mm)	Bandwidth (GHz)
d_1	20.0	18.4	0.167
d_2	20.0	16.9	1.0
d_3	15.0	13.0	1.5

Table 2.4: Unit cell dimensions and AMC bandwidths for the second dielectric (m_2) with three different thicknesses

	L (mm)	a (mm)	Bandwidth (GHz)
d_1	18.2	16.4	0.139
d_2	15.0	13.8	0.72
d_3	15.0	12.1	1.33

Table 2.5: Unit cell dimensions and AMC bandwidths for the third dielectric (m_3) with three different thicknesses

	L (mm)	a (mm)	Bandwidth (GHz)
d_1	12.0	9.47	0.111
d_2	12.0	8.5	0.5
d_3	8.0	5.5	1.38

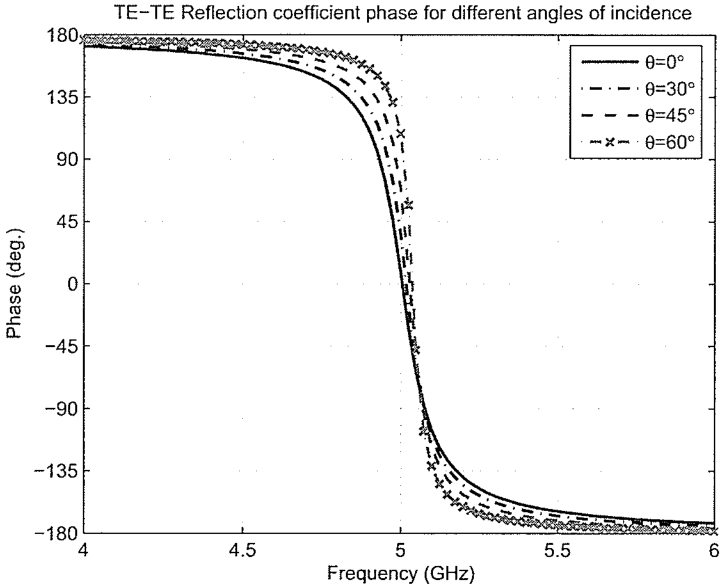

Figure 2.11: Co-polarized reflection coefficient phase for TE^z incident wave. According to Figure 2.10 and Tables 2.1 to 2.5, corresponding dimensions and materials characteristics are, d_1 and m_1, respectively.

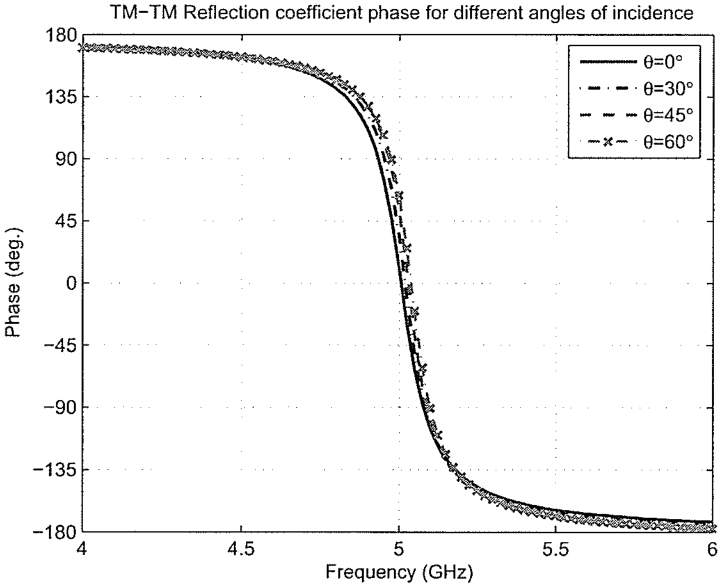

Figure 2.12: Co-polarized reflection coefficient phase for TM^z incident wave. According to Figure 2.10 and Tables 2.1 to 2.5, corresponding dimensions and materials characteristics are, d_1 and m_1, respectively.

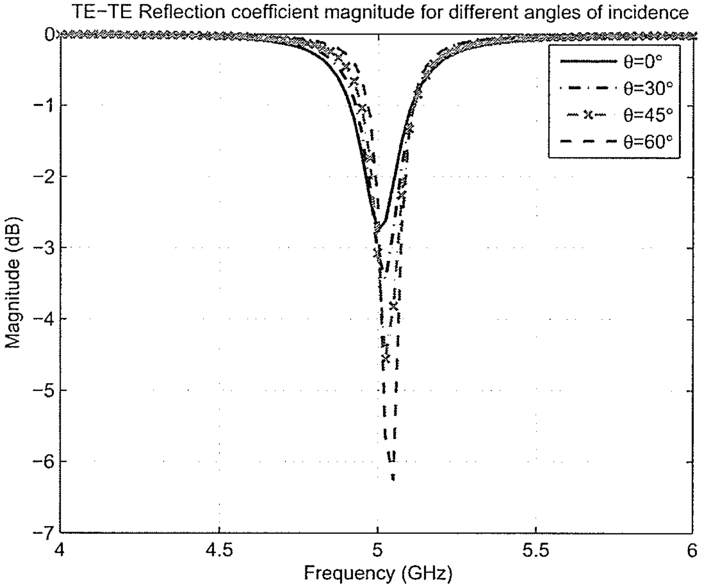

Figure 2.13: Co-polarized reflection coefficient magnitude for TE^z incident wave. According to Figure 2.10 and Tables 2.1 to 2.5, corresponding dimensions and materials characteristics are, d_1 and m_1, respectively.

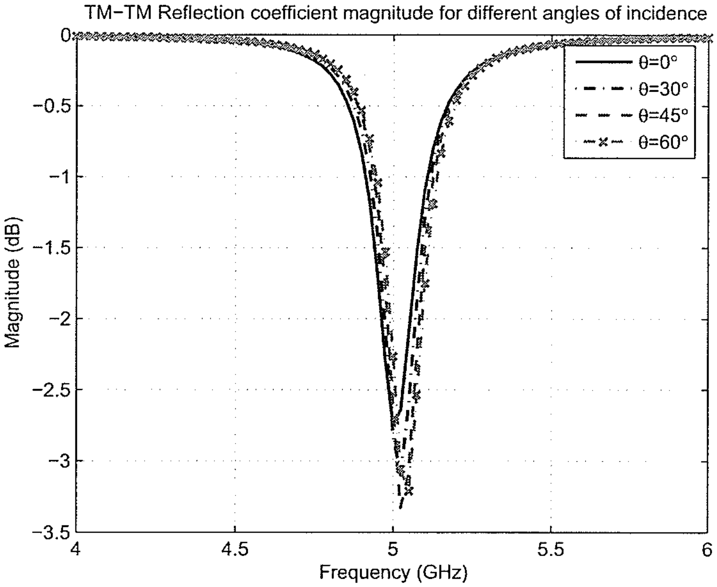

Figure 2.14: Co-polarized reflection coefficient magnitude for TM^z incident wave. According to Figure 2.10 and Tables 2.1 to 2.5, corresponding dimensions and materials characteristics are, d_1 and m_1, respectively.

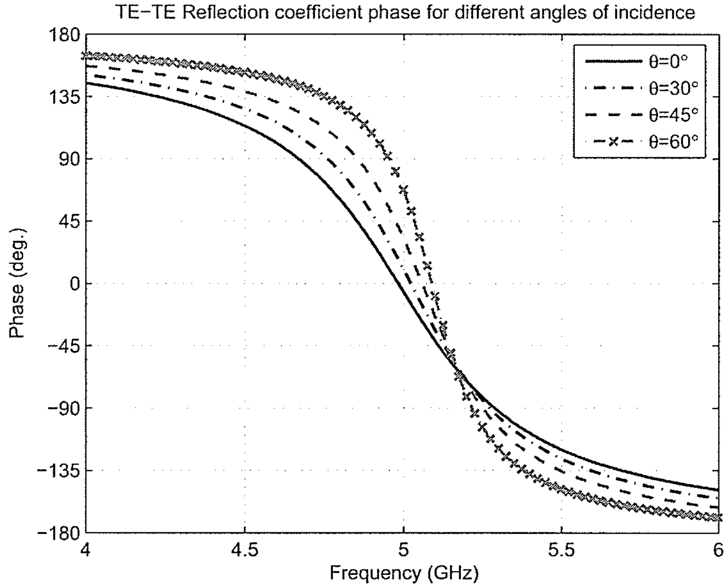

Figure 2.15: Co-polarized reflection coefficient phase for TE^z incident wave. According to Figure 2.10 and Tables 2.1 to 2.5, corresponding dimensions and materials characteristics are, d_2 and m_1, respectively.

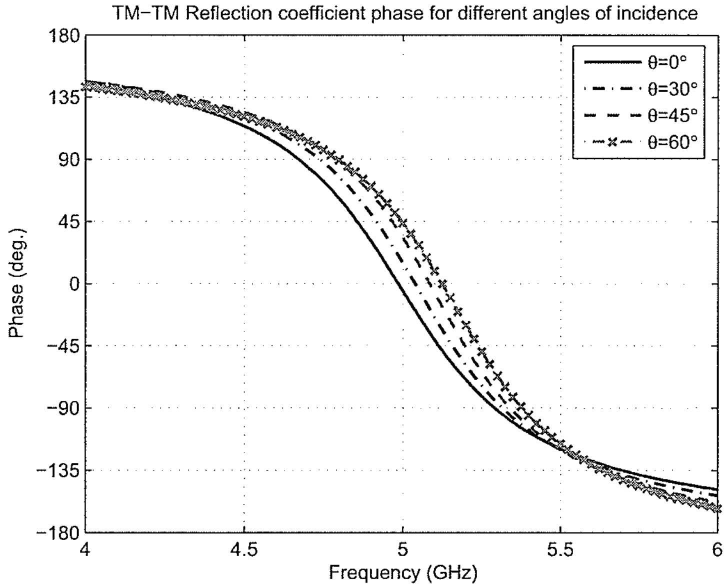

Figure 2.16: Co-polarized reflection coefficient phase for TM^z incident wave. According to Figure 2.10 and Tables 2.1 to 2.5, corresponding dimensions and materials characteristics are, d_2 and m_1, respectively.

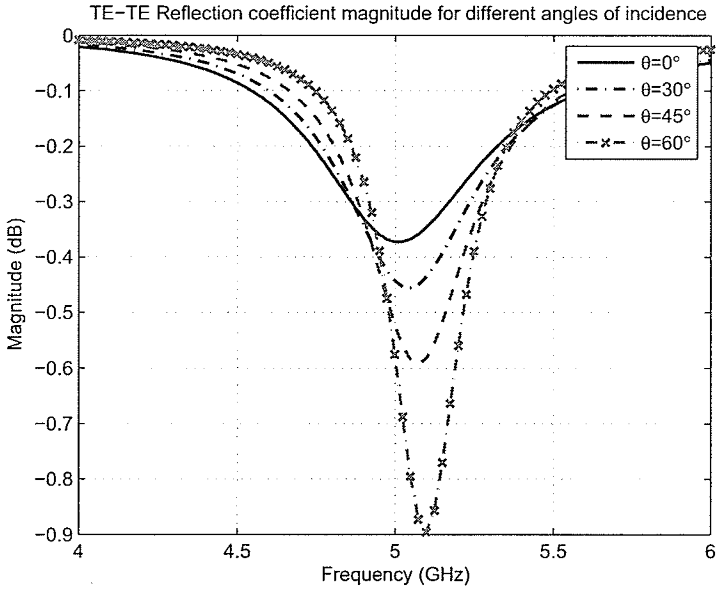

Figure 2.17: Co-polarized reflection coefficient magnitude for TE^z incident wave. According to Figure 2.10 and Tables 2.1 to 2.5, corresponding dimensions and materials characteristics are, d_2 and m_1, respectively.

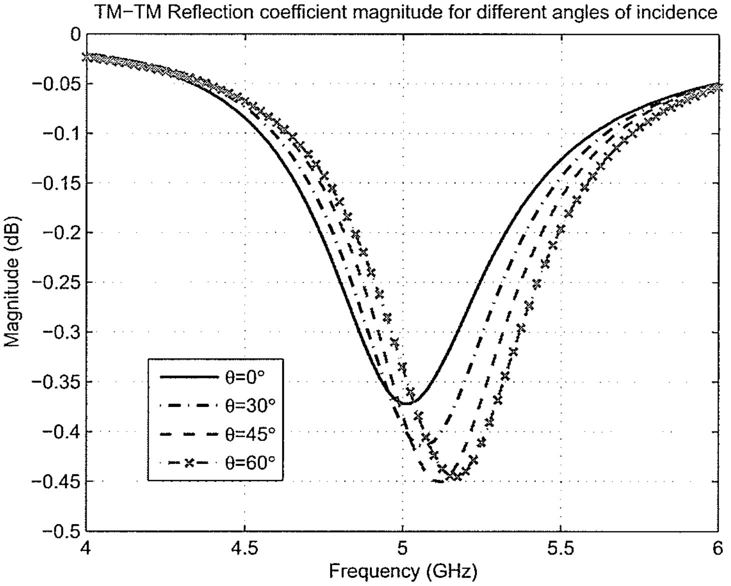

Figure 2.18: Co-polarized reflection coefficient magnitude for TM^z incident wave. According to Figure 2.10 and Tables 2.1 to 2.5, corresponding dimensions and materials characteristics are, d_2 and m_1, respectively.

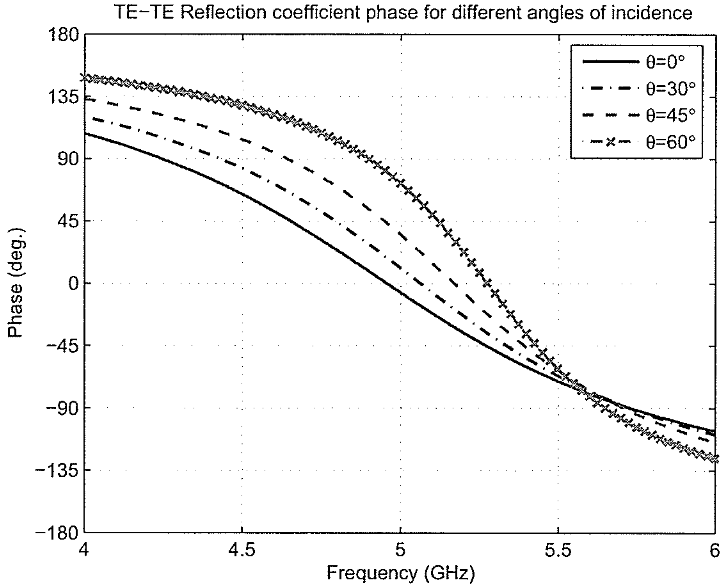

Figure 2.19: Co-polarized reflection coefficient phase for TE^z incident wave. According to Figure 2.10 and Tables 2.1 to 2.5, corresponding dimensions and materials characteristics are, d_3 and m_1, respectively.

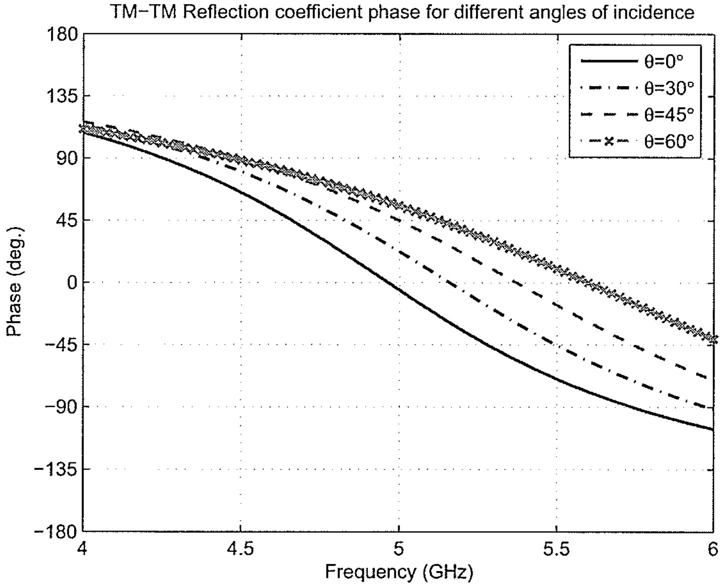

Figure 2.20: Co-polarized reflection coefficient phase for TM^z incident wave. According to Figure 2.10 and Tables 2.1 to 2.5, corresponding dimensions and materials characteristics are, d_3 and m_1, respectively.

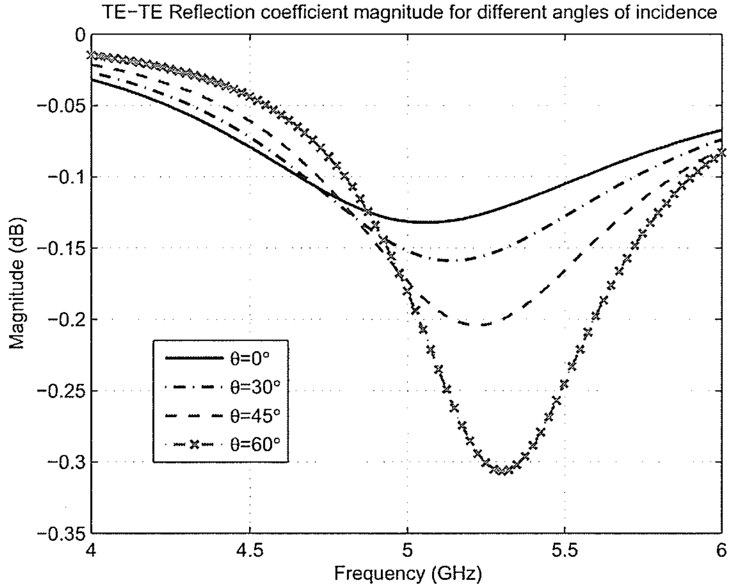

Figure 2.21: Co-polarized reflection coefficient magnitude for TE^z incident wave. According to Figure 2.10 and Tables 2.1 to 2.5, corresponding dimensions and materials characteristics are, d_3 and m_1, respectively.

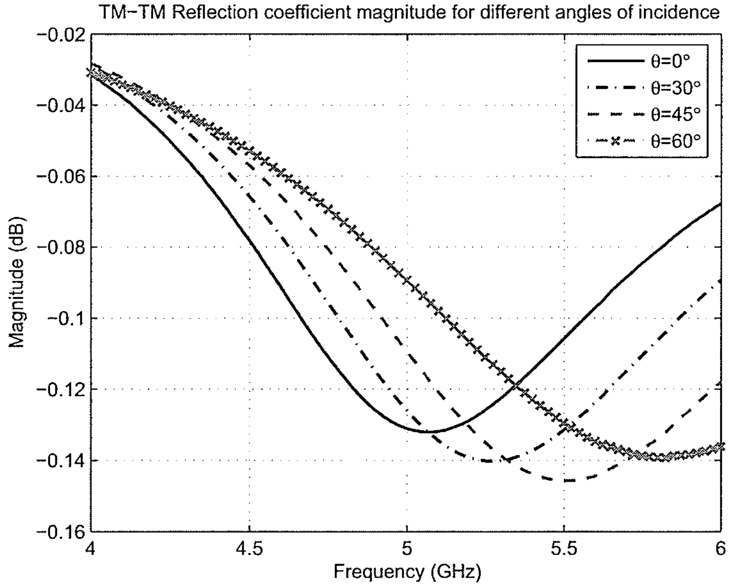

Figure 2.22: Co-polarized reflection coefficient magnitude for TM^z incident wave. According to Figure 2.10 and Tables 2.1 to 2.5, corresponding dimensions and materials characteristics are, d_3 and m_1, respectively.

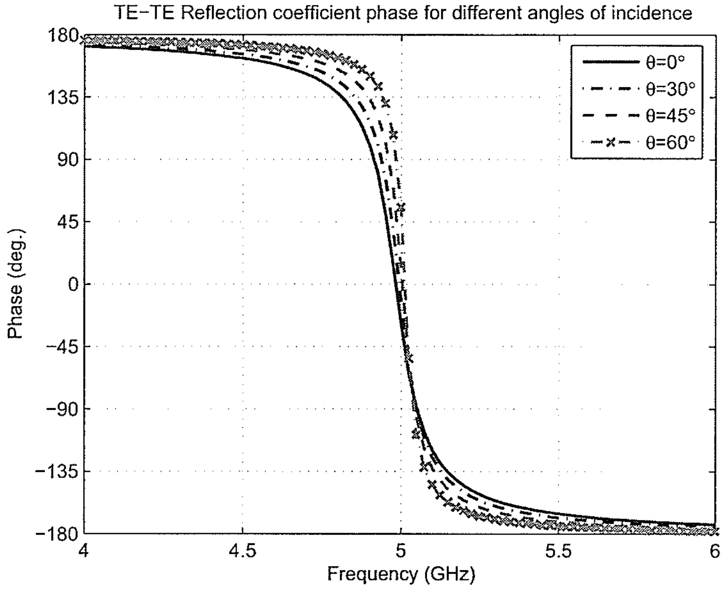

Figure 2.23: Co-polarized reflection coefficient phase for TE^z incident wave. According to Figure 2.10 and Tables 2.1 to 2.5, corresponding dimensions and materials characteristics are, d_1 and m_2, respectively.

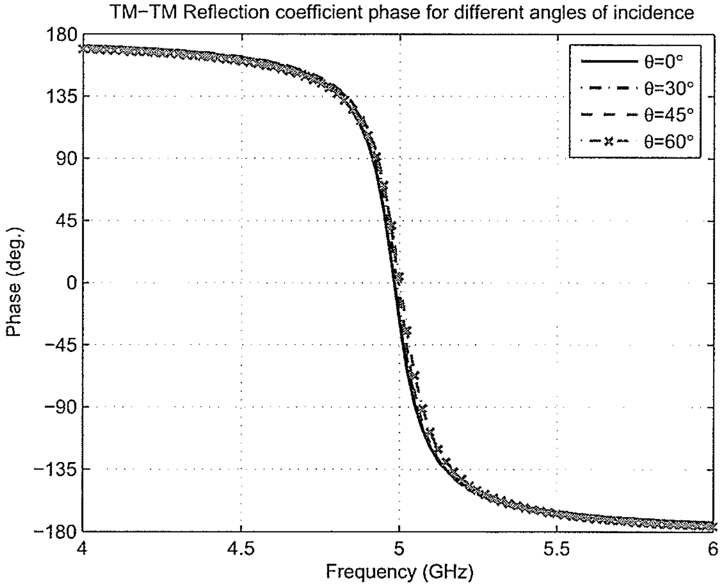

Figure 2.24: Co-polarized reflection coefficient phase for TM^z incident wave. According to Figure 2.10 and Tables 2.1 to 2.5, corresponding dimensions and materials characteristics are, d_1 and m_2, respectively.

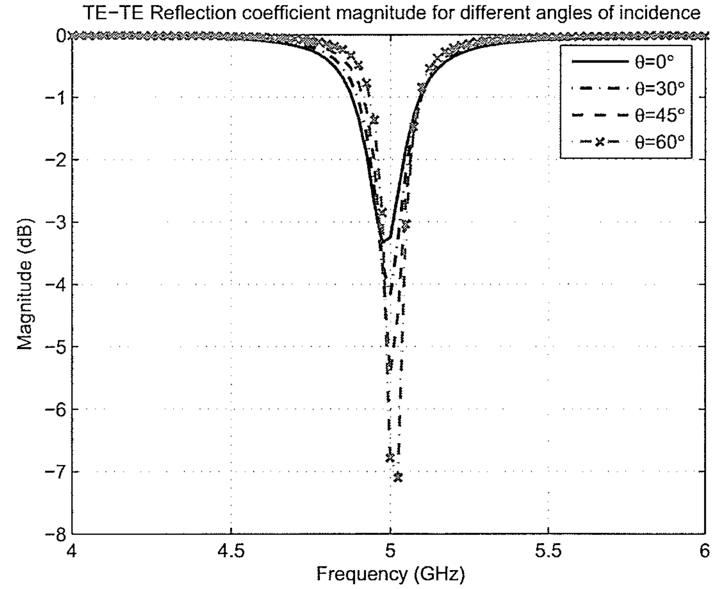

Figure 2.25: Co-polarized reflection coefficient magnitude for TE^z incident wave. According to Figure 2.10 and Tables 2.1 to 2.5, corresponding dimensions and materials characteristics are, d_1 and m_2, respectively.

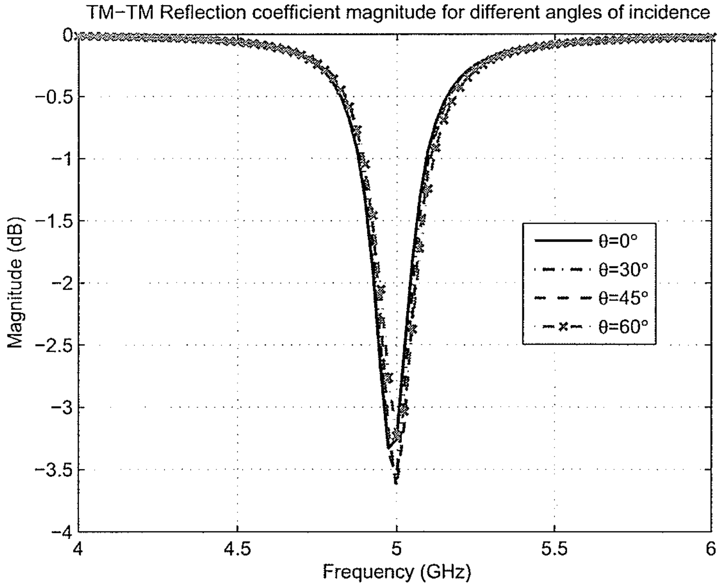

Figure 2.26: Co-polarized reflection coefficient magnitude for TM^z incident wave. According to Figure 2.10 and Tables 2.1 to 2.5, corresponding dimensions and materials characteristics are, d_1 and m_2, respectively.

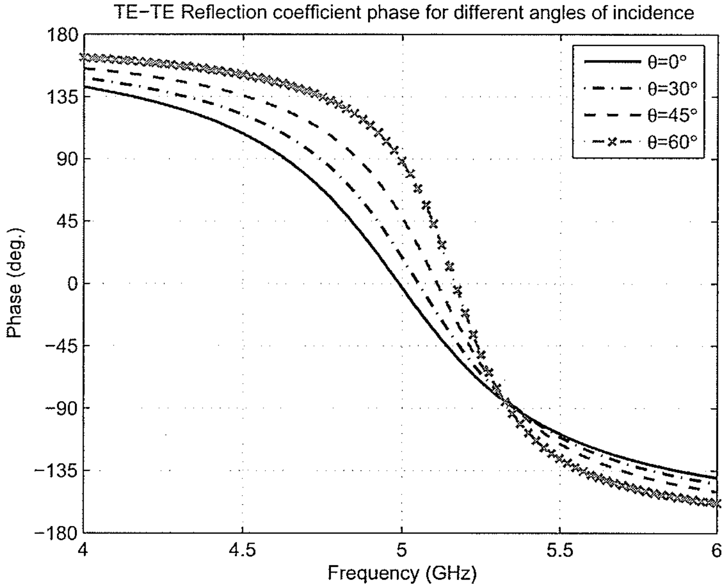

Figure 2.27: Co-polarized reflection coefficient phase for TE^z incident wave. According to Figure 2.10 and Tables 2.1 to 2.5, corresponding dimensions and materials characteristics are, d_2 and m_2, respectively.

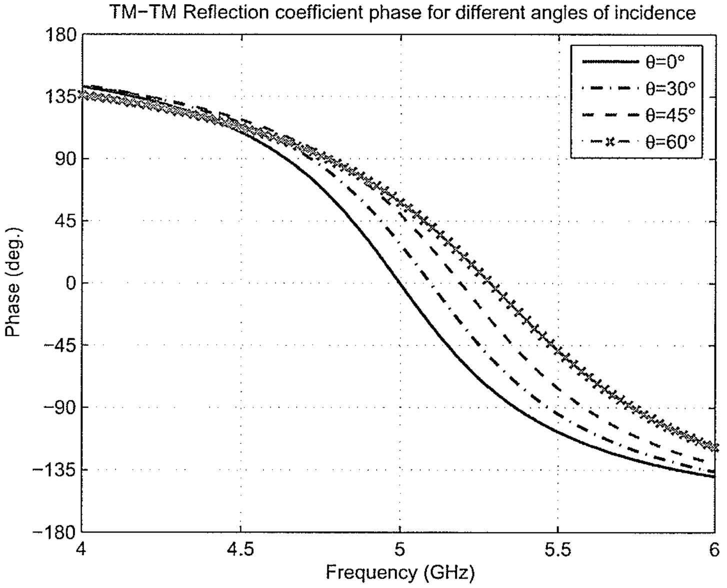

Figure 2.28: Co-polarized reflection coefficient phase for TM^z incident wave. According to Figure 2.10 and Tables 2.1 to 2.5, corresponding dimensions and materials characteristics are, d_2 and m_2, respectively.

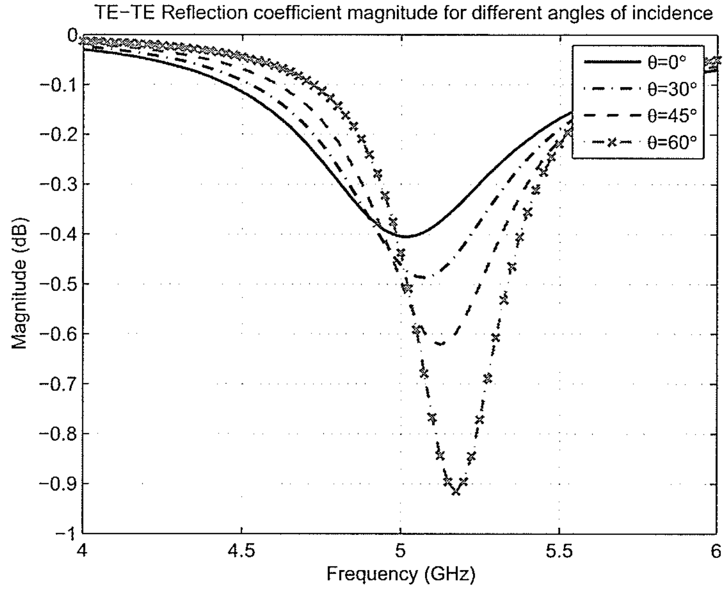

Figure 2.29: Co-polarized reflection coefficient magnitude for TE^z incident wave. According to Figure 2.10 and Tables 2.1 to 2.5, corresponding dimensions and materials characteristics are, d_2 and m_2, respectively.

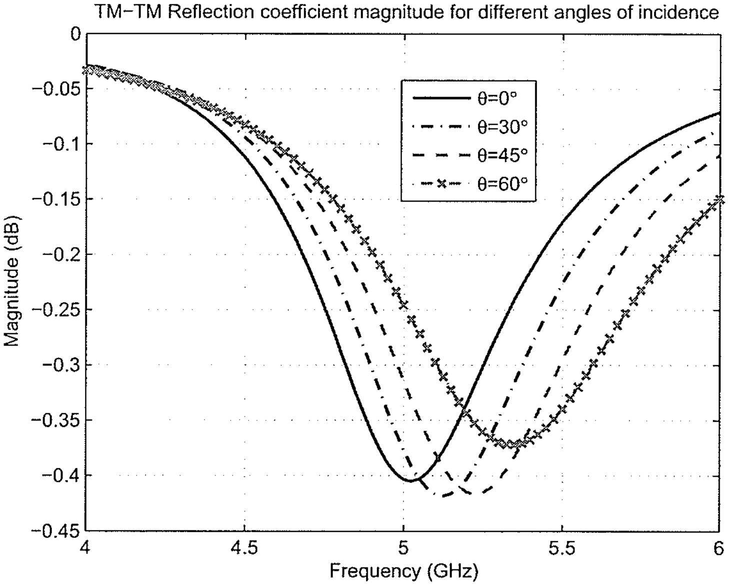

Figure 2.30: Co-polarized reflection coefficient magnitude for TM^z incident wave. According to Figure 2.10 and Tables 2.1 to 2.5, corresponding dimensions and materials characteristics are, d_2 and m_2, respectively.

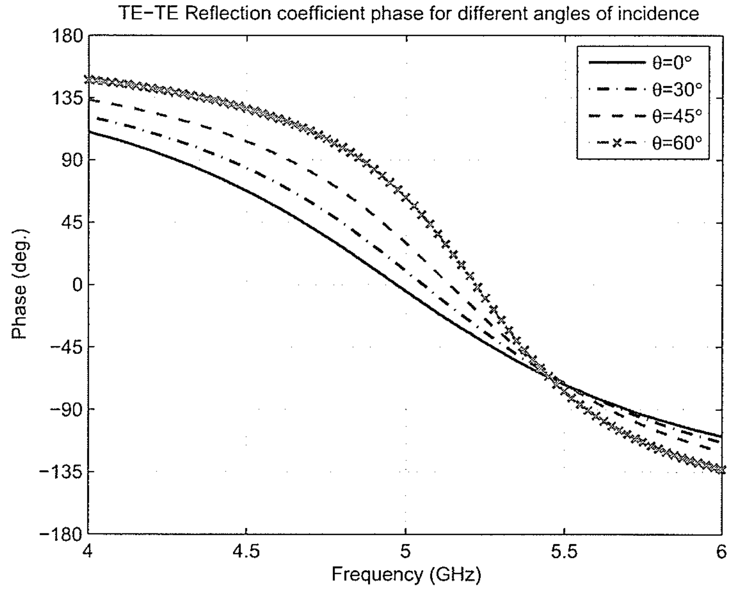

Figure 2.31: Co-polarized reflection coefficient phase for TE^z incident wave. According to Figure 2.10 and Tables 2.1 to 2.5, corresponding dimensions and materials characteristics are, d_3 and m_2, respectively.

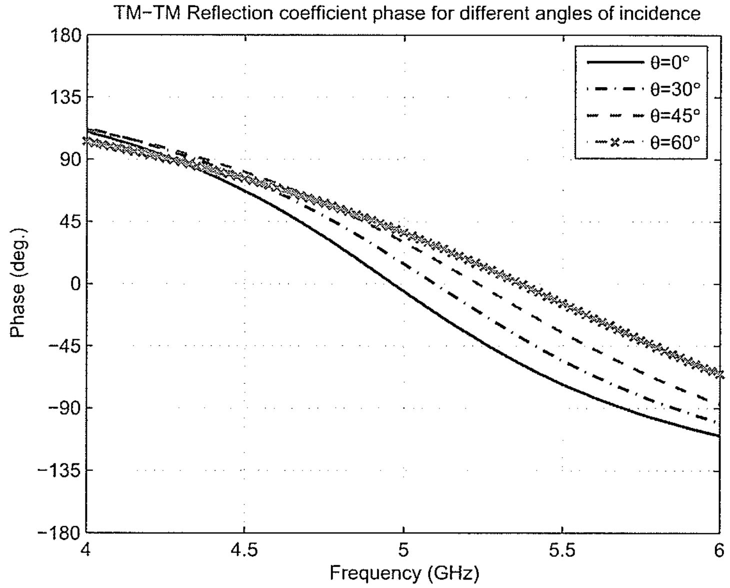

Figure 2.32: Co-polarized reflection coefficient phase for TM^z incident wave. According to Figure 2.10 and Tables 2.1 to 2.5, corresponding dimensions and materials characteristics are, d_3 and m_2, respectively.

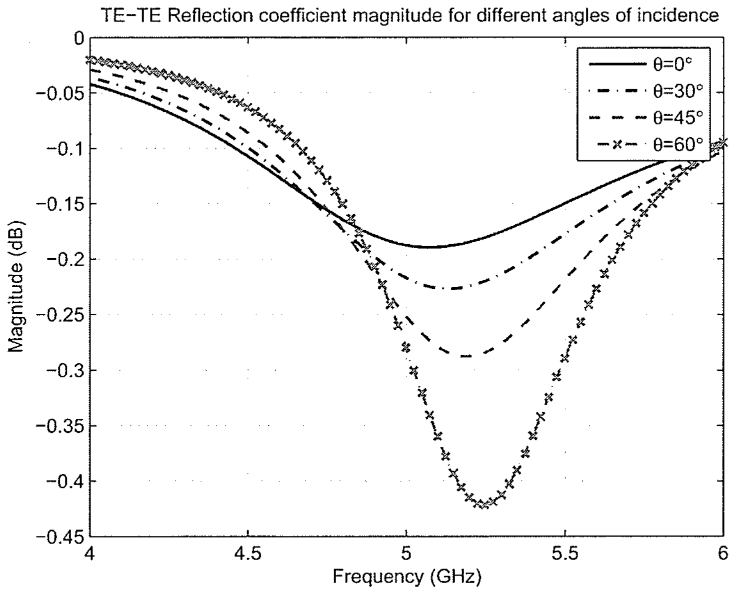

Figure 2.33: Co-polarized reflection coefficient magnitude for TE^z incident wave. According to Figure 2.10 and Tables 2.1 to 2.5, corresponding dimensions and materials characteristics are, d_3 and m_2, respectively.

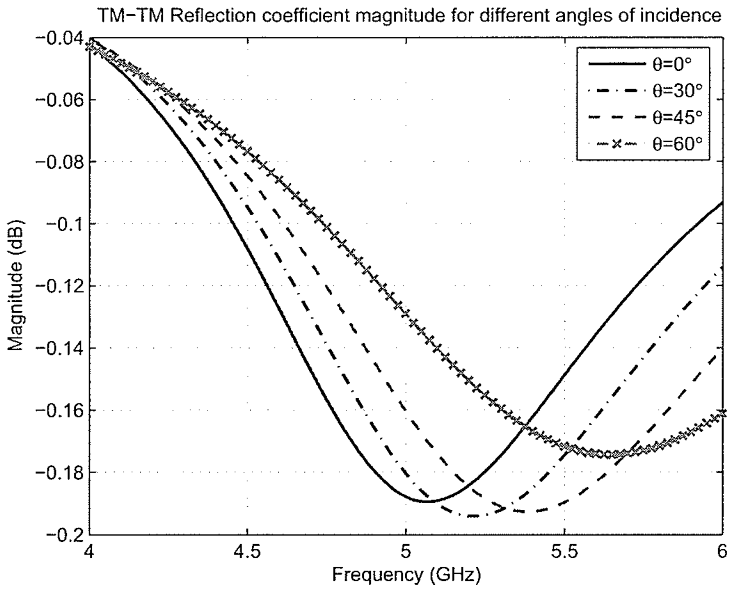

Figure 2.34: Co-polarized reflection coefficient magnitude for TM^z incident wave. According to Figure 2.10 and Tables 2.1 to 2.5, corresponding dimensions and materials characteristics are, d_3 and m_2, respectively.

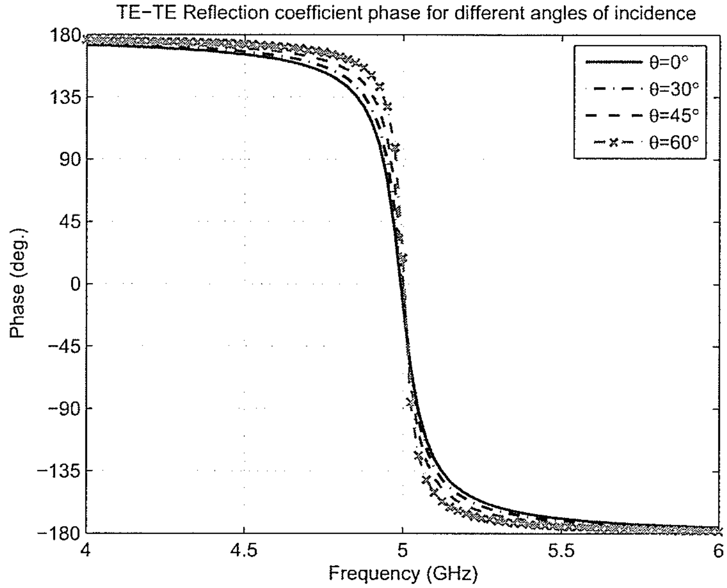

Figure 2.35: Co-polarized reflection coefficient phase for TE^z incident wave. According to Figure 2.10 and Tables 2.1 to 2.5, corresponding dimensions and materials characteristics are, d_1 and m_3, respectively.

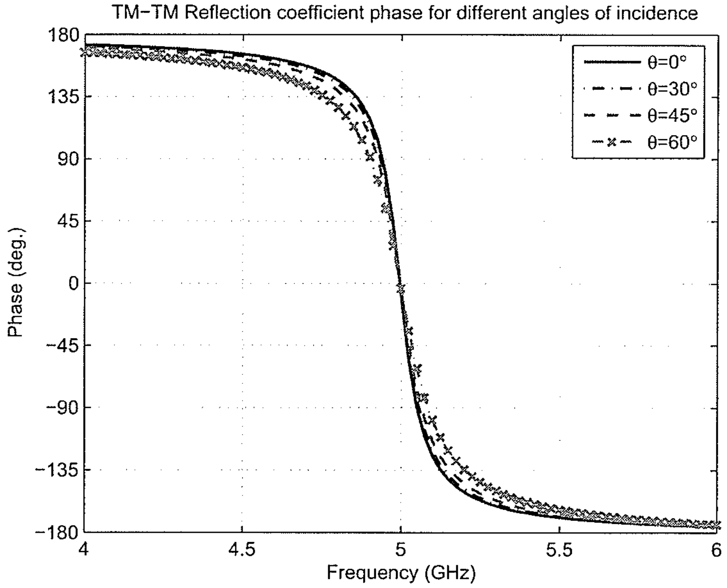

Figure 2.36: Co-polarized reflection coefficient phase for TM^z incident wave. According to Figure 2.10 and Tables 2.1 to 2.5, corresponding dimensions and materials characteristics are, d_1 and m_3, respectively.

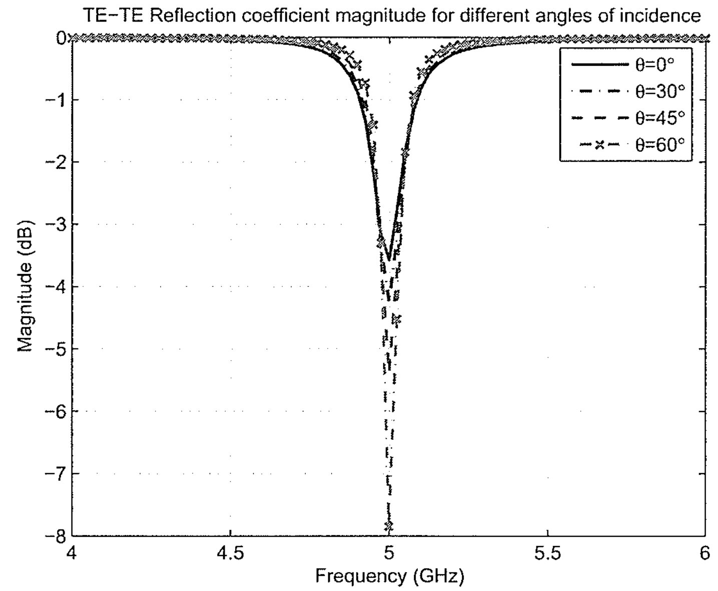

Figure 2.37: Co-polarized reflection coefficient magnitude for TE^z incident wave. According to Figure 2.10 and Tables 2.1 to 2.5, corresponding dimensions and materials characteristics are, d_1 and m_3, respectively.

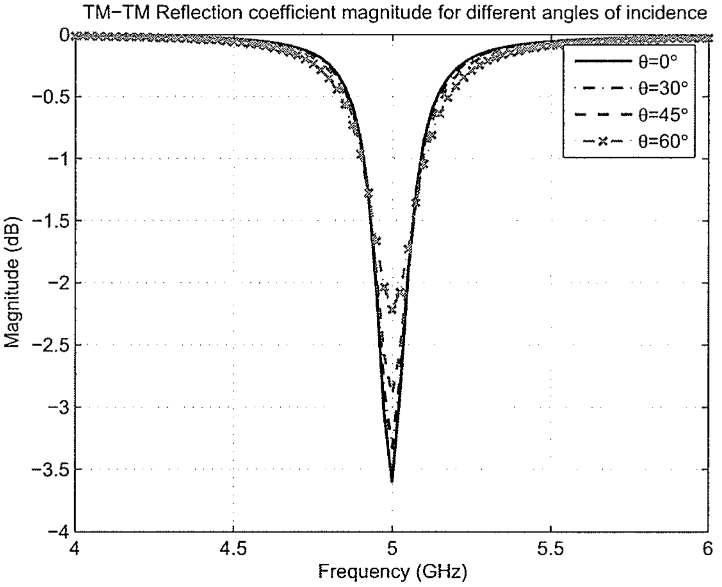

Figure 2.38: Co-polarized reflection coefficient magnitude for TM^z incident wave. According to Figure 2.10 and Tables 2.1 to 2.5, corresponding dimensions and materials characteristics are, d_1 and m_3, respectively.

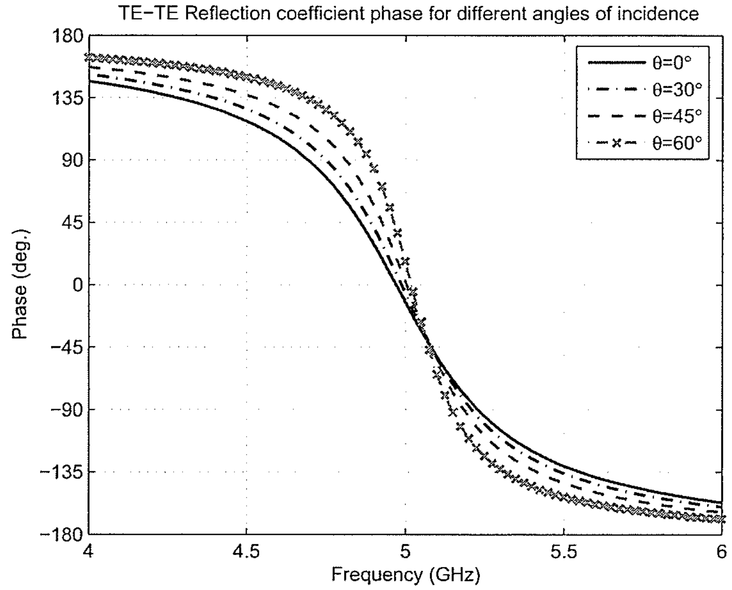

Figure 2.39: Co-polarized reflection coefficient phase for TE^z incident wave. According to Figure 2.10 and Tables 2.1 to 2.5, corresponding dimensions and materials characteristics are, d_2 and m_3, respectively.

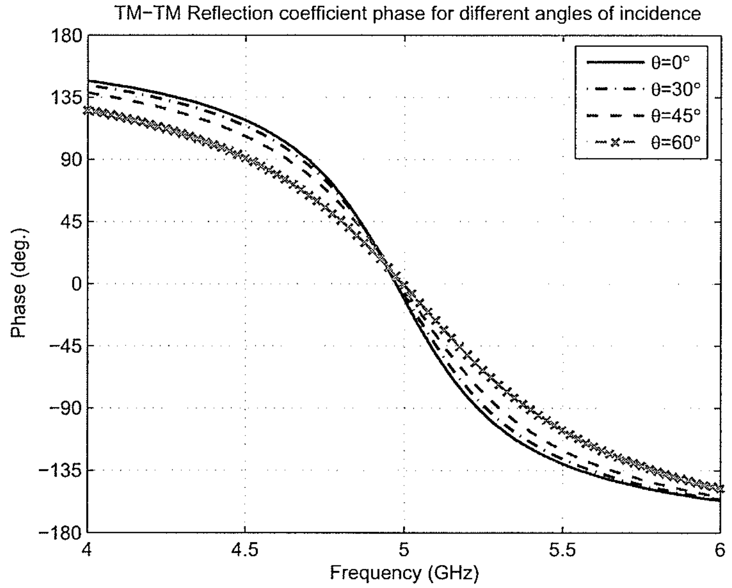

Figure 2.40: Co-polarized reflection coefficient phase for TM^z incident wave. According to Figure 2.10 and Tables 2.1 to 2.5, corresponding dimensions and materials characteristics are, d_2 and m_3, respectively.

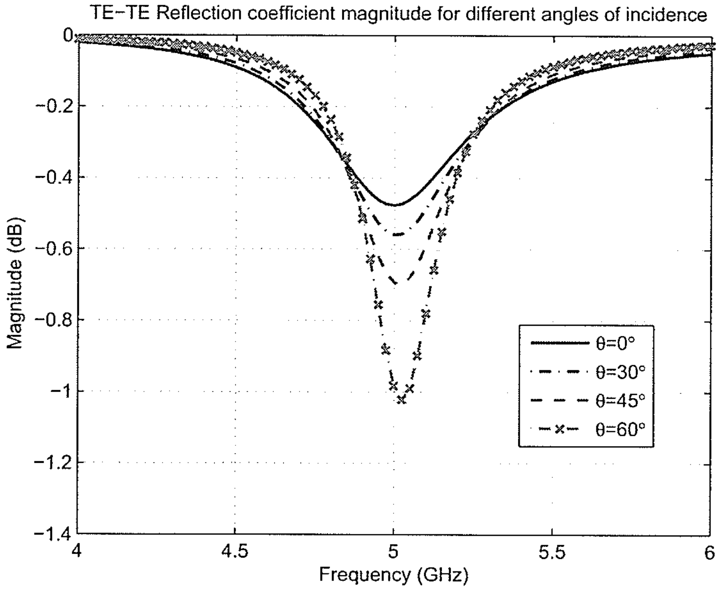

Figure 2.41: Co-polarized reflection coefficient magnitude for TE^z incident wave. According to Figure 2.10 and Tables 2.1 to 2.5, corresponding dimensions and materials characteristics are, d_2 and m_3, respectively.

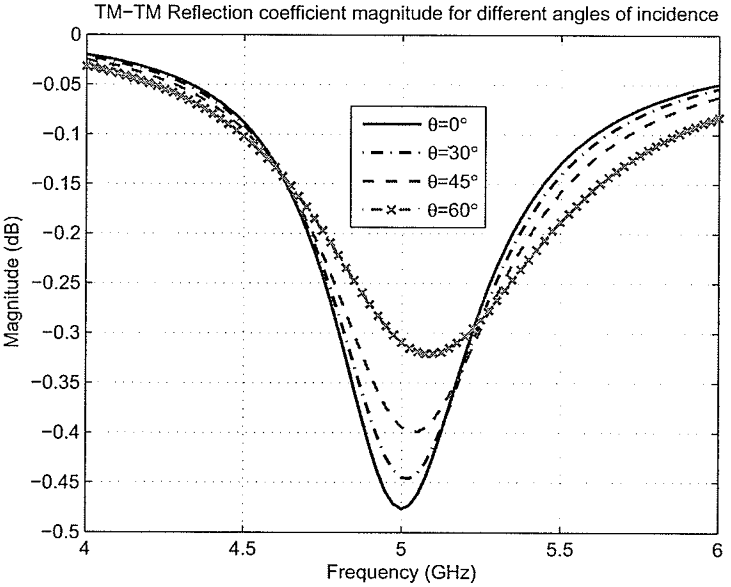

Figure 2.42: Co-polarized reflection coefficient magnitude for TM^z incident wave. According to Figure 2.10 and Tables 2.1 to 2.5, corresponding dimensions and materials characteristics are, d_2 and m_3, respectively.

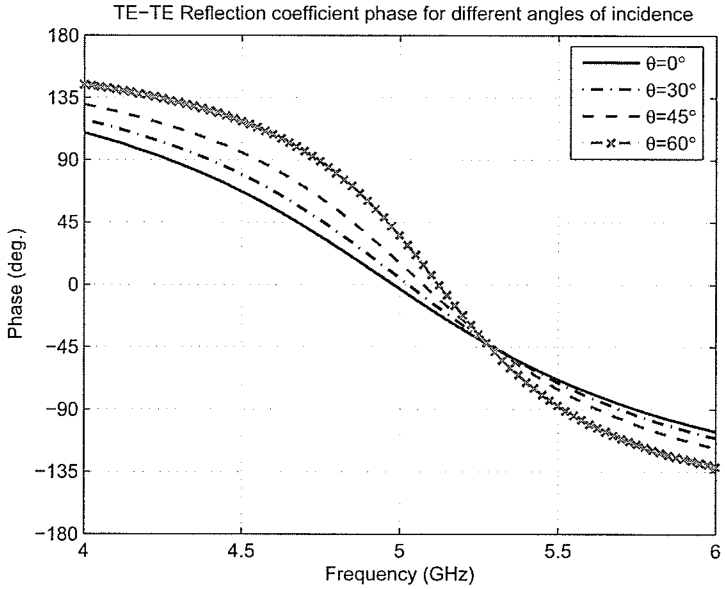

Figure 2.43: Co-polarized reflection coefficient phase for TE^z incident wave. According to Figure 2.10 and Tables 2.1 to 2.5, corresponding dimensions and materials characteristics are, d_3 and m_3, respectively.

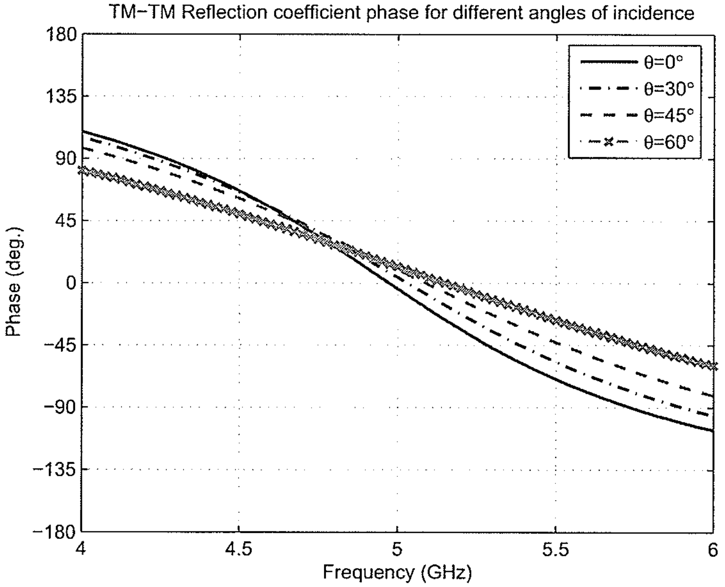

Figure 2.44: Co-polarized reflection coefficient phase for TM^z incident wave. According to Figure 2.10 and Tables 2.1 to 2.5, corresponding dimensions and materials characteristics are, d_3 and m_3, respectively.

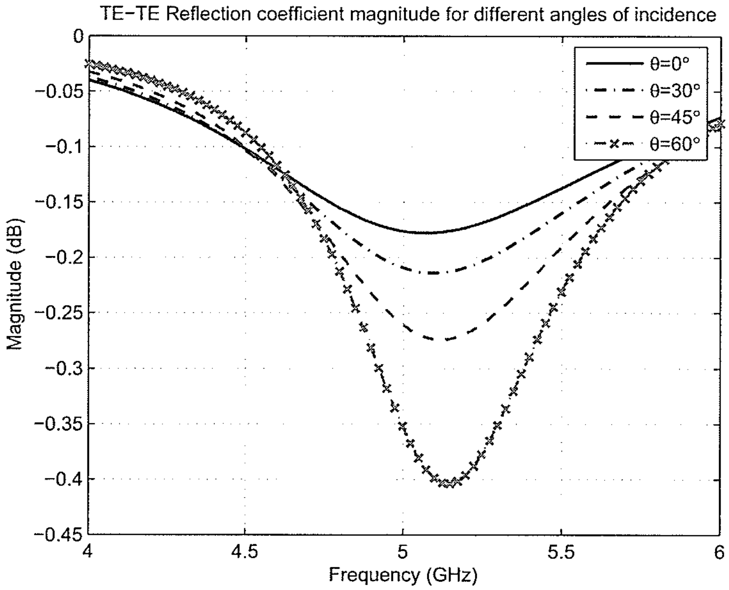

Figure 2.45: Co-polarized reflection coefficient magnitude for TE^z incident wave. According to Figure 2.10 and Tables 2.1 to 2.5, corresponding dimensions and materials characteristics are, d_3 and m_3, respectively.

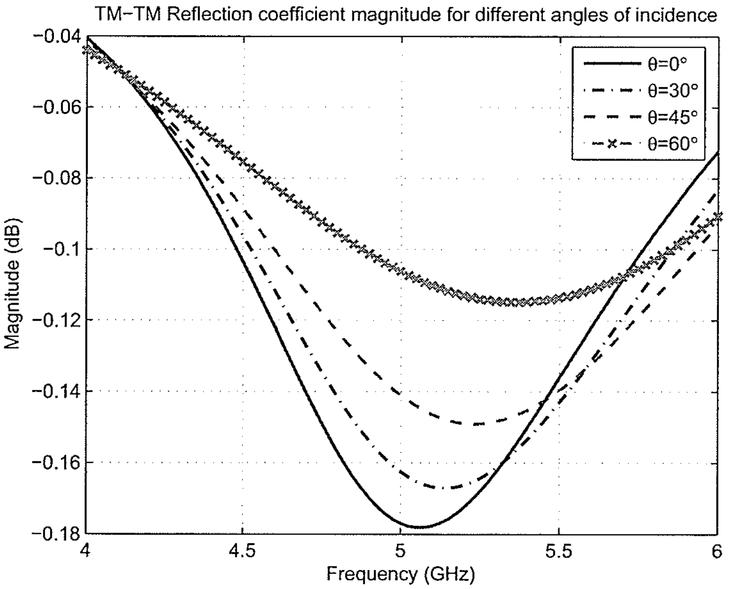

Figure 2.46: Co-polarized reflection coefficient magnitude for TM^z incident wave. According to Figure 2.10 and Tables 2.1 to 2.5, corresponding dimensions and materials characteristics are, d_3 and m_3, respectively.

2.6 AMCs with shorting pins

A grounded dielectric slab loaded by periodic metallic patches with shorting pins was first introduced by Sievenpiper et. al. [24]. They used the term "high impedance surface" for this structure. According to the reflection phase characterization shown in [24], this type of periodic structures acts as an AMC at their resonant frequency and obviously is a high impedance surface around this frequency for the normal incident waves. As well, it has been shown in [24] that this type of surfaces acts as electromagnetic band-gap (EBG) structures for the incident waves at grazing angles. In this section an AMC with shorting pins is discussed and compared with the same AMC without shorting pins.

The unit cells of an AMC with and without shorting pins are depicted in Figures 2.47(a) and (b), respectively.

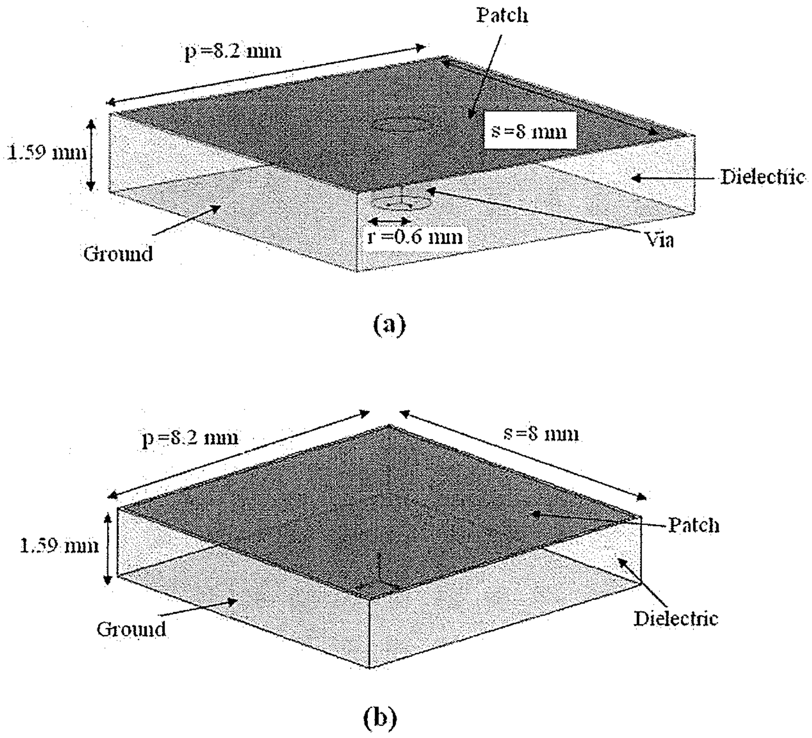

Figure 2.47: The unit cells of an AMC (a) with and (b) without shorting pins. Relative permittivity of the dielectric is assumed to be 2.5.

The corresponding reflection coefficient phases, for different incident angles and polarizations, are shown in Figures 2.48 and 2.49, respectively. It is assumed that the z-direction is normal to the surface of the structure. The resonant frequency, is 6.1 GHz for the normal incidence. As shown in Figures 2.48 and 2.49, the TE^z reflection coefficient phase for different incident angles are the same for both periodic structures, with and without the shorting pins. This phenomenon has also been observed for normal incidence in [25, 26]. In fact, the TE incidence does not strongly excite the currents in the vias. However, the TM^z reflection coefficients are different. The HIS resonant frequency shifts to lower frequencies, in the periodic structure with shorting pins (Figure 2.48), while for the periodic structure without shorting pins, it shifts to higher frequencies (Figure 2.49). The corresponding reflection coefficient magnitudes for the above-mentioned periodic structures are close to unity and are not addressed here for brevity. According to the AMC bandwidth definition, it is observed that the reflection phase of the TE^z polarizations shows less angular sensitivity than those of the TM^z polarizations. As shown in Figures 2.48 and 2.49, with the growing oblique incidence up to 60°, the resonant frequency still resides in the AMC bandwidth in the TE^z polarization case. However, this does not occur for the TM^z polarizations. For these structures, the cross-polar reflection coefficient magnitudes, TE^z and TM^z, are much lower than unity ($<$ -50 dB), and are not reported here. The periodic moment method (PMM) feature of Ansoft Designer was employed to extract reflection phases shown above [27].

A high impedance surface, consisting of 20×18 unit cells, is shown in Figure 2.50. The reflection coefficient phase, when this surface is illuminated as the load of a C-band waveguide is shown in Fig. 2.48(a). The C-band waveguide operates in its first propagating mode (TE_{10}). As shown, the measured phase

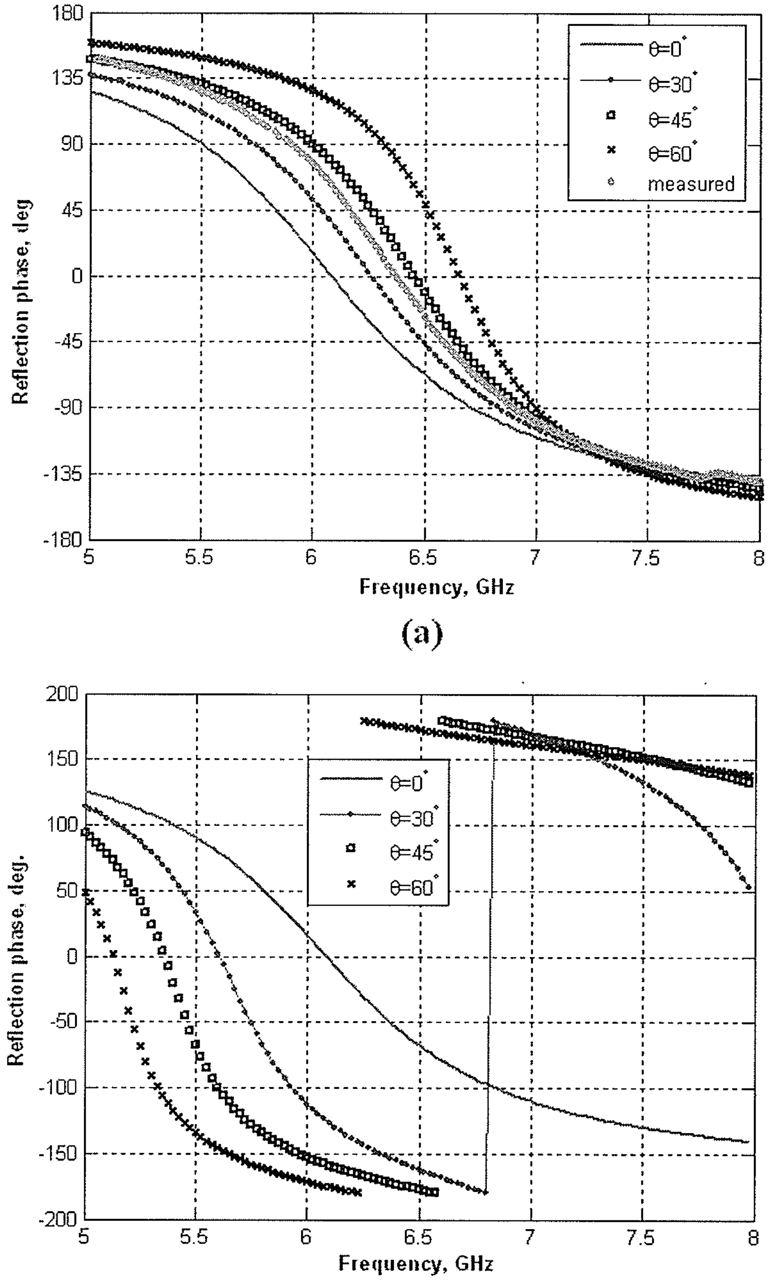

(a)

(b)

Figure 2.48: Reflection coefficient phase for AMC structure consisting of unit cells shown in Figure 2.47(a). (a) TE-TE polarization. (b) TM-TM polarization. Measured reflection phase was done using waveguide simulator.

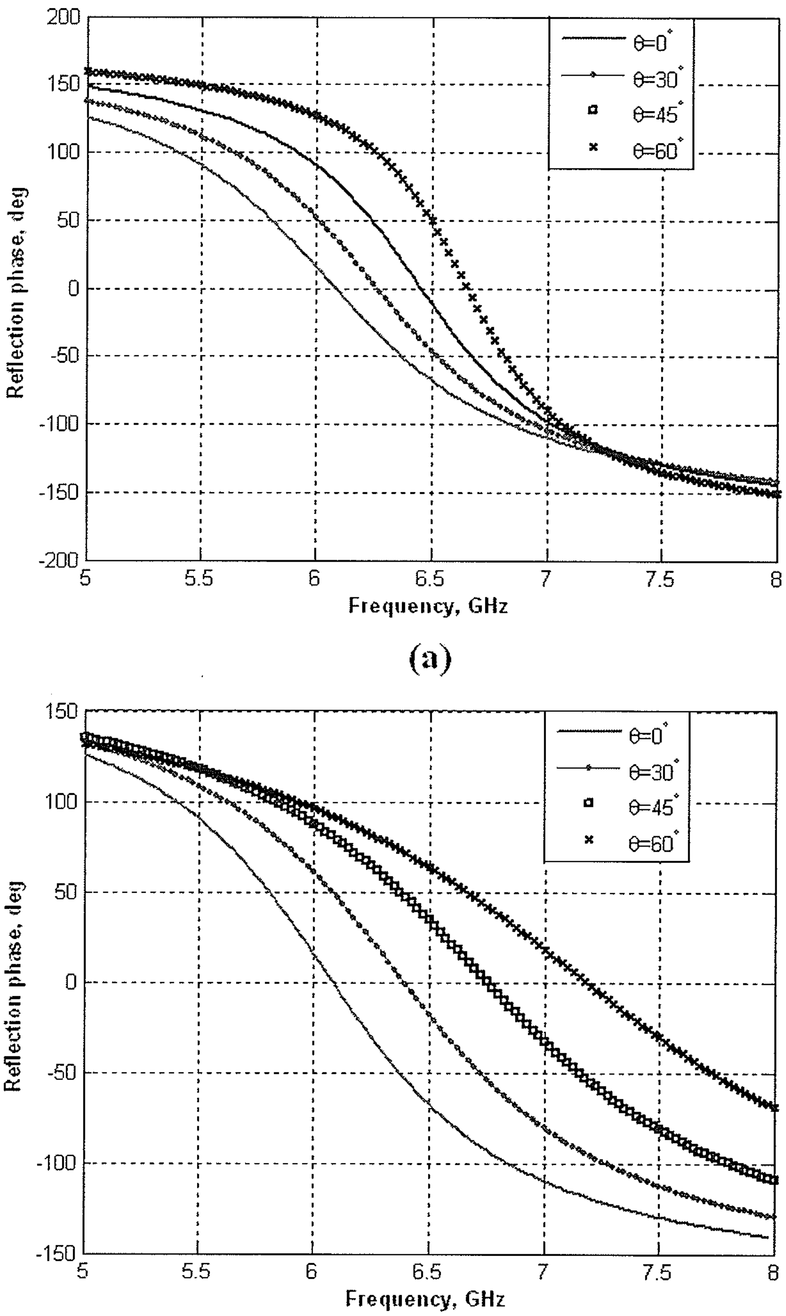

(a)

(b)

Figure 2.49: Reflection coefficient phase for AMC structure consisting of unit cells shown in Figure 2.47(b). (a) TE-TE polarization. (b) TM-TM polarization.

is closer to the curve obtained for the uniform plane wave incident at 45°, rather than the normal incidence. This is because of the fact that at 6.1 GHz (resonant frequency), the waveguide phase constant (β_g) is closer to the phase constant of the uniform plane wave in the free space when incident at 45°. It is calculated as follows.

$$\beta_g = \sqrt{k^2 - k_c^2} = k\sqrt{1 - (\frac{k_c}{k})^2} \tag{2.11}$$

where β_g, k and k_c are the waveguide phase constant, wavenumber in free space and cut off wavenumber of the waveguide, respectively. The first propagating mode in the waveguide is TE_{10}, and the standard C-band waveguide cross section has dimensions 3.485×1.580 cm^2.

The cut off wavenumber of the first mode is calculated as follows (a is the larger side of the rectangular waveguide cross section).

$$k_c = \frac{\pi}{a} \tag{2.12}$$

Hence, the first mode cut off wavenumber of the standard C-band waveguide is $\frac{\pi}{3.485\times10^{-2}} = 90.1$ m^{-1}. Also, the wave number in free space is

$$k = \omega\sqrt{\mu\epsilon} = \frac{2\pi f}{c} \tag{2.13}$$

Therefore, at 6.1 GHz, the wavenumber in free space is $\frac{2\pi\times6.1\times10^9}{3\times10^8} = 127.76$ m^{-1}.

According to the above-mentioned calculations, one can write
$\sqrt{1 - (\frac{k_c}{k})^2} = \sqrt{1 - (\frac{90.1}{127.76})^2} = 0.7090 = cos(44.75°)$.

Thus, the phase constant of the waveguide at 6.1 GHz is $\beta_g = k\cos(44.75°)$. This shows that the phase constant experienced by the HIS-EBG structure in the waveguide at 6.1 GHz, is close to the phase constant produced by a wave

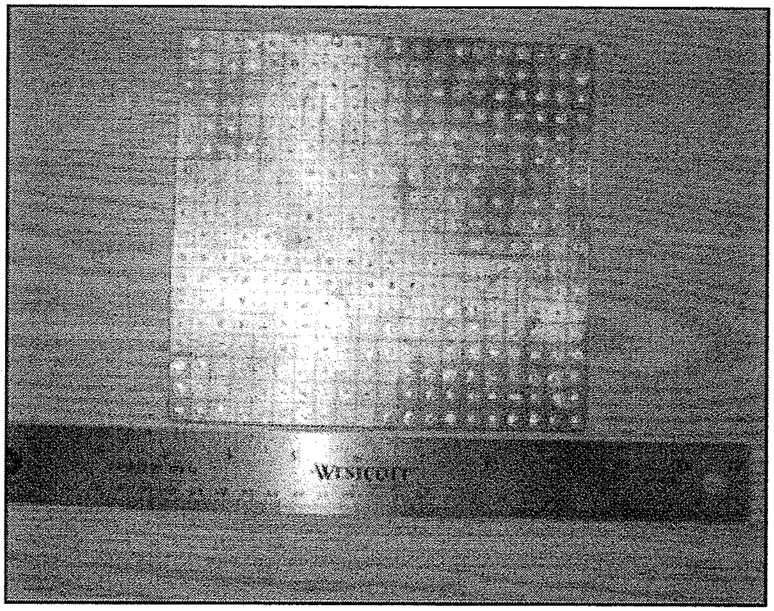

Figure 2.50: AMC structure consisting of 20 × 18 unit cells with dimensions shown in Figure 2.47(a).

incident obliquely at about 45° in free space. This can also be explained with the fact that in a waveguide, there is an equivalent oblique angle of propagation of plane waves [28]. Slight discrepancies observed in Figure 2.48 can be explained as follows. The cross section of the waveguide is not an integer number of the unit cell size of the periodic structure. Yet, in periodic moment method simulations an integer number of unit cells has to be considered. One should note that for different frequencies the equivalent oblique incident changes accordingly.

In order to investigate the operation of the periodic structure as an EBG, its unit cells are placed in a TEM waveguide as shown in Figure 2.51. In the TEM waveguide used here, top and bottom walls are PEC surfaces while the side walls are PMC surfaces. In order for the launched wave to pass through the periodic structure, from one wave-port toward the other, the cross section of the TEM waveguide has to be slightly larger than the unit cell height.

The periodic structures that are truncated to six unit cells and placed in TEM waveguides are shown in Figure 2.51. The reflection and transmission coefficients are also calculated for the case of three unit cells. The results are shown in Figure 2.52. The periodic structure with shorting pins introduces a band-gap in the frequency range of 3.5-7 GHz. It is interesting that even three unit cells can produce such a wide band-gap, Figure 2.52(a). However, the periodic structure without shorting pins does not introduce any band-gap within this frequency band, since the transmission coefficient magnitude is almost unity in this frequency band, Figure 2.52(b).

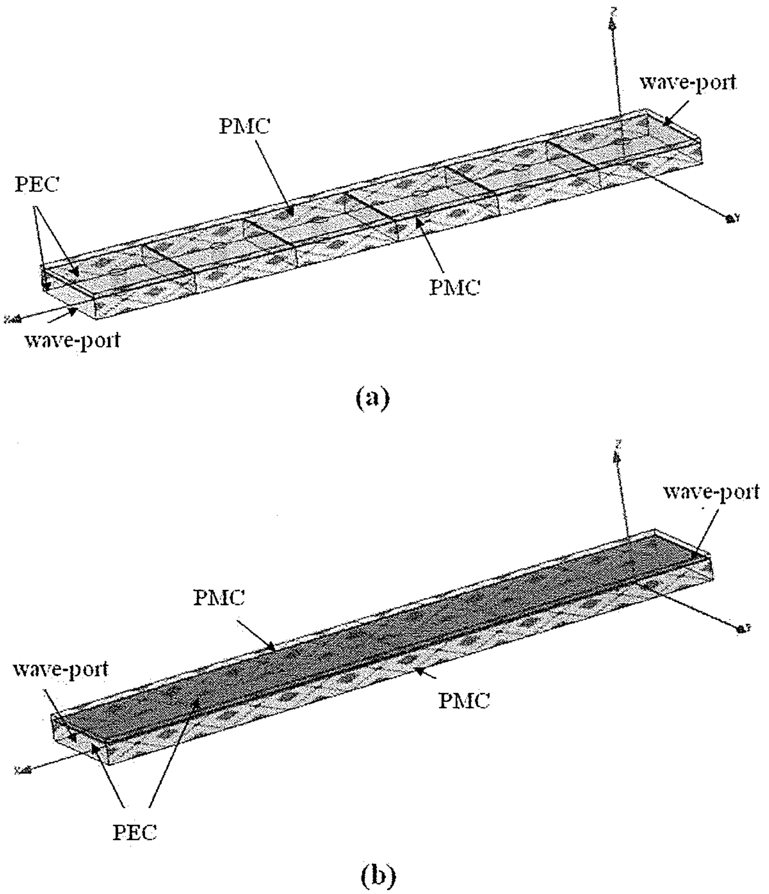

Figure 2.51: Truncated periodic structures in TEM waveguides. (a) Unit cells consisting of patch with shorting pins. (b) Unit cells consisting of patch without shorting pins. Dimensions of the unit cells are given in Figure 2.47

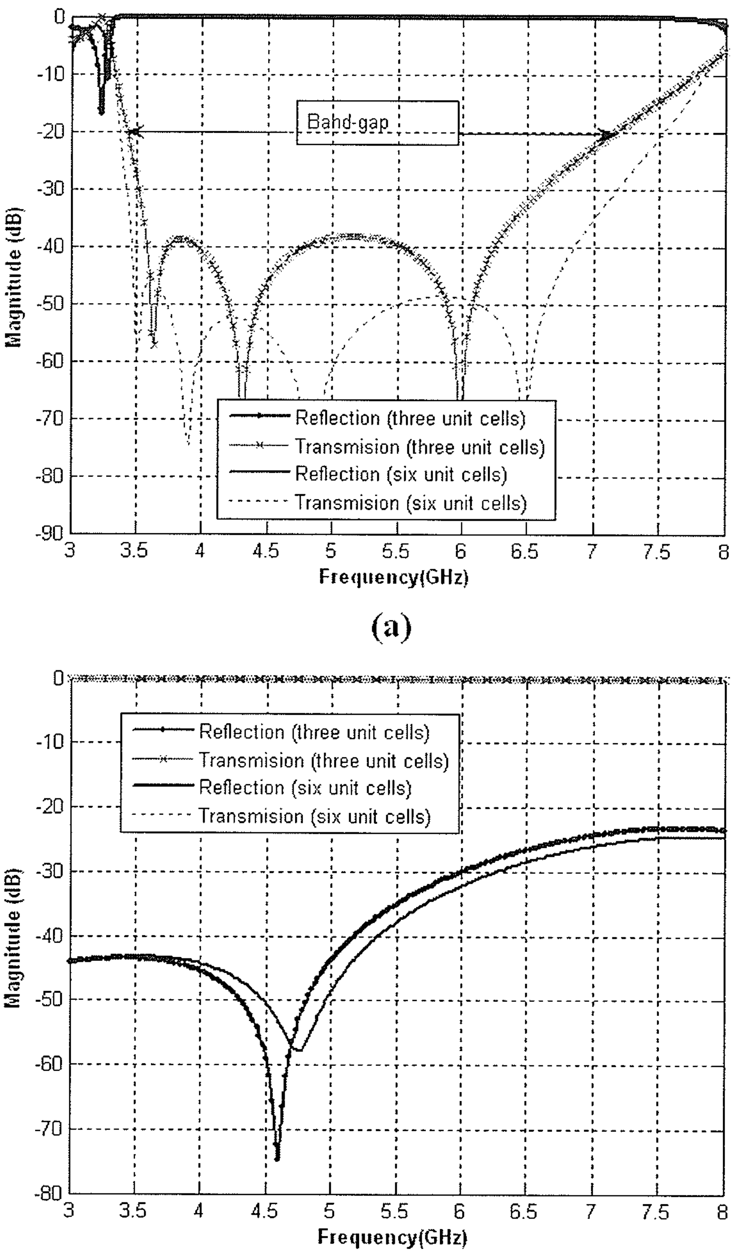

(a)

(b)

Figure 2.52: Transmission and reflection coefficient magnitudes for the periodic structures. (a) Unit cells with shorting pins in Figure 2.51(a). (b) Unit cells without shorting pins in Figure 2.51(b).

In order to obtain the band-gap in all transverse directions, irreducible Brillouin zone diagram has to be used. Since the periodic structure without shorting pins does not show any band-gap in the truncated cases, there is no point to burden the computational load of calculating the band-gap diagram in the irreducible Brillouin zone for this case. Therefore, only the periodic structure with shorting pins is considered here. This can be done by introducing two sets of linked periodic boundary conditions for the adjacent walls of a rectangular cylinder as shown in Figure 2.53(a). The two ends are terminated by the perfect matched layer (PML) absorbing boundary condition and the unit cell. By extracting the pertinent eigen-frequencies of this structure for each set of (k_x,k_y), the dispersion diagram is obtained as depicted in Figure 2.53(b). The Eigenmode solver of Ansoft HFSS has been employed to extract the frequencies for each propagating mode, shown in Figure 2.53(b), [27]. As can be seen, a band-gap has appeared in the frequency range of 5-7 GHz. One could expect the surface wave suppression in all directions, in this frequency band, if this engineered substrate were used as the ground plane [24, 29, 30].

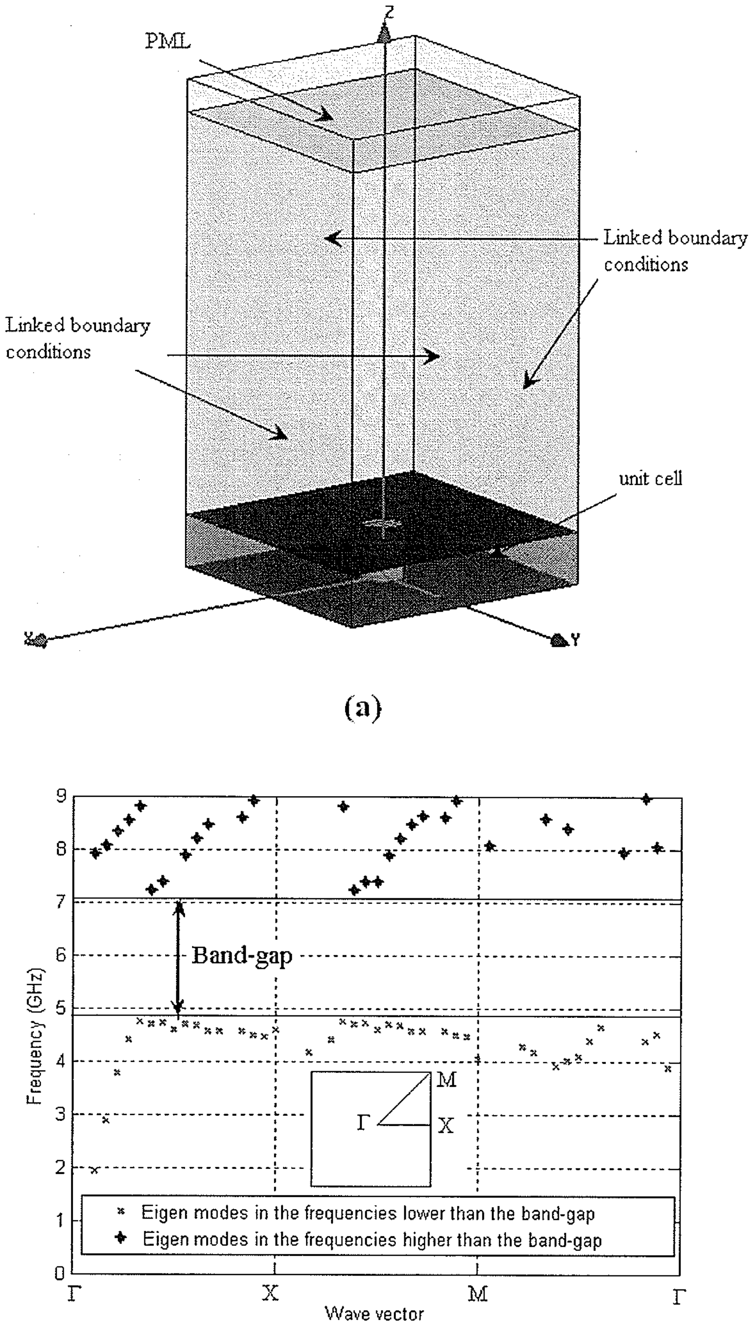

(a)

(b)

Figure 2.53: (a) Unit cell of an HIS-EBG structure (with shorting pins) in a rectangular cylinder with proper boundary conditions. Dimensions and other properties of the unit cell are shown in 2.47. (b) Dispersion diagram obtained using the irreducible Brillouin zone.

2.7 Other types of AMCs

In a more general sense, AMC structures can be obtained, backing FSSs with a ground plane [31]. Three different unit cells that are building blocks of different AMCs are shown in Figure 2.54. Resonant frequency of all of these AMCs is 9.5 GHz. Corresponding reflection coefficient phases of these unit cells are shown in Figures 2.55 to 2.60, for a few different angles and polarizations. The observations that are interesting points for the design purposes are listed as the follows.

- Square Patch unit cells offer AMCs with wider bandwidths than the other metallizations studied in this thesis. This is evident since the variation versus frequency is smoother in the reflection coefficients corresponding to unit cell with square metallic patches. In contrast to patch unit cells, Jerusalem cross offers the narrowest bandwidth.
- Metallic ring unit cells offer the smallest size whereas the Jerusalem cross unit cells have the largest size.
- Resonant frequency shifts to higher frequencies as the incident angle grows in all cases, except for the Jerusalem cross when the incident wave is TE-polarized.

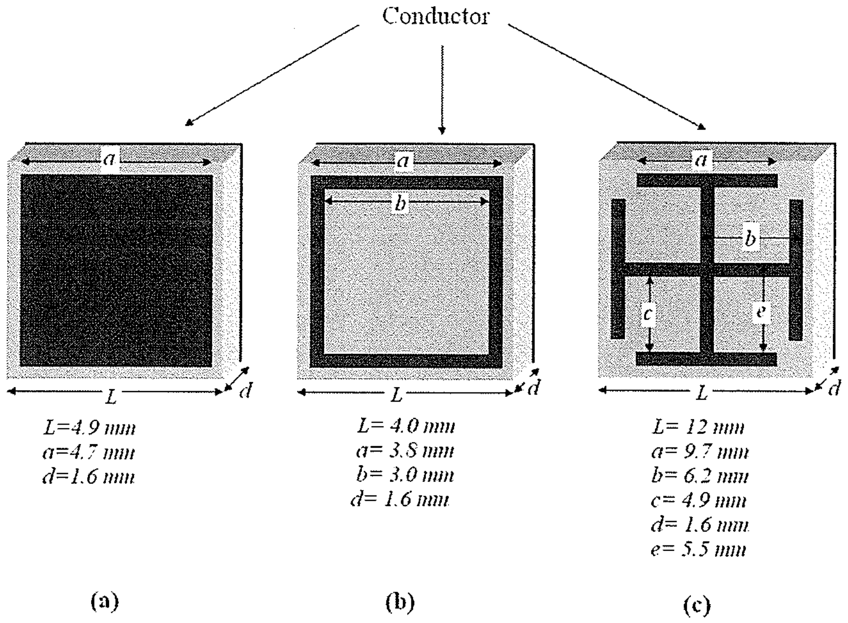
Conductor
a
L
d
L=4.9 mm
a=4.7 mm
d=1.6 mm
(a)
a
b
L
d
L= 4.0 mm
a= 3.8 mm
b= 3.0 mm
d= 1.6 mm
(b)
a
b
c
e
L
d
L= 12 mm
a= 9.7 mm
b= 6.2 mm
c= 4.9 mm
d= 1.6 mm
e= 5.5 mm
(c)

Figure 2.54: Three different AMC unit cells with three different metallic etched shapes. (a) Square patch, (b) square ring and (c) Jerusalem Cross.

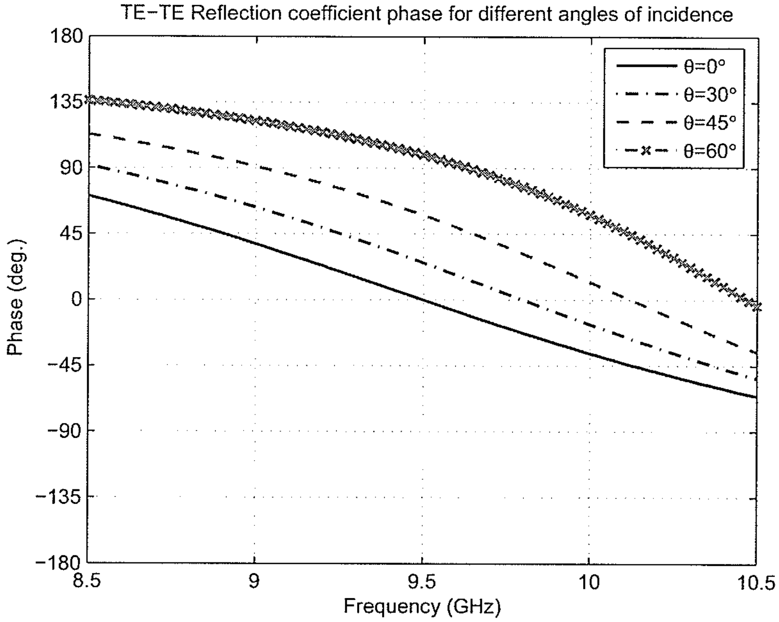

Figure 2.55: Co-polarized reflection coefficient phase for TE^z incident wave, corresponding to Figure 2.54 (a).

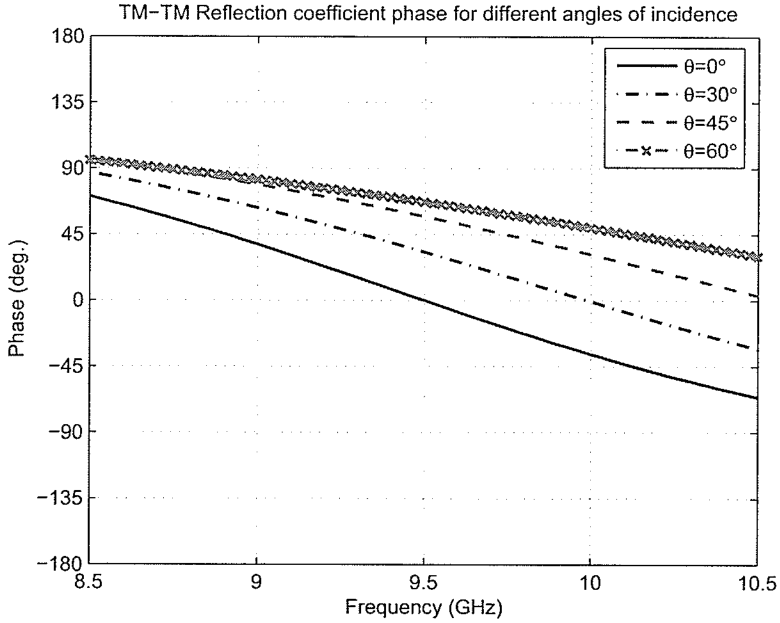

Figure 2.56: Co-polarized reflection coefficient phase for TM^z incident wave, corresponding to Figure 2.54 (a)

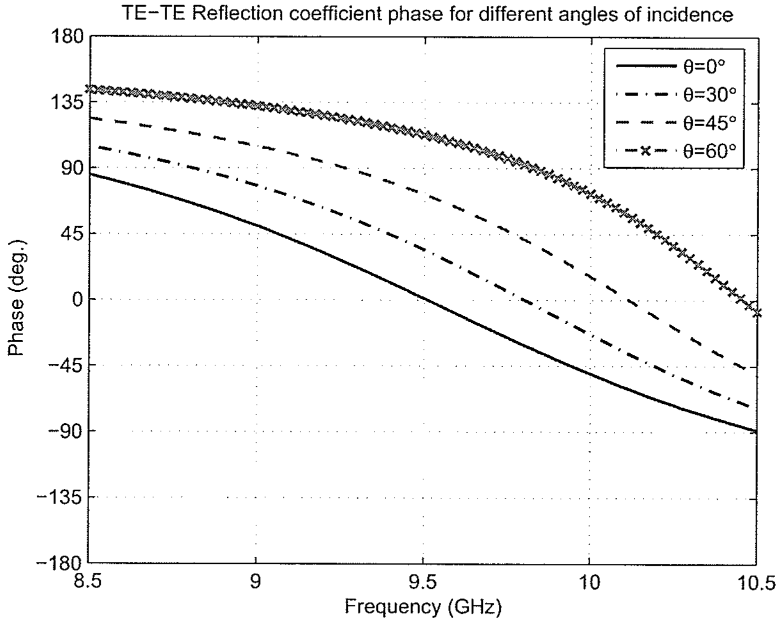

Figure 2.57: Co-polarized reflection coefficient phase for TE^z incident wave, corresponding to Figure 2.54 (b)

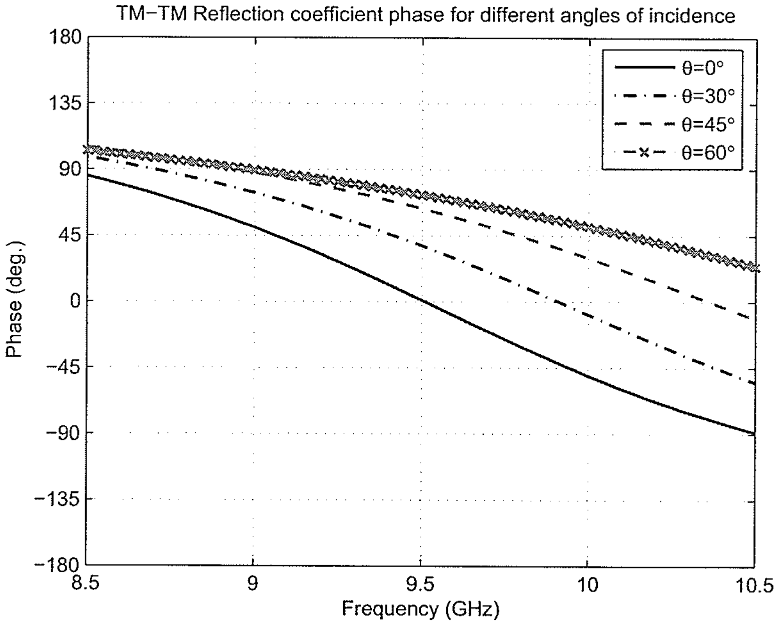

Figure 2.58: Co-polarized reflection coefficient phase for TM^z incident wave, corresponding to Figure 2.54 (b)

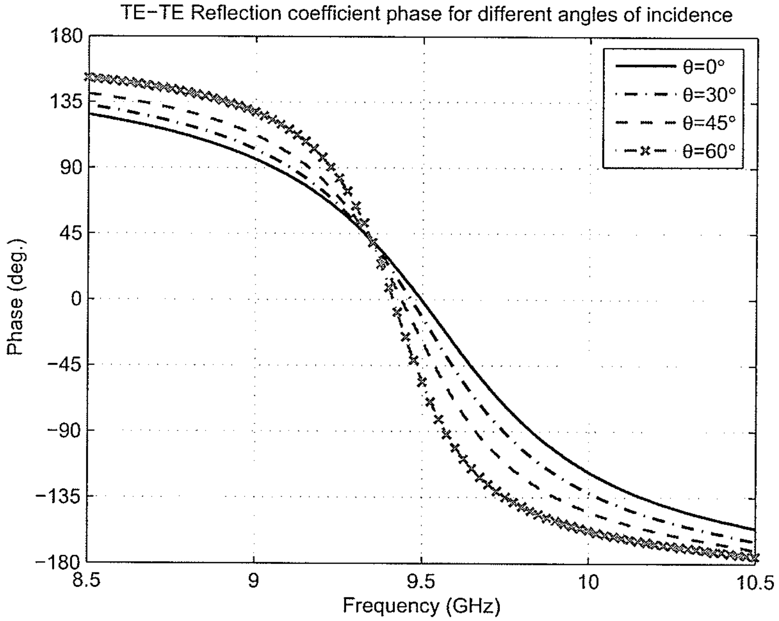

Figure 2.59: Co-polarized reflection coefficient phase for TE^z incident wave, corresponding to Figure 2.54 (c)

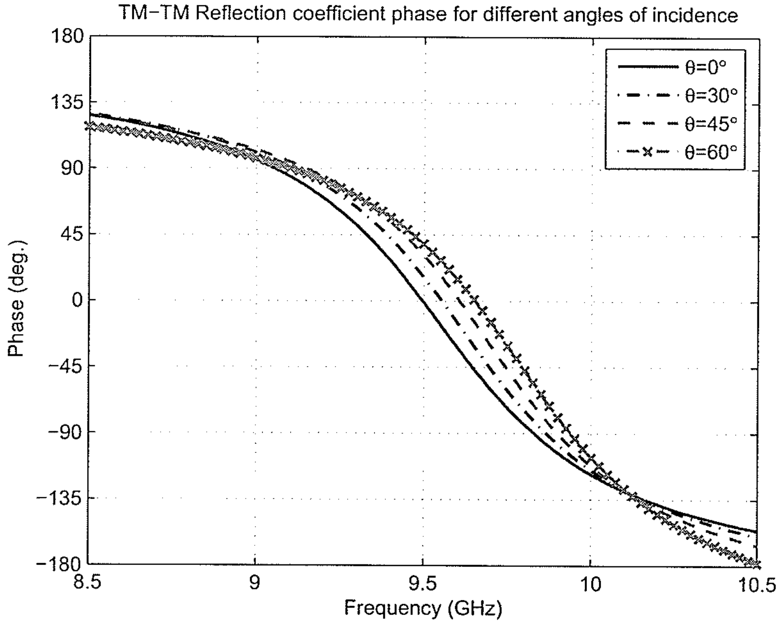

Figure 2.60: Co-polarized reflection coefficient phase for TM^z incident wave. corresponding to Figure 2.54 (c)

2.8 Conclusions

New definitions for PEC and PMC surfaces were introduced from the reflection coefficient phase perspective. These definitions are used throughout this study to implement artificial magnetic conductors (AMCs).

Circuit analogy of AMCs was introduced with the aid of transmission line equivalent theory. This analogy gives physical insight to AMC design and implementation.

A simple AMC structure consisting of grounded dielectric slab loaded by periodic patches was introduced and analyzed. Basic definitions useful in AMC characterization such as resonant frequency and bandwidth were pointed out.

Effects of various parameters on AMC characteristics were studied. These included thickness, permittivity and loss of the substrate dielectric as well as unit cell periodicity and patch length.

An AMC comprising periodic patches shorted to the PEC ground plane via metallic pins was studied and compared to its counterpart without the shorting pins. Both measured and simulated results were demonstrated and studied in detail. It was shown that for the case of the unit cell with shorting pin the AMC resonant frequency lies in the band-gap of the structure when it acts as an EBG. This phenomenon has also been observed in [24, 32]. Few other AMCs consisting of conventional FSS structures backed by a ground plane were analyzed as well.

Chapter 3

Surfaces consisting of infinitely-long periodic metallic strips on the grounded dielectric slab

In this chapter, scattering from grounded dielectric slabs loaded by periodic metallic strips is investigated. In the literature, employing these periodic structures is a way to synthesize soft/hard surfaces. The terms "soft and hard" surfaces were first introduced in [33]. They originally come from well-known soft and hard boundary conditions in acoustic [33]. The soft and hard boundary conditions are also known as Dirichlet and Neumann boundary conditions [33]. Rather than loading a grounded dielectric slab by periodic patches, there are other different ways to synthesize these surfaces [33, 1], such as introducing periodic corrugations to the conducting surfaces. Detailed studies on "soft/hard" is beyond the scope of this thesis and can be found in the literature (e.g. [33, 1]).

The purpose of this chapter is to introduce an artificial surface consisting of infinitely long metallic strips as opposed to the periodic patches used in the well known AMC cases. As was shown in the previous chapter, for the studied AMCs, both TM and TE reflection coefficient phases are zero when the incident wave is normal. In other words, the behavior of none of those periodic structures, change subjected to the normal incidence whether the applied electric field is x- or y-polarized. This is evident since their unit cells are rotationally symmetric to the rotation of 90°.

In contrast to the periodic structure discussed in the previous chapter, it will be shown in this chapter that a grounded dielectric slab loaded by infinitely conducting periodic strips shows AEC characteristics (reflection phase close to ±180°) for E-polarized incident waves (applied electric field in parallel with metallic strips) whereas acts as AMC (reflection phase of 0°) for H-polarized incident waves (applied electric field perpendicular to the metallic strips). This structure is the most well known periodic surface that is not invariant about a 90° and hence will be studied in this thesis.

The term AEC has been first introduced in this thesis as opposed to the known term AMC, for the structures showing reflection phase close to ±180°) and magnitude of unity. In this chapter, the assumption of reflection coefficient magnitude of unity holds for the following reasons.

1) The material losses, both metallic ohmic and dielectric, are assumed to be negligible,

2) No surface waves excited since the substrate dielectric thickness is very thin according to the criteria demonstrated in [17], and

3) The periodicity is less than half a wavelength at the corresponding frequency. Therefore all non-specular reflection are evanescent and the specular reflection carries the total reflected energy [34]. Also, the grating lobes or

Wood anomalies are not observed [35].

3.1 Characterization of a grounded dielectric slabs loaded by periodic conducting grating strips

The geometry of the problem is shown in Figure 3.1. For certain values of h = 1.59 mm, $2w$ = 5 mm and $2d$ = 10 mm, the reflection coefficient phases are shown in Figure 3.2, when the structure is subjected to normal incidence. The relative permittivity of the dielectric substrate is assumed to be 2.5. These results are obtained using three different software packages based on three different numerical methods. The extraction method of reflection phase characteristics for both E- and H-polarizations are the same for both HFSS (FEM-CAD) and MICROSTRIPES (TLM-CAD) and is described as follows.

A unit cell of periodic structure is placed at the bottom of a TEM waveguide as shown in Figures 3.3 and 3.4. Proper periodicity ($2d$ = 10 mm in this case) has to be considered for the unit cell in the transverse direction (x-direction in this case). The same length of the unit cell is selected in the longitudinal direction of the strips (y-direction in this case). As well, proper PEC or PMC waveguide side walls are set according to the electric field polarization to account for the infinite periodicity of the strips as shown in Figures 3.3 and 3.4. The reflection phase is calculated at the wave-port and the proper phase calibration is performed to the reference case as discussed in [36, 37].

As can be seen in Figure 3.2(a), there exist a resonant case for the TE^y incidence for which the reflection phase is zero. Different resonant frequencies are

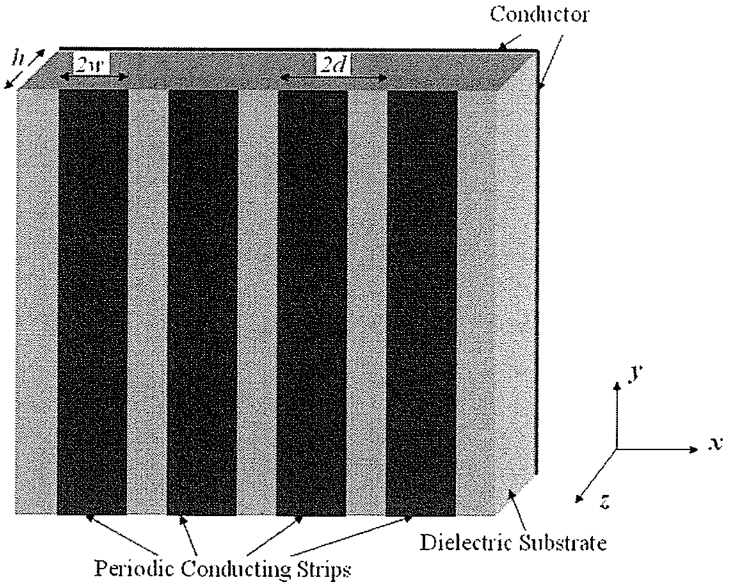

Figure 3.1: Grounded dielectric slab loaded by infinitely-long periodic metallic strips.

obtained using different methods. However, the resonant frequency differences are less than 8%. Interestingly, in the TM^y incidence case, TLM-CAD and FEM-CAD produce consistent results in the whole frequency region whereas the MoM-CAD does not (Figure 3.2(b)). Results obtained from both TLM-CAD and FEM-CAD show the reflection coefficient phases close to 180°, as expected for the TM^y incidence. According to Ansoft Designer software package manual, since the "unit cell walls touch the periodic boundary conditions" MoM-CAD results are not reliable in these cases [27]. Therefore, a few different analysis methods are presented, useful to extract the reflection properties of the grounded dielectric slab, loaded by infinitely-long periodic conducting strips. The first two methods are based on modal expansions of the Floquet's mode plane waves. The first one is a point matching method [35] and the second one is basically an entire-domain basis functions method [38]. The former is studied in details for the H-polarization case in section 3.2, which is

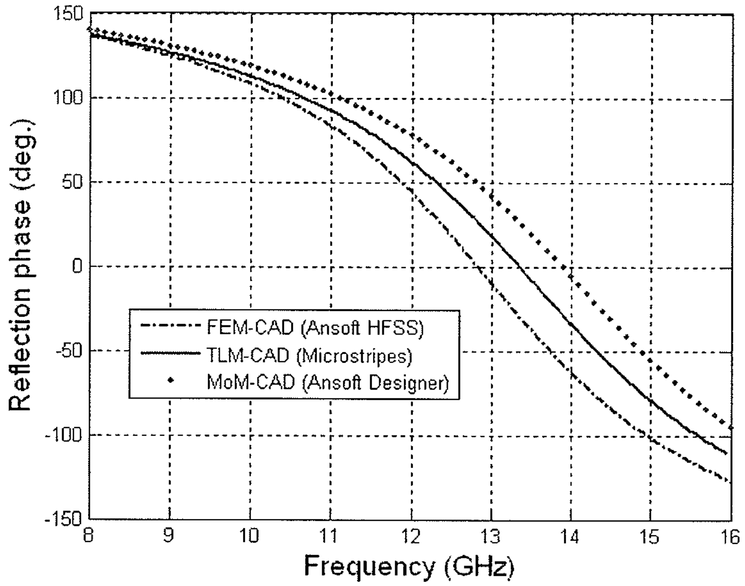

(a)

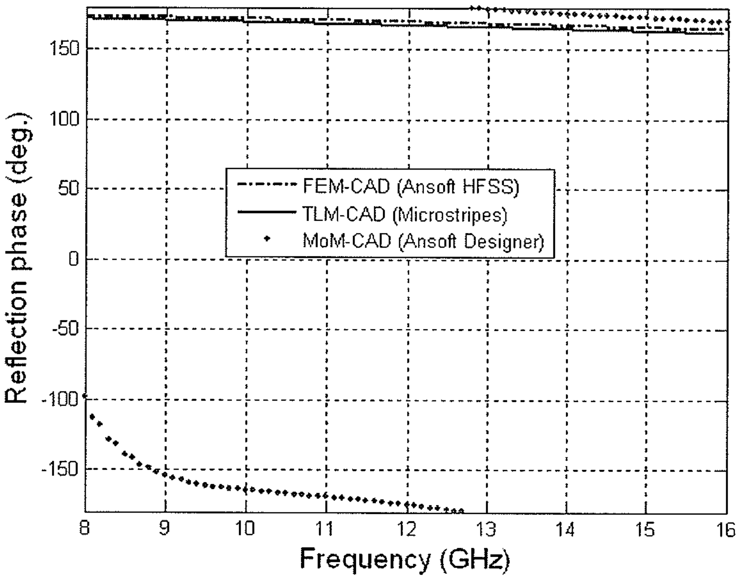

(b)

Figure 3.2: Reflection coefficient phases at normal incident angle, subject to the plane wave with (a) TE^y and (b) TM^y polarization. The geometry of the problem is shown in Figure 3.1. dimensions are $h = 1.59$ mm, $2w = 5$ mm and $2d = 10$ mm, and the relative permittivity of the dielectric substrate is 2.5.

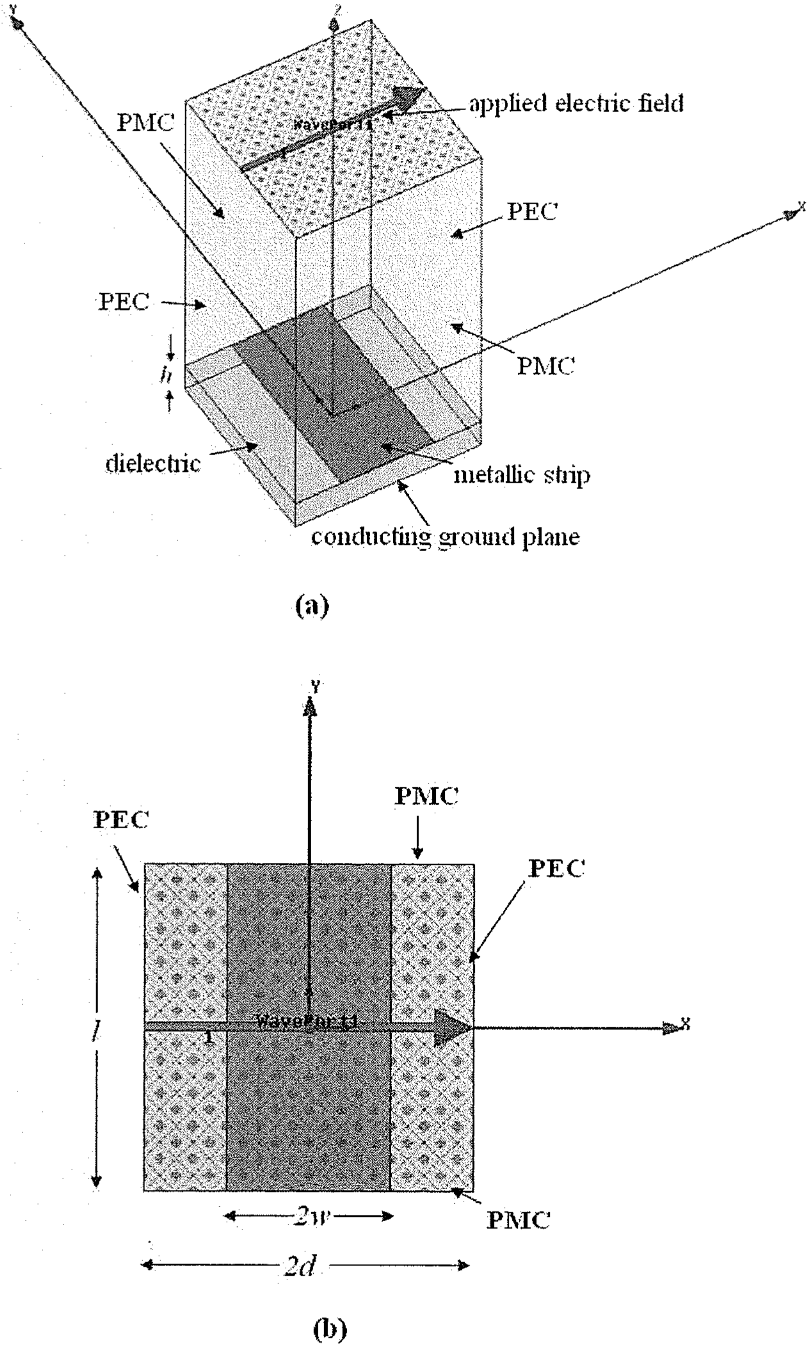
Y
Z
PMC
WavePort1
1
applied electric field
PEC
X
PEC
PMC
h
dielectric
metallic strip
conducting ground plane
(a)
Y
PMC
PEC
PEC
WavePort1
1
X
l
PMC
2w
2d
(b)

Figure 3.3: Schematic of reflection phase retrieving using TEM waveguide. (a) 3D view and (b) top view. Polarization of the incident wave is TE^y.

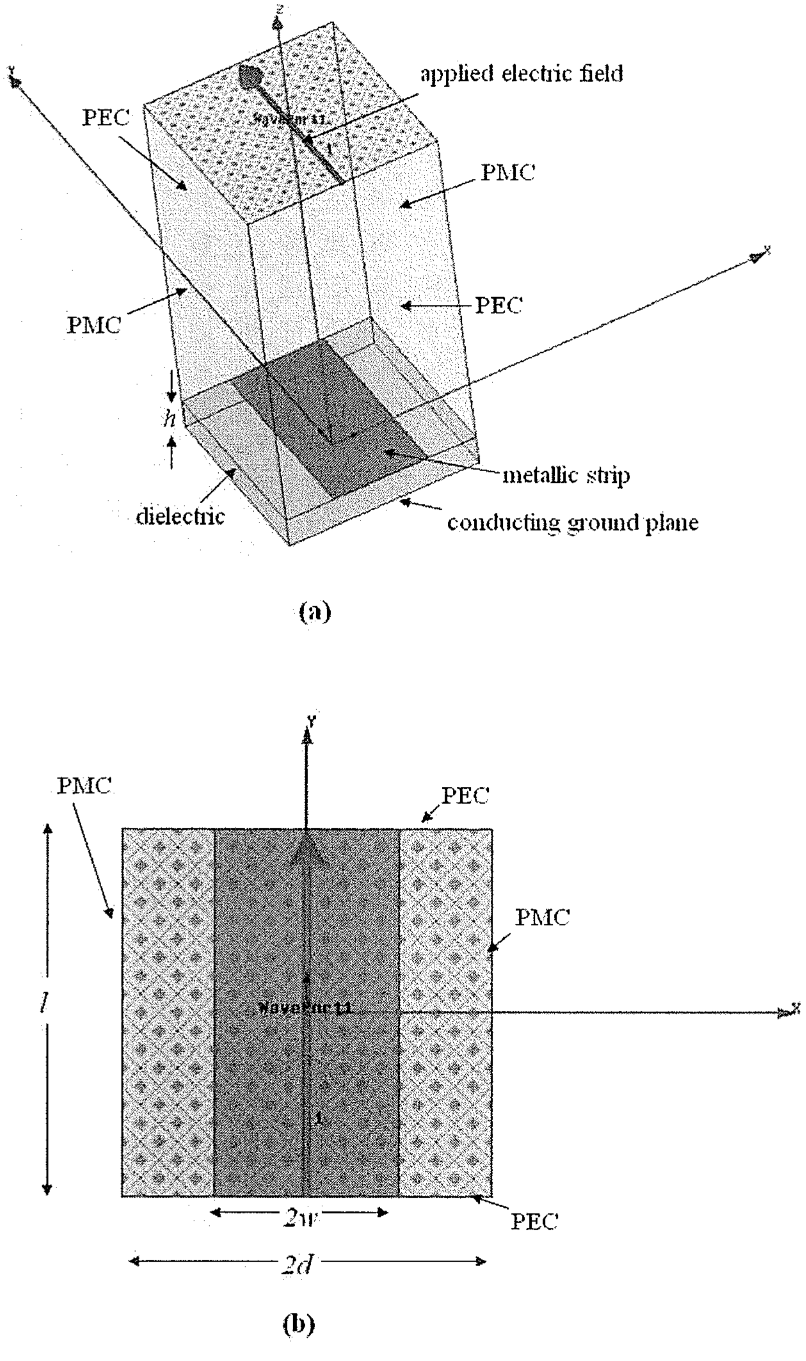
z
y
x
applied electric field
WavePort1
PEC
PMC
PMC
PEC
h
metallic strip
dielectric
conducting ground plane
(a)
Y
PMC
PEC
PMC
l
WavePort1
X
1
PEC
2w
2d
(b)

Figure 3.4: Schematic of reflection phase retrieving using TEM waveguide. (a) 3D view and (b) top view. Polarization of the incident wave is TM^y.

not fully studied in [35]. The latter is improved from what is presented in [38] using surface currents expansions on the strips for both TE and TM polarizations. This will be discussed in details in section 3.3. The results are compared with those obtained from the method of moments (MoM) code, developed by Dr. Malcolm Ng Mou Kehn and the author of this thesis at the University of Manitoba.

3.2 Point matching method (PMM)

The point matching method has been introduced in [35]. The geometry of the problem under study is shown in Figure 3.5. The problem solution is decomposed into the TE (E-polarized case) and TM (H-polarized case), in the same manner as presented in [35].

3.2.1 TE^y (H-polarized case)

The incident plane wave at incident angle θ_i has the following fields (Figure 3.5(a)):

$$\vec{H_i} = \hat{a_y} H_o e^{-j\beta_o x} e^{j\gamma_o z} \tag{3.1}$$

$$\vec{E_i} = -\hat{a_x}[H_o\gamma_o/(\omega\epsilon_o)]e^{-j\beta_o x} e^{j\gamma_o z} - \hat{a_z}[H_o\beta_o/(\omega\epsilon_o)]e^{-j\beta_o x} e^{j\gamma_o z} \tag{3.2}$$

where

$$\begin{aligned} \beta_o &= k_o \sin(\theta_i); \\ \gamma_o &= k_o \cos(\theta_i); \\ k_o &= \omega\sqrt{\mu_o\epsilon_o} \end{aligned} \tag{3.3}$$

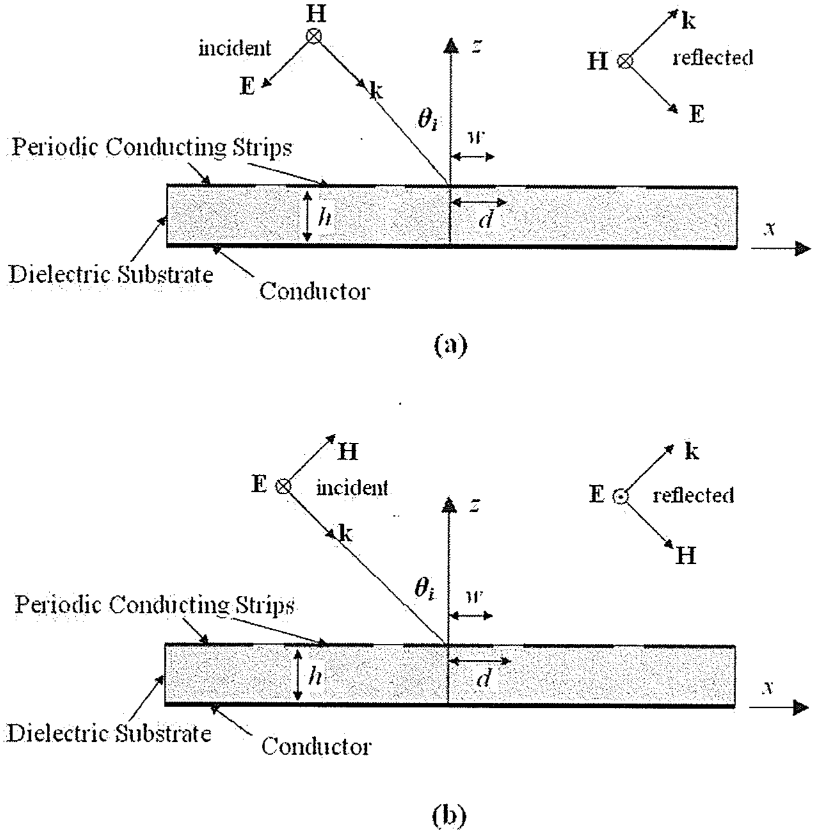
H
incident
E
k
z
θ_i
w
H
k
reflected
E
Periodic Conducting Strips
h
d
x
Dielectric Substrate
Conductor
(a)
H
E
incident
k
z
θ_i
w
E
k
reflected
H
Periodic Conducting Strips
h
d
x
Dielectric Substrate
Conductor
(b)

Figure 3.5: Grounded dielectric slab loaded by infinitely-long periodic metallic strips. (a) TE^y and (b) TM^y polarization.

In the region $z \geq h$, the reflected wave has the following fields:

$$\vec{H}_r = \hat{a_y} \sum_{n=-N}^{N} A_n e^{-j\beta_n x} e^{-j\gamma_n (z-h)} \tag{3.4}$$

$$\begin{aligned} \vec{E}_r = \hat{a_x} & \sum_{n=-N}^{N} [A_n \gamma_n / (\omega \epsilon_o)] e^{-j\beta_n x} e^{-j\gamma_n (z-h)} \\ -\hat{a_z} & \sum_{n=-N}^{N} [A_n \beta_n / (\omega \epsilon_o)] e^{-j\beta_n x} e^{-j\gamma_n (z-h)} \end{aligned} \tag{3.5}$$

where

$$\begin{aligned} \beta_n &= \beta_o + 2n\pi/p, \quad p = 2d \\ \gamma_n &= \sqrt{k_o^2 - \beta_n^2}, \quad \text{for} \quad k_o^2 > \beta_n^2 \\ \gamma_n &= -j\sqrt{\beta_n^2 - k_o^2}, \quad \text{for} \quad k_o^2 < \beta_n^2 \end{aligned} \tag{3.6}$$

A_n's are unknowns to be determined. The specular reflection coefficient is A_o, which is the desired coefficient. β_n is associated with Floquet's mode due to the periodicity in the x direction [39]. N is a large number. The two expressions for γ_n's give propagating and evanescent modes.

In the dielectric slab region, the solution is formed in terms of upward and downward traveling planes waves. Therefore, in the region $h \geq z \geq 0$, the fields are:

$$\vec{H}_d = \hat{a_y} \sum_{n=-N}^{N} [C_n e^{-j\beta_n x} e^{-j\gamma_n z} + D_n e^{-j\beta_n x} e^{j\eta_n z}] \tag{3.7}$$

$$\begin{aligned} \vec{E}_d = \hat{a_x} \sum_{n=-N}^{N} & [(C_n\eta_n/(\omega\epsilon))e^{-j\beta_n x} e^{-j\eta_n z} \\ & -(D_n\eta_n/(\omega\epsilon))e^{-j\beta_n x} e^{j\eta_n z}] \\ +\hat{a_z} \sum_{n=-N}^{N} & [-(C_n\beta_n/(\omega\epsilon))e^{-j\beta_n x} e^{-j\eta_n z} \\ & -(D_n\beta_n/(\omega\epsilon))e^{-j\beta_n x} e^{j\eta_n z}] \end{aligned} \tag{3.8}$$

where

$$\begin{aligned} \eta_n &= \sqrt{k^2 - \beta_n^2}, \quad \text{for} \quad k^2 > \beta_n^2 \\ \eta_n &= -j\sqrt{\beta_n^2 - k^2}, \quad \text{for} \quad k^2 < \beta_n^2 \\ k^2 &= \omega^2 \mu_o \epsilon \end{aligned} \tag{3.9}$$

where ϵ is the permittivity of the dielectric slab.

Applying the boundary conditions at $z = 0$, vanishing the tangential component of the electric fields on the PECs, results in:

$$\sum_{n=-N}^{N} [(C_n\eta_n/(\omega\epsilon))e^{-j\beta_n x} - (D_n\eta_n/(\omega\epsilon))e^{-j\beta_n x}] = 0 \Longrightarrow \boxed{C_n = D_n} \tag{3.10}$$

Applying the boundary conditions at $z = h$, for which the tangential electric field is continuous, results in:

$$\frac{-H_o\gamma_o}{\omega\epsilon_o} e^{-j\beta_o x} e^{j\gamma_o h} + \sum_{n=-N}^{N} \frac{A_n\gamma_n}{\omega\epsilon_o} e^{-j\beta_n x} =$$
$$\sum_{n=-N}^{N} [(C_n\eta_n/(\omega\epsilon))e^{-j\beta_n x} e^{-j\eta_n h} - (D_n\eta_n/(\omega\epsilon))e^{-j\beta_n x} e^{j\eta_n h}] \tag{3.11}$$

Substituting (3.10) in (3.11) and mathematical manipulations result in:

$$\sum_{n=-N}^{N} \frac{A_n\gamma_n}{\omega\epsilon_o} e^{-j\beta_n x} + \sum_{n=-N}^{N} (C_n\eta_n/(\omega\epsilon))e^{-j\beta_n x} \underbrace{[e^{j\eta_n h} - e^{-j\eta_n h}]}_{2j\sin(\eta_n h)}$$
$$= \frac{H_o\gamma_o}{\omega\epsilon_o} e^{-j\beta_n x} e^{j\gamma_n h} \tag{3.12}$$

Eventually, the relationship between the modal coefficients is:

$$C_n = A_n(\frac{\epsilon\gamma_n}{2\epsilon_o\eta_n})\frac{j}{\sin(\eta_n h)} - H_o e^{j\gamma_o h}(\frac{2\epsilon\gamma_n}{\epsilon_o\eta_n})(\frac{j}{\sin(\eta_n h)})\delta(n) \tag{3.13}$$

where $\delta(n)$ is the Kronecker delta, and defined as:

$$\delta(n) = \begin{cases} 1, & n = 0 \\ 0, & n \neq 0. \end{cases} \tag{3.14}$$

Two more boundary conditions can be applied to have the complete set of equations. The tangential component of electric field vanishes on the metallic strips, which results in:

$$-H_o\gamma_o e^{-j\beta_o x} e^{j\gamma_o h} + \sum_{n=-N}^{N} \gamma_n A_n e^{-j\beta_n x} = 0, \quad -w \leq x \leq w \qquad (3.15)$$

and the tangential components of the magnetic field must be continuous in the slot region at boundary $z = h$. Therefore, it is obtained:

$$\begin{aligned} & H_o e^{-j\beta_o x} e^{j\gamma_o h} + \sum_{n=-N}^{N} A_n e^{-j\beta_n x} = \\ & \sum_{n=-N}^{N} [C_n e^{-j\beta_n x} e^{-j\gamma_n h} + D_n e^{-j\beta_n x} e^{j\gamma_n h}], \\ & \qquad d - w > x > w \quad \text{or} \quad -d + w > x > -d \qquad (3.16) \end{aligned}$$

Substituting (3.13) in (3.16) and further mathematical manipulations result in:

$$\begin{aligned} & \sum_{n=-N}^{N} A_n e^{-j\beta_n x} \left(1 - j\frac{\epsilon\gamma_n}{\epsilon_o\eta_n}\cot(\eta_n h)\right) = \\ & -H_o e^{-j\beta_o x} e^{j\gamma_o h} \left(1 + j(\frac{\epsilon\gamma_n}{\epsilon_o\eta_n})\cot(\eta_n h)\right), \\ & d - w > x > w \quad \text{or} \quad -d + w > x > -d \qquad (3.17) \end{aligned}$$

Equations (3.15) and (3.17) are enforced at $(2N+1)$ points over $-d \leq x \leq d$ to obtain $(2N+1)$ equations to solve for unknown A_n. We choose the matching points equally distributed over one period of the structure as stated in [35].

The desired reflection coefficient is the ratio of the tangential component of the electric field of the reflected wave to the tangential component of the electric field of the incident wave, for the specular mode. Therefore, it is:

$$\Gamma_{TE} = \frac{A_o\gamma_o/(\omega\epsilon_o)}{-H_o\gamma_o/(\omega\epsilon_o)} = \frac{-A_o}{H_o} \tag{3.18}$$

3.2.2 TM^y (E-polarized case)

The incident plane wave at incident angle θ_i has the following fields (Figure 3.5(b)):

$$\vec{E_i} = \hat{a_y} E_o e^{-j\beta_o x} e^{j\gamma_o z} \tag{3.19}$$

$$\vec{H_i} = \hat{a_x}[E_o\gamma_o/(\omega\mu_o)]e^{-j\beta_o x}e^{j\gamma_o z} + \hat{a_z}[E_o\beta_o/(\omega\mu_o)]e^{-j\beta_o x}e^{j\gamma_o z} \tag{3.20}$$

In the region $z \geq h$, the reflected wave has the following fields:

$$\vec{E_r} = \hat{a_y} \sum_{n=-N}^{N} A_n e^{-j\beta_n x} e^{-j\gamma_n(z-h)} \tag{3.21}$$

$$\begin{aligned} \vec{H_r} = -\hat{a_x} &\sum_{n=-N}^{N} [A_n\gamma_n/(\omega\mu_o)]e^{-j\beta_n x}e^{-j\gamma_n(z-h)} \\ +\hat{a_z} &\sum_{n=-N}^{N} [A_n\beta_n/(\omega\mu_o)]e^{-j\beta_n x}e^{-j\gamma_n(z-h)} \end{aligned} \tag{3.22}$$

In the region $h \geq z \geq 0$, the fields are:

$$\vec{E_d} = \hat{a_y} \sum_{n=-N}^{N} [C_n e^{-j\beta_n x} e^{-j\gamma_n z} + D_n e^{-j\beta_n x} e^{j\gamma_n z}] \tag{3.23}$$

$$\begin{aligned}\vec{E_d} = \hat{a_x} \sum_{n=-N}^{N} & [(-C_n\eta_n/(\omega\mu_o))e^{-j\beta_n x}e^{-j\eta_n z} \\ & +(D_n\eta_n/(\omega\mu_o))e^{-j\beta_n x}e^{j\eta_n z}] \\ +\hat{a_z} \sum_{n=-N}^{N} & [(C_n\beta_n/(\omega\mu_o))e^{-j\beta_n x}e^{-j\eta_n z} \\ & +(D_n\beta_n/(\omega\mu_o))e^{-j\beta_n x}e^{j\eta_n z}]\end{aligned} \tag{3.24}$$

The presented method is studied in details in [35]. Only the two equations to be solved for A_n's are mentioned here as follows:

$$E_o e^{-j\beta_o x}e^{j\gamma_o h} + \sum_{n=-N}^{N} A_n e^{-j\beta_n x} = 0, \quad -w \leq x \leq w \tag{3.25}$$

$$\begin{aligned}\sum_{n=-N}^{N} A_n e^{-j\beta_n x}\left(\gamma_n - \eta_n \frac{1+e^{-j2\eta_n h}}{-1+e^{-j2\eta_n h}}\right) = & \\ E_o e^{-j\beta_o x}e^{j\gamma_o h}\left(\gamma_0 + j\eta_o \cos(\eta_o h)\right), & \\ d-w > x > w \quad \text{or} \quad -d+w > x > -d & \end{aligned} \tag{3.26}$$

In the same manner as the previous part, equations 3.25 and 3.26 are enforced at $(2N+1)$ points over $-d \leq x \leq d$ to obtain $(2N+1)$ equations to solve for unknown A_n. As before, uniform distributed points are chosen over one period of the structure.

As indicated previously, the desired reflection coefficient is the ratio of the tangential component of the electric field of the reflected wave to the tangential component of the electric field of the incident wave, for the specular mode. Therefore, it is:

$$\Gamma_{TM} = \frac{A_o}{E_o} \tag{3.27}$$

3.2.3 Verification and Numerical results

To verify the implemented code based on PMM, some of the results obtained in [35] are retrieved, here. Table 3.1 shows the normalized power density in mode zero for increasing number of modes for a structure having $2d = 0.75\lambda$, $w = d/2$, $h = 2d$, and relative permittivity of 3 and incident angle of $\theta_i = 60°$. The results are in good agreement with those reported in [35].

Variation of the normalized power of zeroth order reflected wave against the structure period for a structure having $w = d/2$, $h = 2d$, and relative permittivity of 3 ($\epsilon_r = \epsilon/\epsilon_o$) are shown in Figures 3.6(a) and (b), for TE and TM waves, respectively. The incident angle is $\theta_i = 60°$. The results are in excellent agreement with those reported in [35].

The discrepancies between the results reported in [35] and the ones reported here (Figures 3.6and Table 3.1) may be attributed to the different match points chosen in [35] from those selected here.

Reflection phases obtained, using point matching method (PMM), are shown in Figure 3.7(a) and (b), for TE and TM waves, respectively. These reflection phases correspond to the same structures as studied in section 3.1. Good agreement between PMM results and those obtained using FEM-CAD and TLM-CAD is observed in TE cases but not in TM cases. In the conventional periodic structures the reflection phase decreases as frequency increases. The results obtained by the PMM does not show this trend, so this numerical technique is not reliable.

Table 3.1: Normalized power in mode zero (specular mode) for increasing number of modes for a structure having $2d = 0.75\lambda$, $w = d/2$, $h = 2d$, and relative permittivity of 3 and incident angle of $\theta_i = 60°$

modes	H-polarization	E-polarization
7	0.2563	0.8871
11	0.2787	0.8841
15	0.2884	0.8831
19	0.2937	0.8825
23	0.2970	0.8822
27	0.2994	0.8819
31	0.3015	0.8816
35	0.3039	0.8813
39	0.3073	0.8807

3.3 Entire-domain basis functions

The geometry of the problem is shown in Figure 3.8. It is the same as the one introduced in the previous section, except that the parallel strips are placed in the xy plane ($z = 0$) whereas in Figure 3.5, the ground plane was laid in xy plane. Also, in order to keep the notation consistent with [38] the wave is assumed to be propagating in the negative x-direction. The method is analogous to the point matching method except for the modal expansion of the electric surface currents on the conducting strips rather than satisfying boundary conditions for certain points on the interface boundary. Although the method presented in this thesis is similar to the one introduced in [38], it has some differences which will be pointed out and discussed in the following parts.

3.3.1 TE^y (H-polarized case)

The geometry of the problem is shown in Figure 3.8(a). Field components corresponding to TE^y polarization in both spatial and spectral domains are presented in Appendix A, according to the notation used in [28]. Only the

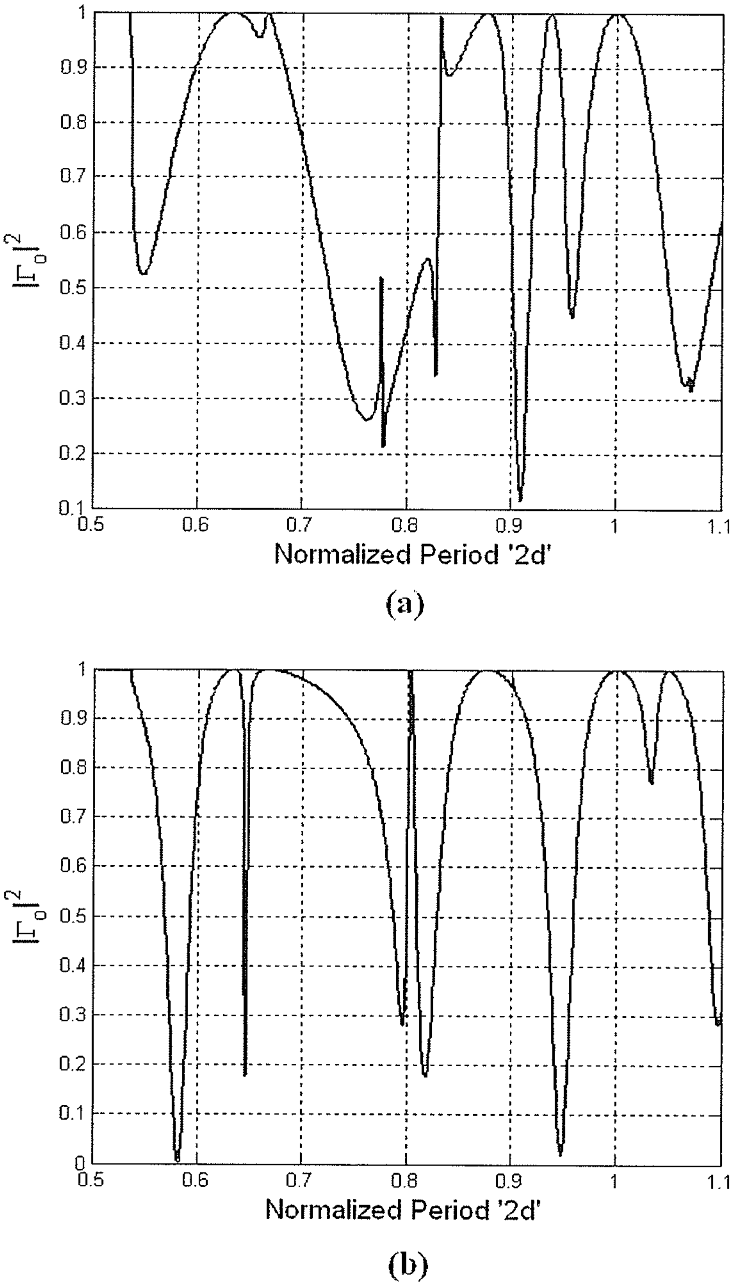

(a)

(b)

Figure 3.6: Variation of the normalized power of zeroth order reflected wave against the structure period (with respect to the wavelength) for a structure having $w = d/2$, $h = 2d$, and relative permittivity of 3 ($\epsilon_r = 3$) at incident angle of $\theta_i = 60°$. (a) TE^y and (b) TM^y polarization.

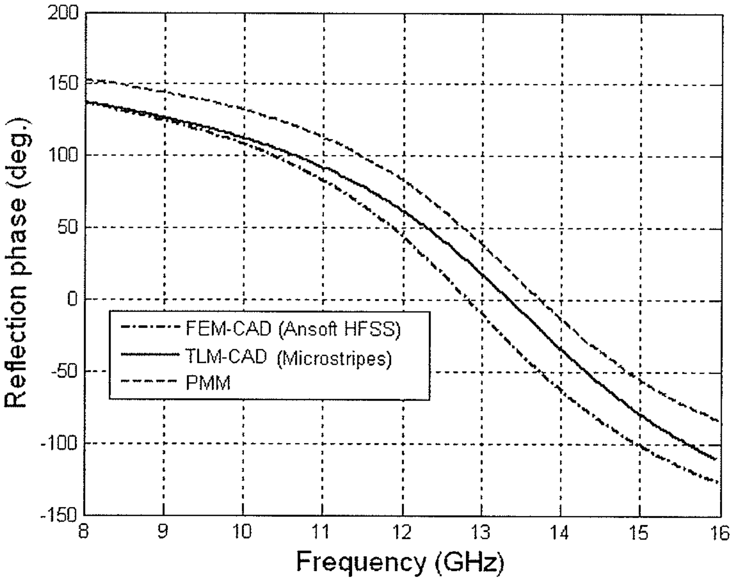

(a)

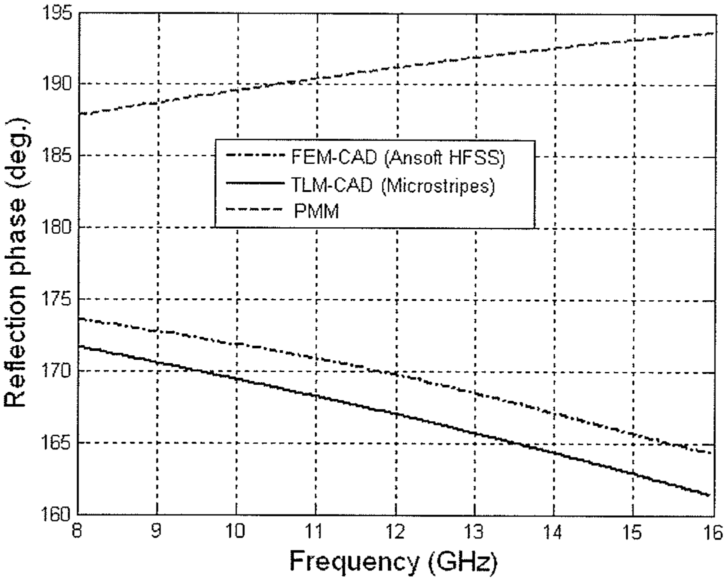

(b)

Figure 3.7: Reflection phase at normal incident angle, subject to the plane wave with (a) TE^y and (b) TM^y polarization. The geometry of the problem is shown in Figure 3.1. dimensions are $h = 1.59$ mm, $2w = 5$ mm and $2d = 10$ mm, and the relative permittivity of the dielectric substrate is 2.5.

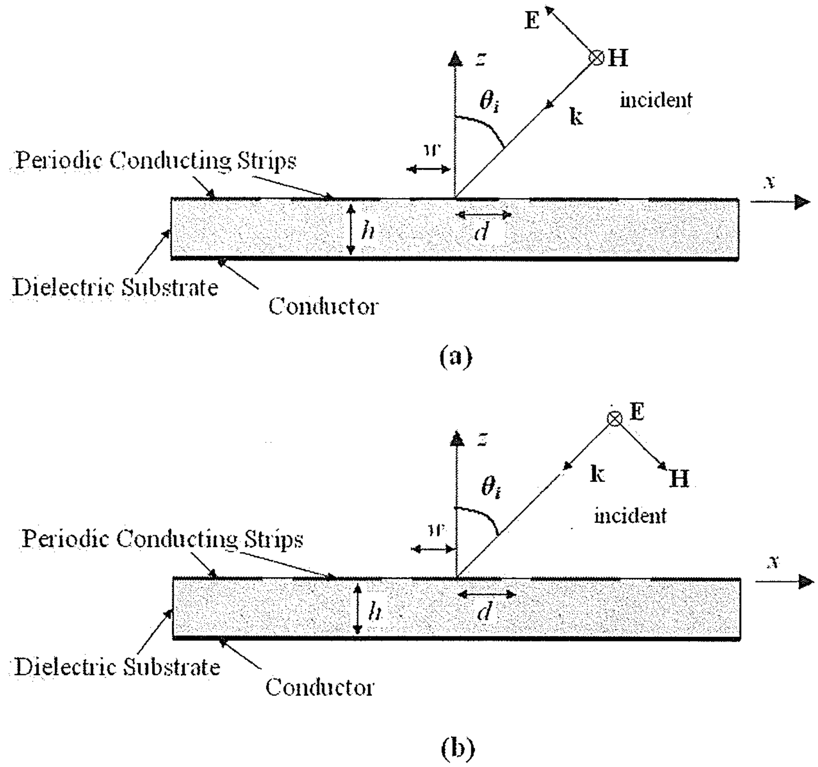
E
H
z
θ_i
k
incident
w
Periodic Conducting Strips
x
h
d
Dielectric Substrate
Conductor
(a)
E
z
θ_i
k
H
incident
w
Periodic Conducting Strips
x
h
d
Dielectric Substrate
Conductor
(b)

Figure 3.8: Grounded dielectric slab loaded by infinitely-long periodic metallic strips. (a) TE^y and (b) TM^y polarization.

tangential field components that are necessary for the modal expansions are employed, as follows.

In the air region (region (1)), one can write:

$$H_y^{(1)}(x,y,z) = \sum_{n=-N}^{N} S_n e^{jk_{xn}x} e^{-jk_{zn}z} + H_y{}^i e^{jk_{x0}x} e^{jk_{z0}z}, \tag{3.28}$$

$$E_x^{(1)}(x,y,z) = -\frac{\omega\mu}{k_0^2}\left(\sum_{n=-N}^{N} -S_n k_{zn} e^{jk_{xn}x} e^{-jk_{zn}z} + H_y{}^i k_{z0} e^{jk_{x0}x} e^{jk_{z0}z}\right). \tag{3.29}$$

In the dielectric region (region (2)), satisfying the appropriate boundary condition at $z = -h$, which is vanishing the tangential component of the electric fields on the PEC ground plane surface, one can write:

$$H_y^{(2)}(x,y,z) = \sum_{n=-N}^{N} Q_n e^{jk_{xn}x}\left(e^{-jk_{1zn}z} + e^{j2k_{1zn}h}e^{jk_{1zn}z}\right), \tag{3.30}$$

$$E_x^{(2)}(x,y,z) = -\frac{\omega\mu}{k_1^2}\left(\sum_{n=-N}^{N} Q_n e^{jk_{xn}x}\left(-k_{1zn}e^{-jk_{1zn}z} + k_{1zn}e^{j2k_{1zn}h}e^{jk_{1zn}z}\right)\right). \tag{3.31}$$

where

$$\begin{aligned} k_{xn} &= k_0\sin(\theta_i) + \frac{2n\pi}{p}, \\ k_{zn} &= \sqrt{k_0^2 - k_{xn}^2}, \\ k_{1zn} &= \sqrt{k_1^2 - k_{xn}^2}, \\ k_0 &= \omega\sqrt{\epsilon_0\mu_0}, \\ k_1 &= k_0\sqrt{\epsilon_r}. \end{aligned} \tag{3.32}$$

Here, S_n and Q_n are unknown complex amplitudes to be determined and k_{xn} is the phase constant associated with the Floquet mode due to the periodicity along the x direction. In order to determine the aforementioned unknowns, the appropriate boundary conditions are imposed at $z = 0$ as follows:

$$E_x^{(1)}(x,y,0) = E_x^{(2)}(x,y,0) \tag{3.33}$$

$$H_y^{(1)}(x,y,0) - H_y^{(2)}(x,y,0) = \begin{cases} -J_x(x,y), & \text{on the strip} \\ 0, & \text{elsewhere.} \end{cases} \tag{3.34}$$

$$E_x^{(1)}(x,y,0) = 0, \qquad \text{on the strip} \tag{3.35}$$

where $J_x(x,y)$ is the unknown surface current on the conducting strips and can be expanded into a product of a series of cosine functions and a function satisfying the edge condition (vanishing the x-directed surface currents at the edges) [38, 40]. For the zeroth strip, this surface current is:

$$J_x(x,y) = e^{jk_{x0}x}\sqrt{1-(\frac{x}{w})^2}\sum_{\nu=0}^{M-1}(j)^{\nu}A_{\nu}\cos(\omega_{\nu}(x+w)), \qquad |x| \leq w \tag{3.36}$$

where $\omega_{\nu} = \nu\pi/2w$. Substituting equations (3.29) and (3.31) in equation (3.33) results in

$$\frac{-S_n k_{zn} + k_{z0}H_y^i\delta(n)}{k_0^2} = \frac{Q_n k_{1zn}(e^{j2k_{1zn}h}-1)}{k_1^2} \tag{3.37}$$

Substituting equations (3.28) and (3.30) in equation (3.34) and multiplying both sides by $e^{-jk_m x}$ yields,

$$\begin{aligned} &\sum_{n=-N}^{N} S_n e^{j(k_{xn}-k_{xm})x} + {H_y}^i e^{j(k_{x0}-k_{xm})x}\delta(n) \\ &\qquad - \sum_{n=-N}^{N} Q_n e^{j(k_{xn}-k_{xm})x}\left(1+e^{j2k_{1zn}h}\right) \\ &= \begin{cases} e^{j(k_{x0}-k_{xm})x}\sqrt{1-(\frac{x}{w})^2}\sum_{\nu=0}^{M-1}(j)^{\nu}A_{\nu}\cos(\omega_{\nu}(x+w)), & \text{on the strips} \\ 0, & \text{elsewhere.} \end{cases} \end{aligned} \tag{3.38}$$

Integrating the left hand side of the (3.38) over the period length ($p = 2d$) results in

$$\begin{aligned} &\int_{-d}^{d}\left(\sum_{n=-N}^{N} S_n e^{j(k_{xn}-k_{xm})x} + {H_y}^i e^{j(k_{x0}-k_{xm})x}\delta(n)\right)dx \\ &\qquad - \int_{-d}^{d}\left(-\sum_{n=-N}^{N} Q_n e^{j(k_{xn}-k_{xm})x}\left(1+e^{j2k_{1zn}h}\right)\right)dx \\ &= \begin{cases} 2dS_n + 2d{H_y}^i\delta(n) - 2dQ_n(1+e^{j2k_{1zn}h}), & m = n \\ 0, & m \neq n. \end{cases} \end{aligned} \tag{3.39}$$

where $\delta(n)$ is the Kronecker delta. On the other hand, integrating the right hand side of the (3.38) over the period length ($p = 2d$) yields

$$-\int_{-d}^{d}\left(e^{j(k_{x0}-k_{xm})x}\sqrt{1-(\frac{x}{w})^2}\sum_{\nu=0}^{M-1}(j)^\nu A_\nu\cos(\omega_\nu(x+w))\right)dx$$
$$= -\frac{1}{2}\sum_{\nu=0}^{M-1}\int_{-w}^{w}(j)^\nu A_\nu\left[e^{j\omega_\nu(x+w)}e^{-j\frac{2m\pi}{p}}+e^{-j\omega_\nu(x+w)}e^{-j\frac{2m\pi}{p}}\right]$$
$$\cdot\sqrt{1-(\frac{x}{w})^2}dx. \qquad (3.40)$$

The following identity presented in [40], relating the integrals of Chebyshev polynomials to Bessel functions, is useful to simplify (3.40) and other similar equations throughout this study, as well:

$$\frac{1}{\pi w}\int_{-w}^{w}U_n(x/w)e^{j\zeta x}\sqrt{1-(\frac{x}{w})^2}dx = j^n\frac{n+1}{\zeta w}J_{n+1}(\zeta w) \qquad (3.41)$$

where $U_n(x)$ is the Chebychev polynomial of the second kind [41]. Owing to the fact that $U_0(x) = 1$, right hand side of equation (3.40) is simplified to

$$\text{RHS of 3.40} = -\sum_{\nu=0}^{M-1}\frac{\pi w}{2}\left[\frac{J_1(\frac{\nu\pi}{2}+\frac{2\pi m w}{p})}{\frac{\nu\pi}{2}+\frac{2\pi m w}{p}}+(-1)^\nu\frac{J_1(\frac{\nu\pi}{2}-\frac{2\pi m w}{p})}{\frac{\nu\pi}{2}-\frac{2\pi m w}{p}}\right]A_\nu (3.42)$$

Therefore, equating the equations (3.39) and (B.9), for $m = n$, one obtains:

$$-\sum_{\nu=0}^{M-1}A_\nu F(n,\nu,w,p) = 2dS_n + 2dH_y{}^i\delta(n) - 2dQ_n(1+e^{j2k_{1zn}h}), \qquad (3.43)$$

where

$$F(n,\nu,w,p) = \frac{\pi w}{2}\left[\frac{J_1(\frac{\nu\pi}{2}+\frac{2\pi n w}{p})}{\frac{\nu\pi}{2}+\frac{2\pi n w}{p}}+(-1)^\nu\frac{J_1(\frac{\nu\pi}{2}-\frac{2\pi n w}{p})}{\frac{\nu\pi}{2}-\frac{2\pi n w}{p}}\right]. \qquad (3.44)$$

The only boundary condition left, is the one presented in equation (3.35).

Substituting (3.29) in (3.35), yields:

$$\sum_{n=-N}^{N} S_n k_{zn} e^{jk_{xn}x} = {H_y}^i k_{z0} e^{jk_{x0}x} \tag{3.45}$$

Multiplying both sides by $(-j)^\mu e^{-jk_{x0}x}\sqrt{1-(\frac{x}{w})^2}\cos(\omega_\mu(x+w))$, integrating over the periodic ($p = 2d$), and following the above-mentioned procedure in the same manner, eventually results in the following equation:

$$\sum_{n=-N}^{N} S_n k_{zn} F(n,\mu,w,p) = {H_y}^i k_{z0} F(0,\mu,w,p) \tag{3.46}$$

Employing equations (3.37) and (3.43) gives a relationship between S_n's in terms of the incident wave and coefficients A_ν's as follows

$$S_n = -\frac{1}{p(1+c_n)}\sum_{\nu=0}^{M} A_\nu F(n,\nu,w,p) - \frac{1-c_0}{1+c_n}{H_y}^i \tag{3.47}$$

where c_n is

$$c_n = \left(\frac{k_1}{k_0}\right)^2\left(\frac{k_{1zn}}{k_{zn}}\right)\left(\frac{1+e^{j2k_{1zn}h}}{-1+e^{j2k_{1zn}h}}\right) = \left(\frac{k_1}{k_0}\right)^2\left(\frac{k_{1zn}}{k_{zn}}\right)(-j\cot(2k_{1zn}h)). \tag{3.48}$$

Substituting 3.47 in 3.46 results in

$$\sum_{\nu=0}^{M-1} A_\nu \sum_{n=-N}^{N} \frac{k_{zn}}{1+c_n} F(n,\nu,w,p)F(n,\mu,w,p) = -{H_y}^i k_{z0} F(0,\mu,w,p)\left(\frac{2p}{1+c_0}\right). \tag{3.49}$$

In order to determine A_ν's, equation (3.49) has to be used for $\mu = 0, 1, ..., M-1$ to produce a complete set of M equations and M unknowns.

3.3.2 TM^y (E-polarized case)

The geometry of the problem is shown in Figure 3.8(b). Field components corresponding to the TM^y polarization in both spatial and spectral domains are presented in Appendix A, according to the notation used in [28]. As before, only the tangential field components that are necessary for the modal expansions are employed, as follows.

In the air region (region (1)), one can write:

$$E_y^{(1)}(x,y,z) = \sum_{n=-N}^{N} R_n e^{jk_{xn}x} e^{-jk_{zn}z} + E_y{}^i e^{jk_{x0}x} e^{jk_{z0}z}, \tag{3.50}$$

$$H_x^{(1)}(x,y,z) = -\frac{\omega\epsilon}{k_0^2}\left(\sum_{n=-N}^{N} -R_n k_{zn} e^{jk_{xn}x} e^{-jk_{zn}z} + E_y{}^i k_{z0} e^{jk_{x0}x} e^{jk_{z0}z}\right). \tag{3.51}$$

In the dielectric region (region (2)), satisfying the appropriate boundary condition at $z = -h$, which is vanishing the tangential component of the electric fields on the PEC ground plane surface, one can write:

$$E_y^{(2)}(x,y,z) = \sum_{n=-N}^{N} P_n e^{jk_{xn}x}\left(e^{-jk_{1zn}z} - e^{j2k_{1zn}h} e^{jk_{1zn}z}\right), \tag{3.52}$$

$$H_x^{(2)}(x,y,z) = -\frac{\omega\epsilon}{k_1^2}\left(\sum_{n=-N}^{N} P_n e^{jk_{xn}x}\left(-k_{1zn} e^{-jk_{1zn}z} - k_{1zn} e^{j2k_{1zn}h} e^{jk_{1zn}z}\right)\right). \tag{3.53}$$

Here, R_n and P_n are unknown complex amplitudes to be determined and the remaining parameters are defined as before. In order to determine these unknowns, the appropriate boundary conditions are imposed at $z = 0$ as follows:

$$E_y^{(1)}(x,y,0) = E_y^{(2)}(x,y,0) \tag{3.54}$$

$$H_x^{(1)}(x,y,0) - H_x^{(2)}(x,y,0) = \begin{cases} J_y(x,y), & \text{on the strip} \\ 0, & \text{elsewhere.} \end{cases} \tag{3.55}$$

$$E_y^{(1)}(x,y,0) = 0, \qquad \text{on the strip} \tag{3.56}$$

where $J_y(x,y)$ is the unknown surface current on the conducting strips and can be expanded into a product of series of cosine functions and a function satisfying the edge condition [40]. The physical description and reasoning of why this edge condition can represent the surface current singularity at the edges has been addressed in [42]. For the zeroth strip, this surface current is:

$$J_y(x,y) = e^{jk_{x0}x} \frac{1}{\sqrt{1-(\frac{x}{w})^2}} \sum_{\nu=0}^{M-1} (j)^\nu A_\nu \cos(\omega_\nu(x+w)), \qquad |x| \leq w \tag{3.57}$$

where $\omega_\nu = \nu\pi/2w$. Substituting equations (3.50) and (3.52) in equation (3.54) results in

$$R_n + E_y^i \delta(n) = P_n(-e^{j2k_{1zn}h} + 1) \tag{3.58}$$

Substituting equations (3.51) and (3.53) in equation (3.55) and multiplying both sides by $e^{-jk_m x}$ yields,

$$\begin{aligned} &\sum_{n=-N}^{N} -k_{zn} R_n e^{j(k_{xn}-k_{xm})x} + E_y{}^i e^{j(k_{x0}-k_{xm})x} k_{z0} \delta(n) \\ &\qquad + \sum_{n=-N}^{N} P_n k_{1zn} e^{j(k_{xn}-k_{xm})x} \left(1 + e^{j2k_{1zn}h}\right) \\ &= \begin{cases} \frac{\omega\mu}{\sqrt{1-(\frac{x}{w})^2}} e^{j(k_{x0}-k_{xm})x} \sum_{\nu=0}^{M-1} (j)^\nu A_\nu \cos(\omega_\nu(x+w)), & \text{on the strips} \\ 0, & \text{elsewhere.} \end{cases} \end{aligned} \tag{3.59}$$

Integrating the left hand side of the (3.38) over the period length ($p = 2d$)

results in

$$\int_{-d}^{d}\left(\sum_{n=-N}^{N} -k_{zn}R_n e^{j(k_{xn}-k_{xm})x} + E_y{}^i e^{j(k_{x0}-k_{xm})x}k_{z0}\delta(n)\right)dx$$
$$+\int_{-d}^{d}\left(\sum_{n=-N}^{N} P_n k_{1zn} e^{j(k_{xn}-k_{xm})x}\left(1+e^{j2k_{1zn}h}\right)\right)dx$$
$$=\begin{cases} -2dk_{zn}R_n + 2dk_{z0}E_y{}^i\delta(n) + 2dP_n k_{1zn}(1+e^{j2k_{1zn}h}), & m=n \\ 0, & m\neq n. \end{cases} \tag{3.60}$$

where $\delta(n)$ is the Kronecker delta as defined before. On the other hand, integrating the right hand side of the (3.38) over the period length ($p = 2d$) yields

$$\int_{-d}^{d}\left(e^{j(k_{x0}-k_{xm})x}\frac{\omega\mu}{\sqrt{1-(\frac{x}{w})^2}}\sum_{\nu=0}^{M-1}(j)^{\nu}A_{\nu}\cos(\omega_{\nu}(x+w))\right)dx$$
$$=\frac{1}{2}\sum_{\nu=0}^{M-1}(j)^{\nu}A_{\nu}\int_{-w}^{w}\frac{\omega\mu\left[e^{j\omega_{\nu}(x+w)}e^{-j\frac{2m\pi}{p}}+e^{-j\omega_{\nu}(x+w)}e^{-j\frac{2m\pi}{p}}\right]}{\sqrt{1-(\frac{x}{w})^2}}dx. \tag{3.61}$$

The following identity presented in [40], relating the integrals of Chebyshev polynomials to Bessel functions, is useful to simplify (3.61) and other similar equations throughout this study, as well:

$$\frac{1}{\pi w}\int_{-w}^{w}\frac{T_n(x/w)e^{j\zeta x}}{\sqrt{1-(\frac{x}{w})^2}}dx = j^n J_n(\zeta w) \tag{3.62}$$

where $T_n(x)$ is the Chebychev polynomial of the first kind [41]. Owing to the fact that $T_0(x) = 1$, right hand side of equation (3.61) is simplified to

$$\text{RHS of 3.61} = \omega\mu\sum_{\nu=0}^{M-1}\frac{\pi w}{2}\left[J_0(\frac{\nu\pi}{2}+\frac{2\pi m w}{p}) + (-1)^{\nu}J_0(\frac{\nu\pi}{2}-\frac{2\pi m w}{p})\right]A_{\nu} \tag{3.63}$$

Therefore, equating the equations (3.60) and (3.63), for $m = n$, one obtains:

$$\sum_{\nu=0}^{M-1} A_\nu(\eta_0 k_0)G(n,\nu,w,p) = -2dk_{zn}R_n + 2dk_{z0}{E_y}^i\delta(n) + 2dP_n k_{1zn}(1 + e^{j2k_{1zn}h}), \tag{3.64}$$

where,

$$G(m,\nu,w,p) = \frac{\pi w}{2}\left[J_0(\frac{\nu\pi}{2} + \frac{2\pi m w}{p}) + (-1)^\nu J_0(\frac{\nu\pi}{2} - \frac{2\pi m w}{p})\right], \tag{3.65}$$

and $\eta_0(=\omega\mu/k_0)$ is the characteristics impedance of the free space. The only boundary condition left, is the one presented in equation (3.56). Substituting (3.50) in (3.56), yields:

$$\sum_{n=-N}^{N} R_n e^{jk_{xn}x} = -{E_y}^i e^{jk_{x0}x} \tag{3.66}$$

Multiplying both sides by $(-j)^\mu e^{-jk_{x0}x}\frac{1}{\sqrt{1-(\frac{x}{w})^2}}\cos(\omega_\mu(x+w))$, integrating over the periodic $(p = 2d)$, and following the above-mentioned procedure in the same manner, eventually results in the following equation:

$$\sum_{n=-N}^{N} R_n G(n,\mu,w,p) = -{E_y}^i G(0,\mu,w,p) \tag{3.67}$$

Employing equations (3.58) and (3.64) gives a relationship between R_n's in terms of the incident wave and coefficients A_ν's as follows

$$R_n = \frac{1}{T_n}\left(\sum_{\nu=0}^{M-1} A_\nu(k_0\eta_0)G(n,\nu,w,p) - {E_y}^i\delta(n)b_n\right) \tag{3.68}$$

where b_n is

$$b_n = k_{zn} + k_{1zn}j\cot(k_{1zn}h)), \tag{3.69}$$

and T_n is

$$T_n = -k_{zn} + k_{1zn} j \cot(k_{1zn} h)). \tag{3.70}$$

Substituting (3.67) in (3.68) results in

$$\sum_{\nu=0}^{M-1} A_\nu \sum_{n=-N}^{N} \frac{k_0 \eta_0}{T_n} G(n, \nu, w, p) G(n, \mu, w, p) = E_y{}^i G(0, \mu, w, p) \left(\delta(0) \frac{b_0}{T_0} - 1 \right). \tag{3.71}$$

In order to determine A_ν's, equation 3.71 has to be used for $\mu = 0, 1, ..., M-1$ to produce a complete set of M equations and M unknowns.

Although, the formulations for TM^y appear very similar to those presented in [38], they are different in surface current expansions. In this work, all surface currents are expanded on the PEC strips satisfying the edge condition, whereas in [38] only the surface currents in x directions are considered, either electric surface currents on the strips or magnetic surface currents on the slots. One of the advantages of working with electric surface current is that one can gain physical insight to the current distribution over the strips width.

3.4 Method of moment (MoM) solutions

A computer code developed based on the MoM to treat infinitely periodic strips on multilayered dielectric is briefly explained in Appendix B. The code basically has the subroutine G1DMULT which treats the multilayered Green's functions [43, 44]. As well, it has a core subroutine to solve surface integral equations using MoM and relates the coefficients of the surface current distribution to the reflection coefficient modes. The MoM employs entire-domain basis functions. The entire-domain basis functions are the same as the ones introduced in the previous sections and implemented by this author. The results obtained using this method along with the modal expansion method will be discussed in the next section.

One should note that in MoM analysis the field is decomposed with respect to the z direction (TE^z and TM^z). The corresponding fields and different operating modes of the artificial surface are shown in Figure 3.9.

3.5 Numerical results and Verifications

Reflection phases for the same structure as the one shown in Figure 3.1, and for certain parameters of $h = 1.59$ mm, $2w = 5$ mm and $2d = 10$ mm, are shown in Figure 3.10, when the structure is subjected to normal incidence. Excellent agreement (less than %5 frequency shift) between modal expansion and MoM are observed. The results are also compared against those obtained using commercial software packages. In general, good agreement are observed between the results. For both modal expansion and MoM cases, a total number of 20 modes for the current expansion and 61 Floquet's modes were considered.

Convergence of modal expansion and MoM

The convergence of the modal expansion method is investigated using different total number of current basis functions (M) and total number of Floquet's modes ($2N + 1$). Good convergence has been acvhieved as M and N grows. the Reflection phases versus frequency for four different choices of M and N are shown in Figure 3.11.

The convergence of the MoM code is also investigated in the same manner. The total number of current basis functions (M) and total number of Floquet's modes ($2N + 1$) are considered. Good convergence has been achieved as M and N grows. The reflection phases versus frequency for four different choice of M and N are shown in Figure 3.12.

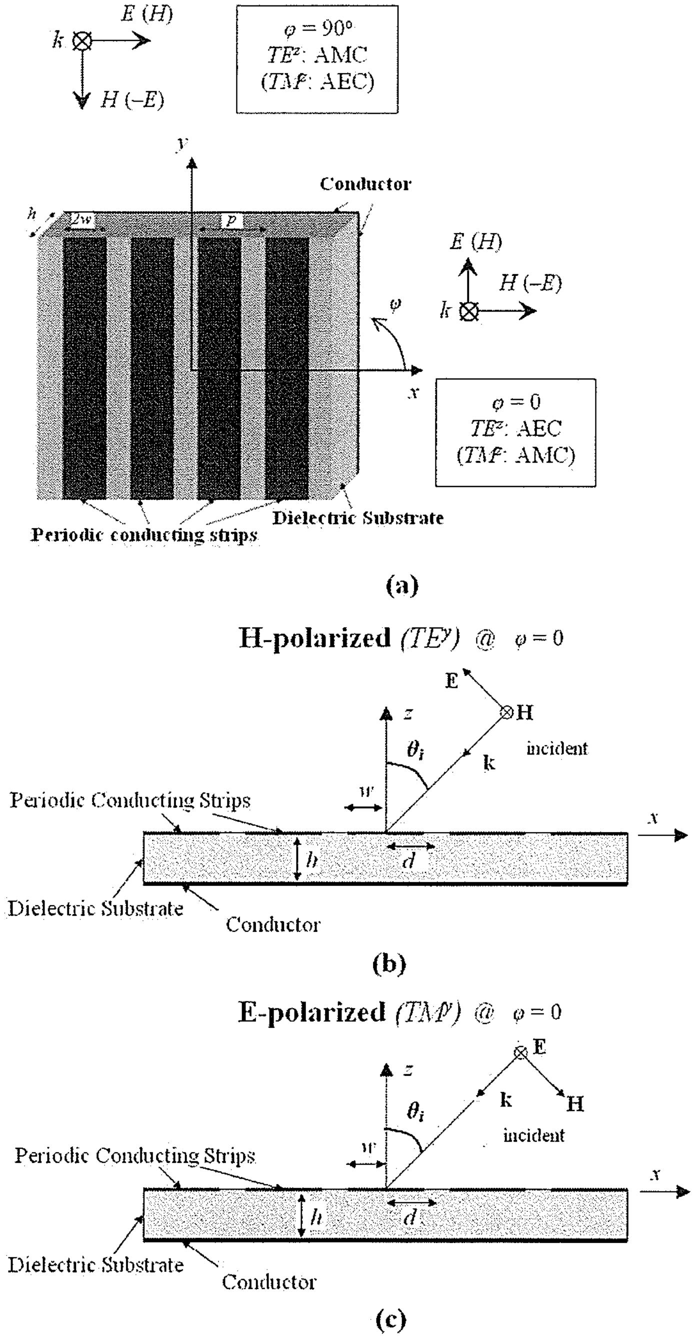
E (H)
k
H (−E)
φ = 90°
TE^z: AMC
(TM^z: AEC)
y
Conductor
h
2w
p
E (H)
H (−E)
k
φ
x
φ = 0
TE^z: AEC
(TM^z: AMC)
Dielectric Substrate
Periodic conducting strips
(a)
H-polarized (TE^y) @ φ = 0
E
H
z
θ_i
k
incident
Periodic Conducting Strips
w
x
h
d
Dielectric Substrate
Conductor
(b)
E-polarized (TM^y) @ φ = 0
E
z
θ_i
k
H
incident
Periodic Conducting Strips
w
x
h
d
Dielectric Substrate
Conductor
(c)

Figure 3.9: Periodic strip grating on a grounded dielectric slab. (a) 3-D view and field decompositions with respect to the z direction. (b) H-polarized and (c) E-polarized side views at $\varphi = 0°$.

It is observed that the reflection phases due to the TE_y polarization, obtained using either the MoM code or modal expansion method, are in good agreement (less than 3% frequency shift) . Also, the obtained reflection phases

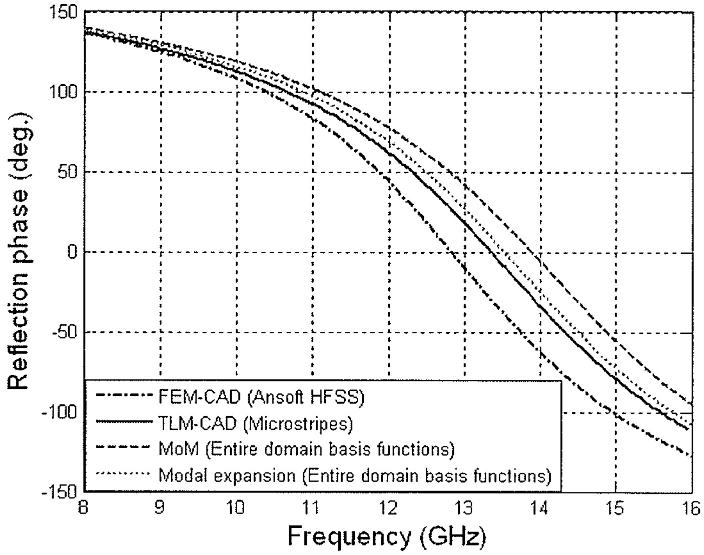

(a)

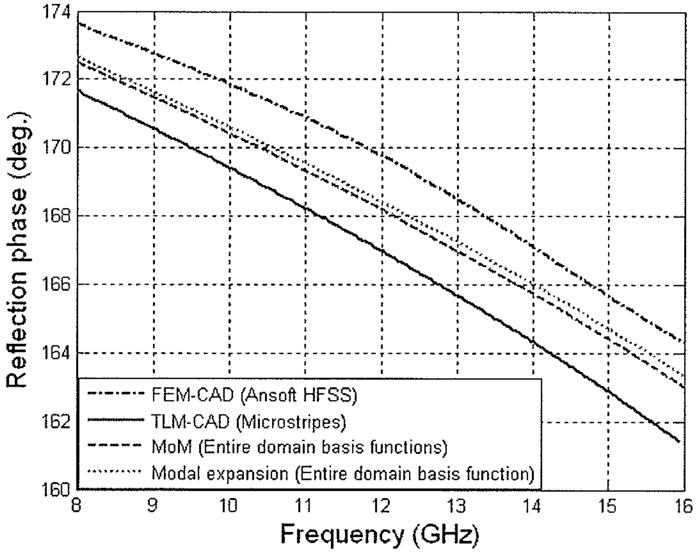

(b)

Figure 3.10: Reflection phases at normal incident angle, subject to the plane wave with (a) TE^y and (b) TM^y polarization. The structure is shown in Figure 3.1, and parameters are $h = 1.59$ mm, $2w = 5$ mm and $2d = 10$ mm.

due to the TM_y polarization are almost identical for both methods.

Surface current distributions on the strips are shown in Figure 3.13. As expected for the H-polarization case (TE^y), the currents are in the x-direction, since there is no electric field component in the y-direction. The edge condi-

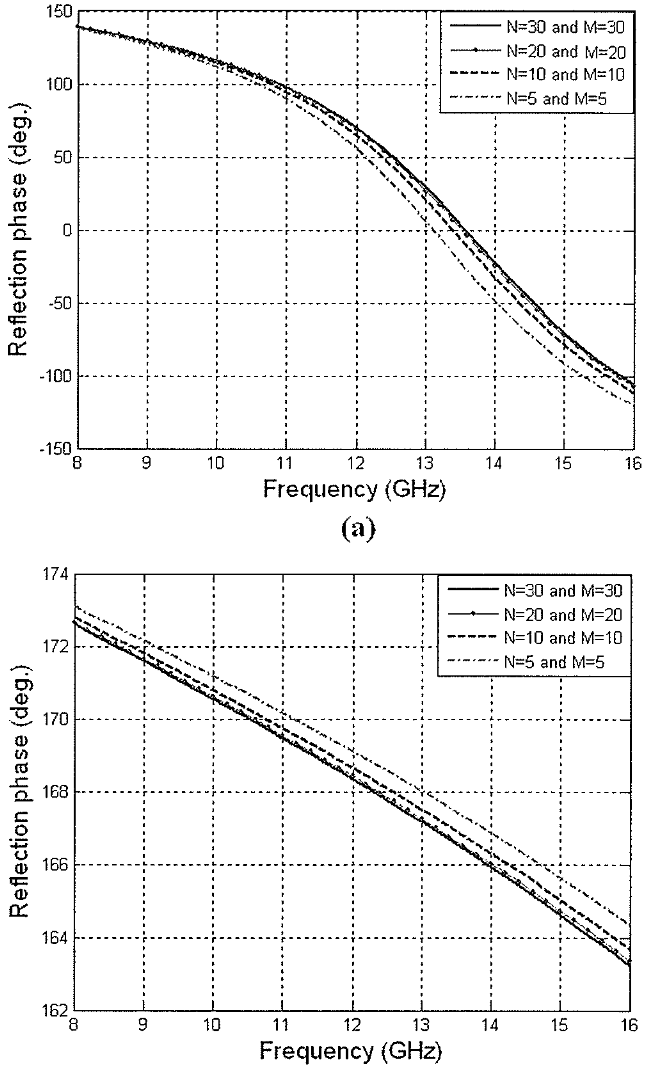

(a)

(b)

Figure 3.11: Reflection phases at normal incident angle, subject to the plane wave using modal expansion method with different number of basis functions and Floquet's modes. (a) TE^y and (b) TM^y polarization. The structure is shown in Figure 3.1, and parameters are $h = 1.59$ mm, $2w = 5$ mm and $2d = 10$ mm.

tion, which is vanishing the surface current at the edges for the currents directed perpendicularly to the strips, have been applied with the proper choice of the basis functions [40]. For the E-polarization case (TM^y), the currents are

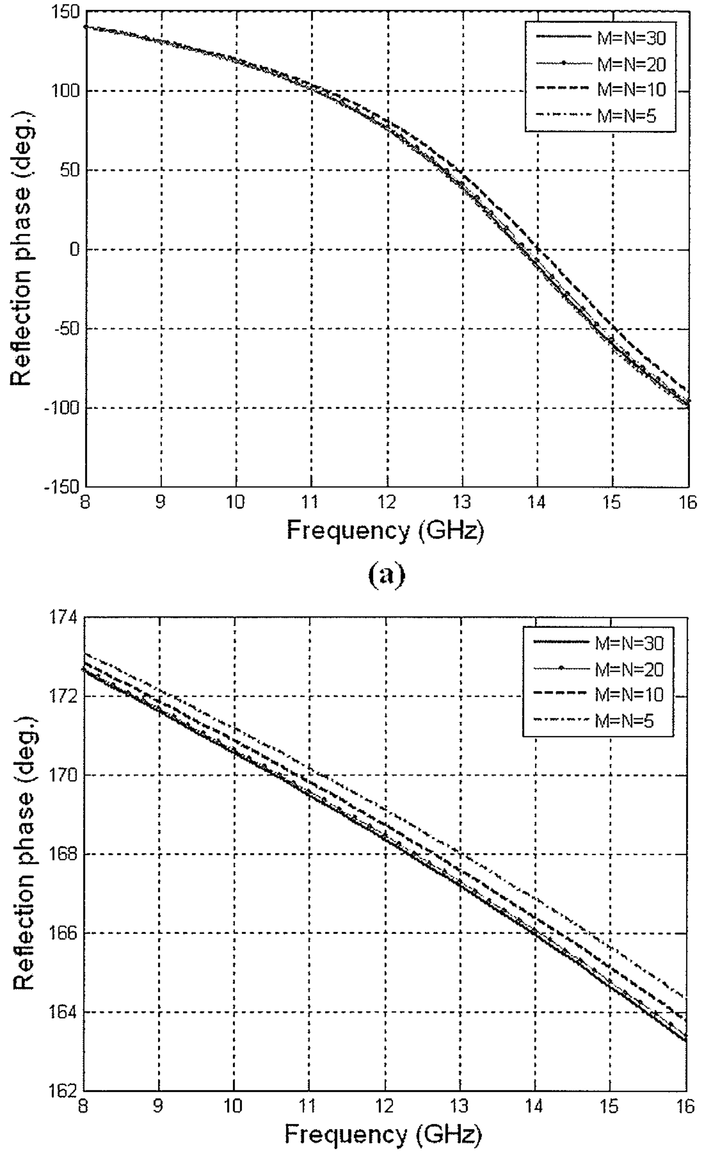

Figure 3.12: Reflection phases at normal incident angle, subject to the plane wave using MoM with different number of basis functions and Floquet's modes.(a) TE^y and (b) TM^y polarization.The structure is shown in Figure 3.1, and parameters are $h = 1.59$ mm, $2w = 5$ mm and $2d = 10$ mm.

in the y-direction, since there is no electric field component in the x-direction. The edge condition, which takes the singularity of the surface current directed along the strips at the edges into account, have been applied with the proper choice of basis functions [40, 42].

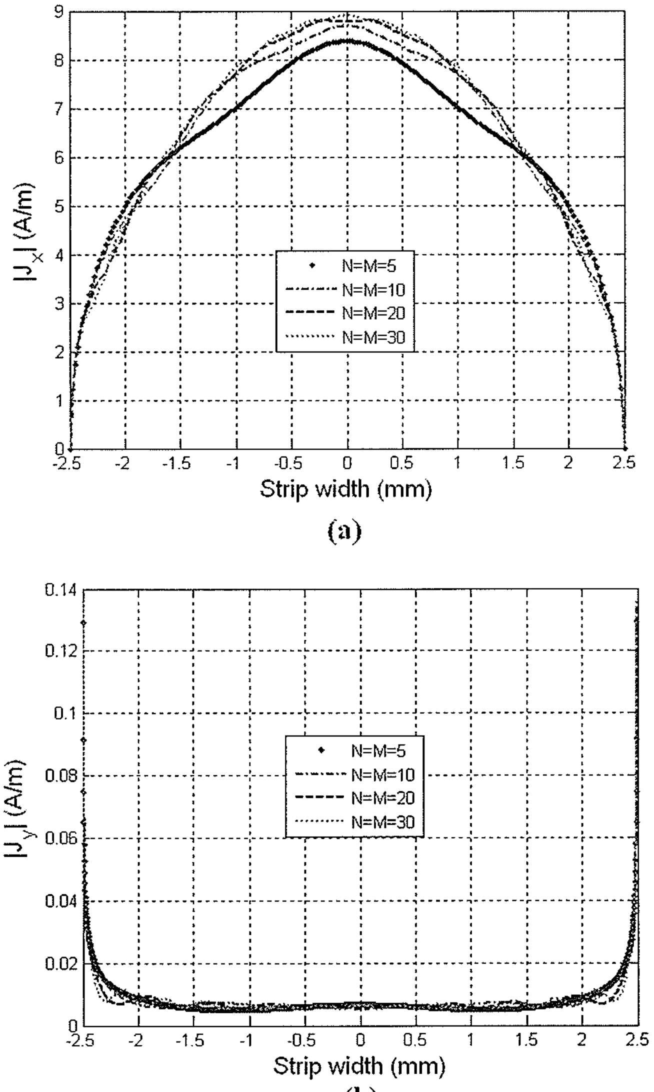

(a)

(b)

Figure 3.13: Surface current distributions on the strip versus its width, for different number of basis functions using modal expansion. The incident plane wave is at normal angle. (a) Induced $|J_x|$ due to the TE^y polarization with ($H_y^i = 1A/m$).(b) Induced $|J_y|$ due to the TM^y polarization with ($E_y^i = 1V/m$). The structure is shown in Figure 3.1, and parameters are $h = 1.59$ mm, $2w = 5$ mm and $2d = 10$ mm.

AEC/AMC ground plane characterization using Modal expansion

As the last part of the study in this chapter, the reflection phases are shown for a few different angles of incident for both TE^y and TM^y. They are obtained using modal expansion methods with entire domain basis functions. As observed, both AMC and PEC-like characteristics tend to be maintained in a noticeable frequency range, which means the structure is wideband in the frequency sense. The obtained results shown in Figure 3.14 correspond to the case with periodicity of $p = 12$ mm and strip width of $2w = 7.76$ mm. The relative permittivity of the dielectric substrate is 2.5. All materials are assumed to be lossless.

AEC/AMC ground plane characterization using MoM

Consider the periodic structure shown in Figure 3.1 with periodicity of $d_x = 12$ mm, strip width of $l_x = 7.86$ mm and dielectric slab thickness of $t = 1.6$ mm. The reflection coefficient phases versus frequency are shown for various incident angles and both TE^z and TM^z in Figures 3.15 and 3.16, for the x-polarized and y-polarized electric field components of the incident field, respectively. One should note that, at $\phi = 0°$, TE^z and TM^z are equivalent to TE^y and TM^y, respectively.

As can be seen, at 9.5 GHz, this artificial ground plane acts as an AMC (reflection phase close to zero at normal incidence) for the incident wave the with x-polarized electric field component, while acts an AEC (reflection phase close to 180° at normal incidence) for the incident wave with y-polarized electric field component.

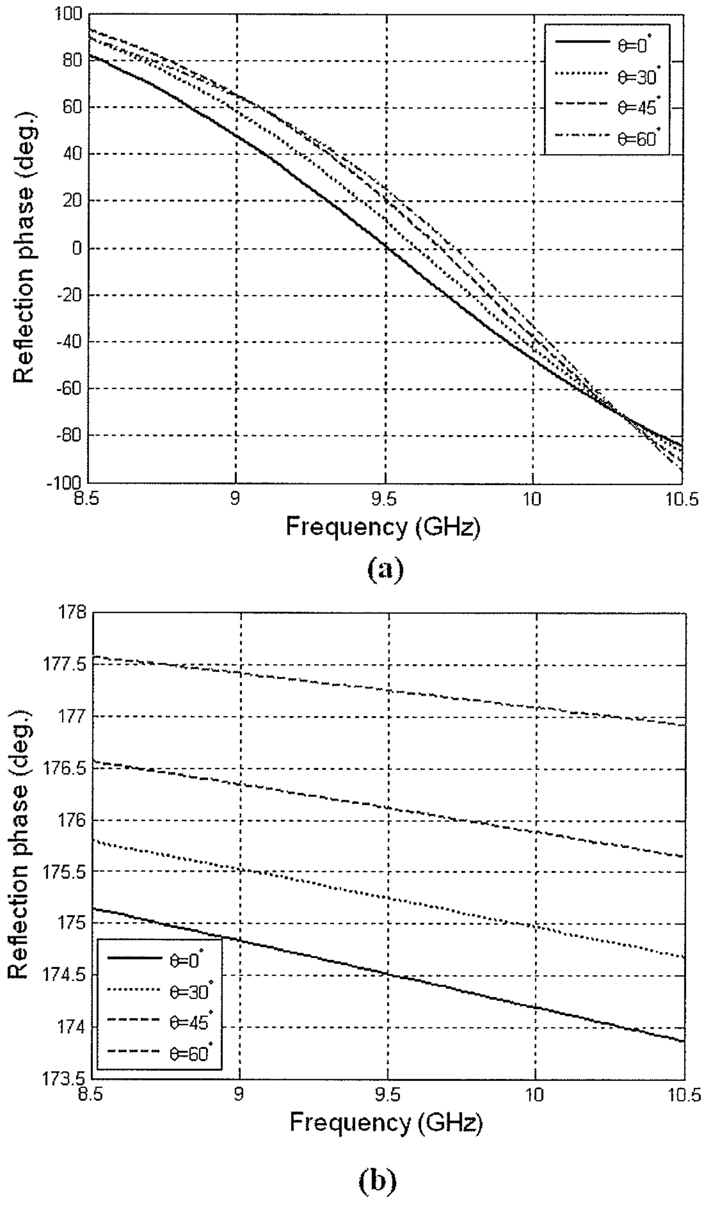

Figure 3.14: Reflection phases at various incident angles, using entire domain modal expansion with $N = M = 20$.(a) TE^y and (b) TM^y polarization. The structure is shown in Figure 3.1 with periodicity of $d_x = 12$ mm, strip width of $l_x = 7.86$ mm and dielectric slab thickness of $t = 1.6$ mm.

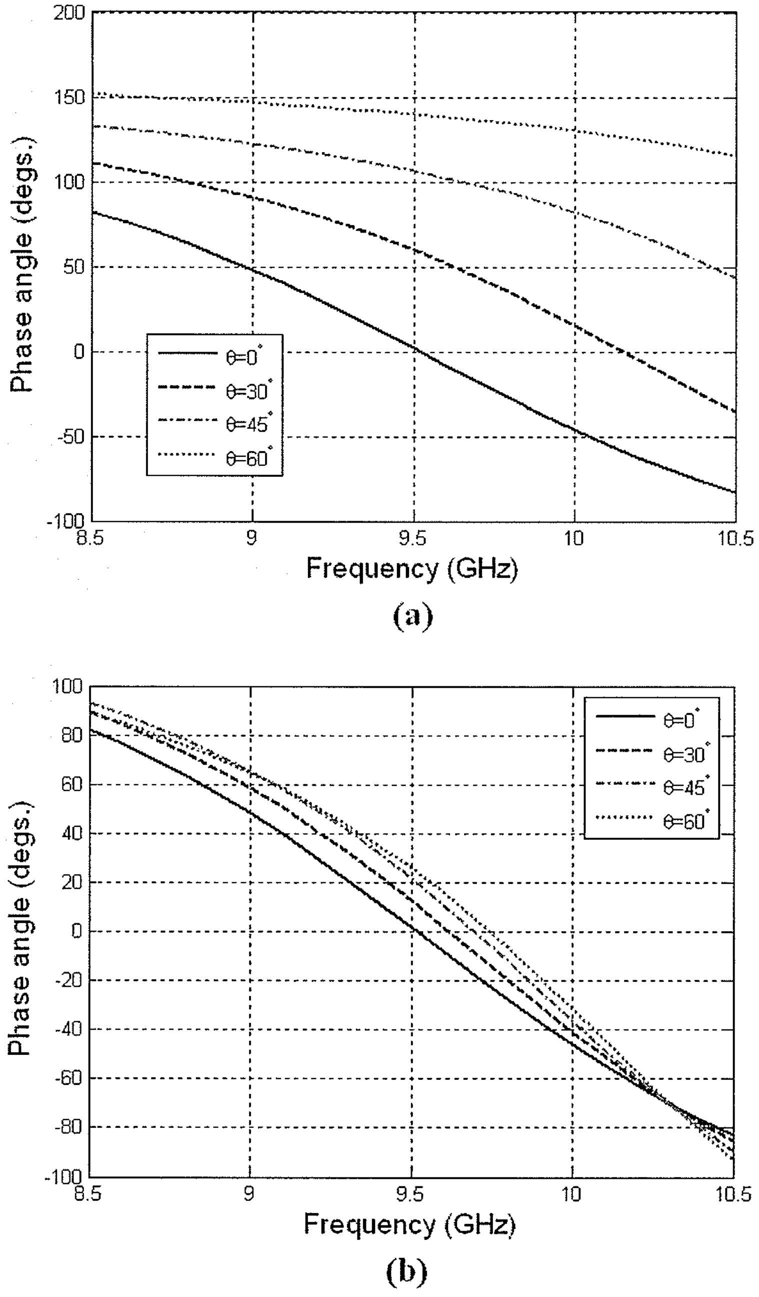

Figure 3.15: Reflection phases of the conducting periodic strip on grounded dielectric slab versus frequency for various incident angles. The electric field of the incident wave is x-directed.(a) TE^z at $\phi = 90°$ and (b) TM^z at $\phi = 0°$. The structure is shown in Figure 3.1 with periodicity of $d_x = 12$ mm, strip width of $l_x = 7.86$ mm and dielectric slab thickness of $t = 1.6$ mm.

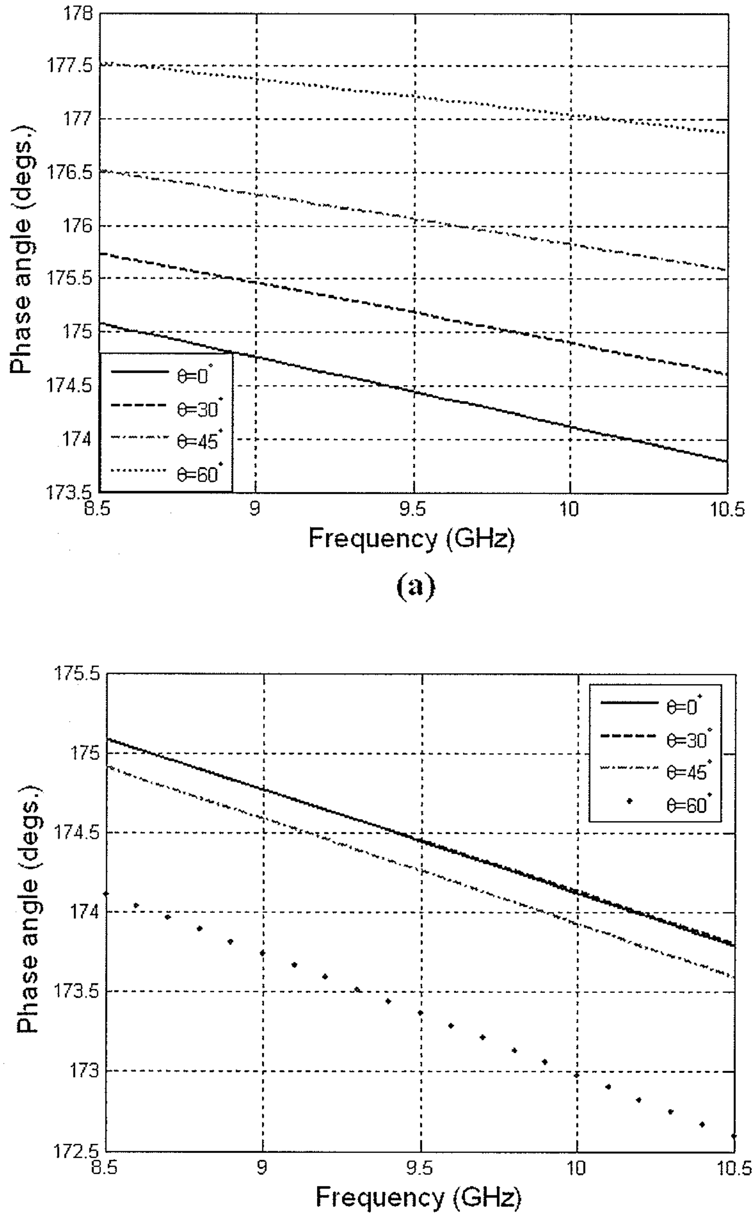

(a)

(b)

Figure 3.16: Reflection phases of the conducting periodic strip on grounded dielectric slab versus frequency for various incident angles. The electric field of the incident wave is y-directed.(a) TE^z at $\phi = 0°$ and (b) TM^z at $\phi = 90°$. The structure is shown in Figure 3.1 with periodicity of $d_x = 12$ mm, strip width of $l_x = 7.86$ mm and dielectric slab thickness of $t = 1.6$ mm.

3.6 Conclusions

In this chapter, the scattering analysis of the infinitely-long periodic conducting strips on the grounded dielectric slab was studied. This periodic structure is the most well-known canonical periodic structure that is not rotationally symmetric around the 90° rotation. This is in contrast to the periodic structures introduced in the previous chapter. If the x and the y axis were switched, the unit cells introduced in the previous chapter would not change. In other words, the electromagnetic properties of these structures are independent on the applied electric field being in x- or y-directions. For normal incidence, either the applied field is x-directed or y-directed, the surfaces worked as an AMC. However, for the infinitely-long periodic conducting strips on the grounded dielectric slab this is different even for the normal incidence. It was shown that the strip-type artificial surface introduced in this chapter, acts as either AMC or AEC when the electric field is perpendicular or parallel to the strips, respectively.

Two methods were implemented based on the plane wave modal expansions. In the second method which was based on entire-domain basis function modal expansion, the electric surface currents was used to analyze the E-polarized case. This requires having a new set of boundary conditions to be satisfied. Therefore, a new formulation, compared to the one introduced in [38] for E-polarized scattering problem was established and solved. In [38], the expansion was instead performed based on the auxiliary magnetic surface currents across the slots between the conducting strips. As well, a computer code based on the method of moment was developed. The results were consistent and in good agreement with the TLM-CAD (Microstripes) and FEM-CAD (Ansoft HFSS) commercial software packages. These two commercial software packages are inefficient in extraction of the scattering properties of the grating periodic structures at oblique incidence. One should note that the available MoM-CAD software package (Ansoft Designer) was incapable of solving this problem.

The obtained results of the in-house developed MoM code will be later used in this work to design novel dual-mode AMC/AEC ground planes. These ground planes will find applications in dual-band dual orthogonally-polarized high gain antenna designs. One should note that the artificial ground planes addressed in the literature such as patches, etc., can only act in a single AMC mode.

Chapter 4

High-gain Planar Antennas with High-permittivity Dielectric Superstrate and Artificial Ground Planes

One of the antenna gain enhancement methods is to place a high permittivity dielectric above a planar antenna as the superstrate [11, 12]. A simple configuration of such an antenna is depicted in 4.1. The resonance concept is illustrated by a simple transmission line analogy in Figure 4.2. In this illustration, the transmission line is terminated by short circuits (PEC). The resonance behavior is illustrated in Figure 4.3, when the substrate is terminated by an open circuit (PMC). As can be seen in Figure 4.3, the substrate thickness is halved. This insight helps an antenna designer to reduce the height of this class of antennas.

In this chapter, the transverse equivalent network (TEN) method is introduced, first. Far-field radiation properties of cavity resonance antenna with

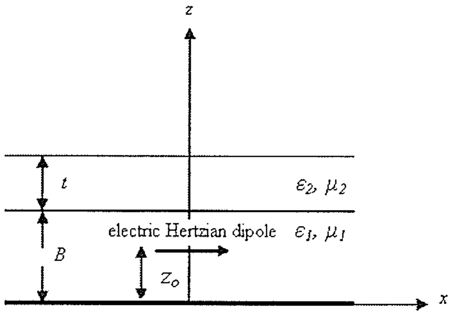
z
t
ε_2, μ_2
B
electric Hertzian dipole ε_1, μ_1
z_o
x

Figure 4.1: An electric Hertzian dipole embedded in a substrate and covered by a superstrate layer. z_0 is the position of the horizontal electric Hertzian dipole. B and t are the thicknesses of the substrate and superstrate, respectively.

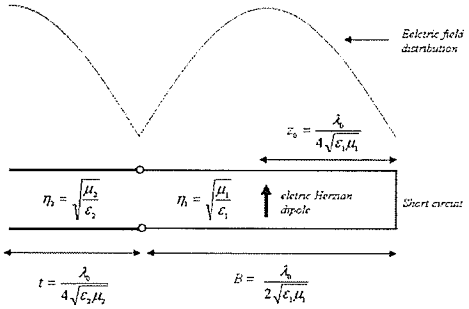
Eelctric field distribution
$z_0 = \frac{\lambda_0}{4\sqrt{\varepsilon_1\mu_1}}$
$\eta_2 = \sqrt{\frac{\mu_2}{\varepsilon_2}}$
$\eta_1 = \sqrt{\frac{\mu_1}{\varepsilon_1}}$
elctric Herzian dipole
Short circuit
$t = \frac{\lambda_0}{4\sqrt{\varepsilon_2\mu_2}}$
$B = \frac{\lambda_0}{2\sqrt{\varepsilon_1\mu_1}}$

Figure 4.2: Resonance behavior of the transmission line model of the antenna structure using superstrate dielectric with high permittivity shown in Figure 4.1.

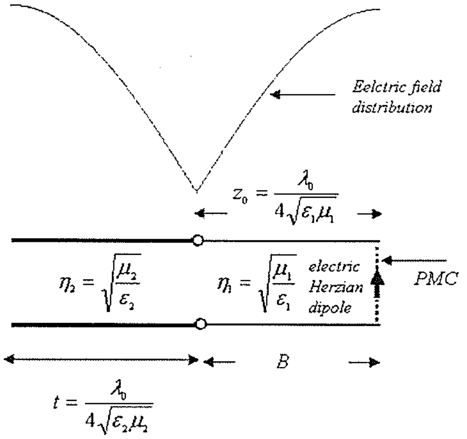
Eelctric field distribution
$z_0 = \frac{\lambda_0}{4\sqrt{\varepsilon_1\mu_1}}$
$\eta_2 = \sqrt{\frac{\mu_2}{\varepsilon_2}}$
$\eta_1 = \sqrt{\frac{\mu_1}{\varepsilon_1}}$
electric Herzian dipole
PMC
B
$t = \frac{\lambda_0}{4\sqrt{\varepsilon_2\mu_2}}$

Figure 4.3: Resonance behavior of the transmission line model of the antenna structure using superstrate dielectric with high permittivity and terminated by an open circuit (PMC).

multilayer dielectric superstrate can be investigated using the TEN method. A Hertzian dipole is used as the excitation/receiving probe. This method has been successfully used to extract the far-field radiation patterns as well as directivity of the Hertzian dipole antenna embedded in multilayer dielectrics [12, 45, 46]. The results are in good agreement with full-wave analysis such as MoM [46], or other complicated mathematical methods based on Green's function calculations [11, 12] or leaky-wave analysis [47]. Moreover, full-wave analysis methods such as FDTD, FEM or MoM are time-consuming and need large amount of computer memory to analyze an antenna from this class.

Next, the Hertzian dipole antenna with various dielectric superstrate with different permittivity are studied when the ground plane is either PEC or PMC. Finally, different AMC surfaces are alternatively employed as the antenna ground plane and their effects on antenna far-field radiation properties are studied.

4.1 Formulation of the problem using TEN method

The geometry of the problem is shown in Figure 4.4(a). When a Hertzian dipole is embedded in the multilayer dielectric structure and subjected to the plane wave incidence, TEN model can be used to extract the far-field radiation pattern of the antenna. The physical description has been studied in detail in [12, 46], and for brevity are not repeated here. One should notice that E_θ is evaluated due to the incident plane wave having TM_z polarization whereas E_ϕ is evaluated due to the incident plane wave having TE_z polarization. The geometry of the problem can thus be simplified to the transmission line (TL) model shown in Figure 4.4(b). This model is now appropriate to be analyzed by TEN method.

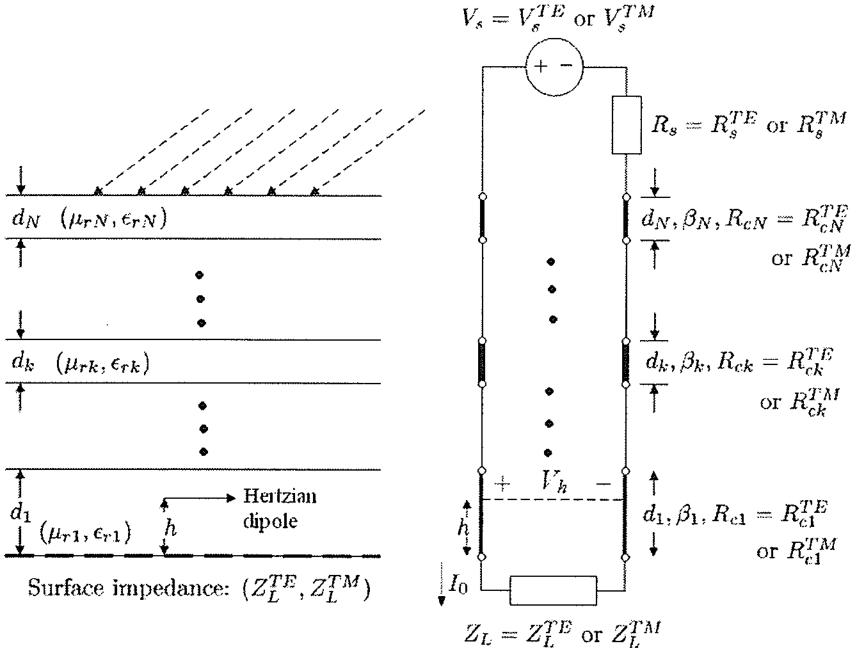
d_N $(\mu_{rN}, \epsilon_{rN})$
d_k $(\mu_{rk}, \epsilon_{rk})$
d_1 $(\mu_{r1}, \epsilon_{r1})$
h
Hertzian dipole
Surface impedance: (Z_L^{TE}, Z_L^{TM})
$V_s = V_s^{TE}$ or V_s^{TM}
+ -
$R_s = R_s^{TE}$ or R_s^{TM}
$d_N, \beta_N, R_{cN} = R_{cN}^{TE}$ or R_{cN}^{TM}
$d_k, \beta_k, R_{ck} = R_{ck}^{TE}$ or R_{ck}^{TM}
+ V_h -
h
$d_1, \beta_1, R_{c1} = R_{c1}^{TE}$ or R_{c1}^{TM}
I_0
$Z_L = Z_L^{TE}$ or Z_L^{TM}

Figure 4.4: (a) An electric Hertzian dipole embedded between multilayer dielectric structure and above an impedance surface acting as a ground plane. (b) Transmission line circuit representing transverse equivalent network to calculate the horizontal electric field induced on the electric Hertzian dipole due to the plane wave incidence in the far-field region.

All quantities V_s, R_s, R_{ck} and Z_L, shown in Figure 4.4(b), are polarization (TM or TE) and angular dependent, in general. Their corresponding relations to the plane wave incident angles, and constitutive parameters of the dielectric layers for different TE and TM mode are as follows

$$V_s^{TE} = 1 \qquad V_s^{TM} = V_s^{TE}\cos(\theta_i) \tag{4.1}$$

$$R_s^{TE} = \eta_0/\cos(\theta_i) \qquad R_s^{TM} = \eta_0\cos(\theta_i) \tag{4.2}$$

$$R_{ck}^{TE} = \eta_0\frac{\mu_{rn}}{\sqrt{\mu_{rn}\epsilon_{rn} - \sin^2(\theta_i)}} \qquad R_{ck}^{TM} = \eta_0\frac{\sqrt{\mu_{rn}\epsilon_{rn} - \sin^2(\theta_i)}}{\epsilon_{rn}} \tag{4.3}$$

$$\beta_n = k_0\sqrt{\mu_{rn}\epsilon_{rn} - \sin^2(\theta_i)} \qquad \eta_0 = \sqrt{\mu_0/\epsilon_0}. \tag{4.4}$$

As illustrated in Figure 4.4, the multilayer dielectric structure is considered as the cascaded transmission line segments terminated by the impedance surface of the ground plane.

Given A_k, B_k, C_k and D_k as the $ABCD$ matrix elements of the kth TL segment, the $ABCD$ matrix of the entire multilayer dielectric structure is

$$\begin{bmatrix} A & B \\ C & D \end{bmatrix} = \prod_{k=1}^{N} \begin{bmatrix} A_k & B_k \\ C_k & D_k \end{bmatrix} \tag{4.5}$$

where A, B, C and D are the elements of the $ABCD$ matrix of the entire cascaded multilayer dielectric structure. The $ABCD$ matrix of the kth TL segment is obtained as below

$$\begin{bmatrix} A_k & B_k \\ C_k & D_k \end{bmatrix} = \begin{bmatrix} \cos(\beta_k d_k) & jR_{ck}\sin(\beta_k d_k) \\ j\sin(\beta_k d_k)/R_{ck} & \cos(\beta_k d_k) \end{bmatrix} \tag{4.6}$$

Assuming A', B', C' and D' as the elements of the transmission line portion below the dashed line, voltage V_h and I_h can be obtained using two sets of linear equations, expressed as

$$\begin{bmatrix} V_s - I_N R_s \\ I_N \end{bmatrix} = \begin{bmatrix} A & B \\ C & D \end{bmatrix} \begin{bmatrix} I_0 Z_L \\ I_0 \end{bmatrix} \tag{4.7}$$

$$\begin{bmatrix} V_h \\ I_h \end{bmatrix} = \begin{bmatrix} A' & B' \\ C' & D' \end{bmatrix} \begin{bmatrix} I_0 Z_L \\ I_0 \end{bmatrix}, \tag{4.8}$$

By solving for I_0 in (4.7), and substituting it into (4.8), V_h and I_h can be found as

$$V_h = V_s \frac{A'Z_L + B'}{CZ_LR_s + DR_s + AZ_L + B} \tag{4.9}$$

$$I_h = V_s \frac{C'Z_L + D'}{CZ_LR_s + DR_s + AZ_L + B}. \tag{4.10}$$

4.2 Calculation of the far-field properties

The induced horizontal electric field on the electric Hertzian dipole shown in Figure 4.4(a) is proportional to V_h [46]. The actual induced field value is different from V_h. However, for simplicity of the calculations the maximum induced electric field is equated to V_h, and is calculated as follows

$$E_h = V_h e^{jk_0 \sin\theta_i (x_J \cos\phi_i + y_J \sin\phi_i)}, \qquad (4.11)$$

where (x_J,y_J) is the coordinate where the electric Hertzian dipole is located and (θ_i, ϕ_i) specifies the incident angle. The direction of the electric Hertzian dipole is defined as follows:

$$\hat{\rho_J} = \hat{x} cos(\phi_J) + \hat{y} sin(\phi_J), \qquad (4.12)$$

Since the far-field radiation patterns and directivity of the antenna is independent of the magnitude of the electric field induced on the Hertzian dipole, (4.11) is valid for calculation of the aforementioned antenna parameters. It is evident that if the Hertzian dipole is located at the origin, $E_h = V_h$ will hold.

As mentioned before, in order to obtain E_ϕ and E_θ, they should be equated to E^{TE} and E^{TM}, respectively. The following equations relates E_ϕ and E_θ

$$\begin{aligned} E^{TE} = E_\phi = E_h \hat{a_{\phi_i}}.(\hat{a_x} \cos(\phi_J) + \hat{a_y} \sin(\phi_J)) \sin(\theta_i) \\ = E_h sin(\phi_J - \phi_i), \end{aligned} \qquad (4.13)$$

$$\begin{aligned} E^{TM} = E_\theta = (E_h \hat{a_{\phi_i}} \times \hat{a_z}).(\hat{a_x} \sin(\theta_J) \cos(\phi_J) + \hat{a_y} \sin(\theta_J) \sin(\phi_J)) \\ = E_h \cos(\phi_J - \phi_i), \end{aligned} \quad (4.14)$$

where $\hat{a_{\phi_i}} = -\hat{a_x}\sin\phi_i + \hat{a_y}\cos\phi_i$, and (ϕ_J, θ_J) shows the direction of the Hertzian dipole.

Throughout this study, antenna directivity is calculated using the following formula [12]

$$D(\theta,\phi) = \frac{4(\sin^2(\phi)|V_h^{TE}(\theta)|^2 + \cos^2(\phi)|V_h^{TM}(\theta)|^2)}{\int_0^{\pi/2}\sin(\theta)\left[|V_h^{TE}(\theta)|^2 + |V_h^{TM}(\theta)|^2\right]d\theta}. \tag{4.15}$$

Note that the factor $exp(-jkR)/4\pi R$ is suppressed in all far-field equations above. As can be seen, in equation (4.15), the directivity and far-field radiation pattern are related to the absolute value of the field (voltages). Also, integration in the denominator is performed only on angles. Therefore, the suppression of the factor $exp(-jkR)/4\pi R$ does not affect these two quantities which are studied in this work.

4.3 Radiation properties study through some examples

According to equations 4.13 and 4.14, far-field radiation patterns corresponding to the x-directed Hertzian dipole placed at the origin and used as the receiving probe are calculated as below

$$E^{TE} = E_\phi = -V_h^{TE}\sin(\phi) \tag{4.16}$$

$$E^{TM} = E_\theta = V_h^{TM}\cos(\phi) \tag{4.17}$$

which is consistent with the results obtained in [46]. Note that V_h has been replaced by V_x, here.

In this section, aforementioned Hertzian dipole antenna, shown in Figure

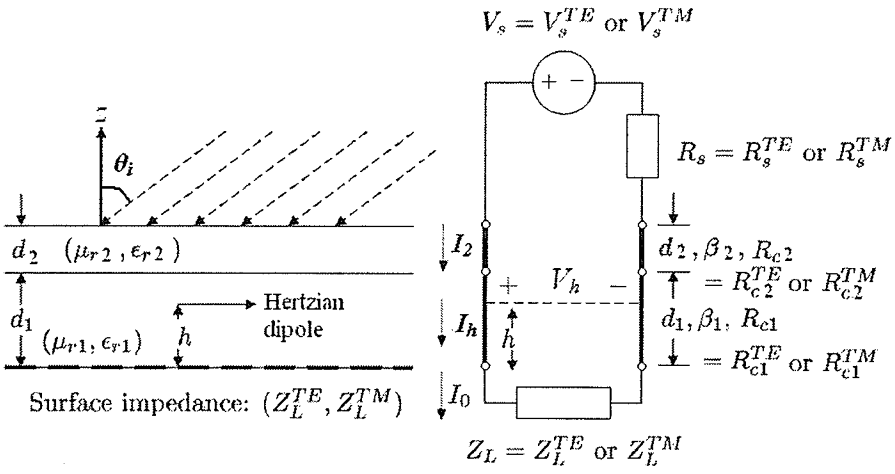
z
θ_i
d_2 $(\mu_{r2}, \epsilon_{r2})$
d_1 $(\mu_{r1}, \epsilon_{r1})$
h
Hertzian dipole
Surface impedance: (Z_L^{TE}, Z_L^{TM})
$V_s = V_s^{TE}$ or V_s^{TM}
+ −
$R_s = R_s^{TE}$ or R_s^{TM}
I_2
I_h
I_0
+ V_h −
h
d_2, β_2, R_{c2}
$= R_{c2}^{TE}$ or R_{c2}^{TM}
d_1, β_1, R_{c1}
$= R_{c1}^{TE}$ or R_{c1}^{TM}
$Z_L = Z_L^{TE}$ or Z_L^{TM}

(a) (b)

Figure 4.5: (a) A Hertzian dipole above surface impedance ground plane and beneath a dielectric superstrate layer. (b) TEN model to calculate the horizontal electric field induced on the electric Hertzian dipole due to the plane wave incidence in the far-field region.

4.4(a), is considered with PEC, PMC or AMC ground planes. Far-field radiation patterns and directivity of these different antenna configurations are studied using the TEN formulations described above.

4.3.1 Antenna with 1-layer superstrate and PEC ground plane

A two layer dielectric structure consisting of an air-gap layer (substrate with $\epsilon_{r1} = 1$ according to [12]) and a dielectric superstrate cover is shown in Figure 4.5. The ground plane is assumed to be PEC, implying that the load impedance in the transmission line model is zero ($Z_L = 0$). The Hertzian dipole is embedded in the middle of the air-gap ($h = d_1/2$).

The antenna directivity versus air-gap height and superstrate thickness is shown in Figure 4.6, when the relative permittivity of the superstrate is 9.8 ($\epsilon_{r2} = 9.8$). It is observed that the maximum directivity, corresponding to the first resonance, occurs when the air-gap height and dielectric superstrate thickness are around half wavelength and quarter wavelength, respectively. This is consistent with the resonance conditions obtained in the previous chapter as well as the ones presented in [12]. The maximum directivities of this antenna configuration for various superstrate layers with different dielectric permittivity, are listed in Table 4.1. However, for the sake of brevity, the antenna directivity versus air-gap height and superstrate are not plotted for all cases othar than $\epsilon_{r2} = 9.8$ (Figure 4.6).

One should note that $\lambda_e = \lambda_0/\sqrt{\epsilon_{r2}}$, where λ_0 is free space wavelength at the operating frequency and ϵ_{r2} is dielectric relative permittivity of the superstrate, respectively.

As listed in Table 4.1, the maximum directivity is obtained for the superstrate dielectric thickness of about quarter-wavelength ($\sim \lambda_e/4$) and air-gap height of about half-wavelength ($\sim \lambda_0/2$). Corresponding radiation patterns of the above-mentioned antenna configurations are shown in Figure 4.7.

4.3.2 Antenna with 1-layer superstrate and PMC ground plane

When the ground plane is PMC in Figure 4.5(a), the load impedance in the transmission line model is imaginary infinity ($Z_L = j\infty$). Hertzian probe is placed on the PMC ground plane ($h = 0$), as the maximum voltage V_x occurs at this height when the load is an open circuit (Figure 4.3).

Table 4.1: Antenna directivities for PEC ground plane and different dielectric superstrate permittivities. Antennas configuration is shown in Figure 4.5.

ϵ_r	Directivity at first resonance	d_1/λ (dBi)	d_2/λ_e
9.8	16.88	0.49	0.26
8.8	16.45	0.49	0.26
6.8	15.46	0.49	0.25
5.5	14.62	0.49	0.24

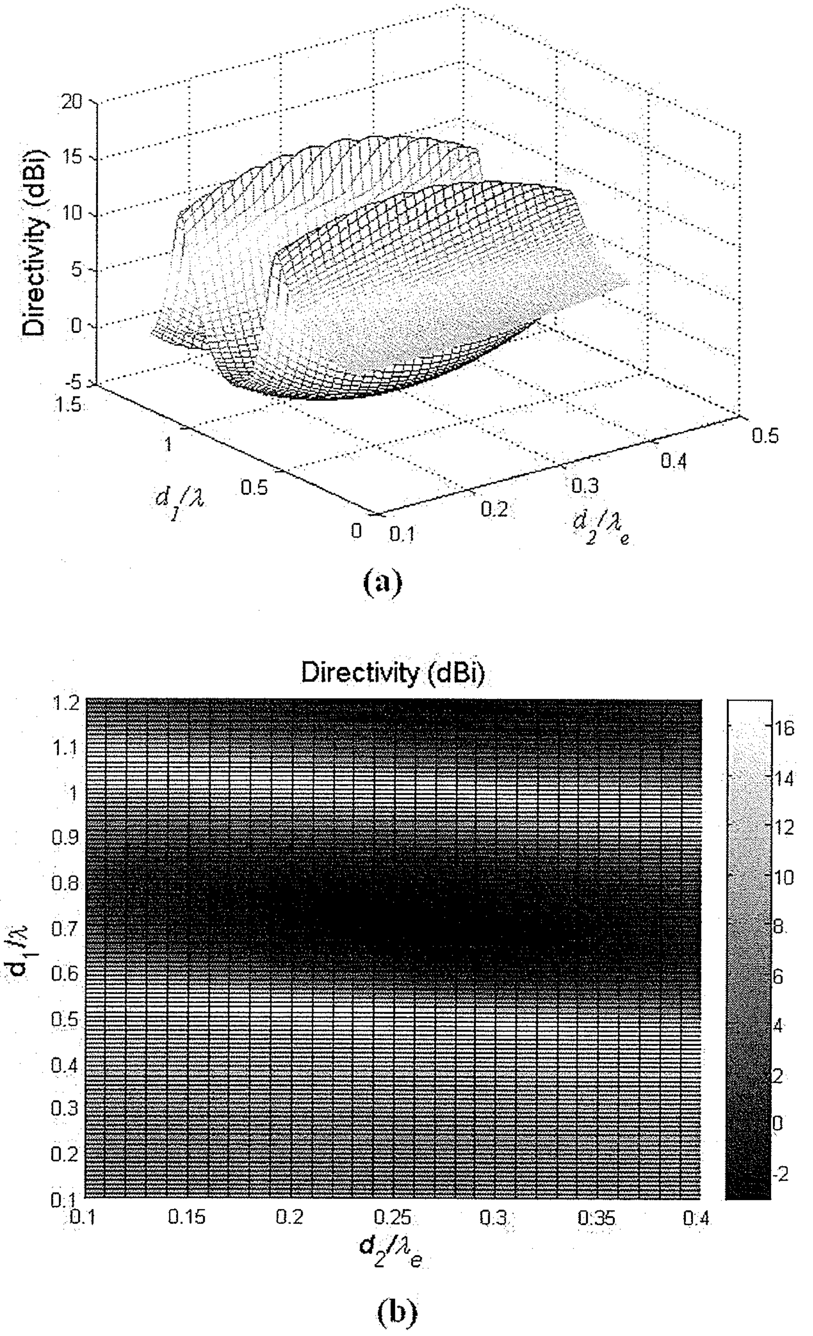

(a)

(b)

Figure 4.6: Directivity versus air-gap height (d_1/λ_0) and dielectric superstrate thickness (d_2/λ_e) for the cavity resonance antenna shown in Fig. 4.5 with PEC ground plane. Superstrate relative permittivity is $\epsilon_2 = 9.8$.

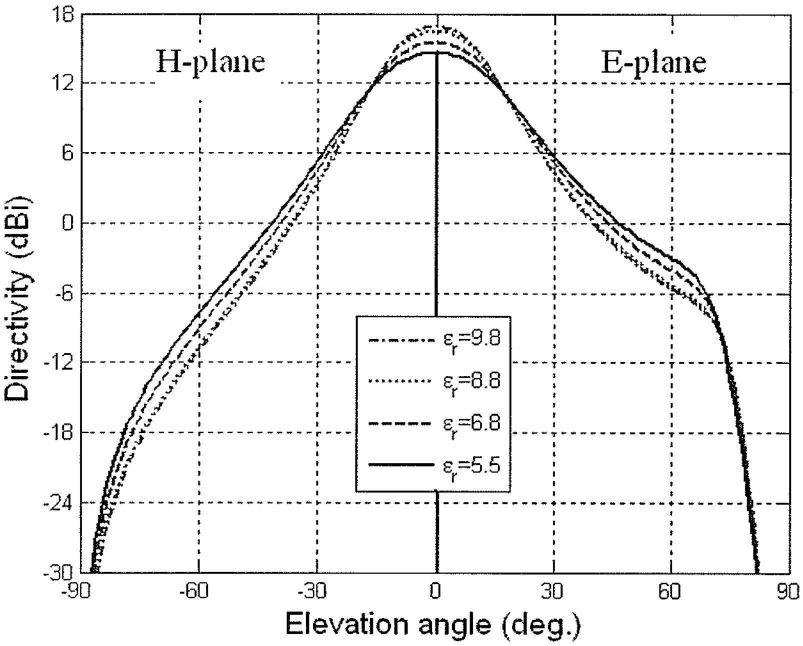

Figure 4.7: Radiation patterns of the antenna shown in Fig. 4.5 with PEC ground plane for different superstrate relative permittivities and thicknesses listed in Table 4.1

The antenna directivity versus air-gap height and superstrate thickness is shown in Figure 4.8, when the relative permittivity of the superstrate is 9.8 ($\epsilon_{r2} = 9.8$). It is observed that the maximum directivity, corresponding to the first resonance, occurs when the air-gap height and dielectric superstrate thickness are both around corresponding quarter wavelength. The maximum directivities of this antenna configuration for various superstrate layers with different dielectric permittivity, are listed in Table 4.2. However, for the sake of brevity, the antenna directivity versus air-gap height and superstrate are not plotted for all other cases except for the case with $\epsilon_{r2} = 9.8$ (Figure 4.8).

As listed in Table 4.2, the maximum directivity is obtained for the dielectric thickness and air-gap height of about quarter wavelength of their pertaining medium, namely, ($\sim \lambda_c/4$) and ($\sim \lambda_0/4$), respectively. Corresponding radiation patterns of the above-mentioned antenna configurations are shown in Figure 4.9.

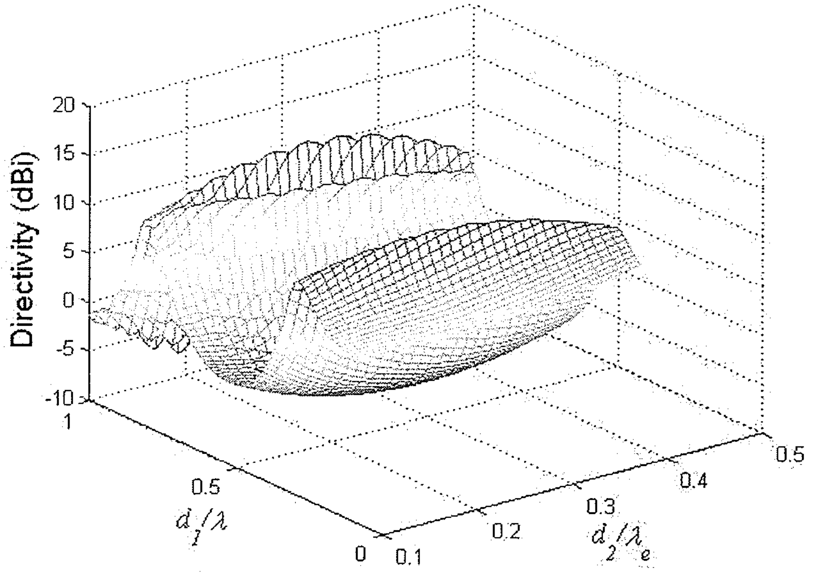

(a)

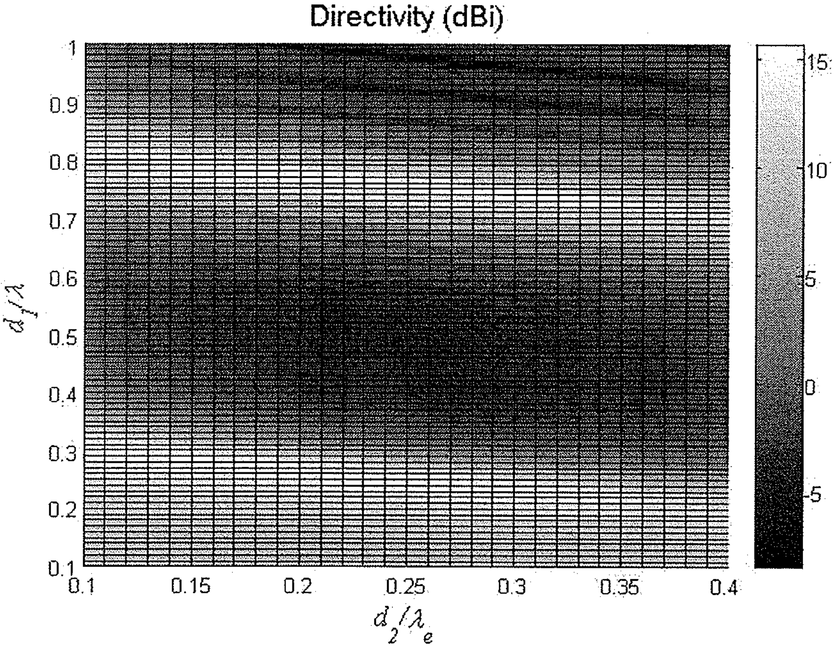

(b)

Figure 4.8: Directivity versus air-gap height (d_1/λ_0) and dielectric superstrate thickness (d_2/λ_e) for the cavity resonance antenna shown in Fig. 4.5 with PMC ground plane. Superstrate relative permittivity is $\epsilon_2 = 9.8$.

Therefore, using a PMC surface as the ground plane, the air-gap height can be reduced by half. This size reduction (low profile design) is at the expense of about 3 dB gain loss. These results are consistent with those presented in [13], although finite dielectric superstrate has been used in [13].

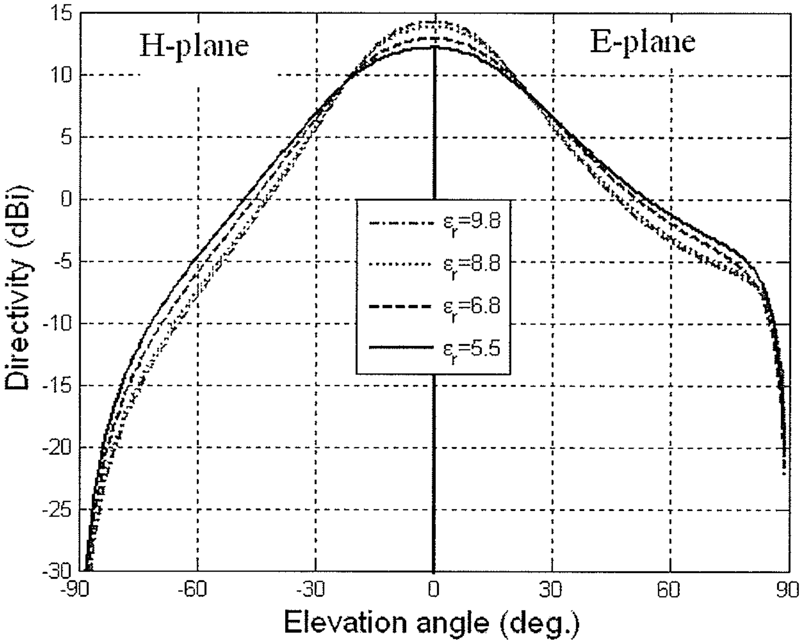

Figure 4.9: Radiation patterns of the antenna shown in Fig. 4.5 with PMC ground plane for different superstrate relative permittivities and thicknesses listed in Table 4.2.

Table 4.2: Antenna directivities for PMC ground plane and different dielectric superstrate permittivities. Antennas configuration is shown in Figure 4.5.

ϵ_r	Directivity at first resonance	d_1/λ (dBi)	d_2/λ_e
9.8	14.18	0.25	0.23
8.8	13.77	0.25	0.23
6.8	12.85	0.24	0.25
5.5	12.11	0.24	0.24

4.3.3 Antenna with 1-layer superstrate and AMC ground plane

As mentioned before, PMC does not exist in nature. Therefore, in practical applications AMC is used. In the following part, the antenna configuration shown in Figure 4.5(a) with AMC ground plane is considered. First, a few AMC structure is designed for the desired frequency. Then, the radiation patterns of the antenna shown in Figure 4.5(a) are studied, when these AMCs are individually employed as the antenna ground plane.

AMC design

Three different AMCs are designed at the proper frequency and later will be used individually as the antenna ground plane. Corresponding unit cells of these AMCs are depicted in Figure 4.10. These unit cells consist of well-known frequency selective surface shapes, such as metallic square patch (Figure 4.10(a)), metallic square patch (Figure 4.10(b)) and Jerusalem cross (Figure 4.10(c)), backed by a grounded dielectric slab. They are all designed to demonstrate reflection coefficient phase of zero at normal incident angle at the operating frequency (9.5 GHz in this study). All corresponding dimensions are presented in Figure 4.10. Relative permittivity of the substrate dielectric is 2.5. The conductor and dielectric slab are assumed to be lossless. Thus, reflection coefficient magnitude is assumed to be unity for all the above cases. Corresponding reflection coefficient phases to these AMCs are shown in Figure 4.11 versus incident angle, for both TE and TM polarization. Both TE and TM polarizations are respect to the normal to the surface. These graphs plotted in Figure 4.11 were obtained using Ansoft Designer software package (MoM-CAD).

Some interesting points are observed from the reflection phases shown in

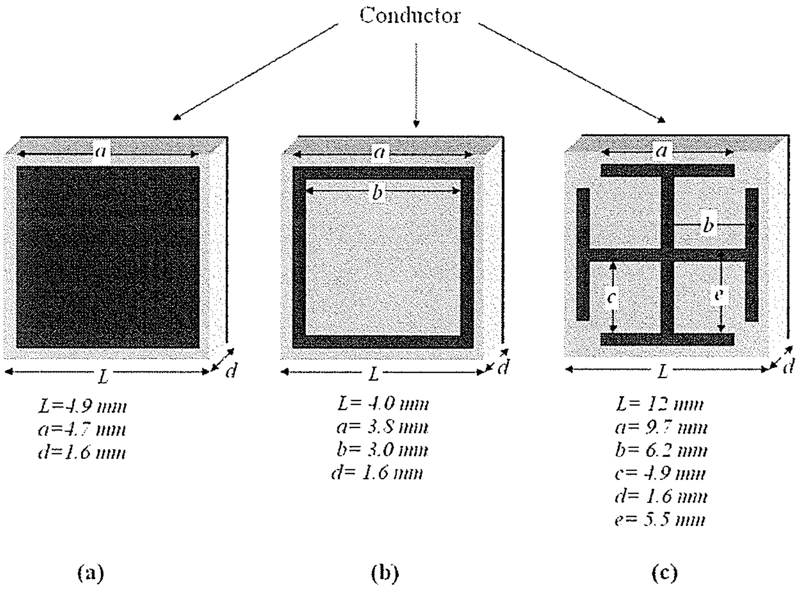
Conductor
a
L
d
L=4.9 mm
a=4.7 mm
d=1.6 mm
a
b
L
d
L= 4.0 mm
a= 3.8 mm
b= 3.0 mm
d= 1.6 mm
a
b
c
e
L
d
L= 12 mm
a= 9.7 mm
b= 6.2 mm
c= 4.9 mm
d= 1.6 mm
e= 5.5 mm
(a)
(b)
(c)

Figure 4.10: Three different unit cells as AMC building blocks. (a) AMC1, (b) AMC2 and (c) AMC3 unit cells.

Figure 4.11, as follows:

- Reflection phases are both polarization and angular dependent for these synthesized AMCs whereas uniform over all incident angles and polarizations for the PMC surface.
- Reflection phase variation versus incident angles are different for different unit cell metallizations. However, they are quite similar in some cases, such as AMC1 and AMC2.

In order for the above-mentioned AMCs to be used in TEN antenna model, corresponding Z_L is to be calculated. Having reflection coefficient phase, the surface impedance of the load for the TM polarization is [48, 34]

$$Z_L^{\mathrm{TM}} = Z_0^{\mathrm{TM}} \frac{1+\Gamma_{\mathrm{TM}}}{1-\Gamma_{\mathrm{TM}}} \tag{4.18}$$

where Z_0^{TM} is the characteristic impedance of the free space. The same for-

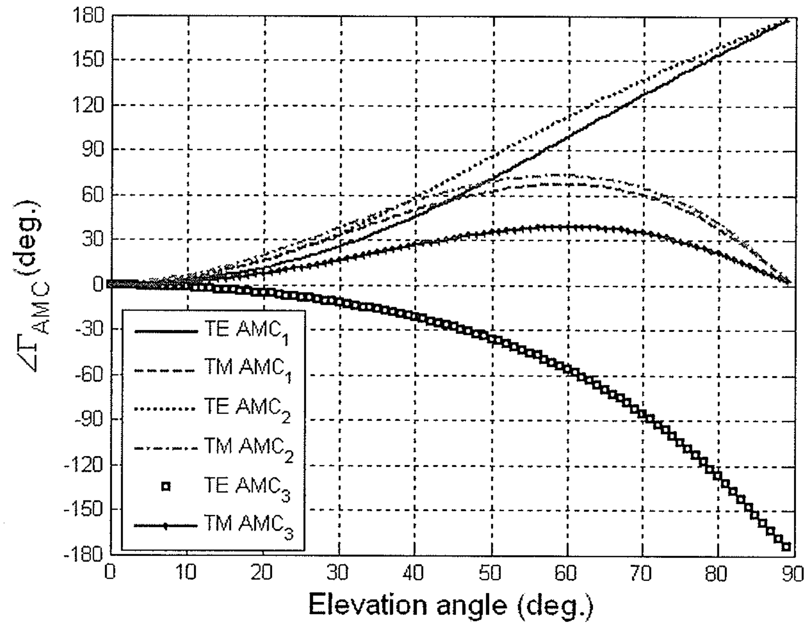

Figure 4.11: Reflection coefficient phases corresponding to the AMCs with unit cells shown in Figure 4.10.

mula applies for the TE polarization. One should note the reflection magnitude coefficients are unity for all cases and are not reported here for the sake of brevity. As can be seen the load impedance is both polarization and angular dependent when the AMC ground plane is modeled in TEN method. Load impedances, corresponding to aforementioned synthesized AMCs (Figure 4.10), are shown in Figure 4.12.

The following observation are made according to the Figure 4.12:

- $|Z_L|$ is high close to normal incidence angles (high impedance surface). In general, when the reflection phase is close to zero the surface impedances are high. When the reflection phase is close to ±180° the surface impedance is low. These are consistent with the concept of high and low impedance surfaces.

- In the case of AMC3, and for TM-polarized incidence, surface impedance phase is −90° for the normal incident angle and first few angles close normal. Also, for the first few angles from normal, the surface impedance magnitude increases. This is due to the fact that the reflection phase of AMC3 shown in Figure 4.11, are very close to zero but negative for these incident angles. These values are listed in Table 4.3, for the very

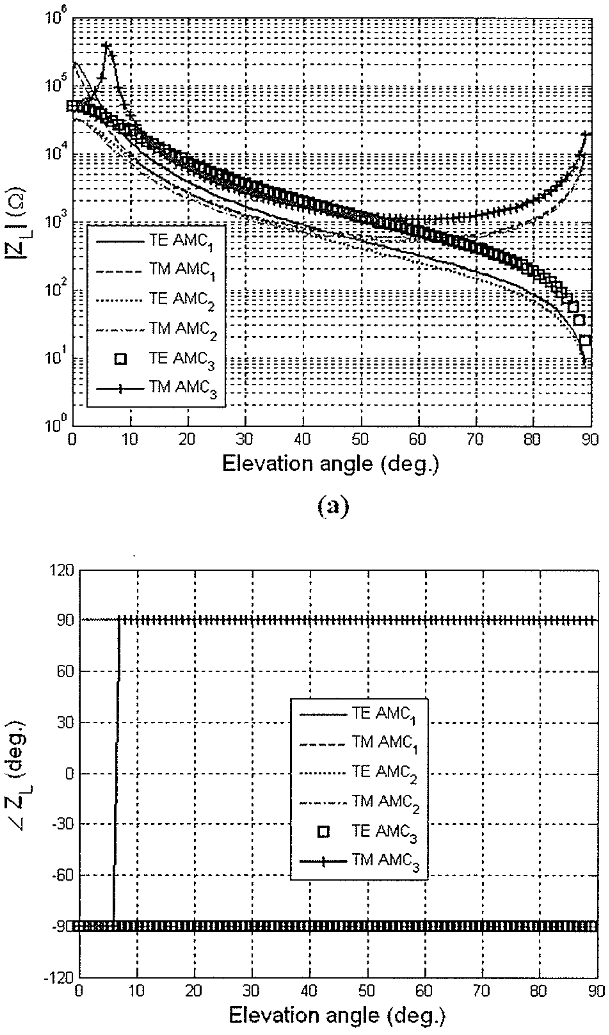

(a)

(b)

Figure 4.12: Surface impedances corresponding to the AMC unit cells shown in Figure 4.10 having reflection coefficient phase shown in Figure 4.11. (a) Surface impedance magnitude (b) surface impedance phase.

Table 4.3: Corresponding reflection phase of the AMC3 unit cell, for the very close-to-normal incident angles. Both TE and TM polarizations (with respect to z) are considered. The corresponding reflection coefficient phase is shown in Figure 4.11. The corresponding surface impedances are shown in Figure 4.12.

incident angle	$\angle\Gamma_{TE}$ (degs.)	$\angle\Gamma_{TM}$ (degs.)
0.0	-0.88	-0.88
1.0	-0.89	-0.86
2.0	-0.93	-0.80
3.0	-0.99	-0.69
4.0	-1.07	-0.54
5.0	-1.18	-0.35
6.0	-1.31	-0.12
7.0	-1.47	0.19
8.0	-1.65	0.47
9.0	-1.85	0.83
10.0	-2.08	1.23

close-to-normal incident angles.

Far-field radiation patterns

Each of the aforementioned AMCs, is separately used as the ground plane of the antenna shown in Figure 4.5(a). Then, their radiation properties are investigated using TEN method. For all cases the Hertzian dipole is placed on the AMC surface ($h = 0$).

1) Antenna configuration with AMC1 as the ground plane: Antenna1

Directivity versus air-gap height and dielectric superstrate thickness of the antenna shown in Figure 4.5(a) are plotted in Figure 4.13 when the ground plane is made of AMC1 surface. The relative permittivity of the dielectric superstrate is assumed to be 9.8 ($\epsilon_{r2} = 9.8$). It is observed that the maximum directivity, corresponding to the first resonance, occurs when the air-gap height and dielectric superstrate thickness are both around corresponding quarter wavelength. The maximum directivities of this antenna configuration for various superstrate layers with different dielectric permittivity, are listed

Table 4.4: Antenna directivities for AMC1 ground plane and different dielectric superstrate permittivities. Antennas configuration is shown in Figure 4.5.

ϵ_r	Directivity at first resonance (dBi)	d_1/λ	d_2/λ_e
9.8	17.00	0.24	0.26
8.8	16.55	0.26	0.24
6.8	15.48	0.24	0.25
5.5	14.60	0.24	0.25

Table 4.5: Antenna directivities for AMC2 ground plane and different dielectric superstrate permittivities. Antennas configuration is shown in Figure 4.5.

ϵ_r	Directivity at first resonance (dBi)	d_1/λ	d_2/λ_e
9.8	17.45	0.25	0.24
8.8	16.97	0.25	0.23
6.8	15.89	0.24	0.26
5.5	14.99	0.24	0.25

in Table 4.4. However, for the sake of brevity, the antenna directivity versus air-gap height and superstrate are not plotted for all other cases except for the case with $\epsilon_{r2} = 9.8$ (Figure 4.13).

Interestingly, for the this antenna, the directivity is about 3 dB higher than the antenna configuration having a PMC ground plane. These directivities are about the same as the one demonstrated by the antenna configuration with PEC ground plane. Radiation patterns of these antenna configurations are shown in Figure 4.14.

2) Antenna configuration with AMC2 as the ground plane: Antenna2

The maximum directivities of this antenna configuration for various superstrate layers with different dielectric permittivity, are listed in Table 4.5. For the sake of brevity, the antenna directivity versus air-gap height and superstrate are not plotted (They are similar to Figure 4.13.). Radiation patterns of these antenna configurations are shown in Figure 4.15.

3) Antenna configuration with AMC3 as the ground plane: Antenna3

The maximum directivities of this antenna configuration for various superstrate layers with different dielectric permittivity, are listed in Table 4.6. As

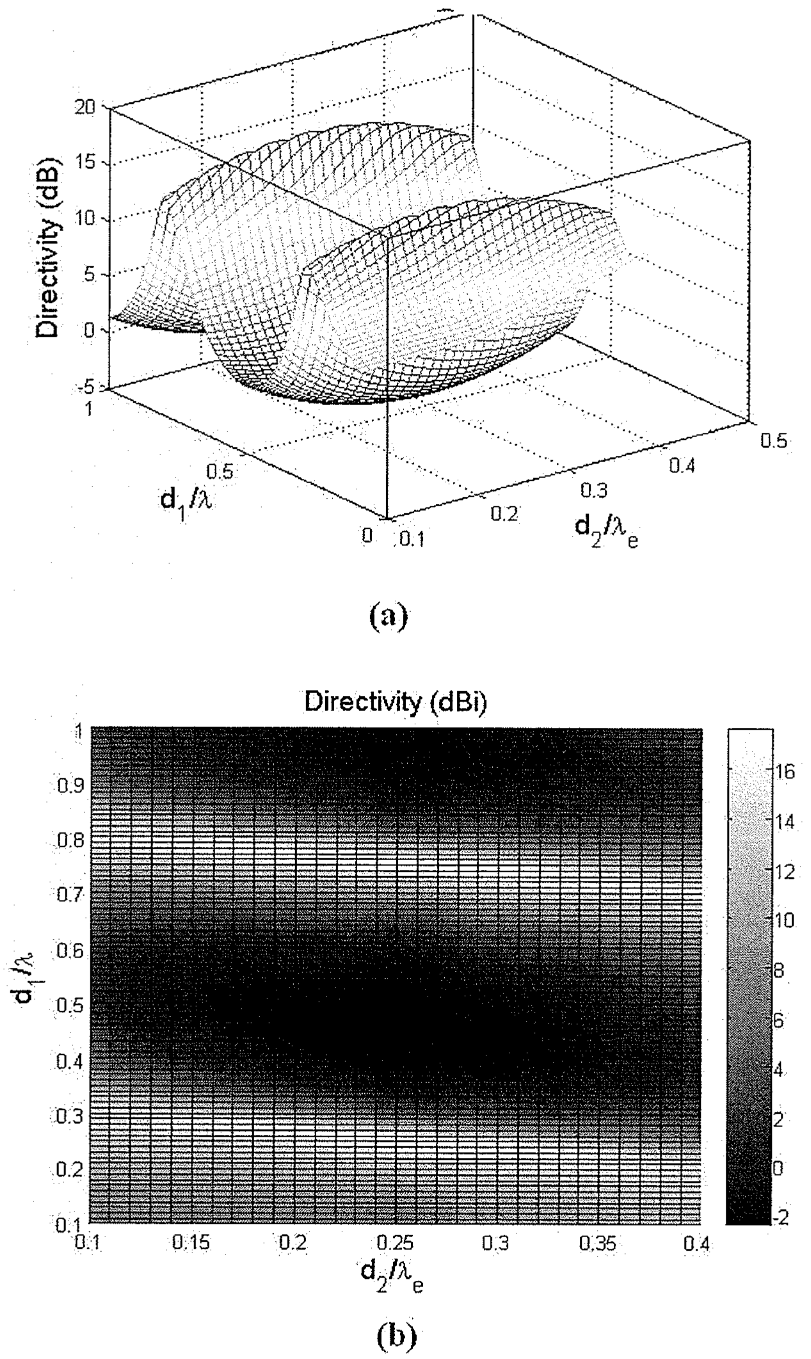

Figure 4.13: Directivity versus air-gap height (d_1/λ_0) and dielectric superstrate thickness (d_2/λ_e) for the cavity resonance antenna shown in Fig. 4.5 with AMC1 ground plane. Superstrate relative permittivity is $\epsilon_2 = 9.8$.

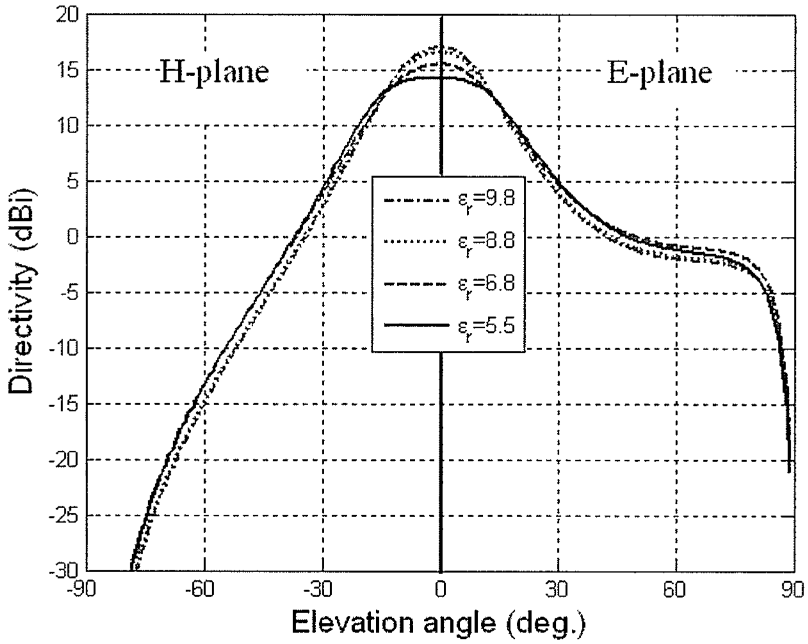

Figure 4.14: Radiation patterns of the antenna shown in Fig. 4.5 with AMC1 ground plane for different superstrate relative permittivities thicknesses listed in Table 4.4.

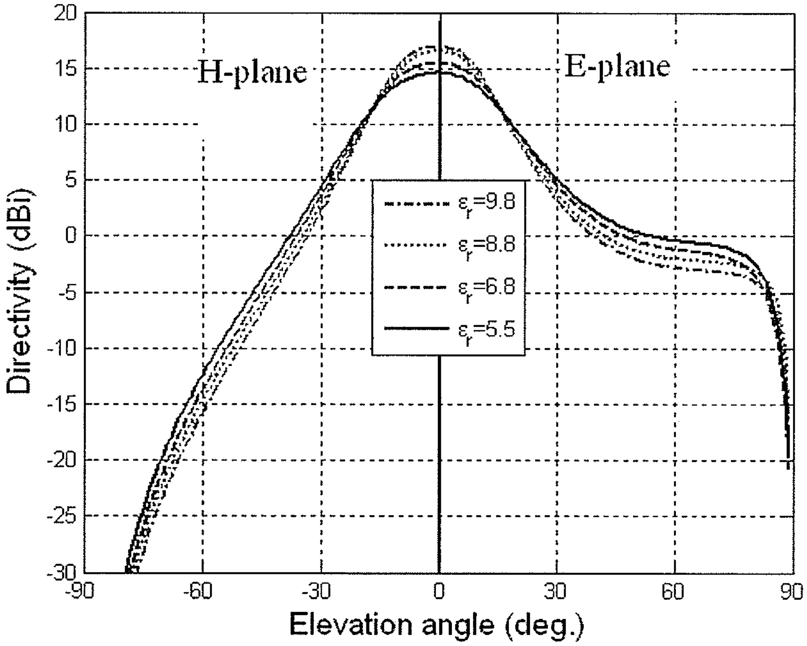

Figure 4.15: Radiation patterns of the antenna shown in Fig. 4.5 with AMC2 ground plane for different superstrate relative permittivities thicknesses listed in Table 4.5.

Table 4.6: Antenna directivities for AMC3 ground plane and different dielectric superstrate permittivities. Antennas configuration is shown in Figure 4.5.

ϵ_r	Directivity at first resonance (dBi)	d_1/λ	d_2/λ_e
9.8	10.71	0.25	0.23
8.8	10.34	0.24	0.25
6.8	9.56	0.24	0.25
5.5	8.97	0.24	0.24

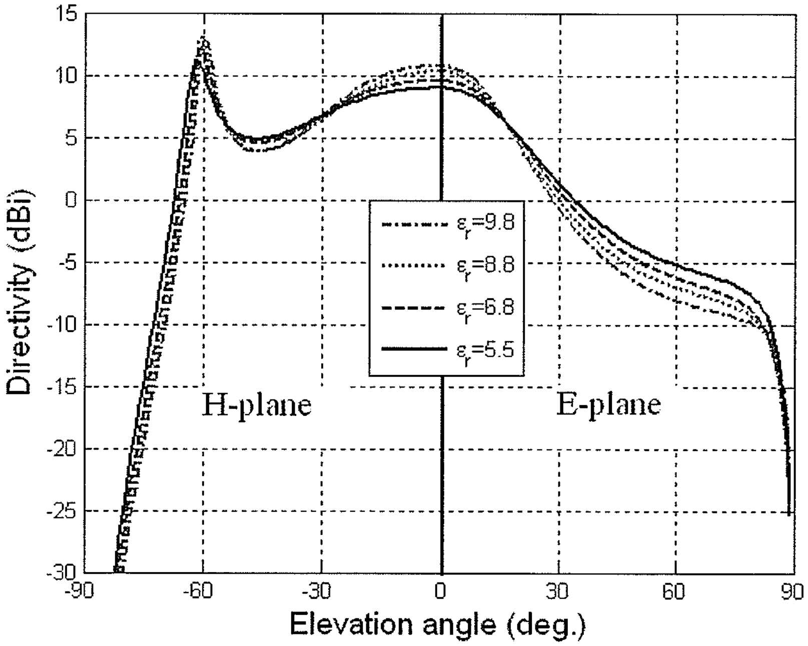

Figure 4.16: Radiation patterns of the antenna shown in Fig. 4.5 with AMC3 ground plane for different superstrate relative permittivities and thicknesses listed in Table 4.6.

the for the previous case and for brevity, the antenna directivity versus air-gap height and superstrate are not plotted. Radiation patterns of these antenna configurations are shown in Figure 4.16.

Observations

According to the results presented above, a few observation and recommendations are made as follows:

- Comparison between the antenna directivity in Tables 4.4 and 4.5 as well as radiations patterns between Figures 4.14 and 4.15 reveals that the results are quite similar. This is because of the fact that the reflection coefficient of AMC1 and AMC2 surfaces are very similar as shown in Figure 4.11 for both polarizations.

- Owing to the fact that employing AMC1 and AMC2 surfaces as the ground plane of the Antenna1 and Antenna2, respectively, produces similar results, it is recommended to use AMC2 surface. This is because of the fact that AMC2 unit cell are smaller than AMC1 unit cell in size. Therefore, for the practical applications where the ground plane is to be truncated more unit cell numbers can be accommodated on the ground surface.

- From Table 4.6, it is evident that directivities of the Antenna3 are drastically lower than their corresponding counterparts of Antenna1 and Antenna2. This can be investigated, paying more attention to the far-field radiation patterns. The radiation patterns of Antenna3 is different from those of Antenna1 and Antenna2. This difference is more severe in the H-plane. Since the excitation probe is x-directed in these antennas, their radiation patterns in the H-plane are obtained by calculating E_ϕ at $\phi = \pi/2$. As presented in equation 4.17, E_ϕ is caused by E^{TE}. On the other hand, TE reflection phase of AMC3, is different from that of AM2 and AMC1. This difference is much more severe than TM reflection phases. One should note that TE reflection phase of AMC3 is negative and monotonically decreasing all over entire incident angles, whereas TE reflection phase of AMC1 and AMC2 are both positive and moronically increasing over the incident angles. However, TM reflection phases of AMC1, AMC2 and AMC3 are more similar in shape and form of the phase variations versus incident angles. Thus, it is observed that the radiation patterns in the E-plane are close to each other in the shape and form sense. It should be noted that, since the excitation probe is x-directed in these antennas, their radiation patterns in the E-plane are obtained by calculating E_θ at $\phi = 0$.

4.3.4 Antenna with 2-layer superstrate and either PEC or PMC ground plane

Using more high-permittivity superstrate layers increases the antenna directivity [49]. Antenna configuration with two superstrate layers is shown in Figure 4.17. The corresponding dielectric constitutive parameters are listed in Table 4.7. As well, corresponding dimensions which maximizes the directivity are listed in 4.7, when either PEC or PMC is used as the antenna ground plane. Radiation patterns of these two antennas are shown in Figures 4.18 and 4.19, for the cases having PEC and PMC ground planes, respectively. As observed, the antenna with PEC ground plane produces higher directivity by about 3 dB. The first air-gap region is also half-wavelength and twice of that of the antenna having PMC ground plane. These results are obtained based on the TEN method and formulations presented earlier in this chapter.

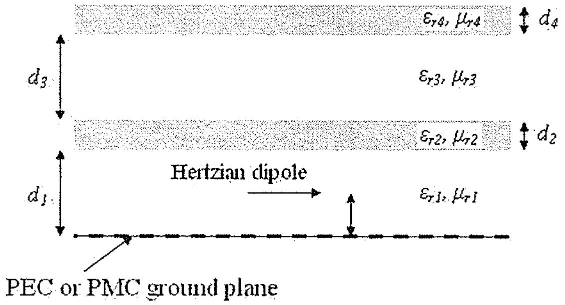
$\varepsilon_{r4}, \mu_{r4}$
d_4
d_3
$\varepsilon_{r3}, \mu_{r3}$
$\varepsilon_{r2}, \mu_{r2}$
d_2
Hertzian dipole
d_1
$\varepsilon_{r1}, \mu_{r1}$
PEC or PMC ground plane

Figure 4.17: Hertzian dipole embedded between double-layer dielectric superstrate and a ground plane.

Table 4.7: Antenna directivities for ideal PMC and PEC ground plane and different dielectric superstrate permittivities. The antennas configuration is shown in Figure 4.17. Constitutive parameters of the embedding dielectrics are: $\epsilon_{r1} = 1, \epsilon_{r2} = 9.8, \epsilon_{r3} = 1, \epsilon_{r4} = 9.8$ and $\mu_{r1} = \mu_{r2} = \mu_{r3} = \epsilon_{r4} = 1$.

Ground plane type	Directivity at first resonance	d_1/λ	d_2/λ_e	d_3/λ	d_4/λ_e
PEC	26.66 (dBi)	0.50	0.25	0.24	0.26
PMC	23.89 (dBi)	0.25	0.25	0.24	0.26

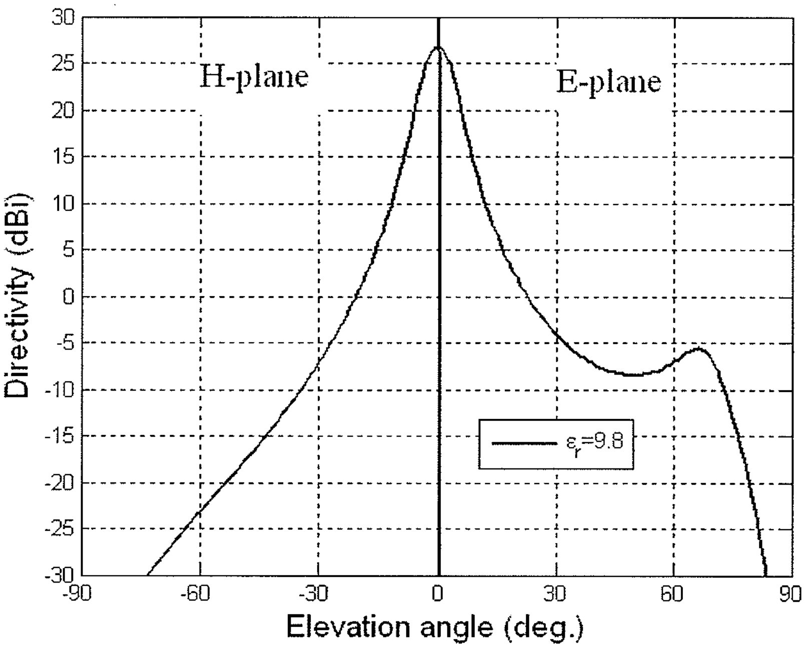

Figure 4.18: Radiation patterns of the antenna shown in Figure 4.17 having PEC ground plane for superstrate relative permittivity of $\epsilon_r = 9.8$. Dimensions are given in Table 4.7

4.3.5 Antenna with AEC/AMC ground plane

In this part, the antenna configuration as shown in Figure 4.5 is considered with the ground plane shown in Figure 4.20. As was introduced in Chapter 3, periodic strip grating on a grounded dielectric slab shows either artificial magnetic conducting or artificial electric conducting (AEC) behavior depending on the electric field direction and polarization of the incident wave. This surface can act as an AMC for the x-polarized incident wave showing reflection phase of zero at normal incidence. As well, it can act as an AEC for the y-polarized

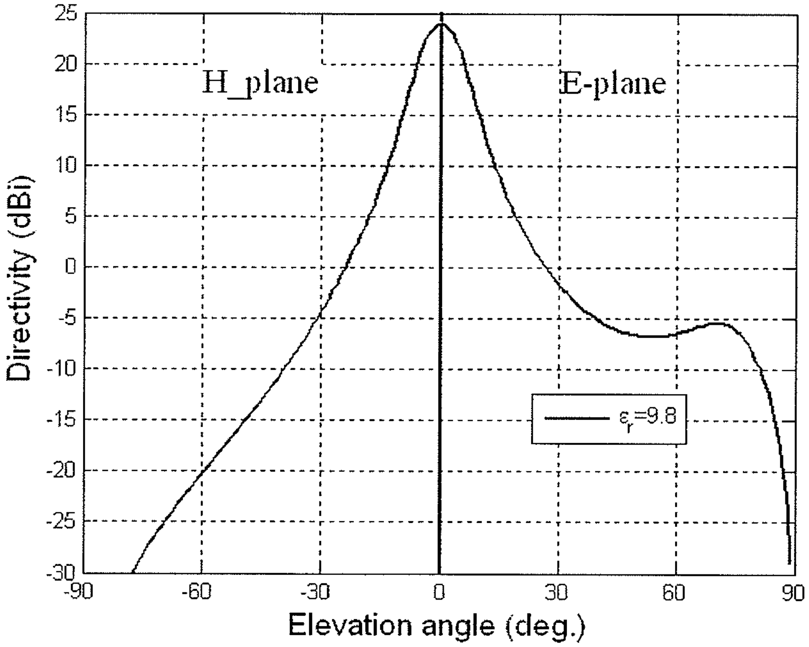

Figure 4.19: Radiation patterns of the antenna shown in Figure 4.17 having PMC ground plane for superstrate relative permittivity of $\epsilon_r = 9.8$. Dimensions are given in Table 4.7

incident wave showing reflection phase close to 180°. These two modes are studied in more details through an example as follows.

The periodic strip grating on the grounded dielectric slab is considered with the following dimensions. Periodicity (d_x) is 6 mm, strip width (l_x) is 5.54 mm, and the dielectric thickness (t) is 1.6 mm. The relative permittivity of the dielectric is 2.5. This artificial ground plane works in two different modes, namely AMC and AEC as described above. The results presented in the next parts are obtained at frequencies of 9.5 and 19.0 GHz for AMC and AEC modes, respectively.

Antenna with artificial ground plane in AMC mode

The reflection phase versus incident angle is shown in Fig. 4.21 for both TE^z (at $\phi = 90°$) and TM^z (at $\phi = 0°$) polarizations, when the artificial ground plane works in AMC mode. In this mode, the electric field of the

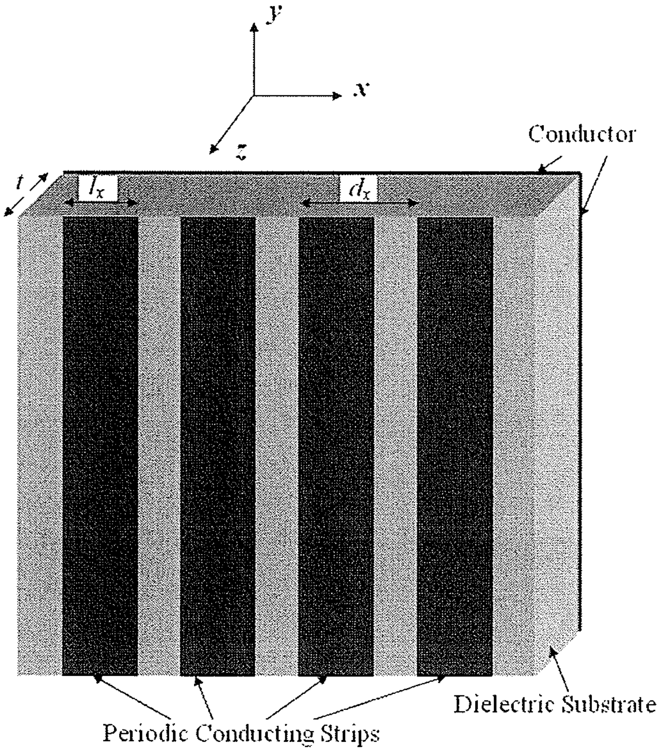

Figure 4.20: Grounded dielectric slab loaded by infinitely-long periodic metallic strips. Periodicity (d_x) is 6 mm, strip width (l_x) is 5.54 mm, and the dielectric thickness (t) is 1.6 mm. The relative permittivity of the dielectric is 2.5.

incident wave is x-directed. Intuitively, this is expected, since the periodic strips exhibits capacitive behavior to the x-polarized incident wave [19]. This capacitance is in parallel with the grounded dielectric slab having inductive characteristics. Therefore, the resonance occurs and the periodic structure demonstrates reflection phase close to zero, resulting in a high impedance surface. Surface impedances corresponding to both TE^z (at $\phi = 90°$) and TM^z (at $\phi = 0°$) polarizations are shown in Figure 4.22. In fact these surface impedances are the load impedance in the TEN model (Figure 4.5) and they have been calculated as using equation (4.18).

As can be seen in Figure 4.22, the corresponding surface impedances to AMC surface is high at normal incidence. However, at grazing angles the surface impedance is very low. This is consistent with the fact that reflection phase is about 180° for TE^z polarization (Figure 4.21). Interestingly, the surface impedance magnitude is about 400 Ω for TM^z polarization as shown in Figure 4.22. This is consistent with the fact that the reflection phase is almost uniform and about 90° at grazing angle for this polarization. Therefore, the surface impedance magnitude is about that of free space as supposed to be. The surface impedance phase is 90° and constant over the incident angles. Thus, the surface is high impedance and inductive. This is because of the fact that reflection coefficient phase is always positive from very close to zero at normal incidence up to about 180° at grazing angles.

Consider the above-mentioned artificial ground plane in AMC mode, as described above, for the antenna configuration shown in Fig. 4.5. The excitation is an x-polarized electrical Hertzian dipole. The antenna directivity versus air-gap height and superstrate thickness is shown in Fig. 4.23 for $\epsilon_r = 9.8$. The maximum directivities of this antenna configuration for various superstrate

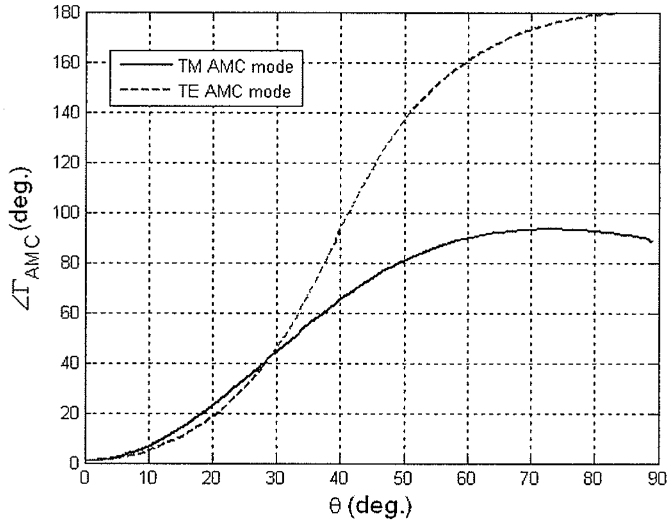

Figure 4.21: Corresponding reflection phase versus incident angles of the structure shown in Figure 4.20 in AMC mode with dimensions of d_x= 6 mm, l_x= 5.54 mm, and t= 1.6 mm. The relative permittivity of the dielectric is 2.5 and the operating frequency is 9.5 GHz.

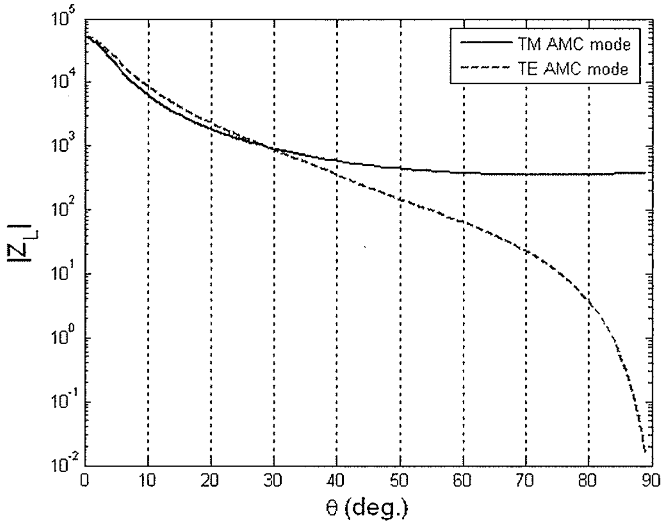

Figure 4.22: Surface impedance magnitude of the structure shown in Figure 4.20 with dimensions of d_x= 6 mm, l_x= 5.54 mm, and t= 1.6 mm. The relative permittivity of the dielectric is 2.5. Operating frequency for AMC is 9.5 GHz.

layers with different dielectric permittivities, are listed in Table 4.8. These maxima are obtained for air-gap heights (d_1) and dielectric superstrate thicknesses (d_2) as addressed in Tables 4.9 and 4.10. The values presented in Tables 4.9 and 4.10 correspond to the first resonance which introduces the lowest profile design. As can be seen in Tables 4.9 and 4.10, the maximum directivities are obtained for both air-gap height and dielectric thickness of about quarter-wavelength of their corresponding media. For all cases studied in this section, the Hertzian dipole is placed on the AMC ground plane, as the maximum voltage V_h occurs at this height. The corresponding radiation patterns of the above-mentioned antenna configurations are shown in Fig. 4.24.

Antenna with artificial ground plane in AEC mode

The reflection phase versus incident angle is shown in Figure 4.25 for both TE^z (at $\phi = 0°$) and TM^z (at $\phi = 90°$) polarizations, when the artificial ground plane works in AEC mode. In this mode, the electric field of the incident

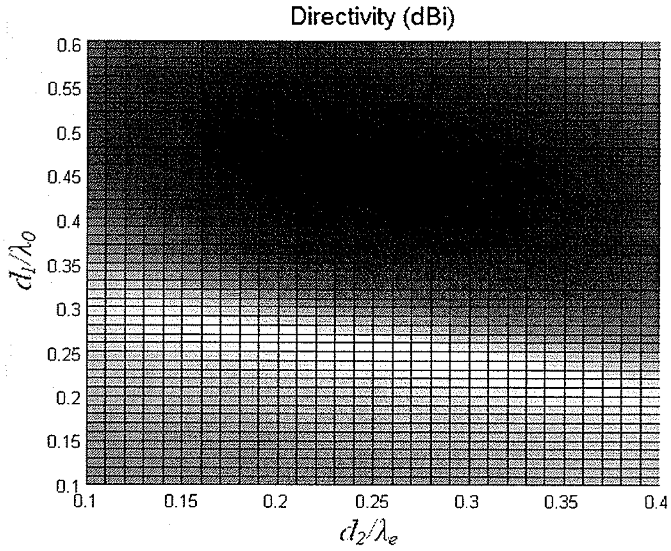

Figure 4.23: Directivity versus air-gap height (d_1/λ_0) and dielectric superstrate thickness (d_2/λ_e) for the cavity resonance antenna shown in Figure 4.5 with the ground plane shown in Figure 4.20 operating in AMC mode. Superstrate relative permittivity is $\epsilon_2 = 9.8$.

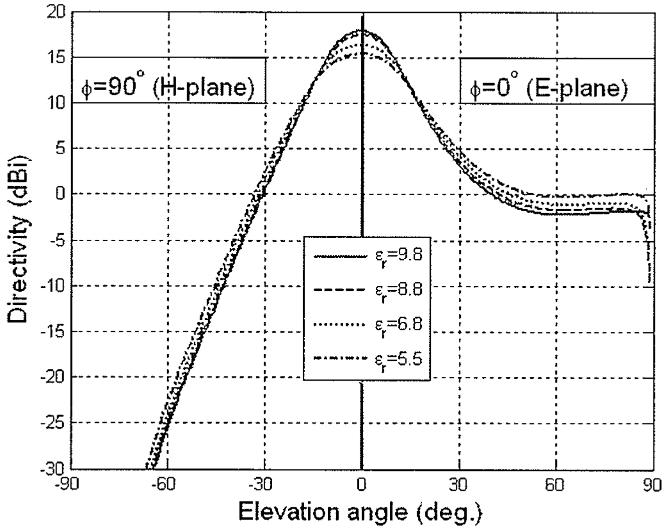

Figure 4.24: Radiation patterns of the antenna shown in Figure 4.5 with the ground plane shown in Figure 4.20, operating in AMC mode, and different superstrate relative permittivities.

wave is y-directed. The periodic strips exhibits inductive behavior to the y-polarized incident wave [19]. This inductance is in parallel with the grounded dielectric slab having inductive characteristics, too. Therefore, the resonance does not occur. Instead, the equivalent inductance of the two parallel inductance introduces lower inductance value resulting in a low impedance surface. Pertaining surface impedances corresponding to both TE^z (at $\phi = 0°$) and TM^z (at $\phi = 90°$) polarizations are shown in Figure 4.26. As before, these surface impedances are the load impedance in the TEN model (Figure 4.5) and they have been calculated using equation (4.18).

As can be observed in Figure 4.26, the corresponding surface impedances to AEC surface is low at normal incidence ($\sim 1\ \Omega$). For TE^z (at $\phi = 0°$) polarization, the surface impedance magnitude decreases toward zero (PEC) at grazing angles, since the reflection phase increases toward 180°. For TM^z (at $\phi = 90°$) polarization, however, the surface impedance magnitude increases at grazing angles, since the reflection phase decreases from 179.6° to 171°. Nevertheless, the impedance is still considered low ($\sim 30\ \Omega$). The surface impedance phase is 90° and constant over the incident angles. Thus, the surface is low impedance and inductive. This is because of the fact that reflection coefficient

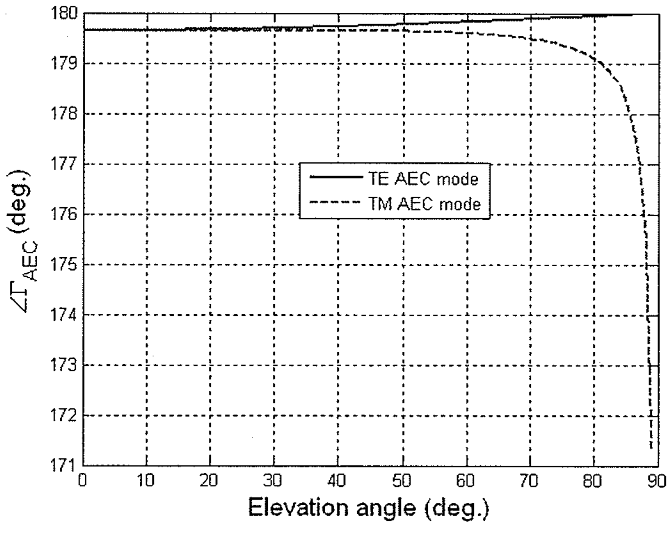

Figure 4.25: Corresponding reflection phase versus incident angles of the structure shown in Figure 4.20 in AEC mode with dimensions of d_x= 6 mm, l_x= 5.54 mm, and t= 1.6 mm. The relative permittivity of the dielectric is 2.5 and the operating frequency is 19.0 GHz.

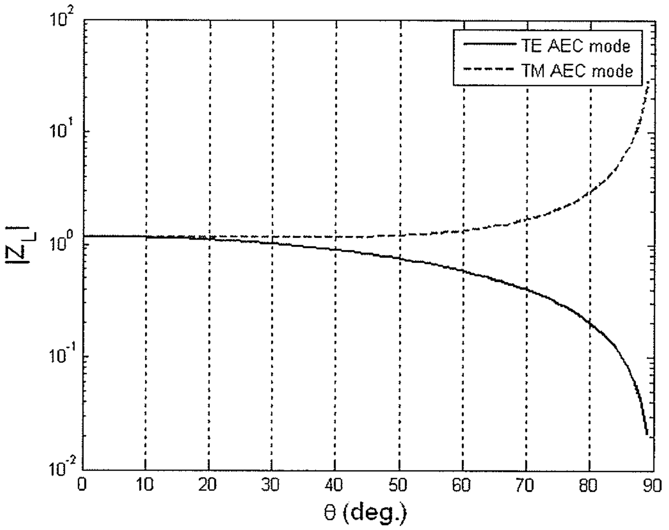

Figure 4.26: Surface impedance magnitude of the structure shown in Figure 4.20 with dimensions of d_x= 6 mm, l_x= 5.54 mm, and t= 1.6 mm. The relative permittivity of the dielectric is 2.5. Operating frequency is 19.0 GHz.

phase is always positive and about 180° for all incident angles.

Consider the above-mentioned artificial ground plane in AEC mode, as discussed above, for the antenna configuration shown in Fig. 4.5. The excitation is an y-polarized electrical Hertzian dipole. The antenna directivity versus air-gap height and superstrate thickness is shown in Figure 4.27 for $\epsilon_r = 9.8$. The maximum directivities of this antenna configuration for various superstrate layers with different dielectric permittivities, are listed in Table 4.8. These maxima are obtained for air-gap heights (d_1) and dielectric superstrate thicknesses (d_2) as addressed in Tables 4.9 and 4.10. The values presented in Tables 4.9 and 4.10 correspond to the first resonance which introduces the lowest profile design. As can be seen in Tables 4.9 and 4.10, the maximum directivities are obtained for air-gap height about half-wavelength and dielectric thickness of about quarter-wavelength of their corresponding media. For all cases studied in this section, the Hertzian dipole is placed at the air-gap height of ($d_1/2$) from the AEC ground plane, as the maximum voltage V_h is

Table 4.8: Antenna directivities for different ground planes and dielectric superstrate permittivities. Antenna configuration is shown in Figure 4.5. AMC and AEC ground planes are shown in Figure 4.20

ϵ_r	PEC	PMC	AMC	AEC
9.8	16.88	14.18	17.89	16.87
8.8	16.45	13.77	17.44	16.45
6.8	15.46	12.85	16.32	15.44
5.5	14.62	12.11	15.38	14.61

Table 4.9: Air-gap heights corresponding to maximum antennas directivities addressed in Table 4.8. The lengths are normalized to the free space wave length (d_1/λ_0).

ϵ_r	PEC	PMC	AMC	AEC
9.8	0.49	0.25	0.25	0.49
8.8	0.49	0.25	0.24	0.49
6.8	0.49	0.24	0.24	0.49
5.5	0.49	0.24	0.24	0.49

Table 4.10: Dielectric thicknesses corresponding to maximum antennas directivities addressed in Table 4.8. The lengths are normalized to the corresponding wave-length in each dielectric (d_2/λ_e).

ϵ_r	PEC	PMC	AMC	AEC
9.8	0.26	0.25	0.23	0.26
8.8	0.26	0.25	0.26	0.25
6.8	0.25	0.24	0.26	0.25
5.5	0.24	0.24	0.25	0.24

supposed to occur at this height [12]. The corresponding radiation patterns of the above-mentioned antenna configurations are shown in Fig. 4.28.

Antenna with artificial ground plane in dual-mode

As it was discussed above, this antenna configuration can work in dual-frequency and dual-polarization mode. Top-view of such configuration is shown in Figure 4.29. One should note that the air-gap height and superstrate dielectric thickness must be selected properly. It was shown that for the AMC and AEC mode the air-gap height is about a quarter and half wavelength, respectively. The thickness of the superstrate dielectric is about a quarter wavelength for both cases. Therefore, the AMC mode is selected for the lower frequency (9.5 GHz),

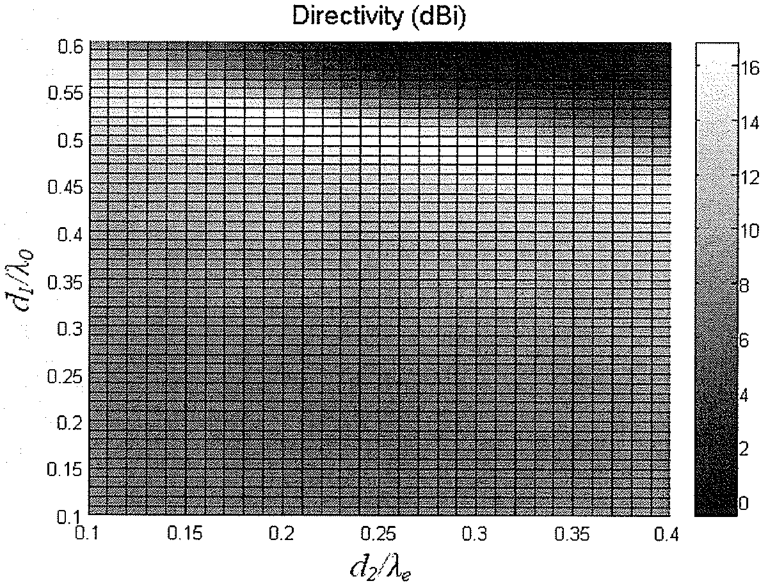

Figure 4.27: Directivity versus air-gap height (d_1/λ_0) and dielectric superstrate thickness (d_2/λ_e) for the cavity resonance antenna shown in Figure 4.5 with the ground plane shown in Figure 4.20, operating in AEC mode. Superstrate relative permittivity is $\epsilon_2 = 9.8$.

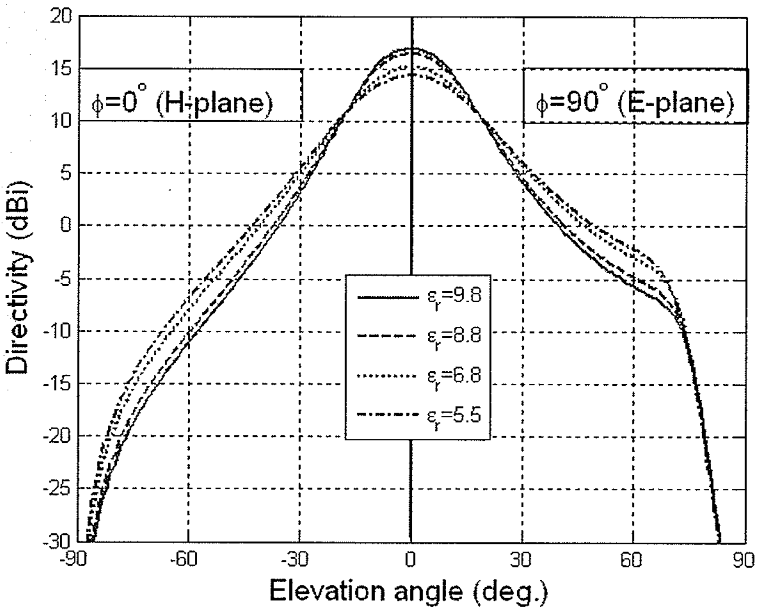

Figure 4.28: Radiation patterns of the antenna shown in Figure 4.5 with the ground plane shown in Figure 4.20, operating in AEC mode, and different superstrate relative permittivities.

and the AEC mode is selected for the upper frequency (19.0 GHz). One should note that the upper frequency is twice as the lower frequency. Therefore, the air-gap height can be kept the same for both frequencies. However, the dielectric thickness cannot be maintained quarter-wavelength for both modes. Thus, an objective function based on the multiplication of the directivities of the antenna operating in both modes, is considered. The function values versus dielectric thickness and air-gap height is shown in Figure 4.30. One should note that the dielectric thickness and air-gap height are normalized to the corresponding wavelength media operating at the lower frequency (9.5 GHz). The maximum occurs at the corresponding values of $d_1 = 0.245\lambda_0$ and $d_2 = 0.135\lambda_e$ for lower frequency ($f_r = 9.5$ GHz). The directivity of 14.05 dBi is achieved. At the higher frequency ($2f_r = 19.0$ GHz), the directivity of 17.10 dBi is achieved. Obviously, the corresponding values of $d_1 = 0.49\lambda_0$ and $d_2 = 0.27\lambda_e$ are obtained. The results are summarized in Table 4.11. Dual-band orthogonally polarized configuration is obtained at the expense of about 3 dB loss in directivity for AMC mode. The above results were obtained when the electric Hertzian dipole is fixed at $h = \lambda/8$ above the ground. In this case, λ is the wavelength of the the lower frequency (9.5 GHz). This is because of the fact that in practical applications a single microstrip antenna can be used as the excitation for both modes. Therefore, both x-polarized and y-polarized electric Hertzian dipoles must have the same height from the artificial ground plane. The radiations patterns of this antenna configuration are shown in Figure 4.31. These results are obtained when the relative permittivity of the superstrate dielectric is 9.8.

Interestingly, in spite of changing the probe positions, the antennas still demonstrate as high directivity as 17.1 dBi, slightly larger than the one shown in Table 4.8. Although the resonance condition introduced in [12] specifies

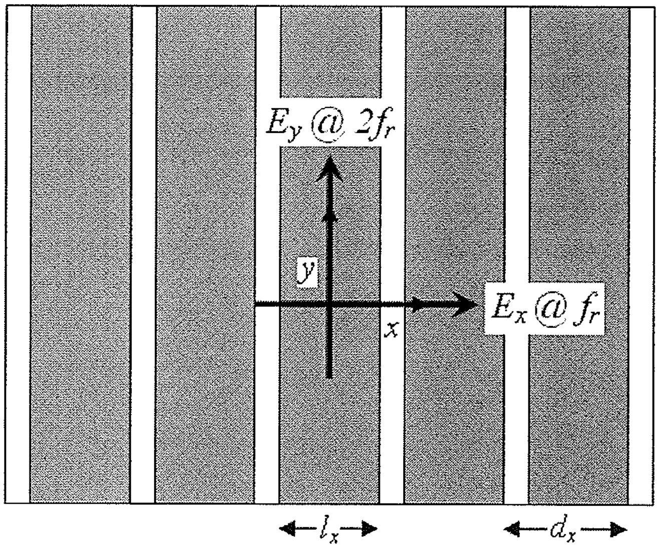

Figure 4.29: Top-view of the dual-polarized antenna configuration with artificial ground plane. Strips are infinitely long in the y-direction. Antenna side view is similar to the one shown in Figure 4.5.

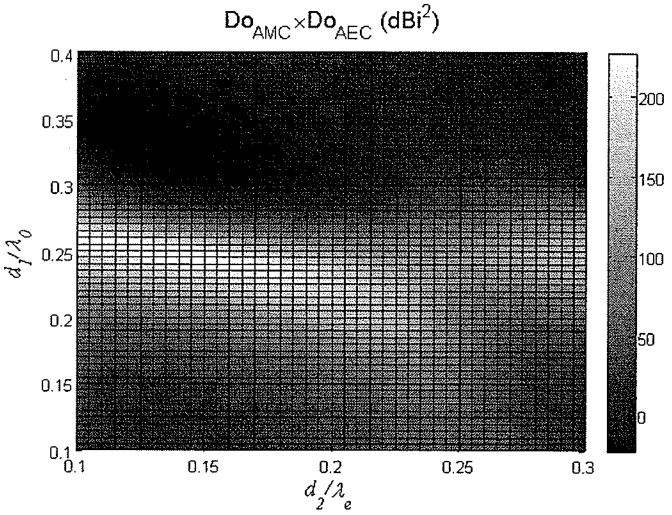

Figure 4.30: Product of the antenna directivities in AEC and AMC modes, versus air-gap height and dielectric thickness. Antenna configuration is shown in Figure 4.29.

certain height for the excitation probe, it has been shown for a certain range of probe heights the high directivity can be maintained [50, 51].

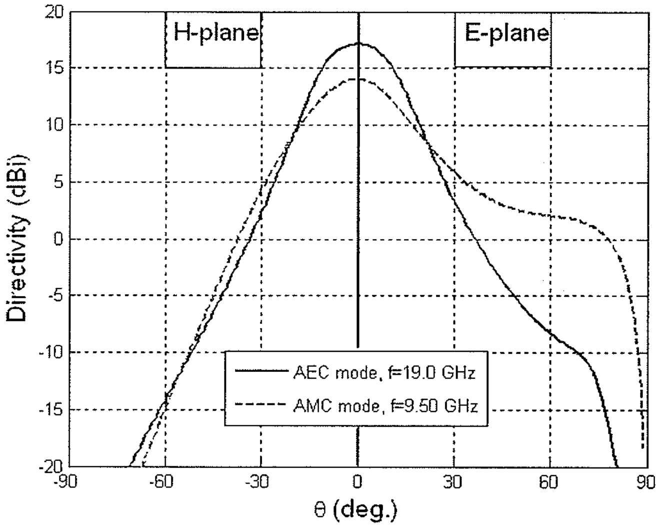

Figure 4.31: Radiation patterns of the designed antenna in two different modes. Superstrate relative permittivity is $\epsilon_2 = 9.8$. Antenna configuration is shown in Figure 4.29.

Table 4.11: Properties of the optimized dual-band orthogonally polarized antenna shown in Figure 4.29.

Ground plane mode	Directivity	d_1/λ_0	d_2/λ_e	frequency
AMC	14.05 dBi	0.245	0.135	9.50 GHz
AEC	17.10 dBi	0.490	0.270	19.0 GHz

4.4 Analysis of electric Hertzian dipole over different ground plane without superstrate using TEN

In this section, a few examples of the electric Hertzian dipole antenna over different ground planes are analyzed using the TEN model, when the structure does not have any superstrate cover. In other words the source antennas are exposed to the free space. The antenna configuration is the same as the one shown in Figure 4.5, except that the superstrate dielectric relative permittivity is unity ($\epsilon_{r2} = 1$). In fact, this corresponds to the limiting cases of the antenna configurations discussed earlier in this chapter. The analysis of these configurations have two advantages as follows.

- Analyzing the electric Hertzian dipole antenna over ground planes using TEN produce some results. The results are compared to the canonical cases existing in the literature to check the accuracy of the TEN model.
- When the contribution of each electric Hertzian dipole in different configurations without superstrate are calculated, the significance of the high-permittivity dielectric superstrate will be more pronounced. Moreover, the effect of the ground plane in far-field properties will be better understood.

As is well-known, the directivity of the electric Hertzian dipole is 1.5 or 1.76 dBi [52]. Its far-field radiation patterns are omnidirectional (constant value of 1.76 dBi) in the H-plane and it is a sine function ($sin(\theta)$) in the E-plane. Now, the antenna configuration shown in Figure 4.5 is considered when the ground plane is an ideal infinite PMC and the electric Hertzian dipole is placed immediately on the PMC ($h = 0$). According to the image theory [28], the image of the source antenna is identical as the source antenna provided the PMC plane is removed. This problem is the same as that the radiation of one electric Hertzian dipole in the upper half space. Since the radiated power occurs only in one half space, and the directivity is inversely proportional to the radiated power (equation (2-16) [52]), the directivity of this antenna is twice that of the single electric Hertzian dipole antenna radiating in the entire free space. Therefore, the directivity of this antenna is 3.03 dB more than that of the electric Hertzian dipole. Its value thus is: 3.03 dB+1.76 dBi=4.79 dBi. As well, the radiation pattern maintains its shape except that it is only valid in the upper half space.

For the same antenna configuration, the obtained radiation patterns using the TEN model are shown in Figure 4.32. As can be seen, the directly is 4.8 dBi in an excellent agreement of what above-mentioned theory presents. Also, it is observed that the half power beamwidth occurs at about 45° in the E-plane. This agrees with the above-mentioned theory, since the electric Hertzian dipole has a sine shape radiation pattern ($sin(\theta)$) in the E-plane and its half-power beamwidth is 45° [53].

The next example considers the case when an electric Hertzian dipole antenna is placed infinitely close to the ideal infinite PEC ground plane. As is well known, when the electric Hertzian dipole is placed on the PEC surface, it will be shorted out or will be canceled out with its image. Therefore, the case of very close to the PEC ($h = \lambda/40 \approx 0$) is considered here. The following asymptotic formula relates the directivity of an electric Hertzian dipole close to its distance from infinite PEC ground plane (equation (4-124) [52]):

$$D_0 = \lim_{kh \to 0} 7.5 \left(\frac{\sin(kh)}{kh} \right)^2 \tag{4.19}$$

Knowing the equation 4.19, the directivity of a Hertzian dipole very close to the PEC ground plane is about 7.5 or 8.75 dBi. Radiation patterns obtained using the TEN model are shown in Figure 4.33. As can be seen in Figure 4.33(b), the directivity is almost 8.75 dBi which is in an excellent agreement with the aforementioned theory. The other example is the case that an electric Hertzian dipole is placed quarter-wavelength above an infinite PEC ground plane. This case is very important since in all TEN modelings presented in the previous sections, when the ground plane is PEC or AEC, the electric Hertzian dipole was placed at the distance of quarter-wavelength above the ground plane (unless otherwise mentioned). As well, it gives very good input impedance

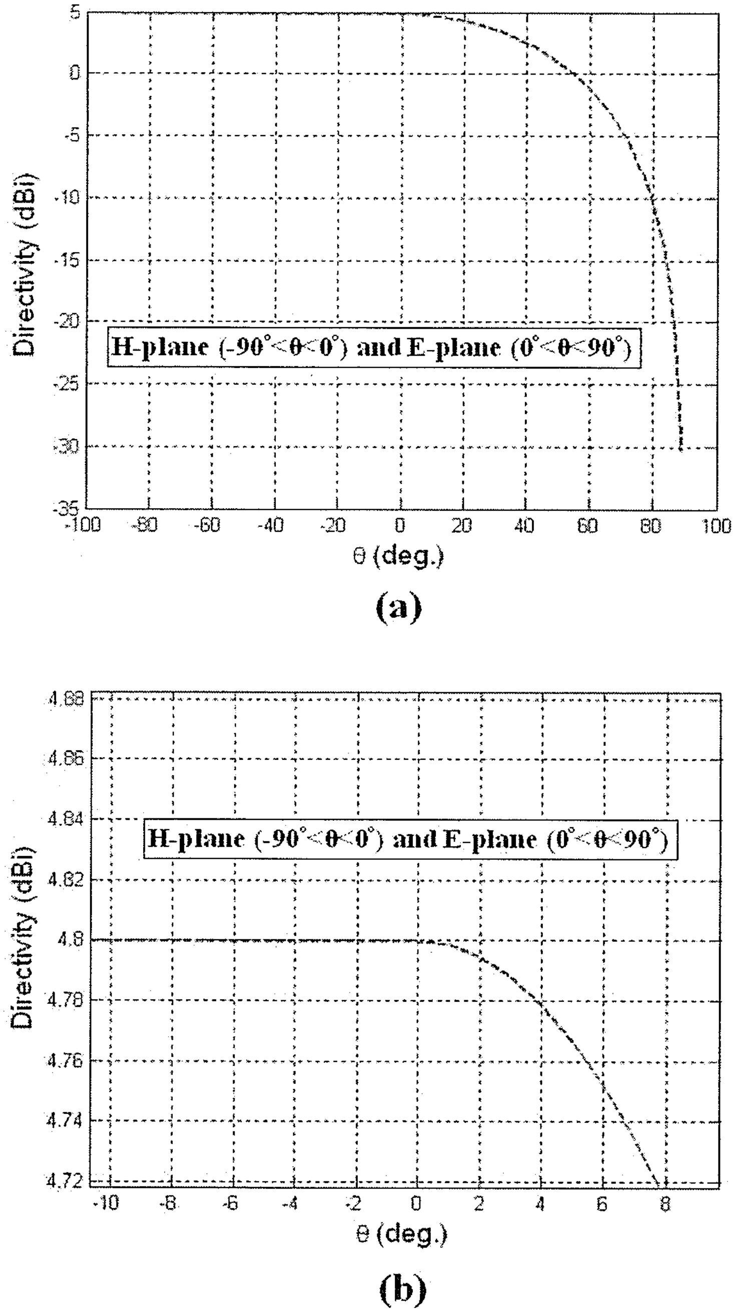

Figure 4.32: Radiation patterns of an electric Hertzian dipole antenna placed on an infinite PMC ground plane, using TEN model. (a) The E-plane and H-plane radiation patterns over the entire half-space, (b) magnified radiation patterns around the boresight angle.

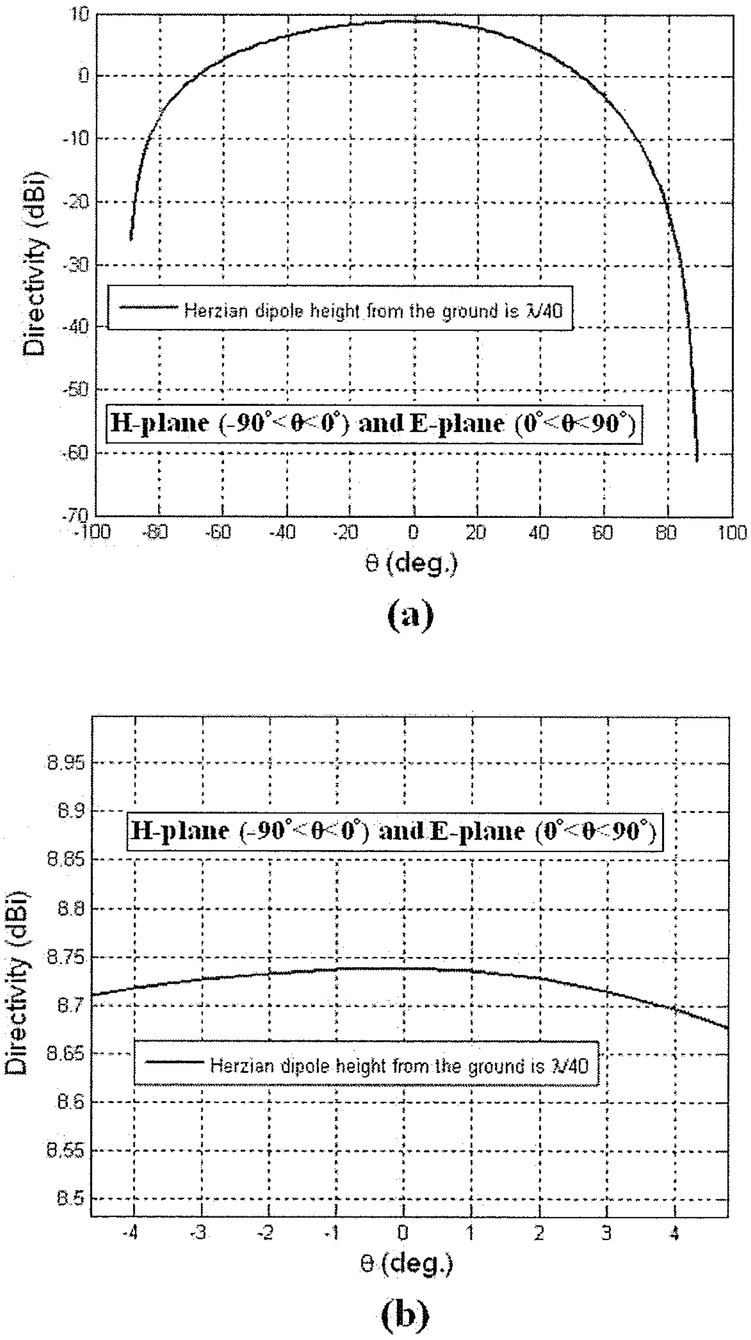

Figure 4.33: Radiation patterns of an electric Hertzian dipole antenna placed at a very close distance above an infinite PEC ground plane ($\lambda/40$), using TEN model. (a) The E-plane and H-plane radiation patterns over the entire half-space, (b) magnified radiation patterns around the boresight angle.

matching compared to all other cases [37]. According to the equation presented in [52], the corresponding maximum directivity of the electric Hertzian dipole above the ground plane at broadside is

$$D_0 = \frac{4\sin^2(kh)}{R(kh)}, \quad \text{for} \quad h \leq \lambda/4 \tag{4.20}$$

where $R(kh)$ is determined by

$$R(kh) = \left[\frac{2}{3} - \frac{\sin(2kh)}{2kh} - \frac{\cos(2kh)}{(2kh)^2} + \frac{\sin(2kh)}{(2kh)^3}\right]. \tag{4.21}$$

When the electric Hertzian dipole is placed at the distance of quarter-wavelength above an infinite PEC ground plane its directivity becomes about 5.208. This value is equivalent to 7.167 dBi. The radiation patterns, obtained using the TEN model are shown in Figure 4.34. As can be seen in Figure 4.34(b), the directivity is almost 7.17 dBi which is in an excellent agreement with the results obtained from theory [52].

As the last example, an electric Hertzian dipole is considered on the ground plane shown in Figure 4.20 acting in the AMC mode. The radiation patterns obtained using the TEN model are shown in Figure 4.35. As can clearly be seen in Figure 4.35(b) the directivity has increased to about 9 dBi. Considering the fact that the electric Hertzian dipole is immediately over the AMC ground plane, the low profile design has been achieved. Also, the impedance matching characteristics is expected to be good since the Hertzian dipole and its image are not canceling each other as was the case in PEC-type ground planes.

The directivity enhancement is attributed to the angular and polarization dependency of the reflection coefficient properties of the AMC ground plane to the various incident angles. Since the AMC is lossless as well as the ideal PMC, the angular- and polarization dependence of the AMC is the only parameter

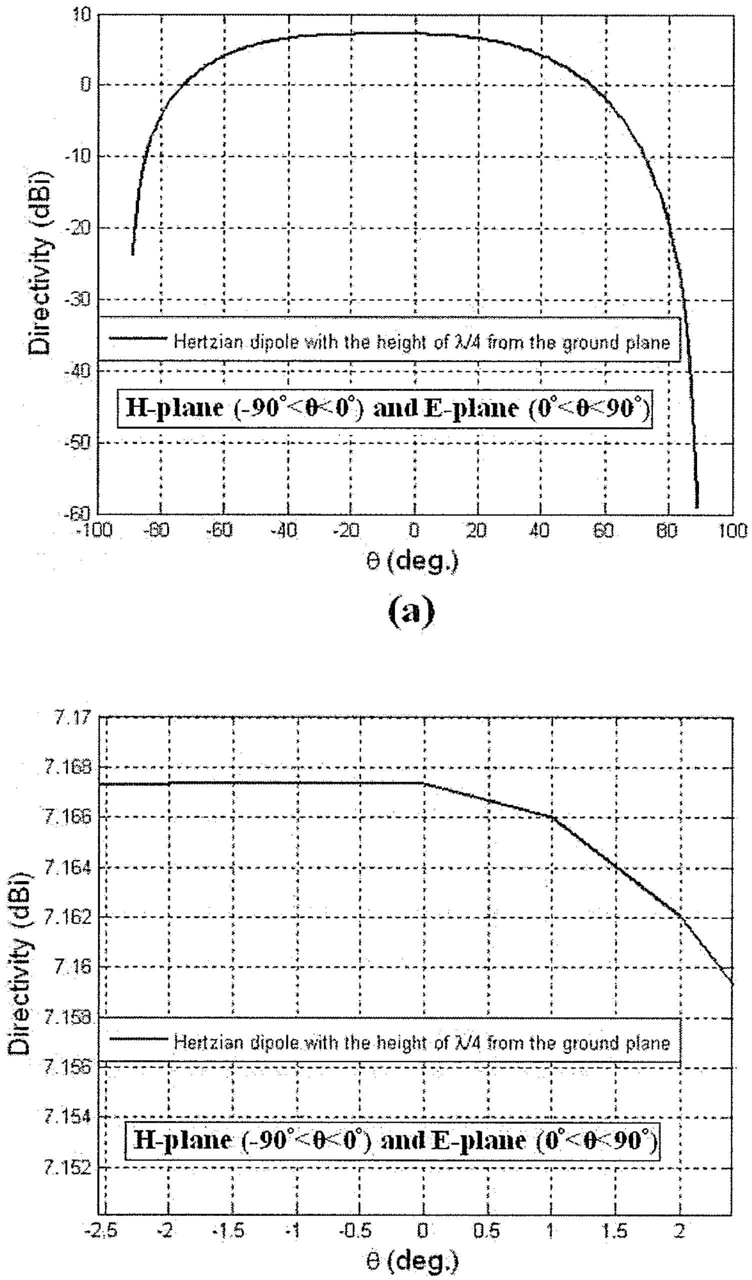

(a)

(b)

Figure 4.34: Radiation patterns of an electric Hertzian dipole antenna placed at a quarter-wavelength distance above an infinite PEC ground plane ($\lambda/4$), using TEN model. (a) The E-plane and H-plane radiation patterns over the entire half-space, (b) magnified radiation patterns around the boresight angle.

which differentiates between PMC and AMC and therefore has beneficial factor on gain enhancement.

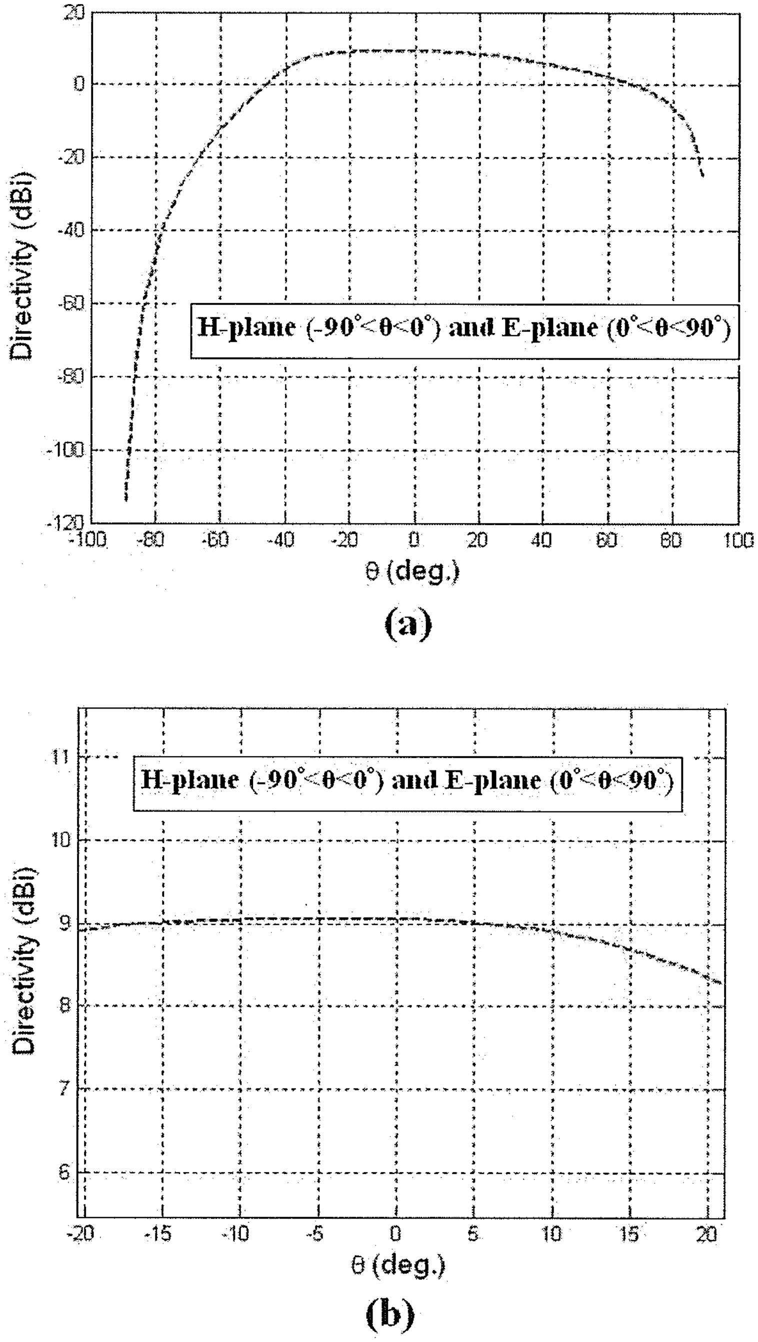

Figure 4.35: Radiation patterns of an electric Hertzian dipole antenna placed on an infinite ground plane shown in Figure 4.20 acting in AMC mode, using TEN model. (a) The E-plane and H-plane radiation patterns over the entire half-space, (b) magnified radiation patterns around the boresight angle.

4.5 Conclusions

In this chapter, the cavity resonance antennas with the dielectric superstrate and different ground planes were investigated. This was achieved by introducing the TEN models for this class of antennas. A simple and efficient method to extract the far-field properties of this class of antennas from its TEN model was studied in detail.

The radiation properties of several antennas of this type were studied. First, antennas with a single-layer dielectric superstrate and PEC ground plane were investigated as the conventional cases. Then, the same antennas were studied when their ground plane were replaced by PMC surfaces. It was shown that the antennas with PMC ground planes have shorter heights than their counterparts with PEC ground planes. However, their directivities were typically less than their counterparts by almost 2.5 dB.

Three AMCs were designed at the operating frequency and employed as the ground plane of the resonance cavity antennas with a dielectric superstrate. For two types of AMCs (square patch and square metallizations), the antenna height was reduced to half, while showing similar directivity levels as their counterparts having PEC ground planes. For the other case (Jerusalem cross metallization), this was not achieved. It was shown that this is due to the different reflection phase response of the ground planes versus incident angles. The study of the angular and polarization dependence of the ground plane and its effect in far-field radiation patterns has not been addressed in the literature and done for the first time in this thesis.

Two-layer dielectric superstrates were also investigated through a quick example. Only PEC and PMC ground planes were used as their ground planes. For the PMC case the first air-gap length is half of that of the PEC case.

As another application, an AEC/AMC ground plane was used to design dual-band high-gain antennas with orthogonally polarized excitations. The AEC/AMC ground plane surface basically consisted of infinitely periodic gratings backed by a grounded dielectric slab. It acted as an AMC for a given frequency and polarization, while it acted as an AEC for twice that frequency and the orthogonal polarization to the first one. The proposed deign, which uses this artificial ground plane, is novel compared to the designs proposed in [54]. It also reduced the profile of the antenna by a factor of two for the lower frequency of operation.

As the last case studies, electric Hertzian dipole antennas were considered over PMC, PEC and AMC ground planes with no superstrate above the antennas. The accuracy of the TEN model was checked by few examples comparing the results to the canonical forms. As well, it was shown that the electric Hertzian dipole antenna on an AMC ground plane provides a directivity of about 9 dBi. This value is 4.2 dBi higher than the same antenna on a PMC ground plane. Once again, this example showed the benefits of angular, and polarization dependent AMC ground planes.

Exhibition of directivity enhancement of the source antenna over some types of AMCs, is the most important contribution of this work. In order to highlight this contribution, a chronological improvement of the antenna designs using AMCs and HIS is addressed below.

Improving antenna input impedance matching using HIS has been shown in [24]. Improving antenna input impedance bandwidth using HIS or AMC ground plane has been shown in [55, 56]. In [24], the improvement in the radiation patterns and directivity of a horizontal wire antenna or a patch antenna over an HIS have been attributed to the suppression of surface waves using the EBG-HIS ground planes consisting of unit cells with shorting pins. In [57, 58], an AMC ground plane using unit cells without shorting pins has been introduced that does not introduce any band-gap around the operating frequency. Then, this AMC ground plane has been employed as the ground plane of a microstrip patch antenna and, has improved the antenna directivity significantly. It has also been shown that this AMC without shorting pins has enhanced the antenna directivity even more than the AMC with shorting pins [58, 59]. Therefore, exhibiting the band-gap frequency by the ground plane is not the main reason for the antenna directivity enhancement. The study in the previous section, reveals that it is the angular and polarization dependency of the AMC ground plane that contributes significantly to the directivity enhancement of the horizonal antenna (electric Hertzian dipole in this work).

Chapter 5

High-gain Planar Antennas with Highly-Reflective Surface Superstrate and Artificial Ground Planes

One of the powerful gain enhancement methods is to place a partially reflective surfaces consisting of periodic patches above the antenna as the superstrate [60]. Through a simple intuitive ray-tracing method, it was illustrated that in order for the antenna to be high-gain the periodic patch superstrates must be highly reflective at the operating frequency [60]. Though, these surfaces are also called highly reflective frequency selective surfaces (HR-FSSs). This concept was also validated through rigorous careful studies using the TEN model, for the cases with conventional PEC ground planes and one layer FSS superstrates [34, 61, 62].

In this chapter, the TEN model is extended to the cavity resonance antennas with artificial ground plane and multilayer FSS superstrates. The effect of the artificial ground plane and FSS on performance enhancement of the antennas will be investigated through a few examples. It is shown that the reflection phase of the FSS superstrate is an instrumental factor to make the antenna size low-profile.

5.1 Formulation of the problem using TEN method

The geometry of the problem is shown in Figure 5.1(a). When a Hertzian dipole is embedded in the multilayer FSS superstrate structure and subjected to the plane wave incidence, TEN model can be used to extract the far-field radiation pattern of the antenna. The physical description has been studied in details in [34, 61, 62], and for brevity are not repeated here. As was discussed in chapter 4, E_θ is evaluated due to the incident plane wave having TM^z polarization whereas E_ϕ is evaluated due to the incident plane wave having TE^z polarization. The geometry of the problem can thus be simplified to the transmission line (TL) model shown in Figure 5.1(b). This model is now appropriate to be analyzed by TEN method.

All quantities V_s, R_s, R_{ck}, Y_B and Z_L, shown in Figure 5.1(b), are polarization (TM or TE) and angular dependent, in general. Each FSS layer is presented by an admittance. These admittances can be found using reflection or transmission properties of the FSS later in this chapter. For now, the relations between the plane wave incident angles, and constitutive parameters of

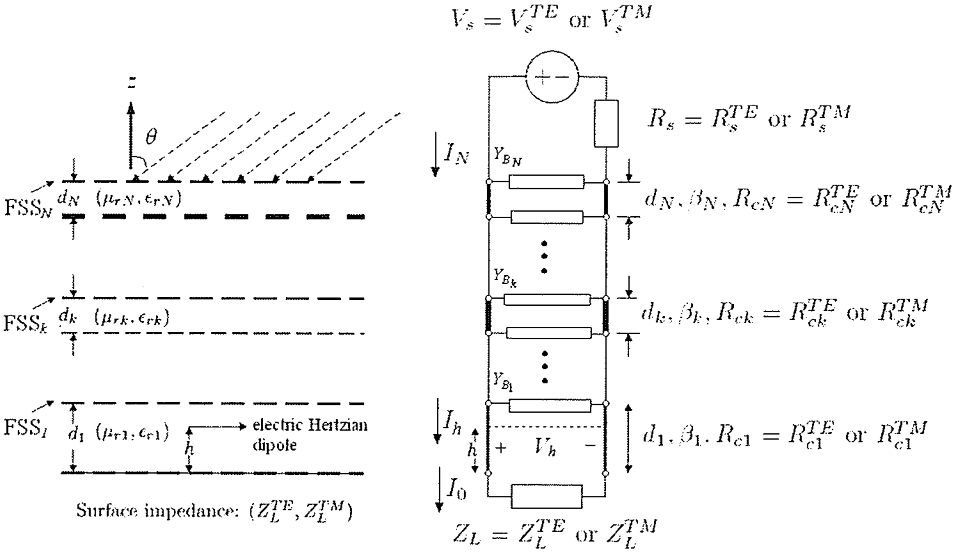
z
θ
FSS_N
d_N $(\mu_{rN}, \epsilon_{rN})$
FSS_k
d_k $(\mu_{rk}, \epsilon_{rk})$
FSS_1
d_1 $(\mu_{r1}, \epsilon_{r1})$
h
electric Hertzian dipole
Surface impedance: (Z_L^{TE}, Z_L^{TM})
$V_s = V_s^{TE}$ or V_s^{TM}
$+ -$
$R_s = R_s^{TE}$ or R_s^{TM}
I_N
Y_{B_N}
$d_N, \beta_N, R_{cN} = R_{cN}^{TE}$ or R_{cN}^{TM}
Y_{B_k}
$d_k, \beta_k, R_{ck} = R_{ck}^{TE}$ or R_{ck}^{TM}
Y_{B_1}
I_h
h
$+ \quad V_h \quad -$
$d_1, \beta_1, R_{c1} = R_{c1}^{TE}$ or R_{c1}^{TM}
I_0
$Z_L = Z_L^{TE}$ or Z_L^{TM}

Figure 5.1: (a) an electric Hertzian dipole embedded between combination of multilayer dielectric and FSS superstrate structure and above and impedance surface acting as a ground plane. (b) Transmission line circuit representing transverse equivalent network to calculate the horizontal electric field induced on the electric Hertzian dipole due to the plane wave incidence in the far-field region.

the dielectric layers for different TE and TM mode are presented as follows

$$V_s^{TE} = 1 \qquad V_s^{TM} = V_s^{TE} \cos(\theta_i) \tag{5.1}$$

$$R_s^{TE} = \eta_0 / \cos(\theta_i) \qquad R_s^{TM} = \eta_0 \cos(\theta_i) \tag{5.2}$$

$$R_{cn}^{TE} = \eta_0 \frac{\mu_{rn}}{\sqrt{\mu_{rn}\epsilon_{rn} - \sin^2(\theta_i)}} \qquad R_{cn}^{TM} = \eta_0 \frac{\sqrt{\mu_{rn}\epsilon_{rn} - \sin^2(\theta_i)}}{\epsilon_{rn}} \tag{5.3}$$

$$\beta_n = k_0 \sqrt{\mu_{rn}\epsilon_{rn} - \sin^2(\theta_i)} \qquad \eta_0 = \sqrt{\mu_0/\epsilon_0}. \tag{5.4}$$

As illustrated in Figure 5.1, the multilayer dielectric structure is considered as the cascaded transmission line segments and admittances terminated by the impedance surface of the ground plane.

Given A_k, B_k, C_k and D_k as the $ABCD$ matrix elements of the kth TL segment, the $ABCD$ matrix of the entire multilayer dielectric structure is

$$\begin{bmatrix} A & B \\ C & D \end{bmatrix} = \prod_{k=1}^{N} \begin{bmatrix} A_k & B_k \\ C_k & D_k \end{bmatrix} \tag{5.5}$$

where A, B, C and D are the elements of the $ABCD$ matrix of the entire cascaded multilayer dielectric and FSS structure. The $ABCD$ matrix of the kth TL segment is obtained as below

$$\begin{bmatrix} A_k & B_k \\ C_k & D_k \end{bmatrix} = \begin{bmatrix} \cos(\beta_k d_k) & jR_{ck}\sin(\beta_k d_k) \\ j\sin(\beta_k d_k)/R_{ck} & \cos(\beta_k d_k) \end{bmatrix} \begin{bmatrix} 1 & 0 \\ Y_{B_k} & 1 \end{bmatrix} \tag{5.6}$$

Assuming A', B', C' and D' as the elements of the transmission line portion below the dashed line, voltage V_h and I_h can be obtained using two sets of linear equations, expressed as

$$\begin{bmatrix} V_s - I_N R_s \\ I_N \end{bmatrix} = \begin{bmatrix} A & B \\ C & D \end{bmatrix} \begin{bmatrix} I_0 Z_L \\ I_0 \end{bmatrix} \tag{5.7}$$

$$\begin{bmatrix} V_h \\ I_h \end{bmatrix} = \begin{bmatrix} A' & B' \\ C' & D' \end{bmatrix} \begin{bmatrix} I_0 Z_L \\ I_0 \end{bmatrix}, \tag{5.8}$$

By solving for I_0 in (5.7), and substituting it into (5.8), V_h and I_h can be found as

$$V_h = V_s \frac{A'Z_L + B'}{CZ_L R_s + DR_s + AZ_L + B} \tag{5.9}$$

$$I_h = V_s \frac{C'Z_L + D'}{CZ_L R_s + DR_s + AZ_L + B}. \tag{5.10}$$

One should note that in the case of multiple FSS superstrates, there exist coupling between different FSS layers, if the spacers between them are too short in terms of the corresponding wavelength. This coupling should also be taken into account or TEN model does not work effectively. In general, the evanescent modes introduced by non-specular reflection at the surface of one periodic structure should decay enough at the other periodic structure. Details can be found in [18, 63].

5.2 Calculation of the far-field properties

The calculation of the far-field properties such as radiation patterns and antenna directivity is the same as was presented in Section 4.2.

5.3 Radiation properties study through some examples

Cavity resonance antenna with FSS superstrate is shown in Figure 5.2(a). Its corresponding TEN model is shown in Figure 5.2(b). Different surfaces such as PMC and AMC are considered as the antenna ground plane. Far-field radiation patterns and directivities are obtained in the same manner as explained in section 4.2.

5.3.1 FSS design

Two different FSS unit cells are shown in Figure 5.3. The FSSs can be modeled by their equivalent admittances as shown in Figure 5.4, providing that their corresponding reflection coefficients are known. The reflection magnitude and phase of the FSSs depicted in Figure 5.3 are shown in Figure 5.5. As can be seen, the reflection coefficient magnitudes of both FSSs are very close to each other and close to unity at normal incidence. As discussed in [60], using the asymptotic ray-tracing formula, the higher the reflection coefficient magnitude

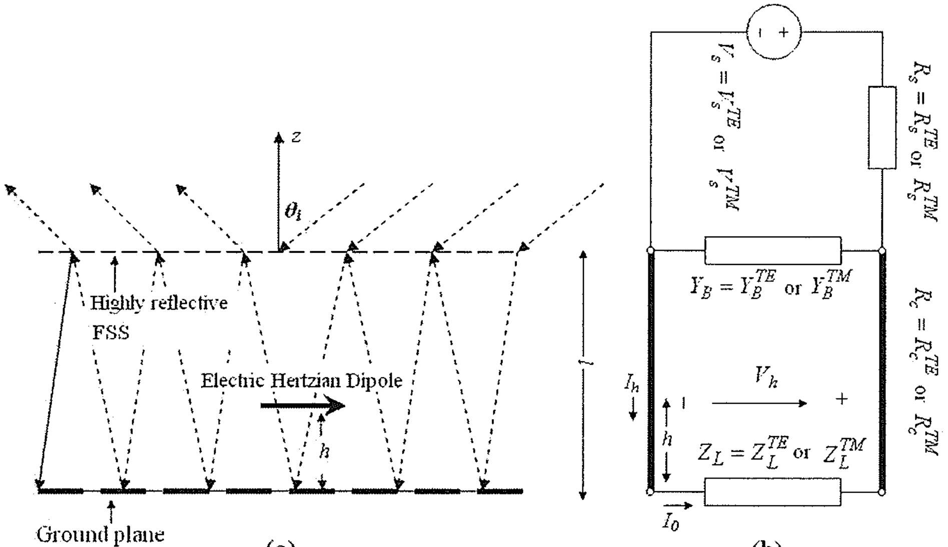
z
θ_i
Highly reflective FSS
Electric Hertzian Dipole
h
Ground plane
l
$V_s = V_s^{TE}$ or V_s^{TM}
$R_s = R_s^{TE}$ or R_s^{TM}
$Y_B = Y_B^{TE}$ or Y_B^{TM}
$R_c = R_c^{TE}$ or R_c^{TM}
I_h
V_h
h
$Z_L = Z_L^{TE}$ or Z_L^{TM}
I_0

(a) (b)

Figure 5.2: (a) A Hertzian dipole above surface impedance ground plane and beneath a free-standing FSS superstrate layer. (b) TEN model to calculate the horizontal electric field induced on the electric Hertzian dipole due to the plane wave incidence in the far-field region.

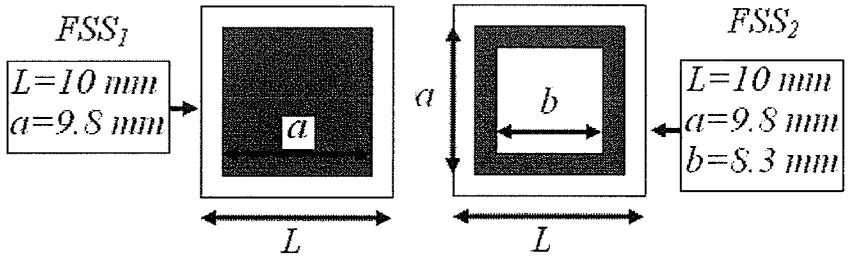
FSS_1
$L=10$ mm
$a=9.8$ mm
a
a
b
FSS_2
$L=10$ mm
$a=9.8$ mm
$b=8.3$ mm
L
L

Figure 5.3: Two different free-standing highly reflective FSS unit cells consisting of metallic patch (right-hand-side) and metallic ring (left-hand-side).

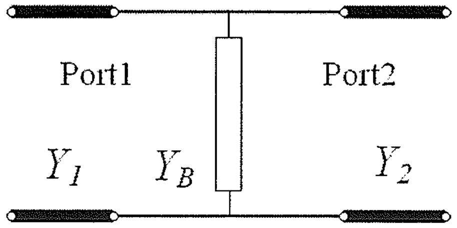
Port1
Port2
Y_1
Y_B
Y_2

Figure 5.4: Equivalent admittance of an FSS to be used in TEN model.

of an FSS is, the higher the directivity becomes. It is interesting to note that as the incident angle increases toward the grazing angle, the reflection coefficient magnitude increases toward unity for TE polarizations whereas it decreases for TM polarizations. However, the phase of these two FSSs are completely different. The phase of the FSS_1 (the FSS with metallic square patch unit cells) are mostly negative over the incident angle range. On the contrary, the phase of the FSS_1 (the FSS with metallic square ring unit cells) are always positive over the incident angle range.

As mentioned above, equivalent admittance (or susceptance in the lossless cases) of FSSs can be obtained using their reflection or transmission coefficients. An admittance Y_B with normalized impedance ports of Y_1 and Y_2 is shown in Figure 5.4. Pertaining scattering parameters are calculated as follows [64].

$$S_{11} = \frac{Y_1 - Y_B - Y_2}{Y_1 + Y_B + Y_2} \tag{5.11}$$

$$S_{22} = \frac{Y_2 - Y_B - Y_1}{Y_2 + Y_B + Y_1} \tag{5.12}$$

$$S_{12} = S_{21} = \frac{2\sqrt{Y_2 Y_1}}{Y_2 + Y_B + Y_1} \tag{5.13}$$

Assuming a free-standing FSS, FSS is embedded between two layers of air, one finds $Y_2 = Y_1 = Y_0$, where Y_0 is air characteristics admittance. Thus, equation 5.13 is simplified as

$$S_{11} = \frac{-Y_B}{2Y_0 + Y_B}. \tag{5.14}$$

Knowing the reflection coefficient (S_{11}) of a free-standing FSS, its corre-

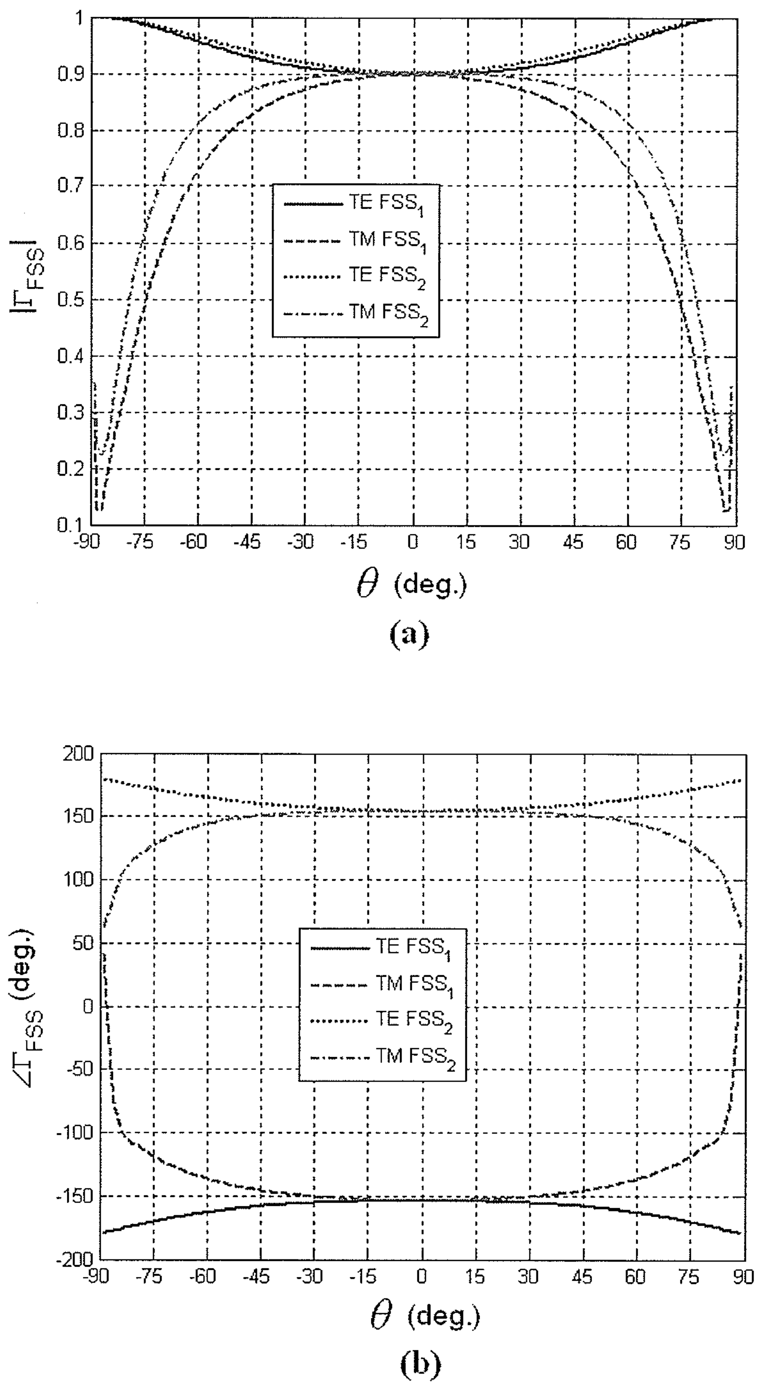

Figure 5.5: Reflection coefficients of the FSS structures shown in Figure 5.3, (a) magnitude and (b) phase. Operating frequency is 9.5 GHz.

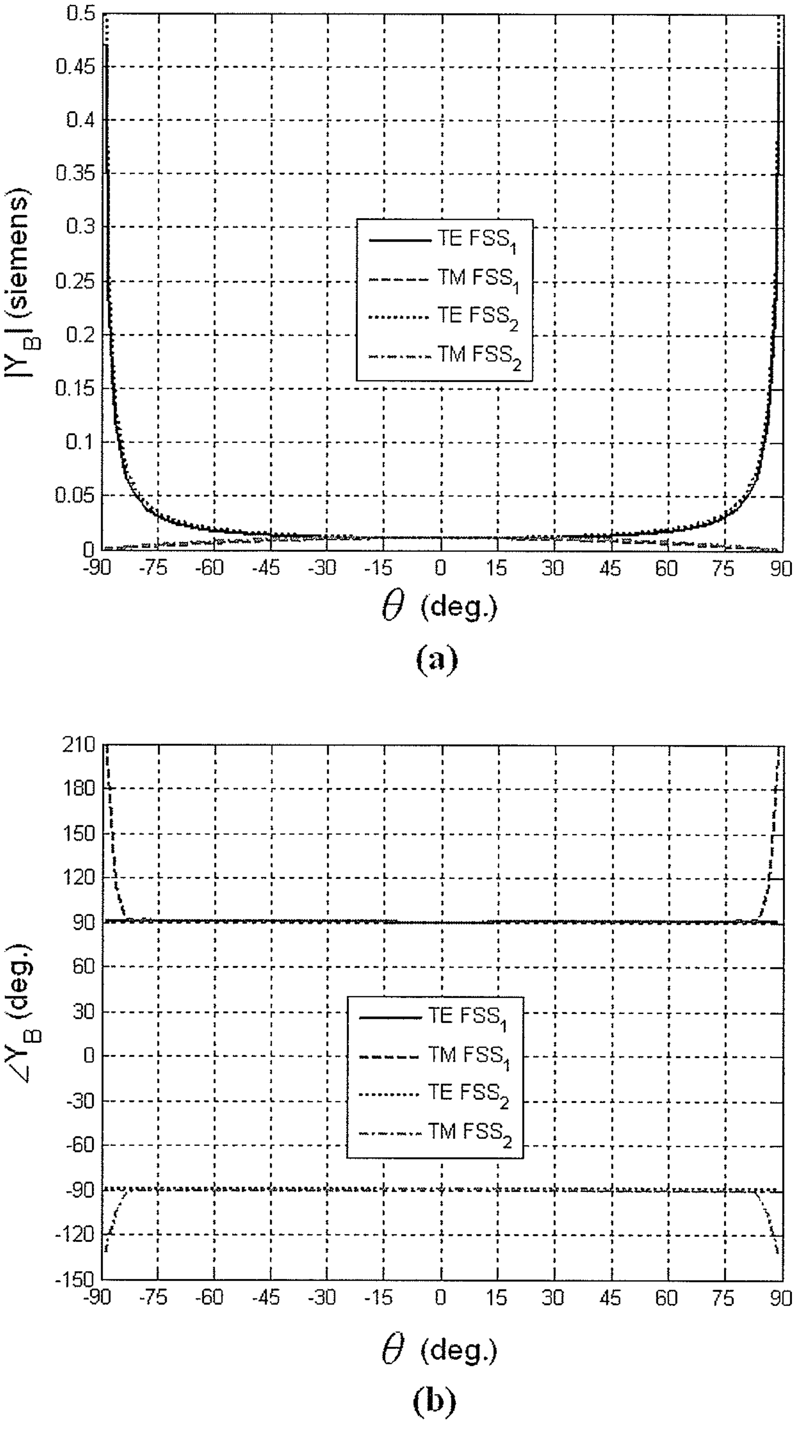

Figure 5.6: Equivalent admittance of the corresponding FSS structures shown in Figure 5.3, (a) magnitude and (b) phase. Operating frequency is 9.5 GHz.

sponding equivalent admittance is obtained as

$$Y_B = \frac{2S_{11}}{1+S_{11}} Y_0. \tag{5.15}$$

The corresponding admittance of the FSSs shown in Figure 5.3 are plotted in 5.6. The magnitude of the admittances are very close, whereas the phases are different. The FSS consisting of metallic patch shows capacitive behavior (admittance phase is 90°, whereas the FSS consisting of metallic rings shows inductive behavior (admittance phase is −90°), over the incident angles.

5.3.2 Cavity resonance antennas with PEC or PMC ground planes and FSS superstrate

A cavity resonance antenna, shown in Figure. 5.2, with either of these two superstrate and either PEC or PMC ground plane is considered. As it was considered before, corresponding impedance surface in TEN model is zero and infinity for PEC and PMC ground planes, respectively. Directivity versus air-gap height is shown in Figure 5.7 for all four combinations of FSSs and the ideal ground planes. Their corresponding radiation patterns are shown in Figure 5.8.

The pertaining values which optimize the antenna directivity for each case are addressed in Tables 5.1 and 5.2. As can be seen, higher directivities are obtained compared to the cases with high-permittivity dielectric superstrate studied in the previous chapter. It is because of the fact that reflectivity of these FSSs (about 0.9) are higher than those introduced by high-permittivity dielectrics ($|\frac{1-\sqrt{9.8}}{1+\sqrt{9.8}}| = 0.5158$). This shows that FSS superstrates offer higher gains in resonance cavity antenna design.

Another important point is that the maximum air-gap heights do not occur

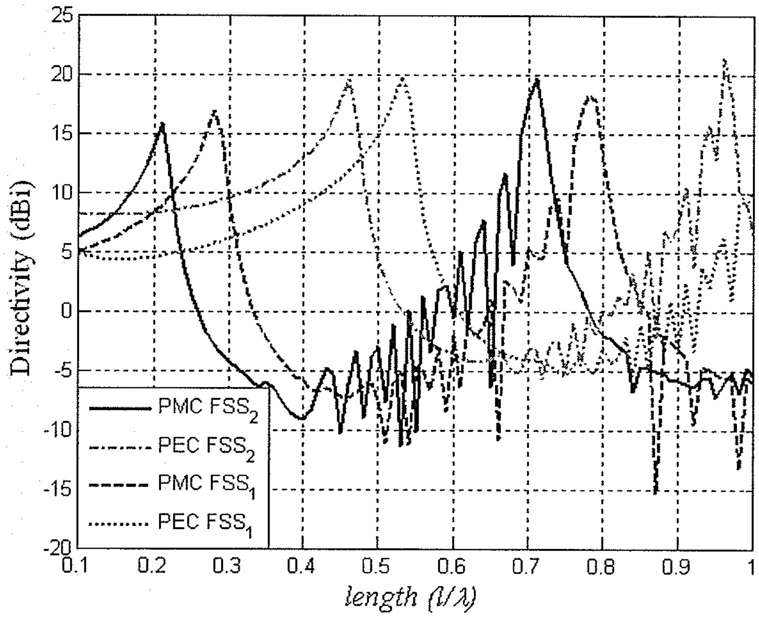

Figure 5.7: Directivity versus air-gap height of the antenna configuration shown in 5.2. Four different combinations of ideal ground planes (PEC and PMC) and FSS superstrates (FSS_1 and FSS_2), shown in Figure 5.3, are considered.

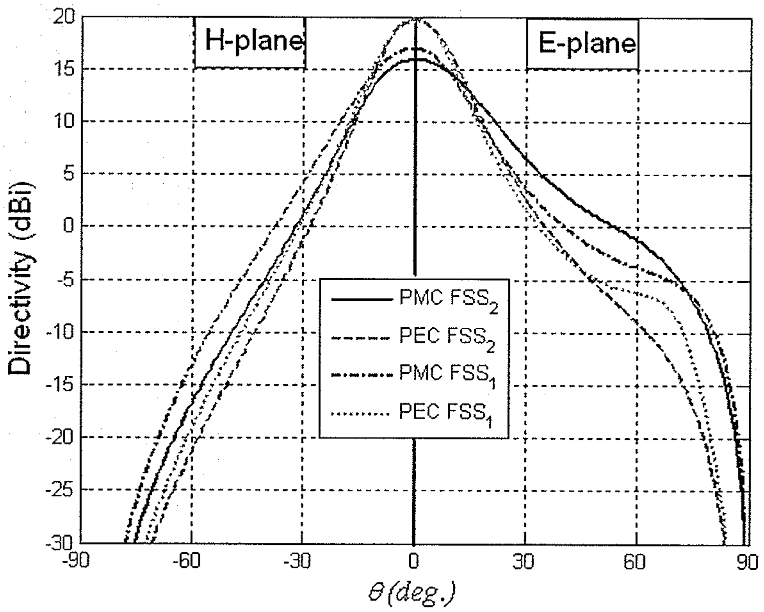

Figure 5.8: E- and H-plane co-polar radiation patterns versus zenith angle of the antenna configuration shown in 5.2. Four different combinations of ideal ground planes (PEC and PMC) and FSS superstrates (FSS_1 and FSS_2), shown in Figure 5.3, are considered.

in the vicinity of $0.25\lambda_0$ or $0.5\lambda_0$ for PMC or PEC ground planes, respectively. This is because of the effects of the reflection coefficient phase of the FSS superstrates. In the case of FSS_1 superstrate, maximum gain happens for air-gap of $l = 0.28\lambda_0$ and $l = 0.53\lambda_0$ for PMC and PEC ground planes, respectively. In the case of FSS_2 superstrate, the maximum gain happens for air-gap of $l = 0.21\lambda_0$ and $l = 0.46\lambda_0$ for PMC and PEC ground planes, respectively.

This fact can be further investigated using the ray optic method introduced in [60]. When the reflection phase of the FSS superstrate is $\Phi_\Gamma(\theta, f)$ and reflection phase of the artificial ground plane is $\Psi_\Gamma(\theta, f)$ the resonance condition presented in [12] is modified as follows [6]

$$-\frac{4\pi}{\lambda} l \cos(\theta) + \Psi_\Gamma(\theta, f) + \Phi_\Gamma(\theta, f) = 2N\pi. \tag{5.16}$$

where $N = 0, 1, 2, \cdots$. According to equation 5.16 the air-gap resonance length at boresight ($\theta = 0$) is obtained as

$$l = (\Psi_\Gamma(0, f) + \Phi_\Gamma(0, f))\frac{\lambda_0}{4\pi} + N\frac{\lambda_0}{2} \tag{5.17}$$

In accordance with Figure 5.7 and Tables 5.1 and 5.2, four different resonance lengths are calculated for four different cases as follows.

- Case1: Antenna with FSS_1 superstrate and PMC ground plane

  $l = (\pi\frac{-153.83}{180} + 0)\frac{\lambda_0}{4\pi} + \frac{\lambda_0}{2} = 0.2863\lambda_0$

- Case2: Antenna with FSS_1 superstrate and PEC ground plane

  $l = (\pi\frac{-153.83}{180} + \pi)\frac{\lambda_0}{4\pi} + \frac{\lambda_0}{2} = 0.5363\lambda_0$

- Case3: Antenna with FSS_2 superstrate and PMC ground plane

  $l = (\pi\frac{154.29}{180} + 0)\frac{\lambda_0}{4\pi} = 0.2143\lambda_0$

- Case4: Antenna with FSS_2 superstrate and PEC ground plane

  $l = (\pi\frac{154.29}{180} + \pi)\frac{\lambda_0}{4\pi} = 0.4643\lambda_0$

As can be observed, these resonance lengths obtained using ray optic method are in very good agreement with those obtained using TEN model and shown in Tables 5.1 and 5.2 .

5.3.3 Cavity resonance antennas with AMC ground planes and FSS superstrate

A cavity resonance antenna, shown in Figure. 5.2, with either of these two superstrate and AMC ground plane is considered. Three different AMCs unit cells are the ones shown in Figure 4.10. Antenna directivities versus air-gap height are shown in Figure 5.9 for the combination of FSS_1 and three different above-mentioned AMCs. The first resonance occurs at $0.28\lambda_0$ as listed in Table 5.1. As well the antenna directivity reaches to about 20 dBi for the antennas with AMC_1 and AMC_2 ground planes. The corresponding radiation patterns are shown in Figure 5.10. Interestingly, the radiation patterns of antennas with AMC_1 and AMC_2 ground planes are very close. However, the antenna with AMC_3 ground plane does not produce the maximum directivity at boresight ($\theta = 0$). This can be attributed to the difference in reflection phases of these three AMCs and explained in the same manner as discussed in Chapter 4. For brevity it is not included here. In the same manner antenna directivities versus air-gap height are shown in Figure 5.11 for the combination of FSS_2 and three different above-mentioned AMCs. Their corresponding radiation patterns are shown in Figure 5.12. The first resonance occurs at $0.21\lambda_0$ as listed in Table 5.2. As before, the antenna directivity reaches to the level of about 20 dBi for the cases with AMC_1 and AMC_2 ground planes. It is interesting that

Table 5.1: Resonance air-gap length and their corresponding maximum directivities with different ground plane types and FSS_1 superstrate shown in Figure 5.3.

Ground plane type	Air-gap height (l/λ_0)	Directivity (dBi)
PMC	0.28	16.94
PEC	0.53	19.75
AMC_1	0.28	19.63
AMC_2	0.28	19.81
AMC_3	0.28	12.28

Table 5.2: Resonance air-gap length and their corresponding maximum directivities with different ground plane types and FSS_2 superstrate shown in Figure 5.3.

Ground plane type	Air-gap height (l/λ_0)	Directivity (dBi)
PMC	0.21	15.88
PEC	0.46	19.75
AMC_1	0.21	19.50
AMC_2	0.21	19.78
AMC_3	0.21	14.32

using appropriate AMC ground planes the directivity enhancement can be performed as well as the air-gap height reduction. The antenna directivities of the amount of PEC ground plane can be achieved, yet the air-gap heights are at the level of those offered by the antenna with PMC ground plane.

5.3.4 Dual-band highly-reflective FSS design

Two different FSS unit cells are shown in Figure 5.13. Both of them consist of two concentric square rings, i.e., they have the same shapes but their dimensions are slightly different as shown in Figure 5.13. In fact, FSS_4 is a detuned version of FSS_3 to show less reflections.

Reflection coefficients of both FSS_3 and FSS_4 versus frequency are shown in Figure 5.14 for the normal incidence. As can be seen, the FSS_3 demonstrates the highest reflectivity at frequencies of 9.50 GHz and 19.0 GHz. These two frequencies are indeed the resonant frequencies of the FSS_3, since the reflection phase changes abruptly from $-180°$ to $+180°$ at these frequencies.

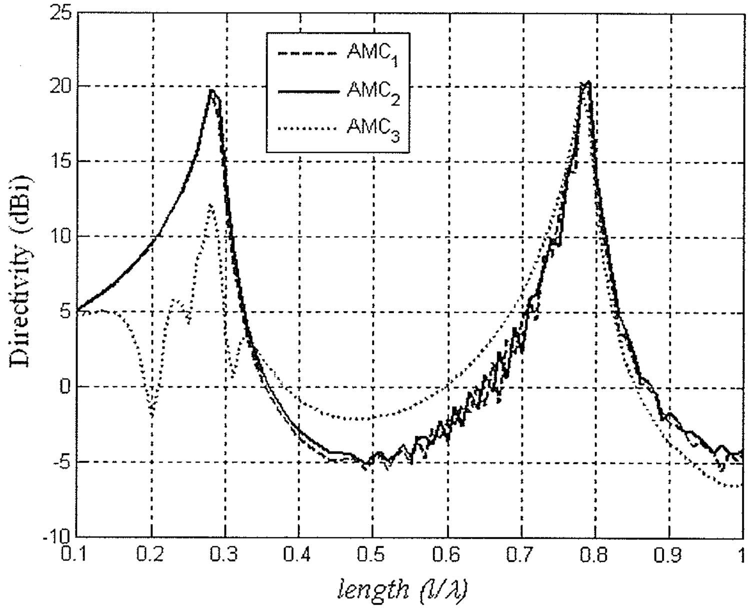

Figure 5.9: Directivity versus air-gap length of the cavity resonance antenna configurations shown in 5.2. Three different combinations of AMC ground planes, shown in Figure 4.10, and FSS_1 superstrate, shown in Figure 5.3, are considered.

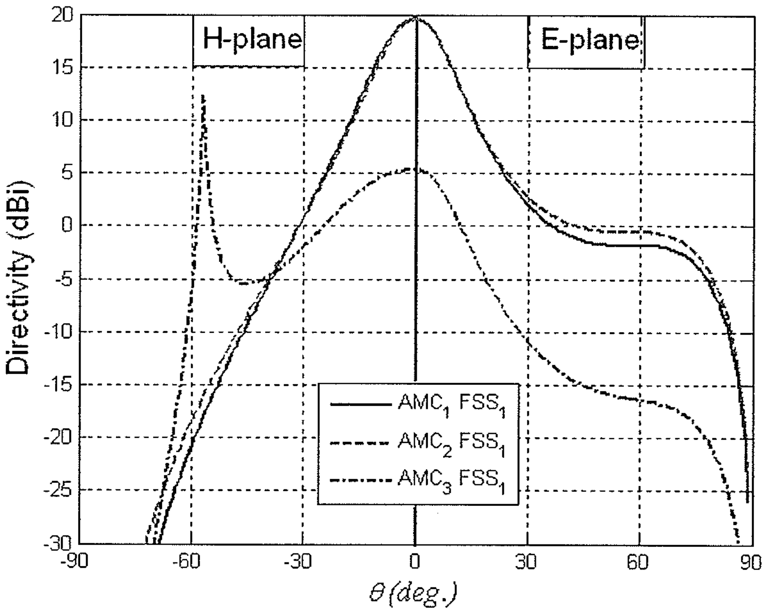

Figure 5.10: Radiation patterns of the cavity resonance antenna configurations shown in 5.2. Three different combinations of AMC ground planes, shown in Figure 4.10, and FSS_1 superstrate, shown in Figure 5.3, are considered.

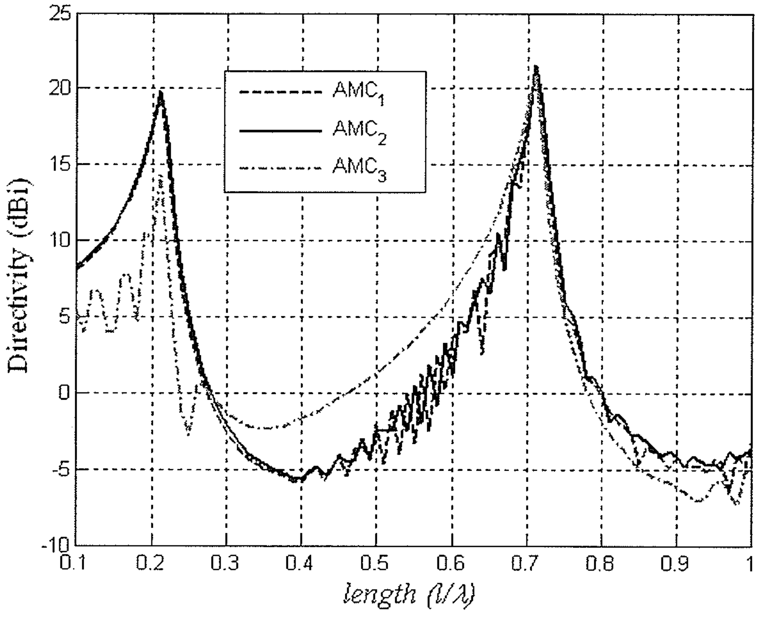

Figure 5.11: Directivity versus air-gap length of the cavity resonance antenna configurations shown in 5.2. Three different combinations of AMC ground planes, shown in Figure 4.10, and FSS_2 superstrate, shown in Figure 5.3, are considered.

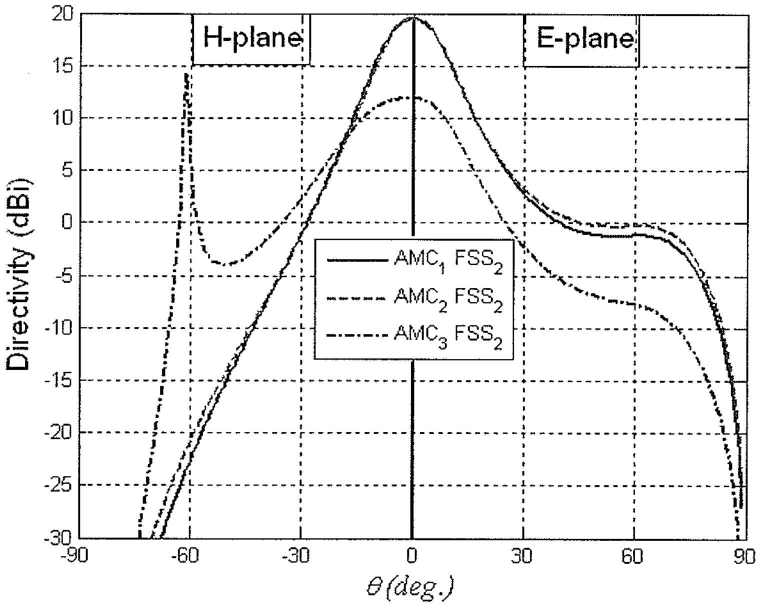

Figure 5.12: Radiation patterns of the cavity resonance antenna configurations shown in 5.2. Three different combinations of AMC ground planes, shown in Figure 4.10, and FSS_2 superstrate, shown in Figure 5.3, are considered.

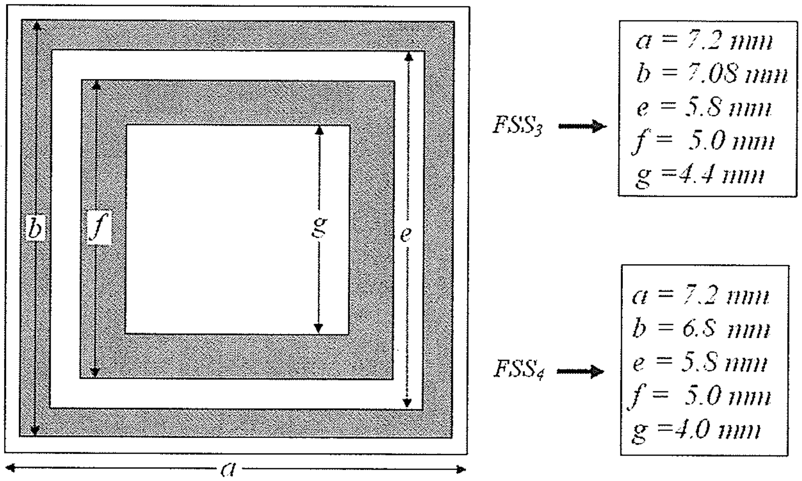

Figure 5.13: Unit cell of a double-band free-standing FSS. Two sets of dimensions are shown for two different design namely FSS_3 and FSS_4.

The FSS_4 is slightly detuned to show slightly less reflectivity than FSS_3. At normal incidence, it shows the reflectivity of 0.95 which is still considered as high reflectivity.

Reflection coefficient magnitude of both FSS_3 and FSS_4 versus incident angle are shown in Figure 5.15(a) and (b) for frequencies of 9.50 and 19.0 GHz, respectively. Reflection coefficient phase of both FSS_3 and FSS_4 versus incident angle are shown in Figure 5.16(a) and (b) for frequencies of 9.50 and 19.0 GHz, respectively.

5.3.5 Cavity resonance antennas with AEC/AMC ground planes and FSS superstrate

The cavity resonance antenna shown in Figure 5.2 is considered when either FSS_3 or FSS_4 (Figure 5.13) is employed as the superstrate and the AEC/AMC artificial surface characterized in the previous chapter is used as the ground plane. The antenna directivities versus the air-gap height are shown in Figure 5.17 of each configuration, and compared against the cases where the

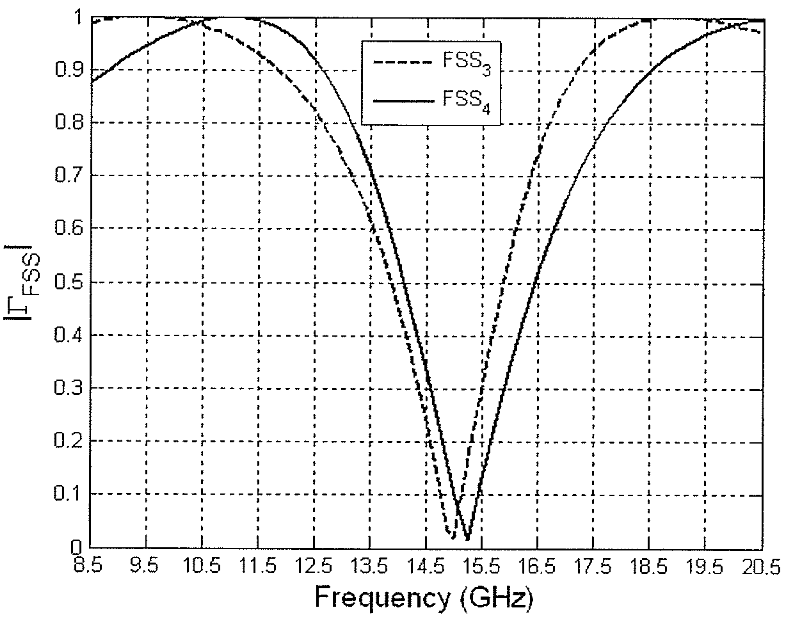

(a)

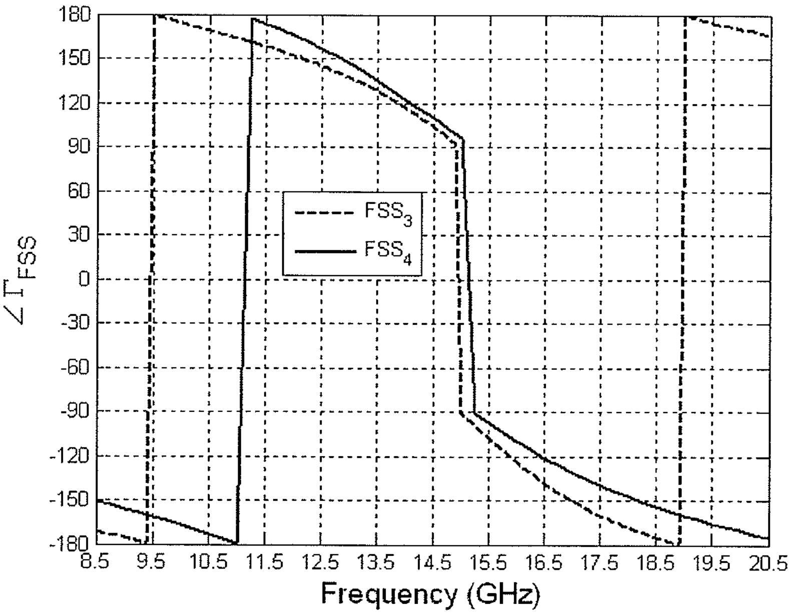

(b)

Figure 5.14: Reflection coefficient of the FSS_3 and FSS_4 versus frequency subject to the normal incident. Dimensions of the corresponding FSSs are shown in Figure 5.13. (a) magnitude and (b) phase.

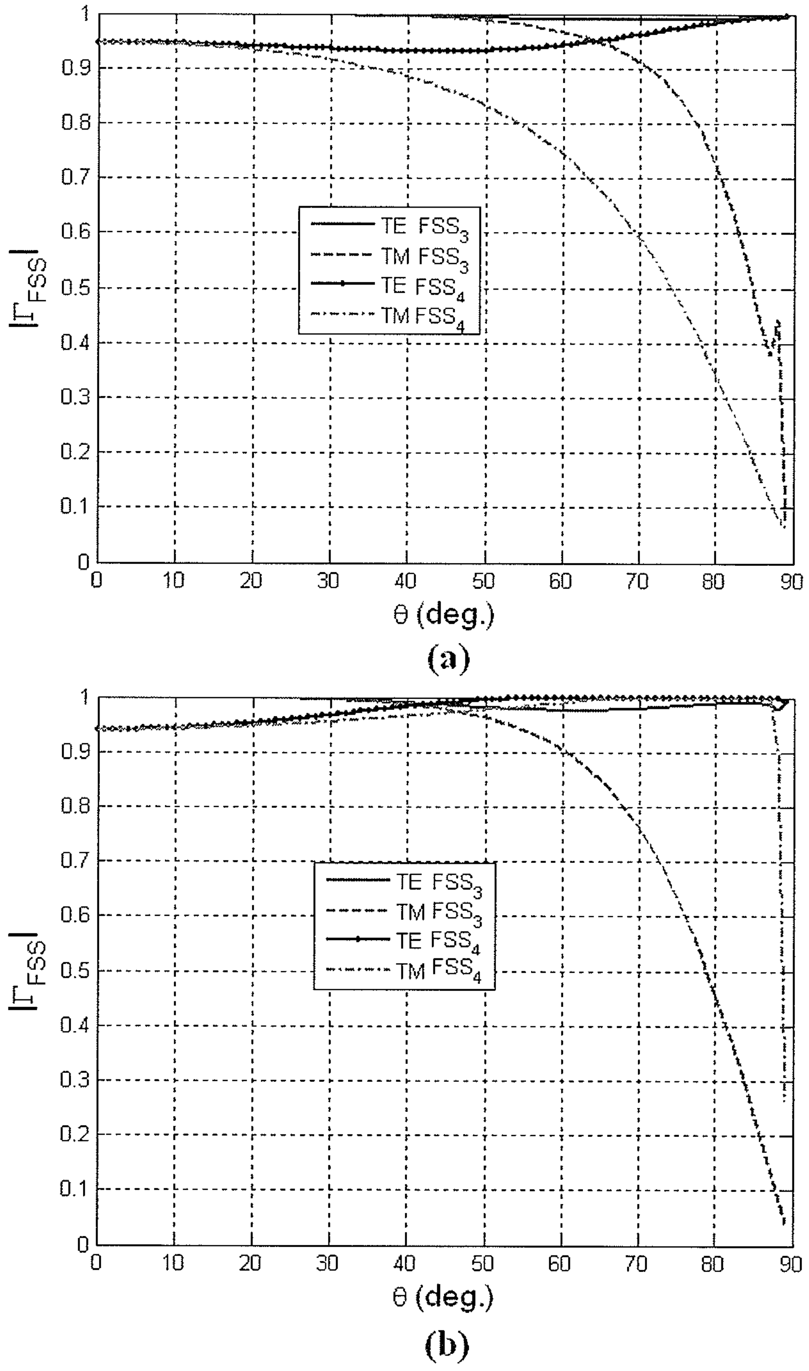

Figure 5.15: Reflection coefficient magnitude versus incident angle of FSS_3 and FSS_4 shown in Figure 5.13 at (a) 9.5 GHz and (b) 19.0 GHz.

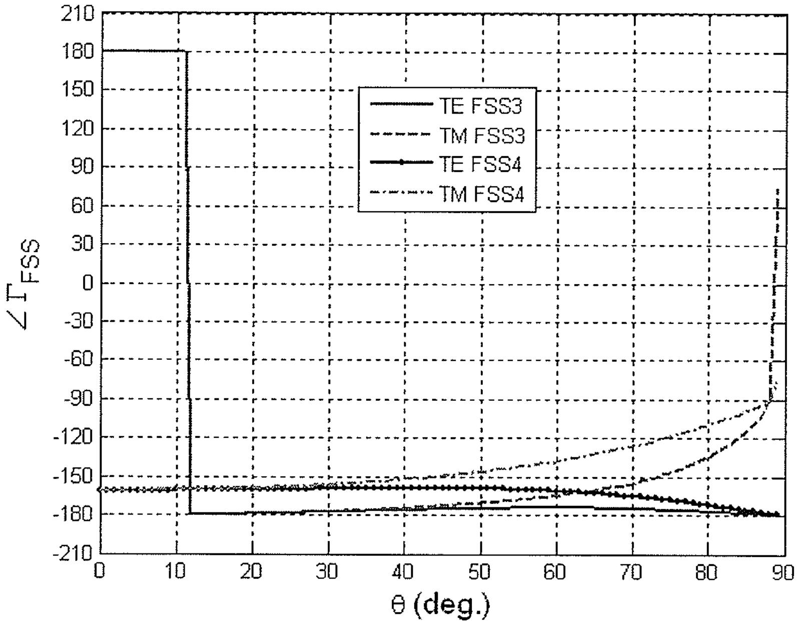

(a)

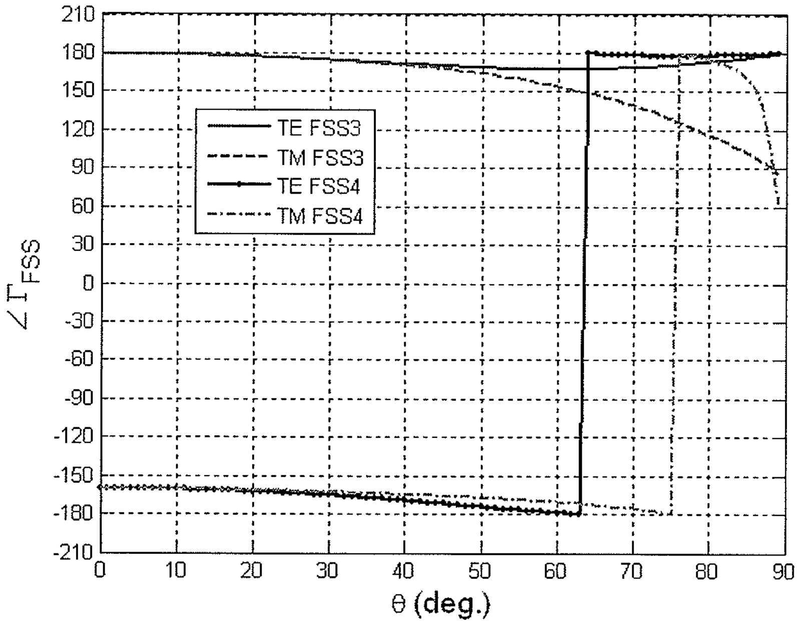

(b)

Figure 5.16: Reflection coefficient phase versus incident angle of FSS_3 and FSS_4 shown in Figure 5.13 at (a) 9.5 GHz and (b) 19.0 GHz.

ground plane is ideal PEC or PMC surfaces. The TEN model has been used to analyze their far-field properties. The corresponding graphs shown in Figures 5.17(a) and (b), are for the antennas having FSS_3 and FSS_4 superstrate, respectively.

The resonance directivities and their corresponding air-gap height are listed in Tables 5.3 and 5.3, for the antennas using FSS_3 and FSS_4 superstrate, respectively. A comparison between these results reveals that the one using FSS_3 superstrate gives more directivity. This is consistent with the theory presented in [60, 34], which states that the higher reflective superstrate provides higher directivity. On the other hand, the resonance directivity is less sensitive to the air-gap height when the reflectivity of the FSS superstrate is less. In another interpretation, the directivity bandwidth of the cavity resonance antenna with lower-reflective FSS is wider, although its peak directivity is lower.

Radiation patterns of the aforementioned antennas are shown in Figure 5.18. As can be seen, the main beam in the antennas having FSS_3 superstrate is narrower than the ones having FSS_4 superstrate. This indicates the higher directivity is achieved with higher reflective superstrates. Another interesting feature is using AMC surfaces instead of conventional PEC ones as the ground plane in cavity resonance antenna in order to reduce the air-gap height by two times (almost $\lambda/4$ instead of $\lambda/2$) which results in a compact antenna design. This phenomenon has been proposed and studied in [6]. Fabricated results have also been provided in [6, 65]. However, in this work, the beneficial impact of angular dependence of the AMC on directivity enhancement (Figure 5.18(b) and Table 5.4), over ideal PMC ground plane is shown which is not addressed in the literature. The reflection coefficient of an AMC is 0° at the normal incidence and may be different for other incident angles, whereas that

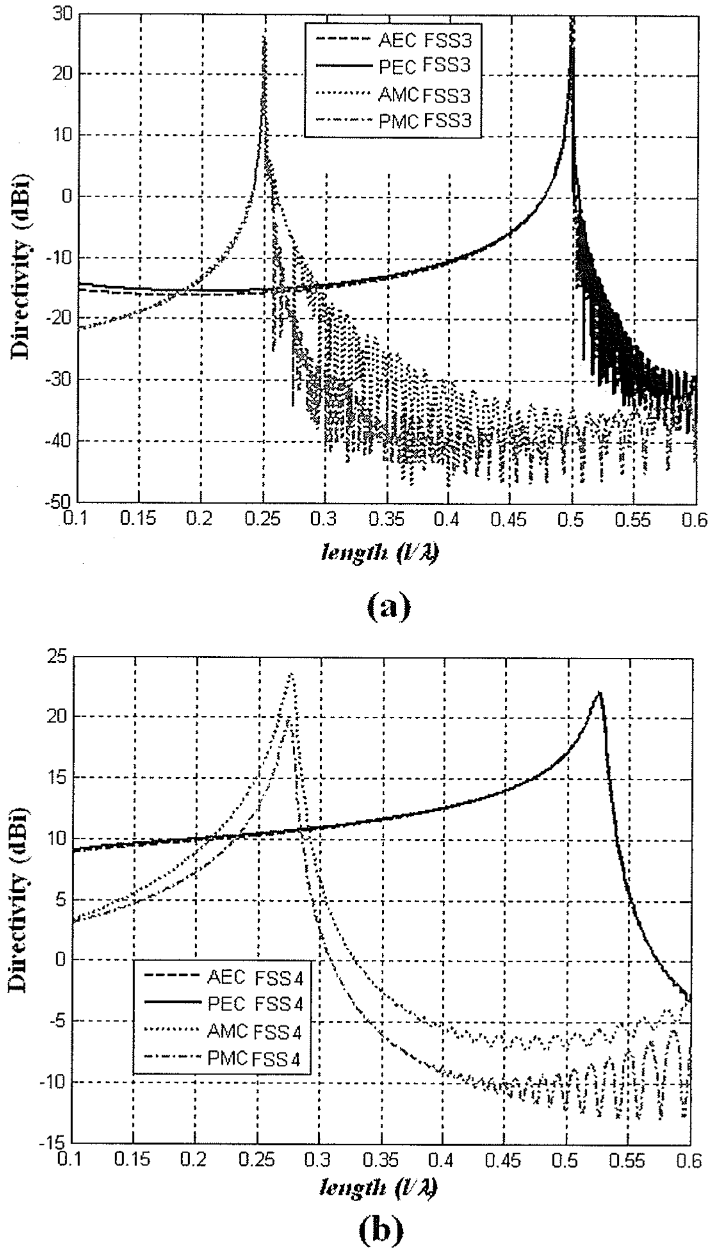

Figure 5.17: Directivity versus air-gap length of the cavity resonance antenna configurations shown in 5.2. Four different combinations of ground planes AEC, AMC, PEC and PMC are considered. Artificial ground planes are shown in Figure 4.20 with the dimensions of d_x= 6 mm, l_x= 5.54 mm, and t= 1.6 mm. The relative permittivity of the dielectric is 2.5. Operating frequency for AMC and AEC are 9.5 and 19.0 GHz. The air-gap incremental length in each step is 0.001λ. (a) FSS_3 and (b) FSS_4 superstrates (shown in Figure 5.3) are used for all cases.

Table 5.3: Resonance air-gap length and their corresponding maximum directivities of the cavity resonance antennas with different ground plane types and FSS_3 superstrate shown in Figure 5.13. Corresponding details are given in Figure 5.17

Ground plane type	Air-gap height (l/λ_0)	Directivity (dBi)
AEC	0.4980	29.617
PEC	0.4980	24.451
AMC	0.2500	25.822
PMC	0.2490	26.425

Table 5.4: Resonance air-gap length and their corresponding maximum directivities of the cavity resonance antennas with different ground plane types and FSS_4 superstrate shown in Figure 5.13. Corresponding details are given in Figure 5.17

Ground plane type	Air-gap height (l/λ_0)	Directivity (dBi)
AEC	0.52	21.62
PEC	0.52	21.50
AMC	0.25	19.13
PMC	0.25	16.52

of the PMC is 0° for all incident angles. In fact, according to the physical description of the phenomenon based on ray tracing by [6, 60], the directivity is highly dependent on the reflection phase of the FSS superstrate as well as the ground plane. However, the angular and polarization dependence has not been considered in their analyses. The key point in this work is that the angular and polarization dependencies of the reflection phases are very important in achieving and controlling the high directivity. Whereas, the resonant length is mainly determined by the reflection phases of the FSS superstrate and the ground plane at normal incidence (Figure 5.17(b) and Table 5.4).

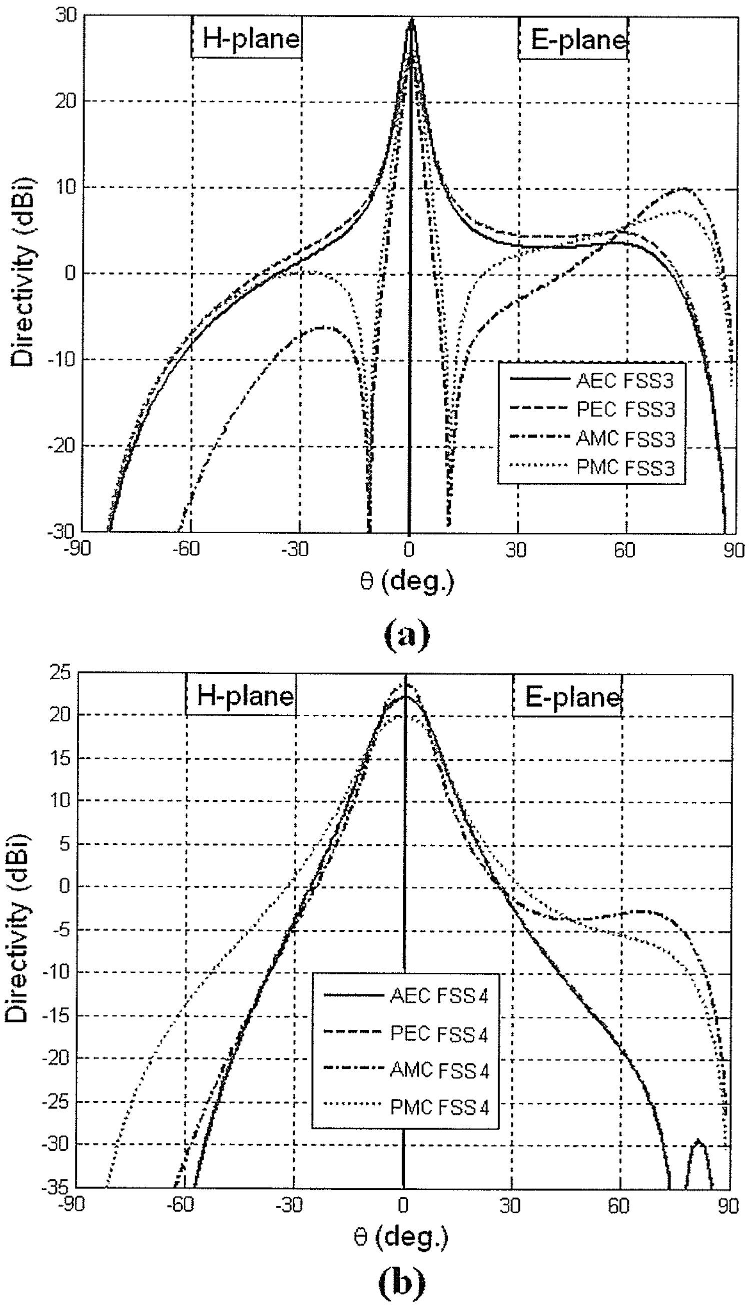

Figure 5.18: E- and H-plane co-polar radiation patterns of the cavity resonance antennas with FSS_3 superstrate layer and different ground planes. Corresponding information is addressed in Table 5.3 and Figure 5.17. Operating frequency is 9.5 GHz for AMC or PMC cases and 19.0 GHz for AEC or PEC cases.

5.4 Conclusions

In this chapter, cavity resonance antennas with FSS superstrate and different ground planes were investigated. To do so, the transverse equivalent network (TEN) model for this class of antennas was introduced first. It can be seen that using highly-reflective FSS superstrate is more versatile than high permittivity dielectric introduced in the previous chapter from the design point of view. Also, higher directivity can be archived controlling the metallization of the FSS unit cell.

The radiation properties of several antennas of this type were studied. First, highly-reflective FSS superstrate design and analysis were considered. Then, the cavity resonance antennas with the designed FSS superstrate and the PEC ground planes were investigated as the conventional case. Next, the same antennas were studied when their ground planes were replaced PMC surfaces. It was shown that the antennas having PMC ground plane have lower profiles than their counterparts having PEC ground plane. However, the directivities of the former cases were less than the latter ones almost 3 to 4 dB.

Designed AMCs in the previous chapter were employed as the ground plane of the resonance cavity antennas with the FSS superstrate, in this chapter. Similar to the observation in the previous chapter, for two types of AMCs, the antenna height was reduced by a factor of two, while showing as high directivity as their counterparts having PEC ground planes. Fabricated results, reported in other works, also verify this theory [6, 65]. For the other case, the high directivity was not achieved. It was shown that this is due to the reflection phase response of the ground plane versus incident angles.

Although reducing the antenna profile by half (using AMc) was proposed in [6], the comparison between PMC and AMC ground planes has not be addressed previously. By this comparison, impact of the angular- and polarization-dependent AMC ground plane on far-field radiation properties was illustrated to be the main contribution of this work.

Finally, dual-band FSS superstrates were designed to be used along with the AEC/AMC ground planes in order to work in a dual-band high-gain dual orthogonally-polarized antenna configuration. Using this new ground plane, the profile of the antenna is reduced to half in the AMC mode. This new design has the advantage of reduced size over those presented in [54, 66]. Also, it has the advantage of a single-layer double-band FSS design over two-layer double-band FSS design in [66].

Chapter 6

Summary and Directions for Future Work

Artificial magnetic conductors were introduced, designed, characterized and extensively investigated in chapter 2. Using circuit and transmission line models, the concept of artificial magnetic conductor was illustrated. This is an important contribution that helps the reader in better understanding the high impedance surface phenomenon. Its implementation was also studied based on the conventional FSS structures backed by a ground plane. A parametric study was performed, through extensive simulations, to investigate the effects of various parameters such as dielectric thickness, permittivity and loss, metallic patch and unit cell sizes, etc., on reflection characteristics of the AMCs. The observations, and contributions provide guidelines in designing AMC structures.

In chapter 3, artificial ground planes consisting of infinitely periodic metallic gratings backed by a grounded dielectric slab were introduced. This artificial ground plane can function in two different modes, namely artificial magnetic conductor (AMC) and artificial electric conductor (AEC), at different frequencies and for different polarizations. Three different methods were implemented to analyze this structure. Two methods were based on modal expansion, one using point-matching method and the other entire-domain surface current basis functions. Using only electric surface currents rather than conventional magnetic surface current for E-polarized was the contribution of this part. As well, a code based on the method of moments was developed to characterize this kind of structure. The above-mentioned numerical methods were employed to design dual-mode artificial surfaces.

In Chapter 4, the transverse equivalent network (TEN) model was extended to the cavity resonance antennas with artificial ground plane and multilayer dielectric superstrate to analyze such antennas. This investigation resulted in the low-profile high-gain antenna design. Using the TEN model analysis circumvents the computational complexity of the full wave analysis of such antennas. Yet, far-field antenna properties can be predicted with good accuracy. However, the most important contribution in this chapter, and actually in this thesis, is to vividly illustrate the importance of the effects of the angular and polarization dependency of the artificial ground planes in the antenna performance. Using TEN model, the medium parameters and artificial ground plane impedance surfaces are interpreted as the transmission lines and load impedances, respectively. All of these parameters are both polarization and angular dependent. This dependency can be clearly observed in the transmission line formulations provided in Chapter 4. In this manner, the TEN model gives an excellent insight which cannot be found in the full-wave analysis model. As well, to the knowledge of this author, none of the available software packages can simulate infinite impedance surfaces in the presence of the excitation source to date. Nor any of them can simulate infinite PMC plane. With the simple formulations of TEN, one can get adequate insights into the understanding of the physics behind the phenomenon and the importance of the surface impedance characteristics as well as enough information to be able to estimate the far-field properties of a cavity resonance antenna. The accuracy of the estimation was checked through few examples. As was shown in Chapter 4, angular and polarization dependency of the reflection coefficient phase of the surface impedances contribute a lot to ultimate performance of the antennas.

Cavity resonance antenna with highly-reflective FSS superstrate artificial ground plane was discussed in Chapter 5. As before, the TEN model was extended to such cavity resonance antennas. A dual-band FSS was designed and used as the superstrate of a dual-band orthogonally-polarized compact high-gain antenna. It is worthwhile to emphasize again that the major contribution of this chapter is to show the impact of the angular and polarization dependency of the surface impedance of the ground plane and reflection coefficient of the FSS superstrate layer in the the performance of the designed antenna.

One of the main contributions in this thesis is to illustrate the effect of the reflection phase properties of the AMCs versus incident angles through plenty of design examples. In both Chapters 4 and 5, it was shown that demonstrating reflection phase of zero degree at normal incidence is not sufficient for the AMC to perform properly. Another important contribution was the effect of polarization dependency. Radiation patterns in E- and H-planes are proportional to the induced V_{TM} and V_{TE} voltages on the electric Hertzian dipole. Hence, polarization dependence of the ground plane play an important role to shape the radiation patterns. To the knowledge of author, these issues have not been previously addressed in the literature. It was the TEN model simulations that facilitated the insight to observe these phenomena.

The term AEC was used for the first time for the surfaces with reflection coefficient close to 180° and magnitude of unity in this work. This is a counterpart of AMC (surface close to AMC) already used in the literature. An artificial surface consisting of conducting grating backed by a grounded slab was studied based on its reflection coefficient phase. It was shown that this surface can act in two different modes depending on the polarization of the applied field. Then, this surface was employed as the ground plane of the cavity resonance antennas to design a compact dual-band dual orthogonally-polarized antenna. This design has novelty over those presented in [54, 66] in terms of compactness and functionality of the ground plane. Also, a highly-reflective dual-band FSS was designed in a single layer to be used as the superstrate. It is an advantage for the FSS to be designed in a single layer rather than two layers as presented in [66].

The main technique that was used to extract the properties of the antenna in the far-field was the TEN. The description of the TEN model can be learned collectively from [46, 12] and for the sake of brevity was not brought in this thesis. This method was first introduced by Jackson and Alexopoulos [12] for the superstrate-substrate structures. As clearly stated in [12], this method circumvents the complexity of tedious calculation of Green's function method done by the same researchers in [11] without loss of any information, and retrieving the same results. This method later was used by Yang and Alexopoulos for multilayer structures [45]. The TEN model was extended for the structures with partially reflective surfaces (PRSs) superstrates by Zhao et al. in [34, 61, 62]. The validity of the model has been checked in the literature. The results obtained using TEN model has been compared with MoM-CAD software package (IE3D) in [46], with another MoM-CAD software package (Ansoft Designer) in [54] and with FEM-CAD software package (Ansoft HFSS) in [67], and in all cases good agreements have been achieved. As well, the TEN results have been compared with those obtained by an in-house MoM in [34, 61, 62] and leaky wave analysis in [47], and in all cases good agreements have been achieved. However, to the knowledge of this author, the TEN has some shortcomings that are summarized as follows.

1) It can only predict far-field properties of the antenna such as directivity and far-field radiation patterns [46].

2) Unlike the full-wave analyzers, it cannot give any information of the input impedance of the antenna [46].

3) When it is used in the presence of the periodic structure such as FSS or AMC, the periodicity, unit cell size and dimensions of the metallizations used in the unit cells must be small compared to the wavelength. Unit cell size of less than half-wavelength has been recommended in [34], which was used throughout this thesis for all cases. The smaller the unit cell size, the more accurate will be the TEN, since it considers the surface collectively as an integrated surface. The advantage of maintaining the periodicity to less than half wavelength is the transition of non-specular waves into evanescent waves. This also prevents grating lobes to be produced. Smaller size of the periodicity in both FSS and AMC reduces the coupling of the evanescent modes between these two, as well.

The application of AMC or other artificial ground planes in the cavity resonance antenna has been verified by showing the good agreement between simulation and measurement results in the literature [6, 65]. From [6, 65], one can understand that large number of unit cells will cause the alignment of the source to be insignificant in antenna performance. Both wire and microstrip patch antenna source verifies this assertion [6, 65].

Considering the previous statements, the following future work is proposed.

6.1 Future work regarding chapter 2

Many different metallizations can be used to produce AMCs, depending on the applications. These surfaces can be designed using method of moment in conjunction with an appropriate optimization method such as genetic algorithm similar to the one introduced in [31].

In-house MoM can be developed to be able to analyze periodic structures consisting of both metallic patches and lumped elements simultaneously. This option does not exist in the available MoM-CAD software package (Ansoft Designer). Implementing such an option in an in-house code, one is able to extend the application of the artificial surfaces to frequency-agile or reconfigurable microwave structures and antennas.

6.2 Future work regarding chapter 3

Modal analysis with entire domain basis function expansions of currents was implemented to extract reflection properties of infinitely long metallic gratings backed by a grounded dielectric slab in two principle planes, namely $\phi = 0$ and $\phi = 180°$. This analysis method can be extended to any arbitrary incident angle and polarization. This can be a noticeable contribution over the one introduced in [38] in terms of using electric surface current in both perpendicular and parallel directions to the metallic strips.

Incorporating ohmic and dielectric losses in the MoM of modal expansion formulations and its impact on antenna performance are interesting tasks that can be done in the future.

6.3 Future work regarding chapter 4

Bandwidth analysis over a frequency range can be performed for the antennas introduced in chapter 5. This is an important study to characterize directivity-bandwidth of the cavity resonance antennas.

It would be very interesting if an AMC ground plane can be designed, through an optimization process to maximize an antenna property such as directivity. The procedure can be done as follows. At first, an optimization method is applied to the TEN model to find impedance Z_L which optimizes the desired parameter, e.g., directivity. Then, this surface can be synthesized using a MoM-CAD in conjunction with an optimization tool.

6.4 Future work regarding chapter 5

The same recommendations as the ones presented in the previous section can be applied for Chapter 5 as well.

6.5 Generalization of the theory

Generalization of the idea of using different reactive impedance surfaces for electromagnetic structures, such as high or low impedance surfaces discussed in this thesis, can be presented as follows.

Generally, the antenna performance is evaluated based on parameters such as radiation patterns, directivity, polarization and input impedance. For microwave components such as cavity resonator, resonance frequency and quality factor are important features. Wave number and characteristic impedance are two important parameters for transmission lines. These parameters are fundamentally related to the solutions of the Helmholtz equation satisfied for the pertaining boundary conditions of their corresponding medium. For example, radiation patterns are related to the far-field electric field components which are the solution of the wave equations in unbounded region. Field polarizations are obtained based on the direction of the electric fields. Resonant frequencies of a cavity resonator or wave number of a waveguide are related to the eigen-values of the Helmholtz equation in their corresponding bounded regions. Owing to this fact, one can select the proper boundary conditions to achieve the desirable solution for the wave equations rather than choosing different shapes of the microwave components or antennas or using different materials inside the region as performed in the conventional methods.

On the other hand, the boundary conditions in applied electromagnetics area are represented by surface impedances. Perfect electric conductor is the most well-known boundary condition in electromagnetics on which the tangential component of the electric field is zero. The surface impedance of the perfect electric conductor is zero. In fact, good conductors such as copper or silver can simulate this boundary condition very well in the practical applications.

Now, with the dawn of the new area of metamaterial surfaces, researchers are able to simulate high impedance surfaces using periodic structures as opposed to the low impedance surfaces found in nature. Artificial magnetic conductors can also be synthesized versus conventional electric conductors. Artificial surfaces can be polarization and angular dependent, i.e., they can have dyadic surface impedance. Employing these kinds of surfaces can significantly be beneficial in microwave component and antenna design. Design, synthesis and fabrication of such surfaces have been thoroughly investigated in this thesis. Their application in efficient high-gain planar antennas was vividly illustrated, as well. However, the impedance surfaces are not limited to the

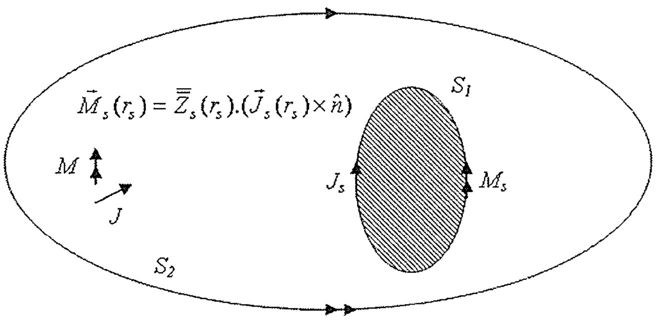
$\vec{M}_s(r_s) = \bar{\bar{Z}}_s(r_s).(\vec{J}_s(r_s)\times\hat{n})$
S_1
M
J
J_s
M_s
S_2

Figure 6.1: A typical schematic of a region and surface impedance boundary conditions relating electric and magnetic surface currents.

high or low impedance. For some applications, a reactive surface impedance, for some value in between of low and high impedances, may optimize the desirable parameter under study. These impedance surfaces can be frequency, angular and polarization dependent. In general for each frequency the surface impedance is a dyadic. This will include all other dependencies.

In summary, as mentioned above, solution of the Helmholtz equation in conjunction with the boundary conditions, determines the fields, modes, resonant frequencies, etc. of the region under study. A typical schematic of such a region is shown in Figure 6.1. As shown, the surface impedance relates the electric and magnetic surface currents on the boundary. Therefore, choosing appropriate impedance boundary conditions, one is able to vary the surface currents on the boundary, resulting in controlling of the radiation fields, existing modes or other electromagnetic properties of interest in the corresponding electromagnetic system.

Appendix A

Decomposition of the field expressions to TE and TM modes

According to [28], any field can be decomposed to a fixed direction in space. In this appendix the notation of [28] is used for TM and TE modes.

Assuming the magnetic vector is chosen as

$$\vec{A} = \hat{a_x}\psi_a \tag{A.1}$$

the corresponding TM to y (TM_y) field is given by

$$\begin{aligned}
E_x &= \frac{1}{\hat{y}}\frac{\partial^2 \psi_a}{\partial x \partial y} & H_x &= -\frac{\partial \psi_a}{\partial z} \\
E_y &= \frac{1}{\hat{y}}(\frac{\partial^2}{\partial y^2} + k^2)\psi_a & H_y &= 0 \\
E_z &= \frac{1}{\hat{y}}\frac{\partial^2 \psi_a}{\partial y \partial z} & H_z &= \frac{\partial \psi_a}{\partial x}
\end{aligned} \tag{A.2}$$

Assuming the magnetic vector is chosen as

$$\vec{F} = \hat{a}_x \psi_f \tag{A.3}$$

the corresponding TE to y (TE_y) field is given by

$$\begin{aligned} E_x &= \frac{\partial \psi_f}{\partial z} & H_x &= \frac{1}{\hat{z}} \frac{\partial^2 \psi_f}{\partial y \partial x} \\ E_y &= 0 & H_y &= \frac{1}{\hat{z}} \left(\frac{\partial^2}{\partial y^2} + k^2 \right) \psi_f \\ E_z &= -\frac{\partial \psi_f}{\partial x} & H_z &= \frac{1}{\hat{z}} \frac{\partial^2 \psi_f}{\partial y \partial z} \end{aligned} \tag{A.4}$$

where $\hat{y} = j\omega\epsilon$ and $\hat{z} = j\omega\mu$. Taking the spatial Fourier transform of equation A.2, the field expressions in spectral domain, for TM to y mode, are given by

$$\begin{aligned} \tilde{E}_x &= -\frac{1}{\hat{y}} k_x k_y \tilde{\psi}_a & \tilde{H}_x &= -j k_z \tilde{\psi}_a \\ \tilde{E}_y &= \frac{1}{\hat{y}} (k^2 - {k_y}^2) \tilde{\psi}_a & \tilde{H}_y &= 0 \\ \tilde{E}_z &= -\frac{1}{\hat{y}} k_y k_z \tilde{\psi}_a & \tilde{H}_z &= j k_x \tilde{\psi}_a \end{aligned} \tag{A.5}$$

where $\tilde{\psi}_a$ is the Fourier transform of ψ_a and k_x, k_y and k_z are propagation constants in x, y and z directions, respectively, and k is the wave number. Taking the spatial Fourier transform of equation A.4, the field expressions in spectral domain, for TE to y mode, are given by

$$\begin{aligned} \tilde{E}_x &= jk_z\tilde{\psi}_f & \tilde{H}_x &= \frac{1}{\hat{z}}k_yk_x\tilde{\psi}_f \\ \tilde{E}_y &= 0 & \tilde{H}_y &= \frac{1}{\hat{z}}(k^2 - {k_y}^2)\tilde{\psi}_f \\ \tilde{E}_z &= -jk_x\tilde{\psi}_f & \tilde{H}_z &= \frac{1}{\hat{z}}k_yk_z\tilde{\psi}_f \end{aligned} \tag{A.6}$$

where $\tilde{\psi}_f$ is the Fourier transform of ψ_f.

Given electric and magnetic fields in the y direction and using the abovementioned expressions, one can obtain the expressions for the fields in the x direction as follows.

$$\tilde{E}_x = -\frac{k_yk_x}{k^2 - {k_y}^2}\tilde{E}_y - \frac{\omega\mu k_z}{k^2 - {k_y}^2}\tilde{H}_y \tag{A.7}$$

$$\tilde{H}_x = \frac{\omega\epsilon k_z}{k^2 - {k_y}^2}\tilde{E}_y + \frac{k_xk_y}{k^2 - {k_y}^2}\tilde{H}_y \tag{A.8}$$

Appendix B

Method of Moment Analysis

In this section method of moment analysis of electromagnetic scattering by a periodic strip grating on a grounded dielectric slab, shown in Figure B.1, for arbitrary plane incident wave is presented. The extracted reflection properties using this method is employed to characterize impedance surface of this periodic structure for both TE^z and TM^z polarizations, and for various incident angles. The impedance surface is in turn used in TEN model of the cavity resonance antenna presented in the next section to extract its far-field radiation properties.

B.1 Expansion of Electric Strip Currents into Entire-Domain Basis Functions

The x-directed electric surface current density over the 0th strip of the periodic conducting strips array is expressed as

$$J_x(x, y) = e^{-jk_{x0}x} e^{-jk_y y} \sum_{p=0}^{N_x} a_p f_{x_p}(x), \quad \text{for} \quad |x| \leq d_x \tag{B.1}$$

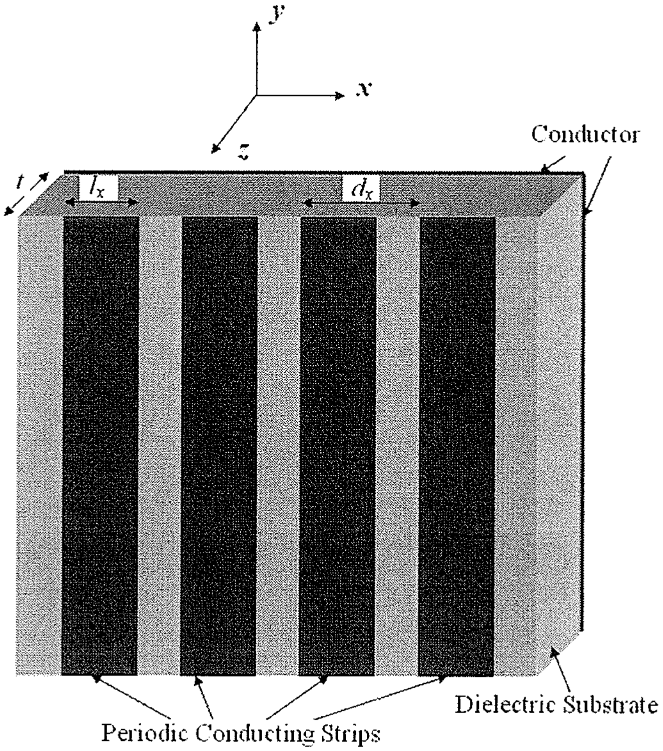
y
x
z
t
l_x
d_x
Conductor
Dielectric Substrate
Periodic Conducting Strips

Figure B.1: Periodic strip grating on a grounded dielectric slab.

$$J_y(x, y) = e^{-jk_{x0}x} e^{-jk_y y} \sum_{p=0}^{N_y} b_p f_{y_p}(x), \quad \text{for} \quad |x| \leq d_x \tag{B.2}$$

where phase variations along x and y are defined with respect to the origin. Due to the periodicity in the x direction and according to Floquet's theorem corresponding phase constant in the x direction can be represented into a discrete form as

$$k_{x_m} = k_0 \sin(\theta_0) \cos(\phi_0) + \frac{2\pi m}{d_x} \tag{B.3}$$

where θ_0 and ϕ_0 determines the direction of the incident wave. The phase propagation along the y direction is

$$k_y = k_0 \sin(\theta_0) \sin(\phi_0). \tag{B.4}$$

The surface current can be expanded into a product of a series of cosine functions and a function satisfying edge condition [40]. The proper basis functions are selected as the ones introduced in [38, 68], i.e.

$$f_{x_p}(x) = \sqrt{1 - (\frac{2x}{l_x})^2} (j)^p \cos(\frac{p\pi}{l_x}(x + \frac{l_x}{2})), \tag{B.5}$$

$$f_{y_p}(x) = \left[\sqrt{1 - (\frac{2x}{l_x})^2}\right]^{-1} (j)^p \cos(\frac{p\pi}{l_x}(x + \frac{l_x}{2})). \tag{B.6}$$

The Fourier transform of the pth x- or y-directed surface current basis function $f_{s_p}(x)$ is signified as $\widetilde{f_{s_p}}(k_x)$ and calculated as

$$\widetilde{f_{s_p}}(k_x) = \int_{-l_x/2}^{l_x/2} f_{s_p}(x) e^{jk_x x} dx, \tag{B.7}$$

where s can be x or y. Thus, the Fourier transform of eqs. (B.5) and (B.6) are

$$\widetilde{f_{x_p}}(k_x) = \frac{\pi l_x}{2} \left[(-1)^p \frac{J_1(\frac{p\pi + k_x l_x}{2})}{p\pi + k_x l_x} + \frac{J_1(\frac{p\pi - k_x l_x}{2})}{p\pi - k_x l_x} \right] \tag{B.8}$$

$$\widetilde{f_{y_p}}(k_x) = \frac{\pi l_x}{4} \left[(-1)^p J_0(\frac{p\pi + k_x l_x}{2}) + J_0(\frac{p\pi - k_x l_x}{2}) \right]. \tag{B.9}$$

The Fourier transforms of the surface currents presented above, are where in the next part, where spectral domain analysis is studied.

B.2 Spectral Electric Field Radiated by Spectral Basis Electric Strip Current

Upon Fourier transforming the electric surface current discussed above, into the spectral k_x domain, we have

$$\widetilde{\vec{J}(k_{x_m})} = \hat{a}_x \sum_{p=0}^{N_x} a_p \widetilde{f_{x_p}}(k_{x_m}) + \hat{a}_y \sum_{p=0}^{N_y} b_p \widetilde{f_{y_p}}(k_{x_m}), \quad m = \cdots, -1, 0, 1, \cdots . \tag{B.10}$$

This surface current corresponds to the discrete spectrum of the periodic structure. The $\widetilde{f_{s_p}}(k_{x_m})$ serves as the driving excitation for the grounded dielectric bare slab without the strips. The spectral field radiated by this spectral basis strip current (located in the layer above the slab) into the region above the grounded substrate is obtained from the numerical Green's function of the unloaded multilayer structure [69, 70], i.e.

$$\widetilde{E^{J_s}_{w_p}}(k_{x_m}) = \widetilde{G^{J_s}_{E_w}} . \widetilde{f_{s_p}}(k_{x_m}). \tag{B.11}$$

where the w subscript may denote either x or y component of the spectral E-field, and the superscript J_s signifies the type and component of the excitation current. The superscript of the Green's function $\widetilde{G}$ indicates the current source type and component, while the subscript represents the field type and component.

B.3 Spatial Electric Field Radiated by Entire Strip Array

Due to the periodicity along x with period dx, the inverse transform from spectral k_x to spatial x domain only requires a summation over discrete spectral components defined in eq. (B.4). Hence, the inverse transform of the spectral electric field of eq. (B.13) is written as

$$\hat{u}E_{u_p}^{J_s} = \frac{1}{d_x}\sum_{m}\left[\hat{a}_x\widetilde{E_{x_p}^{J_s}}(k_{x_m}) + \hat{a}_y\widetilde{E_{y_p}^{J_s}}(k_{x_m})\right]e^{-jk_{x_m}x}, \qquad m = \cdots, -1, 0, 1, \cdots. \tag{B.12}$$

where $\hat{u}$ denotes 'transverse' components. The summation performs through all integers of m. In fact, eq. (B.13) constitutes the spatial transverse component of the electric field radiated by the s-directed spatial pth basis strip current $f_{s_p}(x)$. Eventually, the total transverse spatial electric field radiated by both electric current components J_x and J_y is expressed as

$$\hat{u}E_{u}^{J_s} = \hat{a}_x\sum_{p=0}^{N_x} a_p E_{x_p}^{J_x} + \hat{a}_y\sum_{p=0}^{N_y} b_p E_{y_p}^{J_y}. \tag{B.13}$$

B.4 Spectral Excitation Current Source and its Radiated Electric Field

Depending on the polarization of the incident plane wave on the strip array, different types of spectral excitation current sources are entailed. Let this excitation current source be denoted generally by $\widetilde{K_{x;y}^{ex}}$, where K can be either J (electric) or M (magnetic), and the subscript can be either x or y labeling the component of the current. In the same manner as was shown in eq. (B.11)), the spectral electric field radiated by this excitation source is expressed as

$$\widetilde{E_w^{ex}} = \widetilde{G_{E_w}^{K_s}}.\widetilde{K_{sp}^{ex}} \tag{B.14}$$

evaluated at ($k_x = k_{x0}$, $k_y = k_{y0}$), being the forcing wavenumber of the incident plane wave, constituting the fundamental Floquet mode as well. The spatial field is correspondingly

$$\hat{u}E_u^{ex} = \left(\hat{a_x}\widetilde{E_x^{ex}} + \hat{a_y}\widetilde{E_y^{ex}}\right) e^{-jk_{x0}x}, \tag{B.15}$$

which is in the form of the excitation plane wave pertaining to a single (fundamental) Floquet mode. This source field is determinable with a known excitation current $\widetilde{K_{x,y}^{ex}}$.

The total spatial electric field in the region above the strip array is ultimately written as

$$E_u^{tot} = E_u^{J_s} + E_u^{ex} \tag{B.16}$$

B.5 Galerkin Weighting of Boundary Condition

The boundary condition requires the component of the total electric field tangential to the PEC strips to vanish on the strip surface (at $z = 0$). Applying this boundary condition zeroth strip results in

$$E_u^{tot}(-\frac{l_x}{2} \leq z \leq \frac{l_x}{2}) = 0 \tag{B.17}$$

Upon performing Galerkin weighting, a total number of equations that equals the number of unknown coefficients of the basis functions expanding the strip currents are generated. This system of equation can be cast into a matrix equation:

$$[\bar{Z}][\bar{I}] = [\bar{V}] \tag{B.18}$$

where the matrices involved in eq. (B.18) are defined as follows. The elements of $[\bar{Z}]$ are determined as

$$Z_{qp} = \int_{-\frac{l_x}{2}}^{\frac{l_x}{2}} \hat{u}E^{J_s}_{u_p} \cdot \hat{s} f_{s_q}(x)dx, \tag{B.19}$$

where u is the transverse direction and consisting of both x and y directions. s is the direction of the current basis function and can be either x or y. The elements of $[\bar{I}]$ are unknown current basis function coefficients and are determined as

$$[\bar{I}] = \begin{bmatrix} a_0 \\ \vdots \\ a_{N_x} \\ b_0 \\ \vdots \\ b_{N_y} \end{bmatrix}_{N_x+N_y+2}, \tag{B.20}$$

The elements of $[\bar{V}]$ can be determined as

$$V_q = -\int_{-\frac{l_x}{2}}^{\frac{l_x}{2}} \hat{u}E^{ex}_{u_p} \cdot \hat{s} f_{s_q}(x)dx. \tag{B.21}$$

Bibliography

[1] P.-S. Kildal, A. A. Kishk, and S. Maci, "Special issue on artificial magnetic conductors, soft/hard surfaces, and other complex surfaces," *IEEE Trans. on Antennas and Propagat.*, vol. 53, pp. 2–7, Jan. 2005.

[2] R. W. Ziolkowski and N. Engheta, "Metamaterial special issue introduction," *IEEE Transactions on Antennas and Propagation*, vol. 51, no. 10, pp. 2546–2546, Oct. 2003.

[3] N. Engheta and R. W. Ziolkowski, Eds., *Electromagnetic Metamaterials: Physics and Engineering Explorations.* John Wiley & Sons, July 2006.

[4] C. Caloz and T. Itoh, *Electromagnetic Metamaterials: Transmission Line Theory and Microwave Applications.* John Wiley & Sons, Nov. 2005.

[5] G. V. Eleftheriades and K. Balmain, Eds., *Negative Refraction Metamaterials: Fundamental Principles and Applications.* John Wiley & Sons, July 2005.

[6] A. Feresidis, G. Goussetis, S. Wang, and J. C. Vardaxoglou, "Artificial magnetic conductor surfaces and their application to low-profile high-gain planar antennas," *IEEE Trans. on Antennas and Propagat.*, vol. 53, no. 1, pp. 209–215, Jan. 2005.

[7] S. Wang, A. Feresidis, G. Goussetis, and J. Vardaxoglou, "High-gain subwavelength resonant cavity antennas based on metamaterial ground planes," *IEE Proc.-Microw. Antennas Propag.,*, vol. 153, pp. 1–6, Feb. 2006.

[8] M. Caiazzo, S. Maci, and N. Engheta, "A metamaterial surface for compact cavity resonators," *IEEE Antennas and Wireless Propagation Letters*, vol. 3, pp. 261–264, 2004.

[9] J. McVay, N. Engheta, and A. Hoorfar, "High impedance metamaterial surfaces using Hilbert-curve inclusions," *IEEE Microwave and Wireless Components Letters*, vol. 14, no. 3, pp. 130–132, Mar. 2004.

[10] H. Mosallaei and K. Sarabandi, "Antenna miniaturization and bandwidth enhancement using a reactive impedance substrate," *IEEE Trans. on Antennas and Propagat.*, vol. 52, no. 9, pp. 2403–2414, Sept. 2004.

[11] N. G. Alexopoulos and D. R. Jackson, "Fundamental superstrate (cover) effects on printed circuit antennas," *IEEE Trans. on Antennas and Propagat.*, vol. 32, no. 8, pp. 807–816, Aug. 1984.

[12] D. R. Jackson and N. G. Alexopoulos, "Gain enhancement methods for printed circuit antennas," *IEEE Trans. on Antennas and Propagat.*, vol. AP-33, no. 9, pp. 976–987, Sept. 1985.

[13] A. Foroozesh and L. Shafai, "Size reduction in the high gain antennas with dielectric superstrate using artificial magnetic conductors," in *Proc. ANTEM/URSI Int'l Symp.*, Montreal, QC,, July 17-19 2006, pp. 523–526.

[14] J. A. Kong, *Electromagnetic Wave Theory.* Cambridge, Massachusetts, USA: EMW Publishing, 2000.

[15] S. Tretyakov, *Analytical modeling in applied electromagnetics.* Norwood, MA: Artech house, 2003.

[16] D. K. Cheng, *Field and Wave Electromagnetics*, 2nd ed. USA: Addison-Wesley Publishing company, Inc., 1989.

[17] D. M. Pozar, *Microwave Engineering*, 2nd ed. New York: John Wiley & Sons, Inc., 1998.

[18] T. K. Wu, Ed., *Frequency selective surface and grid array,*. New Yok: John Wiley & Sons, Inc., 1995.

[19] B. Munk, *Frequency selective surface: Theory and Design,*. New York: John Wiley & Sons, Inc., 2000.

[20] J. C. Vardaxoglou, *Frequency Selective surfaces-analysis and design-*. Somerset, England: Research Studies Press LTD., 1997.

[21] R. Mittra, T. Cwik, and C. H. Chan, "Techniques for analyzing frequency selective surfaces-a review," *Proceedings of IEEE*, vol. 76, no. 12, pp. 1593–1615, Dec. 1988.

[22] A. Foroozesh and L. Shafai, "A proposed measurement method to extract the transmission and reflection properties of a periodic structure," in *10th International Symposium on Antenna Technology and Applied Electromagnetics*, Ottawa, Canada, July 2004, pp. 385–388.

[23] J. Huang, T.-K. Wu, and S.-W. Lee, "Tri-band frequency selective surface with circular ring elements," *IEEE Trans. Antennas and Propagat.*, vol. 42, pp. 165–175, Feb 1994.

[24] D. Sievenpiper, L. Zhang, R. F. J. Broas, N. G. Alexopolous, and E. Yablonovitch, "High-impedance electromagnetic surfaces with a for-

bidden frequency band," *IEEE Trans. on Microwave Theory and Tech.*, vol. 47, pp. 2059–2067, Nov. 1999.

[25] L. Akhoondzadeh-As and P. S. Hall, "Comparison of wideband planar dipole antenna performance on EBGs with and without vias," in *Proceeding of IEEE AP-S International Symposium*, no. 538, Albuquerque, NM, July 2006, pp. 2291–2294.

[26] F. Yang, A. Aminian, and Y. Rahmat-Samii, "A novel surface-wave antenna design using a thin periodically loaded ground plane," *Microwave Opt. Technol. Lett.*, vol. 47, pp. 240–245, Nov. 2005.

[27] *Ansoft Designer and HFSS*, www.ansoft.com, Ansoft Corporation, USA.

[28] R. F. Harrington, *Time-harmonic electromagnetic fields.* McGraw-Hill, Inc., 1961.

[29] G. Goussetis, A. P. Feresidis, and J. C. Vardaxoglou, "Tailoring the AMC and EBG characteristics of periodic metallic arrays printed on grounded dielectric substrate," *IEEE Trans. on Antennas Propagat*, vol. 54, pp. 82–89, Jan. 2006.

[30] R. Gonzalo, P. D. Maagt, and M. Sorolla, "Enhanced patch-antenna performance by suppressing surface waves using photonic-bandgap substrates," *IEEE Trans. on Microwave Theory and Tech.*, vol. 47, pp. 2131–2138, Nov. 1999.

[31] D. J. Kern, D. H. Werner, A. Monorchio, L. Lanuzza, and M. J. Wilhelm, "The design synthesis of multiband artificial magnetic conductors using high impedance frequency selective surfaces," *IEEE Trans. on Antennas and Propagat.*, vol. 53, no. 1, pp. 8–17, Jan. 2005.

[32] S. Maci, M. Caiazzo, A. Cucini, and M. Casaletti, "A pole-zero matching method for ebg surfaces composed of a dipole fss printed on a grounded dielectric slab," *IEEE Trans. on Antennas and Propagat.*, vol. 53, no. 1, pp. 70–81, Jan. 2005.

[33] P.-S. Kildal, "Artificially hard and soft surfaces in electromagnetics," *IEEE Trans. on Antennas and Propagat.*, vol. 38, no. 10, pp. 1537–1544, Nov. 1990.

[34] T. Zhao, D. R. Jackson, J. T. Williams, and A. A. Oliner, "General formulas for 2-D leaky-wave antennas," *IEEE Trans. on Antennas and Propagat.*, vol. 53, pp. 3525–3533, Nov. 2006.

[35] H. A. Kalhor, "Electromagnetic scattering by a dielectric slab loaded with a periodic array of strips over a ground plane," *IEEE Trans. on Antennas Propagat*, vol. 36, no. 36, pp. 147–151, Jan. 1988.

[36] A. Foroozesh, M. Fallah-Rad, D. Qu., and L. Shafai., "A wideband high-gain microstrip patch antenna with high-impedance electromagnetic band-gap ground plane," in *Proceedings of 12th International Symp. of ANTEM/URSI*, Montreal, July 2006, pp. 53–56.

[37] F. Yang and Y. Rahmat-Samii, "Reflection phase characterizations of the EBG ground plane for low profile wire antenna applications," *IEEE Trans. Antennas Propagat.*, vol. 51, pp. 2691–2703, Oct. 2003.

[38] C.-W. Lee and H. Son, "Analysis of electromagnetic scattering by periodic strip grating on a grounded dielectric/magnetic slab for arbitrary plane wave incidence case," *IEEE Trans. on Antennas and Propagat.*, vol. 47, no. 9, pp. 1386–1392, Sept. 1999.

[39] A. Ishimaru, *Electromagnetic wave propagation radiation and scattering.* Prentice-Hall international, Inc., 1989.

[40] C. M. Butler, "General solutions of the narrow strips (and slot) integral equations," *IEEE Trans. Antennas Propagat.*, vol. 33, no. 10, pp. 1085–1090, Oct. 1985.

[41] M. R. Spiegel, *Mathematical Handbook of formulas and Tables.* Schaum's outline series, 1968.

[42] J. V. Bladel, *Singular Electromagnetic Fields and Sources.* New York: The Institute of Electrical and Electronics Engineers, Inc., 1991.

[43] M. M. N. Kehn, "Miniaturized hard waveguides in multifunction array antennas," Ph.D. dissertation, Chalmers university of technology, Goteborg, Sweden, 2005.

[44] M. M. N. Kehn and P.-S. Kildal, "Miniaturized rectangular hard waveguides for use in multifrequency phased arrays," *IEEE Trans. on Antennas Propagat*, vol. 53, pp. 100–109, 2005.

[45] H. Y. Yang and N. G. Alexopoulos, "Gain enhancement methods for printed circuit antennas through multiple superstrates," *IEEE Trans. on Antennas and Propagat.*, vol. 35, pp. 860–863, July 1987.

[46] X. H. Wu, A. A. Kishk, and A. W. Glisson, "A transmission line method to compute the far-field radiation of arbitrarily directed hertzian dipoles in multilayer dielectric structure: Theory and applications," *IEEE Trans. on Antennas and Propagat.*, vol. 54, pp. 2731–2741, Oct. 2006.

[47] D. R. Jackson and A. A. Oliner, "A leaky-wave analysis of the high-gain printed antenna configuration," *IEEE Transactions on Antennas and Propagation*, vol. 36, no. 7, pp. 905–910, July 1988.

[48] A. Foroozesh and L. Shafai, "Investigation of reflection properties of reactive impedance substrates," in *19th Canadian Conference on Electrical and Computer Engineering*, Saskatoon, Canada, May 2005, pp. 1881–1884.

[49] F. Kaymaram and L. Shafai, "Enhancement of microstrip antenna directivity using double-superstarte configurations," *Canadian Journal of Electrical and Computer Engineering*, vol. 32, no. 2, pp. 77–82, 2007.

[50] A. Foroozesh and L. Shafai, "Effects of the excitation source position on the radiation characteristics of the antennas with a cover layer: A few case studies," in *Proceeding of IEEE AP-S International Symposium*, July 9-14 2006, pp. 1507–1510.

[51] ——, "2-D truncated periodic leaky-wave antennas with reactive impedance surface ground planes," in *Proc. IEEE Int. Symp.*, Albuquerque, NM,, July 9-14 2006, pp. 15–18.

[52] C. A. Balanis, *Antenna Theory Analysis and Design*, 2nd ed. John Wiley & Sons, Inc., 1997.

[53] W. L. Stutzman and G. A. Thiele, *Antenna Theory and Design.* John Wiley and sons, 1981.

[54] R. Gardelli, M. Albani, and F. Capolino, "Array thinning by using antennas in a fabryperot cavity for gain enhancement," *IEEE Trans. Antennas Propagat.*, vol. 54, pp. 1979–1990, 2006.

[55] D. Qu, L. Shafai, and A. Foroozesh, "Improving microstrip patch antenna performance using ebg substrates," *IEE Proc.-Microw. Antennas Propag.*, vol. 153, no. 6, pp. 558–563, December 2006.

[56] M. A. Hiranandani, A. Yakovlev, and A. Kishk, "Artificial magnetic conductors realised by frequency-selective surfaces on a grounded dielectric slab for antenna applications," *IEE Proc.-Microw. Antennas Propag.*, vol. 153, no. 5, pp. 487–493, October 2006.

[57] A. Foroozesh and L. Shafai, "Performance enhancement of a microstrip patch antenna using high impedance surfaces and different ground plane sizes," in *Proceeding of ISAP07*, Niigata, Japan, August 2007, pp. 1158–1161.

[58] ——, "Application of combined electric and magnetic conductor ground planes for antenna performance enhancement," *To appear in Canadian journal of electrical and computer engineering.*

[59] ——, "Investigation of the soft/hard surface ground plane effects on far-field radiation properties of high-gain planar antennas with hertzian dipole excitation," in *Proceeding of URSI-2007*, Ottawa, Canada, July 2007.

[60] G. Von Trentini, "Partially reflecting sheet arrays," *IRE Trans. on Antennas and Propagat.*, vol. AP-4, pp. 666–671, Oct. 1956.

[61] T. Zhao, D. R. Jackson, J. T. Williams, H. Y. Yang, and A. A. Oliner, "2-D periodic leaky-wave antennaspart i: Metal patch design," *IEEE Trans. on Antennas and Propagat.*, vol. 53, pp. 3505–3514, 2005 2005.

[62] T. Zhao, D. R. Jackson, and J. T. Williams, "2-D periodic leaky-wave antennaspart ii: Slot design," *IEEE Trans. on Antennas and Propagat.*, vol. 53, pp. 3515–3524, 2005 2005.

[63] A. F. Peterson, S. L. Ray, and R. Mittra, *Computational Methods for Electromagnetics.* IEEE press, 1997.

[64] R. E. Collin, *Foundations for microwave engineering*, 2nd ed. USA: McGraw-Hill, 1992.

[65] Y. Vardaxoglou and F. Capolino, "Review of highly-directive flat-plate antenna technology with metasurfaces and metamaterials," in *Proceedings of the 36th European Microwave Conference*, September 2006.

[66] J. Kelly, G. Passalacqua, A. P. Feresidis, F. Capolino, M. Albani, and Y. C. Vardaxoglou, "Simulations and measurements of dual-band 2-D periodic leaky wave antenna," in *Proceedings of Loughborough Antennas and Propagation Conference*, April 2007, pp. 293–296.

[67] X. H. Wu, A. A. Kishk, and A. W. Glisson, "A transmission line method to compute the far-field radiation of arbitrary hertzian dipoles in a multilayer structure embedded with PEC strip interfaces," *IEEE Trans. on Antennas and Propagat.*, vol. 55, no. 11, pp. 3191–3198, 2007.

[68] K. Uchida, T. Noda, and T. Matsunaga, "Spectral domain analysis of electromagnetic wave scattering by an infinite metallic grating," *IEEE Trans. on Antennas and Propagat.*, vol. 35, no. 10, pp. 46–52, Oct. 1987.

[69] Z. Sipus, R. L. P.-S. Kildal, and M. Johansson, "An algorithm for calculating Green's functions of planar, circular cylindrical and spherical multilayer substrates," *Applied Computational Electromagnetics Society (ACES) J.*, vol. 13, no. 3, pp. 243–254, Nov. 1998.

[70] M. Ng Mou Kehn, M. Nannetti, A. Cucini, S. Maci, and P.-S. Kildal, "Analysis of dispersion in dipole-FSS loaded hard rectangular waveguide," *IEEE Trans. on Antennas and Propagat.*, vol. 54, pp. 2275–2282, Aug. 2006.